Magnetic Fields in the Early Solar System

by

Roger R. Fu

B.A. Earth and Planetary Sciences and Astrophysics
Harvard University, 2009

SUBMITTED TO THE DEPARTMENT OF EARTH, ATMOSPHERIC AND PLANETARY SCIENCES IN PARTIAL FULFULLMENT OF THE REQUIREMENTS FOR THE DEGREE OF

DOCTOR OF PHILOSOPHY IN EARTH, ATMOSPHERIC AND PLANETARY SCIENCES
AT THE
MASSACHUSETTS INSTITUTE OF TECHNOLOGY

SEPTEMBER 2015

Signature of Author: Signature redacted
Department of Earth, Atmospheric and Planetary Sciences
June 10, 2015

Certified by: Signature redacted
Benjamin P. Weiss
Professor of Planetary Sciences
Thesis Supervisor

Accepted by: Signature redacted
Robert D. van der Hilst
Schlumberger Professor of Earth Sciences
Department Head, Department of Earth, Atmospheric and Planetary Sciences

Magnetic Fields in the Early Solar System

by

Roger R. Fu

Submitted to the Department of Earth, Atmospheric and Planetary Sciences
on June 10, 2015 in Partial Fulfillment of the
Requirements for the Degree of Doctor of Philosophy in
Earth, Atmospheric and Planetary sciences

ABSTACT

The first magnetic fields in the solar system were embedded in the ionized gas of the protoplanetary disk itself. Soon after, newly formed protoplanets may have harbored magnetic core dynamos. Paleomagnetic analysis of ancient samples permits direct constraints on these early solar system magnetic fields.

Here I present paleomagnetic studies of several classes of meteorites. Experiments on inclusions of chondritic meteorites have led to some of the first constraints on the intensities of protoplanetary disk magnetic fields. Meanwhile, measurements of eucrites, a class of achondrites believed to originate from the asteroid Vesta, suggest that Vesta once hosted a magnetic core dynamo. New techniques developed during the course of these measurements permit ongoing and future investigations of the remanent magnetizations of new meteorites and terrestrial rocks.

In support of the paleomagnetic results, I present analytical and numerical modeling of magnetic dust grain dynamics in the solar nebula and of the interior dynamics of differentiated asteroids capable of hosting magnetic dynamos.

Thesis Supervisor: Benjamin P. Weiss
Title: Professor of Planetary Sciences

Acknowledgments

The first time I talked to Ben Weiss, I had skimmed his MIT homepage (the one paragraph description, not the full website) and understood that his research was on "some planetary sciences thing." Not knowing anything about paleomagnetism, I joined his laboratory as a PhD student because we had a very pleasant lunch at Amelia's Café. Over the course of an hour and a half, Ben struck me as someone with whom I could work very well.

Nearly five years later, it has become clear that that was one of the best decisions I've ever made. I like to think that I was being particularly prescient that day at Amelia's, grasping in some inarticulate way that in the years to come Ben would so charismatically guide me to experience the joys of research. But honestly, I probably just got very lucky.

In any case, the first acknowledgment for this thesis must go to Ben Weiss, from whom I have learned and inherited so much. Another great share of the credit belongs to the other EAPS faculty members who have been so selfless with their time in all of our interactions- Lindy Elkins-Tanton, Tim Grove, Brad Hager, Maria Zuber, Sam Bowring, Hilke Schlichting, and Rick Binzel just to name the most prominent.

To continue the theme of my exceptional luck, I wandered into a community full of kind and communicative people. Even as a young graduate student, establishing a rewarding collaboration was usually as simple as a handshake followed by a thoughtful conversation. I cannot possibly list all of the people whose ideas and advice have been worked into this thesis. Perhaps the most relevant acknowledgment I can give to all of my mentors and collaborators is that I sincerely hope to the privilege of working with you for many more years to come.

Finally, I have been blessed with supportive and stable friends and family. My fellow EAPS students, my parents, and my girlfriend, Teresa Little Condor Pereira. Your companionship kept me going.

Foreword

To orient the readers of this thesis and to direct them to the most relevant text, I have included a brief review of planet formation in Chapter 1, which is limited to the sub-topics most related to the work presented here. The final paragraphs of Chapter 1 summarize the later Chapters and are intended as an expanded Table of Contents.

The Chapters 2 through 6 each stand alone with detailed introductory and summary sections. They are based on the following publications:

Fu, R.R. and Weiss, B.P. (2012) Detrital remanent magnetization in the solar nebula. *J. Geophys. Res. 117*, E02003. (Chapter 3)

R.R. Fu, B.P. Weiss, D.L. Shuster, J. Gattacceca, T.L. Grove *et al.* (2012) An ancient core dynamo in asteroid Vesta. *Science* 338, 238-241. (Chapter 6)

R.R. Fu and L.T. Elkins-Tanton (2014) The fate of magmas in planetesimals and the retention of primitive chondritic crusts. *Earth Planet. Sci. Lett.* 390, 128-137. (Chapter 5)

R.R. Fu, B.H. Hager, A.I. Ermakov, and M.T. Zuber. (2014) Efficient early global relaxation of asteroid Vesta. *Icarus* 240, 133-145. (Chapter 7)

R.R. Fu, E.A. Lima, and B.P. Weiss. (2014) No Nebular magnetization in the Allende CV carbonaceous chondrite. *Earth Planet. Sci. Lett.* 404, 54-66. (Chapter 4)

R.R. Fu, B.P. Weiss, E.A. Lima, R.J. Harrison, X.-N. Bai *et al.* (2014) Solar nebula magnetic fields recorded in the Semarkona meteorite. *Science* 346, 1089-1092. (Chapter 2)

Table of Contents

Chapter 1: Introduction to planet formation

Instead of attempting a more comprehensive review of planet formation, here I focus on two aspects of the process most closely related to the paleomagnetic and theoretical work presented in the following chapters. First, I discuss observations, models, and implications of nebular gas dynamics, which is intimately connected to the presence of magnetic fields. Second, I summarize the formation of the early planetesimals in the 10s to 100s km size range, which were the first bodies in the solar system to undergo igneous differentiation and potentially harbor magnetic dynamos. Additional review of nebula dynamics is provided at the beginning of Chapters 3 and 4. A more comprehensive exposition of the processes and open questions in planet formation and early evolution is provided at the beginning of Chapters 5 and 6.

Planetary systems form in gas-rich protoplanetary accretion disks with half lives of ~3 million years [My; e.g., Haisch, Lada, & Lada, (2001)]. These objects broadly correspond to Class II and Classical T Tauri young stellar object observed in the infrared and visible wavelengths, respectively (Williams & Cieza 2011). The specific protoplanetary disk in which the solar system planets formed is known as the solar nebula.

Fundamental challenges remain in our understanding of protoplanetary disks dynamics and their role in planet formation. At the global scale, depletion of the mass of a protoplanetary disk occurs via accretion onto the star, magnetically launched disk winds, and photoevaporation from stellar irradiation (Alexander et al. 2014). Based on direct observations of evolving protoplanetary disks, the infall of gas onto the host star accounts from between 10^{-9} and 10^{-7} M_{Sun} yr^{-1} for sun-like stars, where M_{sun} is the mass of the sun (Hartmann et al. 1998; Herczeg & Hillenbrand 2008). This mode of disk depletion is likely the dominant effect during the early evolution of protoplanetary disks; therefore, its efficiency exerts a strong effect on the subsequent evolution of the protoplanetary system and the duration of the disk itself (Alexander et al. 2014).

Despite its central role, the physical origin of gas accretion remains contentious. Specifically, the rapid inward transport of gas requires an efficient mechanism for the outward transport of angular momentum transport. The velocity field in a Keplerian disk

implies that viscous coupling between material on adjacent orbits would naturally lead to the outward transfer of angular momentum (Lynden-Bell & Pringle 1974). However, given that the kinematic viscosities of nebular gas are of order 10^3 m^2 s^{-1}, dimensional analysis shows that the viscous coupling of nebular gas alone falls short of supplying the observed accretion rates by $\sim 10^7$. This result implies that more efficient mechanisms of angular momentum transport must operate in protoplanetary disks to explain the brief lifetime of such objects and the emergence of planetary systems.

Magnetic fields lie at the heart of several proposed solutions to the problem of angular momentum transport. A combination of solar x-rays, cosmic rays, radioactive decay, and high temperatures partially ionize the nebular gas. The ionization fraction ($n_{electron}/n_H$, where n is the number density) varies widely throughout the disk, but is predicted to vary between 10^{-14} and 10^{-7} in the planet forming regions, which the disk surfaces sustaining the highest ionization fractions (Turner & Sano 2008; Bai 2011). Despite these low numerical values, this ionization implies a weak but dynamically significant coupling to magnetic fields.

Two distinct proposed mechanisms invoke magnetic fields to explain the rate of nebular gas accretion. First, the magnetorotational instability (MRI) proposes that magnetic fields may introduce significant turbulence and therefore turbulent viscosity to the nebular gas, thereby enhancing the coupling of material at adjacent orbital radii and promoting the outward transfer of angular momentum (Chandrasekhar 1960; Balbus & Hawley 1991; Hawley & Balbus 1991). If the MRI operated in the planet-forming, it has the potential to not only address the question of angular momentum transports, but also provide a mechanism to explain the origin of turbulence and possibly the formation of the first planetesimals (Hughes et al. 2011; Johansen 2009). However, the viability of the MRI in protoplanetary disks hinges on the strength of existing magnetic fields. Strong magnetic fields (greater than several hundred to thousand μT at 1 AU) would preclude the growth of the instability while weak fields of less than ~1 μT would fail to supply the adequate rate of gas accretion (Balbus & Hawley 1998; Wardle 2007). Second, the magnetocentrifugal winds (MCW) predicts that large scale, organized magnetic fields in the absence of magnetohydrodynamic (MHD) turbulence can account for angular momentum transport. To match the observed accretion rates, this mechanism requires

magnetic fields in the range of approximately 0.1 to 10 μT (Bai & Goodman 2009). Direct constraints on magnetic fields strengths are therefore critical for understanding the role of magnetic fields in shaping the fundamental properties of protoplanetary disks.

Turbulence in the solar nebula, potentially due to the MRI or other magnetic mechanisms, may have contributed to the formation of the first planetesimal via the active concentration of solid particles into self-gravitating clumps (Cuzzi et al. 2008; Johansen et al. 2007). Such concentration mechanisms promise to circumvent one of the key problems of planet formation- the destructive collisions between decimeter and greater solid aggregates known as the "meter size barrier." Despite their potential important, no experimental or observational data exist to validate the role of these mechanisms in forming planetesimals in our solar system or others.

After the accretion of the first planetesimal objects, possibly via the turbulent concentration mechanisms named above, sufficiently large objects accreting within ~1.5 My of calcium aluminum-rich inclusions (CAIs) may have differentiated due to the effect of short-lived radionuclides (Ghosh & McSween 1998; Hevey & Sanders 2006; Elkins-Tanton et al. 2011; Sahijpal & Gupta 2011; Šrámek et al. 2012). Such bodies may have harbored conducting metal cores that potentially generated dynamo magnetic fields (Weiss et al. 2008; Weiss et al. 2010; Sterenborg & Crowley 2013). Measurements of the surface magnetic fields on such bodies may therefore constrain the existence of a metal core and the thermal evolution of the deep interior.

In the following chapters, I begin with work relevant to the magnetic environment of the nebular gas itself and proceed to paleomagnetic and theoretical work on the accretion of planetesimals and their development into fully differentiated bodies.

Chapter 2, based on Fu, Weiss, et al. (2014), first reviews previous results contraining magnetic fields in protoplanetary disks and presents our recent paleomagnetic experiments on the Semarkona chondrite. Chondrules from this highly primitive meteorite have led to the first reliable estimates of magnetic field strengths in the planet-forming region of a protoplanetary disk. The Chapter ends with a discussion of astrophysical implications.

Chapter 3 contains exclusively theoretical calculations of a hypothesized mechanism of remanent magnetization acquisition in the solar nebula. This process, which we call

accretional detrital remanent magnetization or ADRM, relies on "compass needle" type alignment of ferromagnetic dust grains to background magnetic fields, which may result in bulk magnetization of chondritic materials detectable via paleomagnetic experiments or spacecraft-borne magnetometry. This Chapter is based on Fu & Weiss (2012).

Chapter 4 presents paleomagnetic work on the Allende CV carbonaceous chondrite. It begins with a review of past attempts to constrain nebular magnetic fields using Allende and other chondrites but ultimately argues that Allende was magnetized in a magnetic field generated by a core dynamo that lasted <40 My. This Chapter is based on Fu, Lima, et al. (2014).

Chapter 5 is composed of theoretical calculations published in Fu & Elkins-Tanton (2014), which show that silicate melts on selected chondritic parent bodies, including that of the CV chondrites, may remain negatively buoyant. This allows for the retention of chondritic lids on differentiated asteroids, supporting the paleomagnetic interpretation of core dynamos on chondritic parent bodies.

Chapter 6 continues the paleomagnetic investigation of planetesimal magnetic fields by analyzing the magnetic recording of an HED meteorite, ALHA81001. This Chapter follows Fu et al. (2012) by presenting paleomagnetic evidence that a magnetic field existed on the Vestan surface 3.7 billion years ago (Ga), suggesting the existence of an early core dynamo.

Chapter 7 presents viscoplastic finite element simulations of global deformation on early Vesta. These models show that early Vesta achieved a degree-2 figure significantly more hydrostatic than that of the present. We use this information and topography data from the Dawn spacecraft to argue that Vesta is the smallest solar system body to have approached hydrostatic equilibrium, which implies an ancient rotation rate and degree of heating required by an ancient core dynamo. This Chapter is based on Fu, Hager, et al. (2014).

Chapter 2: Paleomagnetic determination of accretion disk magnetic fields

2.1. Introduction

Astronomical observations of young stellar objects indicate that early planetary systems evolve through a protoplanetary disk phase in <5 million years (My) following the collapse of their parent molecular clouds (Haisch et al. 2001; Hartmann et al. 1998). Disk evolution on such short timescales requires highly efficient inward transport of mass accompanied by outward angular momentum transfer, which allows disk material to accrete onto the central star while delivering angular momentum out of the protoplanetary system.

The mechanism of this rapid mass and angular momentum redistribution remains unknown. Several proposed processes invoke a central role for nebular magnetic fields. Among these, the magnetorotational instability (MRI) and magnetic braking predict magnetic fields with intensities of ~100 μT at 1 AU in the active layers of the disk (Wardle 2007; Bai & Goodman 2009). Alternatively, transport by magnetocentrifugal wind (MCW) requires large-scale, ordered magnetic fields stronger than ~10 μT at 1 AU. Finally, non-magnetic effects such as the baroclinic and Goldreich-Schubert-Fricke instabilities may be the dominant mechanism of angular momentum transport in the absence of sufficiently strong magnetic fields (Turner et al. 2014). Direct measurement of magnetic fields in the planet-forming regions of the disk can potentially distinguish among and constrain these hypothesized mechanisms.

Although current astronomical observations cannot directly measure magnetic fields in planet-forming regions (Crutcher 2012), paleomagnetic experiments on meteoritic materials can potentially constrain the strength of nebular magnetic fields. Chondrules are millimeter-sized lithic constituents of primitive meteorites that formed in transient heating events in the solar nebula. If a stable field was present during cooling, they should have acquired a thermoremanent magnetization (TRM), which can be characterized via paleomagnetic experiments. Besides assessing the role of magnetic fields in disk evolution, such paleomagnetic measurements would constrain the currently unknown mechanism of chondrule formation.

Chondrules likely constituted a significant fraction of the mass of asteroids and terrestrial planet precursors and may have facilitated the accretion of the first planetesimals (Cuzzi et al. 2008; Nakamura et al. 2011). The formation of chondrules therefore very likely represents a key stage in the evolution of the early solar system. The ambient magnetic field strength is a distinguishing characteristic among chondrule formation models. The x-wind model implies strong stellar fields of >80-400 μT (Shu et al. 1996). In contrast, magnetic fields in the nebular shock and planetesimal collision models are likely significantly lower than 100 μT (Desch & Connolly 2002; Desch & Mouschovias 2001).

The possibility that chondrules in primitive meteorites could constrain nebular magnetic fields has been recognized previously. Lanoix et al. (1978) found that isolated chondrules from the Allende CV carbonaceous chondrite carry a strong component of magnetization blocked above 330°C. They concluded that the apparent paleointensity of this magnetization, which ranged up to 1600 μT, provides evidence for very strong fields in the solar nebula. However, because Lanoix et al. (1978) measured unoriented chondrules, the authors were unable to demonstrate a pre-accretional origin for the observed magnetization (see below). In fact, the very high paleointensities and the failure of later experiments to duplicate these results strongly indicate that the purported pre-accretional magnetization component studied in Lanoix et al. (1978) was due to contamination by strong artificial magnetic fields (e.g., from hand magnets) and does not offer constraints on nebular magnetic fields (Wasilewski 1981; Weiss et al. 2010).

Two later studies of mutually-oriented Allende chondrules (Sugiura et al. 1979; Sugiura & Strangway 1985) identified a high-temperature component of magnetization blocked above 300°C with random directions that passes the paleomagnetic conglomerate test. The authors concluded that this magnetization component represents pre-accretional magnetization.

However, no new paleointensity was reported for this component. More importantly, the conglomerate test alone is insufficient for establishing a primary origin for the high temperature chondrule magnetization. Post-accretional recrystallization of magnetic phases in a weak ambient field may result in the acquisition of random magnetizations at sub-chondrule scales (Gattacceca et al. 2003; Uehara et al. 2011). A recent

paleomagnetic study of Allende chondrules showed that high temperature magnetization directions among *subsamples* of single chondrules are randomly oriented, ruling out a pre-accretional TRM origin for this magnetization component (Fu, Lima, et al. 2014). Furthermore, petrographic studies of Allende show that all magnetic phases likely formed during aqueous alteration on the parent body (Brearley & Krot 2012; Krot, Petaev, Scott, et al. 1998; Krot et al. 1997; Choi et al. 1997; Haggerty & McMahon 1979). Therefore, the heterogeneity of the high temperature magnetization in Allende at the sub-chondrule scale suggests that it is instead a crystallization remanent magnetization (CRM) acquired during formation of magnetic phases in a weak to null field on the CV parent body (Fu, Lima, et al. 2014). This precludes the retention of any pre-accretional magnetization in Allende.

A number of theoretical studies have cited paleointensities of ~100 μT to >1000 μT as experimental constraints of nebular magnetic fields from the Allende studies noted above (Shu et al. 1996; Desch & Connolly 2002; Levy & Araki 1989; Stepinski 1992; Nübold & Glassmeier 2000; Spruit 1996). However, these paleointensities correspond to a low temperature, post-accretional component of magnetization removed below 300°C (Wasilewski 1981; Carporzen et al. 2011) or to magnetization found in unoriented chondrules likely exposed to strong artificial fields as described above (Sugiura et al. 1979). Such paleointensities, because they are derived from post-accretional components of magnetization, offer no constraint on the magnetic field in the solar nebula.

In the case of ordinary chondrites, Funaki et al. (1981) conducted paleomagnetic experiments on separated chondrules from the L6 chondrite ALH-769. These authors found widely scattered NRM directions in chondrules and suggested that they recorded nebular magnetic fields. However, subsequent paleomagnetic work on ordinary chondrites has shown that chondrule magnetizations in high petrologic grade specimens have been strongly overprinted by the post-accretional formation of tetrataenite, which results in random magnetizations at the sub-chondrule scale and may lead to a false-positive conglomerate test (Uehara et al. 2011). Moreover, the >1000°C estimated metamorphic temperature of type 6 chondrites (Bennett & McSween 1996) imply that ALH-769 cannot retain pre-accretional magnetization.

Meanwhile, astronomical observations of T Tauri stars allow the measurement of strong magnetic fields within several radii of the central star by observing the Zeeman splitting of stellar absorption lines (Johns-Krull 2007; Johns-Krull et al. 2009; Donati et al. 2005). Because magnetic fields in the protoplanetary disk are orders of magnitude weaker than the ~0.1 T fields detected near the central star, Zeeman splitting observations of protoplanetary disk fields are limited to low-density regions, which are sampled by lower-frequency lines that can be measured with sufficient signal-to-noise ratio (Crutcher et al. 1996). As a consequence, Zeeman splitting observations in thermal emission lines are currently limited to H_2 number densities $<10^{12}$ m^{-3} [from CN lines; Falgarone et al. (2008)]. Masers, due to their high intensity, can effectively sample higher-density regions with H_2 number density $<10^{17}$ m^{-3} (Crutcher 2012). Assuming a minimum mass solar nebula (MMSN) (Hayashi 1981), such densities occur at several scale heights above the accretion disk midplane at 1 AU or in the midplane at large radii (>25 AU) from the star. Higher mass nebula models would place these densities even farther from the midplane and at greater orbital radii. Finally, polarimetry of molecular clouds can detect the alignment of dust grains, which, combined with knowledge of local turbulence and gas density, may be used to estimate magnetic field strength (Chandrasekhar & Fermi 1953). However, these estimates require spatially resolved maps of local grain polarization direction, which currently limits magnetic field strength measurements to averages across ~100 AU and larger scales (Stephens et al. 2014; Girart et al. 2006), although future observations using the Atacama Large Millimeter Array (ALMA) can potentially provide field strength estimates at smaller scales relevant to the protoplanetary disk (Hughes et al. 2013).

In summary, previous paleomagnetic experiments have been unable to isolate pre-accretional magnetization while astronomical observations of protoplanetary disks cannot currently constrain the magnetic field strength in the planet-forming regions. This motivates the present effort to identify and characterize pre-accretional remanence in chondrules that, unlike those in Allende, escaped significant post-accretional remagnetization.

2.2. The Semarkona meteorite

As summarized above, previous paleomagnetic measurements of individual chondrules have focused mostly on the Allende CV chondrite (Sugiura & Strangway 1985). However, due to extensive aqueous alteration on the CV parent body, magnetic phases in Allende chondrules are secondary and do not retain pre-accretional magnetization [i.e., magnetization acquired after the last heating of chondrules in the nebula and before the accretion of the meteorite's parent body; Fu et al. (2014)]. Reliable recovery of pre-accretional magnetization requires samples that have avoided significant post-accretional remagnetization processes.

Among the most pristine known meteorites is the Semarkona LL3.00 ordinary chondrite. We conducted paleomagnetic studies on Semarkona, focusing in particular on dusty olivine-bearing chondrules (Fig. 2.1). Dusty olivine crystals consist of sub-micrometer sized grains of nearly pure body centered cubic (bcc) Fe (kamacite) embedded in forsteritic olivine (Leroux et al. 2003). Such olivine grains are found in approximately one in ten chondrules in ordinary chondrites.

Since its observed fall and recovery in 1940, the Semarkona chondrite has been studied intensively due to its rarity as an ordinary chondrite that has experienced the mildest metamorphic heating and aqueous alteration on its parent body. As described in the main text, the mild metamorphism of Semarkona to less than 200-260°C (Cody et al. 2008; Weiss et al. 2007) and the lack of significant aqueous alteration or strong shock implies that any pre-accretional magnetization should be isolated upon thermal demagnetization to ~450°C.

Even so, not all magnetic carriers in Semarkona chondrules may retain pre-accretional magnetization. The Ni content of most FeNi metal in ordinary chondrites ranges between 5 and 30% (Reisener & Goldstein 2000; Jarosewich 1990). Metal grains with such Ni concentrations exist as metastable martensite (α_2-FeNi) after their rapid cooling following chondrule formation (Reisener & Goldstein 1999; Reisener & Goldstein 2003). Subsequent metamorphic heating on the parent body, even to the extent

observed in type 3.0 ordinary chondrites, is sufficient to cause exsolution into kamacite (α-FeNi) and taenite (γ-FeNi), which leads to the plessite texture (Kimura et al. 2008). Such recrystallization likely leads to the loss of pre-existing magnetization, especially as the transformation from taenite to kamacite involves a change of lattice symmetry from fcc to bcc (Dunlop & Ozdemir 1997a). Ni-rich (>5.7 wt%) metal grains in Semarkona have been observed with plessitic exsolution textures while metal grains with lower Ni content are within the kamacite stability field and have been observed to be homogeneous with no sign of recrystallization (Reisener & Goldstein 2003; Kimura et al. 2008). Pre-accretional magnetization, if preserved in Semarkona chondrules, is therefore expected to be carried by grains with <5.7 wt% Ni, which are stable against plessitic exsolution.

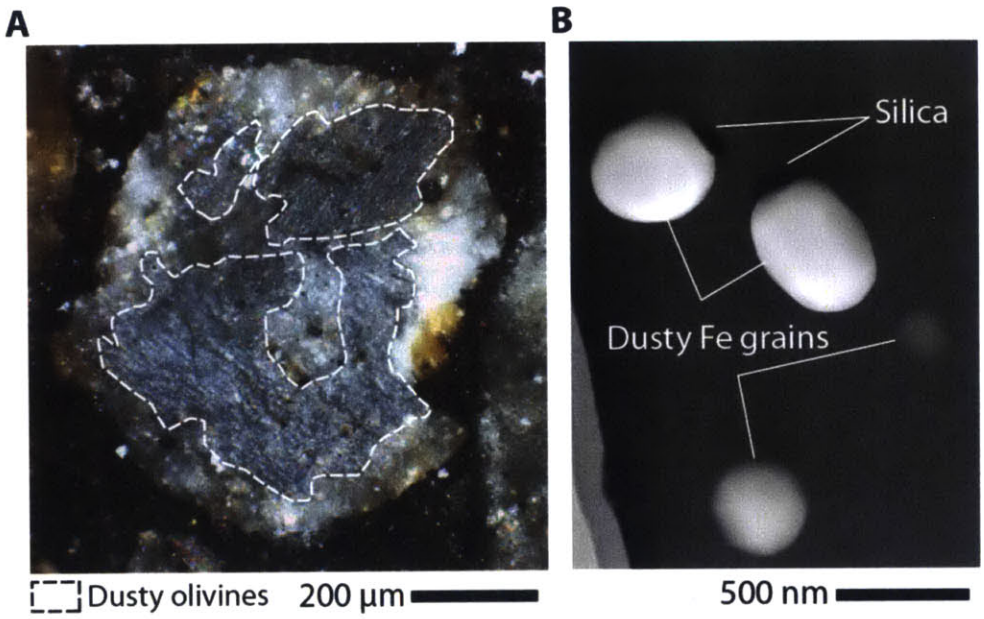

Figure 2.1. Dusty olivine-bearing chondrules from the Semarkona meteorite. (**A**) Optical photomicrograph of chondrule DOC4 showing the location of dusty olivine grains. Image taken in reflected light with crossed polarizers. (**B**) Annular dark field scanning transmission electron microscope (STEM) image of four dusty olivine Fe grains from chondrule DOC5. Brightness in image reflects column-averaged atomic number; darker grains are smaller in size, implying a higher relative abundance of olivine at their location and hence a lower mean atomic number. Note the euhedral morphology and chemical homogeneity of the Fe grains, which indicate the lack of secondary recrystallization and alteration. Such Fe grains are the primary carriers of pre-accretional magnetization in Semarkona chondrules.

Previous petrographic studies of dusty olivine metals have shown that they contain <2 wt% Ni, placing them well within the kamacite stability field and precluding plessitic

exsolution (Rambaldi & Wasson 1982). Furthermore, previous transmission electron microscopy (TEM) imaging of dusty olivine metal grains has revealed no exsolution textures (Leroux et al. 2003).

To confirm the low Ni content of dusty olivine metal grains used in our paleomagnetic experiments, we used energy dispersive spectroscopy (EDS) on a scanning TEM to map elemental composition on a ~900×1900 μm area of sample DOC5 that contains three dusty metal grains (Fig. 2.2). All paleomagnetic measurements were completed prior to these petrographic experiments. We used a FEI Titan 300 kV STEM housed in the Center for Nanoscopy at the Technical University of Denmark. Maps of the elements Fe, Ni, Mg, Si, and O confirm that dusty metal grains contain Fe with <1 wt% Ni and no plessitic exsolution textures. At the same time, the surrounding olivine is essentially pure forsterite with <1 wt% Fe content, which is in agreement with previous studies of dusty olivine compositions (Leroux et al. 2003).

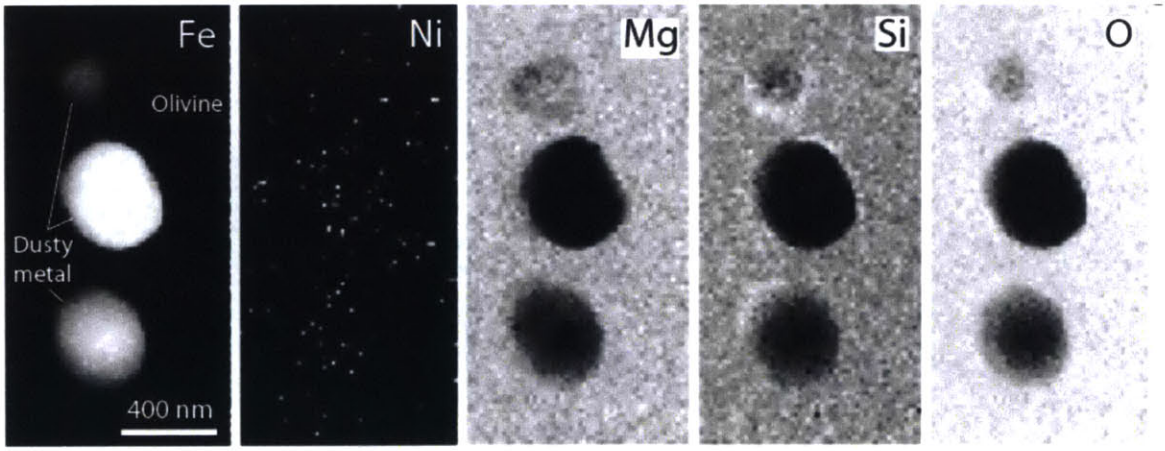

Figure 2.2. STEM elemental maps of three dusty metal grains in the chondrule DOC5. Note the absence of Ni and the forsteritic composition of the surrounding olivine.

Furthermore, to confirm the higher Ni contents of non-dusty olivine metals, we performed quantitative analyses of larger metal grains in the mesostasis of the same chondrule using wavelength dispersion spectroscopy (WDS) on the electron microprobe at the Department of Earth and Planetary Science of the AMNH. We analyzed two large 10-100 μm FeNi grains, which have Ni contents of 0.8 and 7.9 wt%, signifying that mesostasis metal grains span a wide range of compositions. Metal grains with compositions similar to the latter analyzed Ni-rich grain are capable of undergoing plessitic exsolution, which may occur at scales smaller than the ~3 μm resolution of our image on the electron microprobe (Reisener & Goldstein 1999).

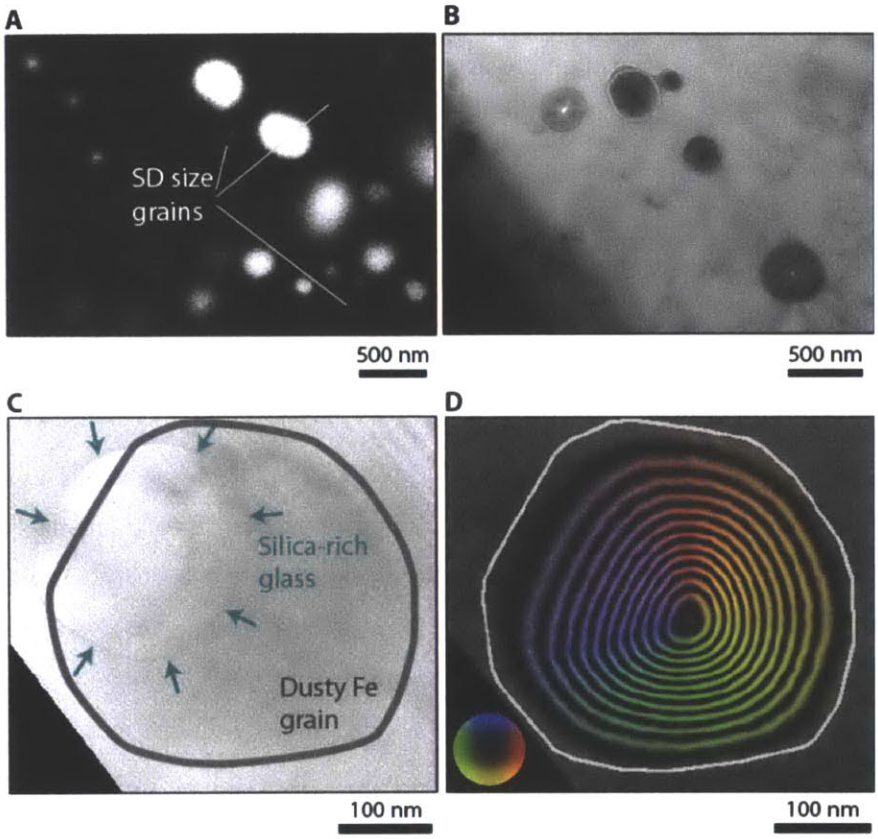

Figure 2.3. High resolution microscopy and electron holography of dusty olivine metals. (**A**) Secondary electron image of dusty olivine metals in chondrule sample DOC4S. Metal grains with size of ~60 nm are likely in the SD state, while the remaining grains are in the SV state. Unsharp grain boundaries in part (A) indicate that the metal grain is not exposed at the sample surface. Grain sizes were determined by integrating the intensity at all azimuths for each radius from the grain center and finding the radius at which the integrated intensity falls to 50% of the interior value. This procedure provides an averaged diameter for non-circular grains and has an uncertainty of ~10 nm in diameter. (**B**) Lorentz image of dusty olivine metals in chondrule DOC5. Particles exhibit a dark or bright spot contrast around the core, suggesting the SV state with different magnetization directions (Phatak et al. 2009). (**C**) Electron hologram of a single dusty olivine Fe grain and associated silica-rich glass in chondrule DOC5 and (**D**) magnetic induction map of the same field of view, showing the azimuthal magnetization expected of a grain in the SV state with vortex core pointing out of the plane. The image in part (A) was obtained using a Zeiss NVision40 SEM with a 15 keV beam at 5.0 mm working distance at the Harvard University Center for Nanoscale Systems. The Lorentz image and the electron hologram in parts (B-D) were obtained with an FEI Titan 300 keV TEM at the Center for Electron Nanoscopy.

In summary, petrographic observations show that dusty olivine metals in Semarkona chondrules have escaped recrystallization since their initial formation during chondrule heating in the solar nebula. While some mesostasis metal may have experienced plessitic exsolution, dusty olivine metals are expected to have escaped all significant post-accretional remagnetization effects and should retain pre-accretional magnetization

blocked above ~450°C. We therefore focus on paleomagnetic data derived from isolated dusty olivine-bearing samples to constrain pre-accretional magnetic fields.

Previous TEM-based studies of dusty olivine-bearing chondrules have reported <100 nm metal grains, which are likely in the single domain (SD) state. Most grains, which are one to several 100s nm in diameter, likely exist in the single vortex (SV) state (Leroux et al. 2003; Lappe et al. 2011). AF demagnetization of our dusty olivine-bearing chondrules shows that seven out of nine samples carry high coercivity magnetization that remains stable above 170 mT, indicating the presence of SD metal grains [Table 2.1; Lappe et al. (2013)].

We directly confirm the presence of both SD and SV metal grains in our dusty olivine-bearing chondrules. After the completion of all paleomagnetic measurements, we imaged sample DOC4S using the secondary electron detector on a Zeiss NVision40 scanning electron microscope (SEM) housed at the Harvard Center for Nanoscale Systems (CNS). These images revealed the presence of ~60 nm, likely SD metal grains (Fig. 2.3). Finally, we obtained electron holograms of several dusty olivine metal grains from sample DOC5 (see above for analytical details), which showed that the majority of visible grains are in the SV state, with only the largest grains (>300 nm) existing in the multi-domain (MD) state (Figs. 2.1, 2.3). We therefore conclude that the primary magnetic carriers in our dusty olivine-bearing chondrules are SD and SV kamacite grains, which are expected to retain magnetization over the age of the solar system (Winklhofer et al. 1997; Garrick-Bethell & Weiss 2010).

Table 2.1: Summary of paleomagnetic results from dusty olivine-bearing chondrules

Sample	Mass (mg)	NRM moment (10^{-4} A m^2 kg^{-1})	Compo-nent	AF or temperature range (mT or °C)	*N*	Dec, Inc (°)	MAD/ α_{95} (°)	DANG (°)	Anisotropy-corrected Dec, Inc (°)
DOC1	0.066	15	LC	0-20	5	297.3, 46.7	10.1		
			HC	20->360	12	84.6, 28.0	10.9	9.4	89.4, 18.4
DOC2	0.027	6.6	LC	0-87.5	11	273.0, 50.6	20.8		
			HC	85-290	6	69.4, -46.4	16.8	1.5	50.5, -38.4
DOC3N	0.0027	3.6	LC	0-20	5	110.0, -65.0	27.0		
			HC	20-290	13	338.8, 76.9	17.8	11.3	3.6, 79.2
DOC3S	0.0094	3.7	LC	0-10	4	330.1, -41.2	7.6		
			HC	10-290	14	110.7,66.1	27.8	11.2	96.5, 59.4
DOC4N	0.019	5.0	LC_1	0-15	4	36.3, 23.0	19.8		
			LC_2	15-55	4	337.8, -35.9	13.1		
			HC	50-290	6	272.3, -6.7	18.6	18.0	264.2, -13.3
DOC4S	0.014	3.1	LC_1	0-40	6	226.3, -12.2	13.3		
			LC_2	40-70	3	84.9, 9.0	18.1		
			HC	65-420	7	251.1, -2.8	13.0	7.4	246.9, -6.8
DOC5	0.085	0.35	LCb	0-15	4	205.9, 4.9	27.3		
			HC	15-290	10	18.1, -1.8	21.4	19.0	25.6, -6.1
DOC6	0.030	9.5	LC	0-50	11	301.2, 25.6	34.9		
			MCa	50-120	5	124.6, -3.7	16.1		
DOC7	0.039	0.18	LC	0-30	7	20.3, 2.3	15.6		
DOC8	0.0077	3.2	LCb	0-22.5	7	179.2, -31.0	24.3		
			HT	350-750	8	80.2, 61.3	17.6	13.3	N/A
LCa					20	92.4, -83.3	8.9		
MCa					14	109.9, -2.0	11.7		
LCb					5	183.9, -9.2	19.2		

Note: All samples in table are mutually oriented to within ~5°. All samples were subjected to AF demagnetization except DOC8, which was subjected to thermal demagnetization after AF cleaning to 22.5 mT. For comparison, the mean direction and 95% confidence interval of the three post-accretional overprints are given at the end of the table. The first column gives the sample name; the second column give the mass; the third column gives the mass-normalized NRM moment; the fourth column gives the component name; the fifth column gives the coercivity or temperature range of the component; the sixth column gives the number of AF or thermal steps in each component or the number of samples in a mean direction; the seventh column gives the direction of the component as calculated from PCA or mean direction; the eighth column gives the maximum angular deviation (MAD) of the component or the 95% confidence interval (α_{95}) of the mean direction (see Section 3.3); the ninth column gives the deviation angle (DANG); the tenth column gives the component direction as given in column seven after correction for anisotropy, which is based on the measured anisotropy of ARM of each sample.

Due to their unique compositional and magnetic properties, dusty olivine grains are expected to retain pre-accretional magnetization. The small grain size of dusty olivine metal implies that most are in the single domain (SD) or single vortex (SV) states, which can retain stable magnetization over the history of the solar system (Uehara & Nakamura 2006; Lappe et al. 2011; Winklhofer et al. 1997; Garrick-Bethell & Weiss 2010). Further, the Ni-poor composition (Ni <2 wt%) of dusty olivine metal precludes metamorphic recrystallization (Leroux et al. 2003; Reisener & Goldstein 1999). The domain states of dusty olivine metals imply very high coercivities ranging up to >200

mT, as confirmed by our demagnetization experiments (see below). The magnetization of grains with such high coercivities should not have been significantly altered by the low shock pressures likely experienced by Semarkona [4-10 GPa (Stöffler et al. 1991; Fu et al. 2012)]. Finally, the low porosities of the surrounding olivine crystals have protected metal from aqueous alteration (Fig. 2.1).

The distinctive, high coercivities of dusty olivine grains allow for the isolation of their remanent magnetization during alternating field (AF) demagnetization as larger (10-100 μm) mesostasis metal grains are expected to demagnetize at AF levels <50 mT (Gattacceca et al. 2014). Furthermore, since the post-accretional peak metamorphic temperature of Semarkona was likely only 200-260°C (Alexander et al. 1989; Cody et al. 2008), pre-accretional remanence in dusty olivine metals should be isolated upon laboratory (1 hour duration) thermal demagnetization to <450°C assuming that metamorphism lasted ~5 My (Uehara & Nakamura 2006; Reisener & Goldstein 1999). In summary, no known post-accretional process is likely to have compromised pre-accretional remanent magnetization in Semarkona dusty olivines; strong field AF demagnetization or thermal demagnetization above ~450°C is expected to isolate the pre-accretional component of magnetization.

2.3. Paleomagnetic measurements

We isolated eight dusty olivine-bearing chondrules from two 15 mm × 10 mm × 150 μm thick sections of Semarkona provided by the American Museum of Natural History (AMNH). Both sections contain fusion crust along one edge. We also extracted five non-dusty olivine-bearing chondrules and twenty-nine bulk (i.e., mixed matrix and chondrule) samples to characterize any post-accretional overprints. All extracted samples are mutually oriented to within 5°. Due to their weak moments [natural remanent magnetization (NRM) ranging between 10^{-10} and 3×10^{-12} Am^2 prior to demagnetization], chondrules were measured using the Superconducting Quantum Interference Device (SQUID) Microscope (Weiss et al. 2007; Lima, Weiss, Fu, et al. 2013) at the MIT Paleomagnetism Laboratory (Fig. 2.4). Supporting magnetic imaging measurements with

higher spatial resolution were performed using a nitrogen-vacancy (NV) quantum diamond microscope.

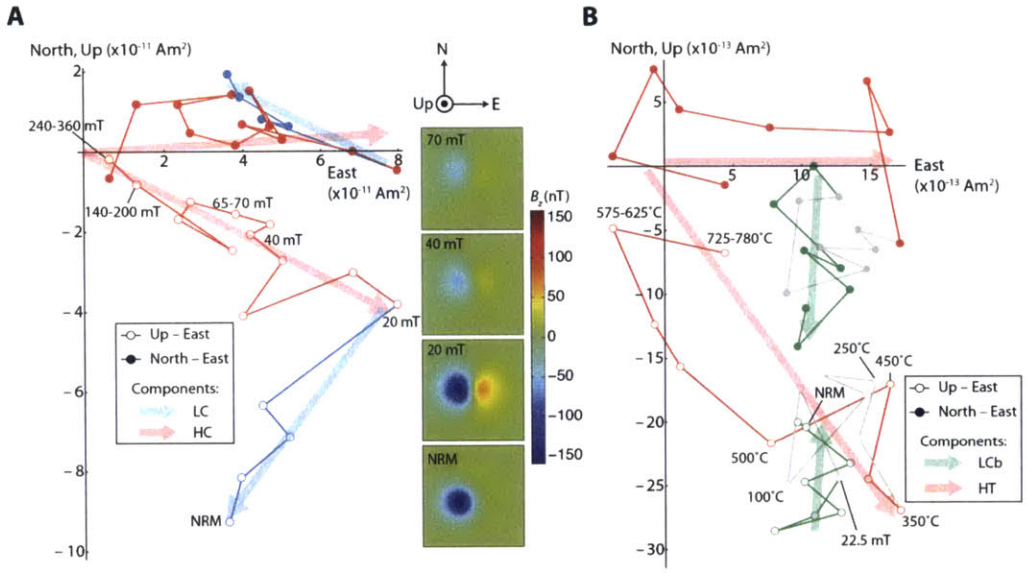

Figure 2.4. AF and thermal demagnetization of single dusty olivine-bearing chondrules measured using SQUID Microscopy. Orthogonal projection diagrams showing the evolution of the natural remanent magnetization (NRM) of two chondrules upon progressive demagnetization. Open and solid circles indicate the projection of the NRM vector onto the vertical (up-east) and horizontal (north-east) planes, respectively. (**A**) AF demagnetization of DOC1 reveals a low coercivity (LC) overprint removed by 20 mT and higher coercivity (HC) magnetization that persists to >290 mT while decaying in magnitude towards the origin. Insets show associated magnetic field maps measured with the SQUID microscope at the indicated demagnetization levels where positive (red) field values are in the up direction. Note the stable directionality and steady decay of the magnetization during AF application above 20 mT. (**B**) Mixed AF and thermal demagnetization of DOC8 shows the removal of the post-accretional LCb overprint by 20.0 mT (green points), a stationary moment between room temperature and ~400°C (gray), and an origin-trending high temperature (HT) component removed by 780°C (red). Steps above 40 mT or 575°C have been averaged to suppress noise.

Sample extraction and measurement. All paleomagnetic measurements were performed on samples extracted from two 15 mm × 10 mm × 150 µm slices of Semarkona designated ps8 and ps3. Both slices were cut from the main sample of Semarkona at the AMNH called AMNH 4128-t4. The slices are separated by a distance of ~0.9 mm. We used a Princeton Scientific Corp. Model WS22 wiresaw at the AMNH with a 50 µm diameter tungsten wire and boron carbide-based cutting fluid to cut each slice from the main sample. Measurement of a single drop of boron carbide cutting fluid in the 2G Enterprises Superconducting Rock Magnetometer (SRM) showed that the magnetic moment is $<10^{-12}$ Am^2, which is the detection threshold of the SRM. Each surface of the

Semarkona slices was then lightly polished with 600 grit, alumina-based sandpaper to flatten the surfaces for optical imaging (see below). Both slices were then washed with acetone and mineral spirits in an ultrasonic cleaner to remove all residual material from the cutting and polishing process.

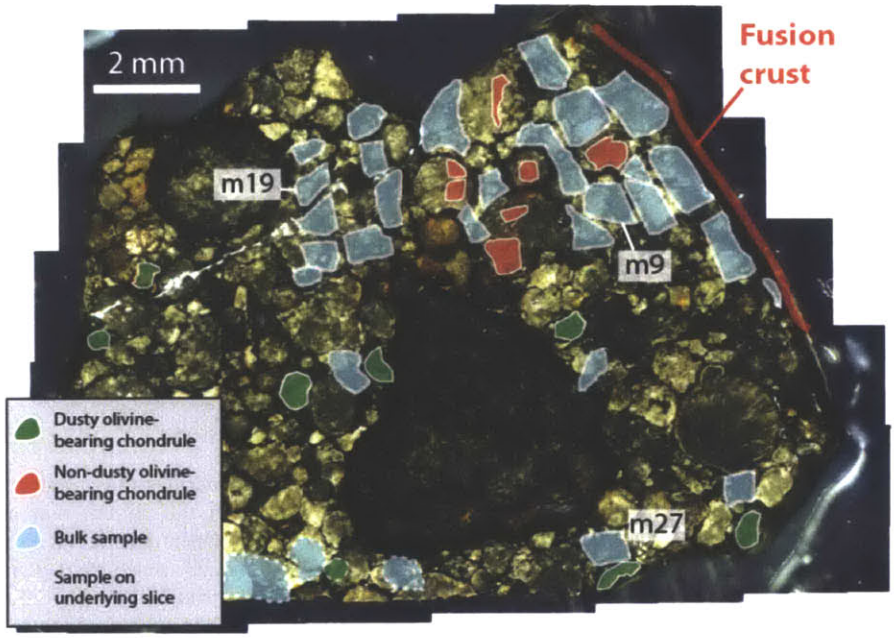

Figure 2.5. (**A**) Optical image of the ps8 slice of the Semarkona meteorite showing locations of all samples used in this study. Highlighted regions with dashed outline denote the approximate locations of samples extracted from the ps3 slice, which lies 0.9 mm beneath ps8. The AF demagnetization sequences of samples labeled m9, m19, and m27 are shown in Fig. 2.7.

Each slice was then glued using non-magnetic cyanoacrylate cement to ~150 μm thick GE124 quartz coverslips. We use the MIT SQUID Microscope, which acquires high-sensitivity maps of the vertical component of the magnetic field above the surface of samples with spatial resolution of ~200 μm and noise threshold of 10 to 100 pT (Fong et al. 2005), to confirm that these coverslips are magnetically clean and contain no contamination with magnetic moment greater than $\sim 10^{-15}$ Am^2. Reflected light optical microscopy was then used to image both sides of each Semarkona slice, permitting the identification of chondrules suitable for extraction (Fig. 2.5). Except during the cutting, polishing, and extraction procedures, all samples were kept in the magnetically shielded room of the MIT Paleomagnetism Laboratory with DC fields <150 nT.

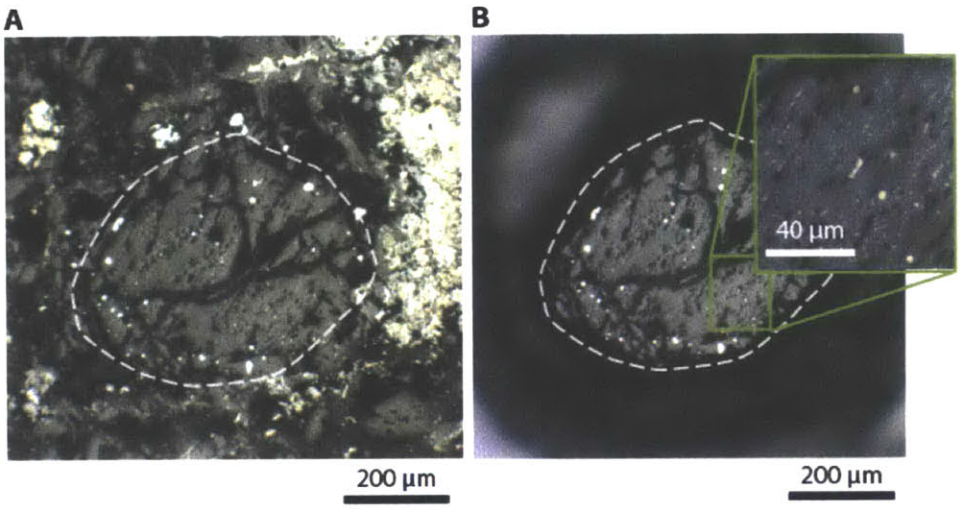

Figure 2.6. Reflected light photomicrographs showing the extraction procedure applied to dusty olivine-bearing chondrule DOC1. The in-section chondrule (**A**) is isolated by the removal of surrounding rim and matrix material using a micromill. The isolated chondrule (**B**) is then magnetically mapped using the SQUID microscope. Inset in part (B) shows a close up reflected light image of dusty olivine metals (white points).

All extraction and measurement of paleomagnetic samples from the Semarkona slices were carried out at the MIT Paleomagnetism Laboratory. We used a degaussed, tungsten-carbide dental scriber mounted on an Electro Scientific Industries Inc. Micromill to excise samples from surrounding material (Fig. 2.6). In the case of chondrule extractions, we took care to fully remove metal and sulfide-rich rims, which suffered aqueous alteration on the LL parent body and may carry secondary magnetization (Church et al. 2012). In the case of dusty olivine-bearing chondrules, we also removed large visible mesostasis metal grains, although some small mesostasis metal grains remain in all dusty olivine-bearing chondrules due to their inaccesible location in the samples. For the dusty olivine-bearing chondrules DOC3 and DOC4, we cut each chondrule into two subsamples to perform the unidirectionality test for pre-accretional TRM. SQUID Microscope scans on sample slices before and after cutting show that this process does not introduce detectable spurious magnetization.

Masses of larger samples were measured directly on a Mettler Toledo electronic scale with ~0.05 mg effective precision. Chondrule masses below the reliable measurement threshold of the electronic scale were estimated using photographically determined

volumes and an assumed density of 3300 kg m^{-3} to approximate the single-grain density of olivine. For all samples, photomicrographs taken of the extracted samples were referenced to those taken of the whole Semarkona slice before extraction, permitting mutual orientations to <5°.

In the case of bulk samples, which have greater masses and higher magnetic moments, we mounted the extracted samples to 3 mm GE124 quartz rods with magnetic moments of less than 2×10^{-12} Am^2 using cyanoacrylate cement and measured their magnetic moments using the SRM. The sample holder moment of 2×10^{-12} Am^2 represents the effect noise level of these measurements. All samples measured using the SRM have NRM moments of greater than 10^{-10} Am^2 to maintain a high signal-to-noise ratio upon demagnetization.

For chondrule samples, which usually have NRM moments below 10^{-11} Am^2, we mounted the extracted samples on magnetically clean GE124 quartz disks using cyanoacrylate for measurement using the SQUID Microscope. We mapped the magnetic field at a sample-sensor distance of 250-350 μm. To better isolate the dipolar component of sample magnetization, we first performed a bilinear interpolation of the field map by a factor of 4 in each horizontal direction and upward continued the field map to achieve an effective sensor-sample distance of 450-550 μm (Lima, Weiss, Baratchart, et al. 2013). We then modeled the upward continued magnetic field using a non-linear optimization algorithm that adjusts the model magnetic moment (direction and magnitude) and sample location to find the sample magnetization that best reproduces the observed field maps. This technique for the recovery of magnetic dipole moment has been tested on both terrestrial and extraterrestrial samples, including chondrules from the Allende CV chondrite (Lima & Weiss 2012). In both cases, SQUID microscope-recovered moments of samples sufficiently strong to be measured on the SRM agreed closely with measurements conducted with the SRM.

Finally, we used NV quantum diamond magnetic imaging (Pham et al. 2011) to map directly the spatial distribution of magnetic sources that contribute to the magnetization of dusty olivine-bearing sample DOC1. The magnetic sensing element was a 2.5 × 2.5 × 0.5 mm diamond chip, grown by chemical vapor deposition and engineered to contain a dense surface layer of nitrogen-vacancy (NV) color centers (estimated density ~ 3×10^{11}

NV/cm^2 in a ~10 nm thick layer at a mean depth of ~20 nm below the diamond surface). This diamond surface was mounted above the sample with a standoff distance of ~20 μm. We acquired images of all three vector components of the magnetic field produced by the sample in the plane of NV sensors using optically-detected magnetic resonance (ODMR) spectroscopy. In this technique, described by Le Sage et al. (2013), the magnetic field is determined from the resonance frequencies of the NV electronic spin-flip transitions $|m_s = 0\rangle \leftrightarrow |m_s = \pm 1\rangle$, which are measured by scanning the frequency of a continuous microwave drive field while monitoring spin-state dependent changes in NV fluorescence that is excited by a low intensity (<240 W/cm^2) laser beam at 532 nm with spot dimensions of approximately 1000 by 400 μm. We imaged the NV fluorescence onto a sCMOS camera, allowing magnetic fields in the plane of the NV sensing layer to be mapped with a spatial resolution of ~1 μm. To spectrally resolve spin-flip transitions of NV centers oriented along different diamond crystal axes, we applied a 1.27 mT magnetic bias field using three orthogonal sets of Helmholtz coils. We were able to distinguish fields generated by remanence-carrying grains from those of soft paramagnetic or superparamagnetic components by carrying out a second measurement with the bias field precisely reversed and summing the field maps measured in each case. We measured the bias reversal precision in a region of the sensor far from the sample, and determined it to be $< 2\times10^{-3}$ of the mean bias field, which was sufficient to cancel all paramagnetic components of the observed signal to below the magnetic noise floor of these measurements, which is ~0.08 μT.

NRM of bulk samples. We extracted a total of 29 bulk samples with masses between 0.08 and 0.59 mg to characterize any post-accretional overprints in our Semarkona samples (Fig. 2.5). We performed stepwise three-axis AF demagnetization up to 85 mT on 22 samples and up to 145 mT on 5 samples. All bulk samples were fully demagnetized by 85 mT. We demagnetized samples in 0.5 mT steps below 25 mT, in 1 mT steps between 25 and 100 mT, and in 2-2.5 mT steps between 100 and 145 mT. We applied the AF and measured the sample moment three times at each field level during AF demagnetization to suppress noise. We then fitted the direction of magnetization components using principal component analysis (PCA) (Kirschvink 1980).

Three samples subjected to AF demagnetization contained fusion crust material while the remainder were separated from the fusion crust by distances between 0.8 and 11.4 mm. We subjected one sample 1.9 mm from the fusion crust (m6) to stepwise thermal demagnetization up to 580°C.

To aid in identifying the origin of each post-accretional overprint, we obtained IRM normalized paleointensities on 11 bulk samples by first applying a 280 mT IRM to the bulk sample and then performing stepwise AF demagnetization up to 85 or 145 mT. The IRM paleointensity for each magnetization component was then calculated using the equation (Gattacceca & Rochette 2004):

$$B_{IRM} = a\frac{\Delta NRM}{\Delta IRM} \tag{2.1}$$

where B_{IRM} is the paleointensity, ΔNRM is the vector-subtracted change in the NRM magnitude in the component's AF interval, ΔIRM is the moment lost from the IRM demagnetized through the same AF range, and a is the ratio between a saturation IRM and a low-field TRM in the relevant coercivity range. In the absence of TRM acquisition experiments on Semarkona bulk samples, we adopt a value of $a=3\times10^3$ (Gattacceca & Rochette 2004), which is typical of metal-bearing samples.

We obtained ARM normalized paleointensities for 11 bulk samples by first imparting an ARM in a 280 mT AC field and a 50 μT bias field. We then subjected each sample to stepwise AF demagnetization up to 85 or 145 mT. The ARM paleointensity for each component was then given by (Stephenson & Collinson 1974):

$$B_{ARM} = f^{-1}B_{bias}\frac{\Delta NRM}{\Delta ARM} \tag{2.2}$$

where B_{ARM} is the paleointensity, B_{bias} is the bias field of the laboratory ARM, ΔARM is the ARM moment acquired in the same AF range as the NRM component, and f is the ratio between the moment of a TRM and that of an ARM acquired in the same bias field. As was the case for the IRM calibration factor a, the value of f has not been determined for Semarkona bulk material using TRM acquisition experiments. We adopt $f=1.34$ as a typical value for metal-bearing samples (Shea et al. 2012; Morden 1992).

Both a and f are subject to uncertainties of a factor of 3-5 (Cisowski et al. 1983). Because the paleointensities of bulk samples are used only as an aid towards determining the origin of post-accretional overprint, uncertainties in the paleointensities within this

range do not affect our conclusions. Paleointensities for dusty olivine-bearing chondrules, which we use to constrain nebular magnetic field strength, are subject to much smaller uncertainties.

The LCa component. AF and thermal demagnetization of both fusion crust and interior samples revealed a unidirectional LCa component of magnetization blocked up to 11.5 mT or 70°C in 20 out of 29 bulk samples (Figs. 2.7 and 2.8). Where observed upon thermal demagnetization in sample m6, we call this component LTa. The presence of the LCa component in these samples regardless of their distance to the fusion crust indicates that the component was acquired after arrival on Earth, while its low unblocking temperature indicates that it is likely a VRM. The mean paleointensity of this component is 94 μT, which is within uncertainty of the terrestrial field strength of ~50 μT. The dominant ferromagnetic phases in the matrix and chondrules rims in Semarkona and similar unequilibrated LL chondrites are kamacite, magnetite, maghemite, Ni-rich metal, and possibly sulfides (Lauretta et al. 2001). Assuming that the LCa component is carried primarily by single domain pyrrhotite, the demagnetization of this component by 70°C is consistent with exposure to a stable Earth-strength magnetic field at 20°C for several decades (Carporzen et al. 2011), such as that expected during long-term storage. If the LCa component is primarily carried by magnetite, maghemite, or FeNi metal, the observed demagnetization temperature would imply storage of <1 year (y) at 20°C (Pullaiah et al. 1975), which may represent the most recent period of undisturbed storage at the AMNH. Either scenario would be consistent with the acquisition of the LCa magnetization during the meteorite's curation since 1940.

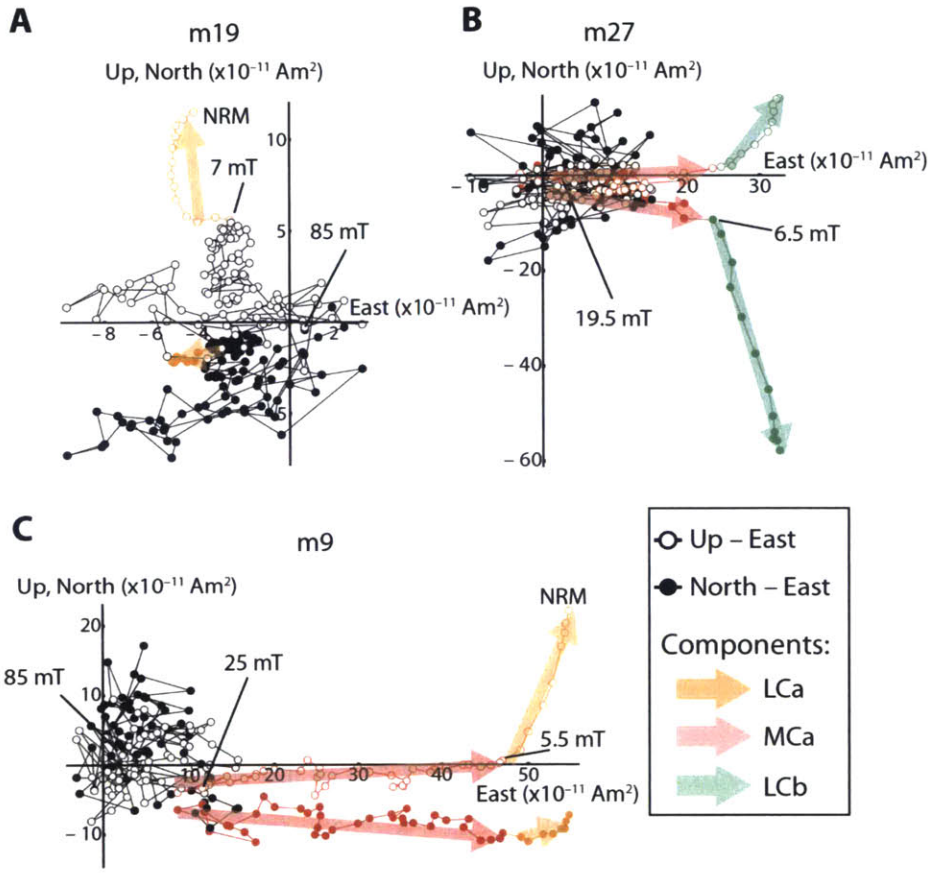

Figure 2.7. Demagnetization sequences of representative bulk samples showing all three post-accretional overprints. Orthogonal vector endpoint diagrams show the evolution of the NRM vector during AF demagnetization up to 85 mT. Open and closed circles indicate the projection of the magnetization vector onto the vertical (up-east) and horizontal (north-east) planes, respectively. Relative positions of the three samples in the parent Semarkona piece are shown in Fig. 2.5.

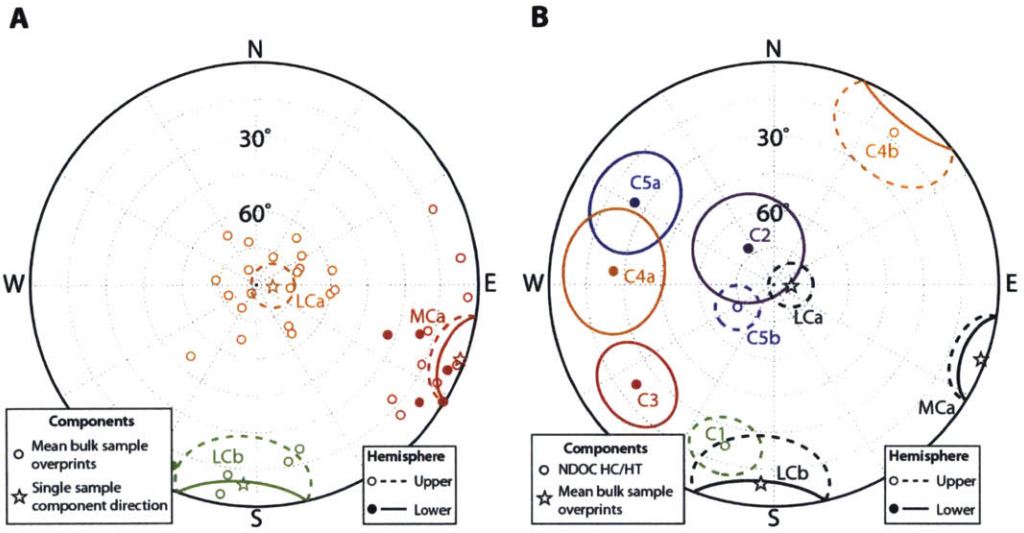

Figure 2.8. Equal area stereonet projections of (**A**) overprint directions in bulk samples and (**B**) highest coercivity directions in NDOC samples. Open (closed) circles denote PCA-fitted directions of components from single samples in the upper (lower) hemispheres while stars represent the mean directions derived from a group of samples. Ovals around circles and stars indicate the MAD and the 95% confidence interval for the true component direction, respectively.

The MCa component. Fourteen out of eighteen samples located 4.7 mm or less from the fusion crust carry the unidirectional MCa overprint while zero out of thirteen samples farther from the fusion crust carries this component. This spatial distribution demonstrates that the MCa magnetization is the result of atmospheric heating in the geomagnetic field. The nearest interior sample to the fusion crust that did not carry the MCa component is m4, which is 0.8 mm away. This implies that all chondrule samples, which were extracted >2.0 mm from the fusion crust, likely carry no MCa component. The heterogeneity of the presence and strength of the MC component between 0.8 and 4.7 mm from the fusion crust may be due to uneven conduction of atmospheric heating into the meteorite interior, which is consistent with the mixture of both non-porous chondrules and porous, insulating matrix. Alternatively, the MCa component may be a thermochemical remanent magnetization (TCRM), whose acquisition varied with the local composition of magnetic phases. Finally, the blocking temperature spectrum of bulk samples may be significantly lower than that of chondrule samples, allowing the recording of a low temperature thermal overprint. Such low blocking temperatures would be consistent with the presence of pyrrhotite in the matrix (Alexander et al. 1989),

which has much lower blocking temperatures compared to those of FeNi metal in chondrules.

The mean paleointensity of 76 μT is also consistent within error with the geomagnetic field. Thermal demagnetization shows that sample m6, which is 1.9 mm from the fusion crust, carries a MCa/MTa component blocked up to 220°C, which is consistent with heating during atmospheric passage based on thermoluminescence studies of ordinary chondrites (Sears 1975). In comparison, all chondrule samples were extracted further from the fusion crust than sample m6. For any chondrule sample that carries the MCa component, the atmospheric heating it experienced was therefore likely lower than 220°C. Therefore, all chondrule samples were heated to a lower temperature during atmospheric entry than during metamorphism on the LL parent body, implying that atmospheric heating did not contribute to the removal of pre-accretional remanence in extracted chondrules.

Seven bulk samples taken from <0.9 mm from the fusion crust contained additional strong components of magnetization. These magnetizations were non-unidirectional across the bulk samples. Due to the closeness of these samples to the fusion crust, we interpret them as TRMs acquired during tumbling of the meteorite during atmospheric entry. In contrast, the MCa component, which penetrated to much greater depths from the fusion crust, was likely acquired during a longer time window during atmospheric entry when the attitude of the meteorite was stable with respect to the Earth's field. As in the case of the LCa and MCa components, the mean paleointensity of U components (70 μT) is consistent with the geomagnetic field. Because all chondrule samples were extracted at least 2.0 mm from the fusion crust, these samples are not expected to carry any U components.

The LCb overprint. Finally, five bulk samples near the southern edge of both ps3 and ps8 slices between 4 and 11 mm from the fusion crust carry a unidirectional LCb overprint blocked between 0 and 6.5-30 mT. The very high NRM to saturation IRM ratio of this component (0.23) indicates that it is an IRM acquired during exposure to artificial fields. The maximum unblocking coercivity suggests that the artificial field had a maximum intensity of ~30 mT (Stephenson 1993), which is consistent with a weak hand magnet

(Weiss et al. 2010). Furthermore, the presence of the LCb overprint only in samples from local area within 2 mm of the sample edge is expected for an origin due to contact with a hand magnet. Two chondrules (DOC5 and DOC8) were extracted from the area carrying the LCb magnetization. AF demagnetization of DOC5 and adjacent bulk sample m29 showed that the LCb component was fully removed by 15 mT and 16 mT, respectively. We performed AF demagnetization of DOC8 up to 22.5 mT before undertaking thermal demagnetization to remove fully the LCb overprint. The resulting demagnetization sequence shows that the LCb component was completely removed by 20 mT (Fig. 2.4). The wide angular separations between the LCb direction and those of higher coercivity and temperature components in both DOC5 and DOC8 confirm that the LCb component was fully removed from these samples.

NRM of dusty olivine-bearing chondrules. The unique compositional and magnetic properties of dusty olivine metals described in the main text and in Section 2 suggest that dusty olivine-bearing chondrules should retain pre-accretional magnetization. To identify and characterize any pre-accretional magnetization, we extracted eight dusty olivine-bearing chondrules with masses between 0.008 and 0.09 mg.

Due to their small size and weak NRM moments (between 9.9×10^{-11} and 9.4×10^{-13} Am^2) (Table 2.1), all dusty olivine-bearing chondrules were measured using the MIT SQUID Microscope. Because measurements on the SQUID Microscope are time-intensive compared to those on the SRM, demagnetization sequences for dusty olivine-bearing chondrules are of lower resolution than those of bulk samples. We applied three-axis AF demagnetization in steps of 5 mT up to 90 mT, in steps of between 5 and 20 mT up to 200 mT, and in steps of between 30 and 50 mT above 200 mT. Most samples were demagnetized up to 290 mT while two chondrules with exceptionally high coercivities, DOC1 and DOC4, were demagnetized up to 360 and 420 mT, respectively. We repeated the AF application and measurement up to five times for each AF level above 40 to 90 mT to minimize noise. For demagnetization steps above 25-40 mT, we averaged the moments of two to four adjacent AF levels to suppress noise further (Weiss et al. 2008).

We carried out thermal demagnetization on sample DOC8 in 50°C steps to 550°C followed by 25°C steps to 750°C and a final step at 780°C. The sample was held at the

peak temperature for ~20 minutes during each heating step. To prevent oxidation of the dusty metal grains upon heating, we used a CO_2 and H_2 gas mixture (Suavet et al. 2014) to maintain the oxygen fugacity at two to three log units below the iron-wüstite buffer (IW-2 to IW-3), which is near the theoretical equilibrium oxygen fugacity of an olivine crystal with Fa_{10} composition (Matas et al. 2000). We averaged the moment measured in each three adjacent demagnetization steps above 575°C to suppress noise. Finally, after the completion of the thermal demagnetization sequence, we attempted partial TRM acquisition experiments on the DOC8 sample with a 50 μT bias field at temperatures between 300 and 780°C. However, apparent sample alteration during heating above 600°C prevented recovery of high-fidelity partial TRM acquisition sequence. We therefore do not include these experiments in our final paleointensities analyses.

The LCa, MCa, LCb overprints. Among the eight extracted dusty olivine-bearing chondrules, DOC6 was 2.1 mm from the fusion crust while all other samples were located >3.4 mm away. As a consequence, DOC6 was the only chondrule sample that carries the MCa overprint due to atmospheric heating, which is blocked between 50 and 120 mT. The presence of the MCa overprint in DOC6 confirms that the mounting and measurement procedure on the SQUID Microscope did not result in significant contamination or remagnetization. No dusty olivine-bearing chondrules carried the LCa component, likely due to differences in the rate of VRM acquisition between chondrule and matrix material. The difference in magnetic mineralogy between the matrix and chondrule materials can account for large variations in the rate of VRM acquisition (Dunlop & Ozdemir 1997a). Finally, as discussed in Section 3.2, the LCb overprint is present in dusty olivine-bearing chondrules DOC5 and DOC8 where it is fully removed by AF demagnetization up to 15 and 20 mT, respectively (Fig. 2.4).

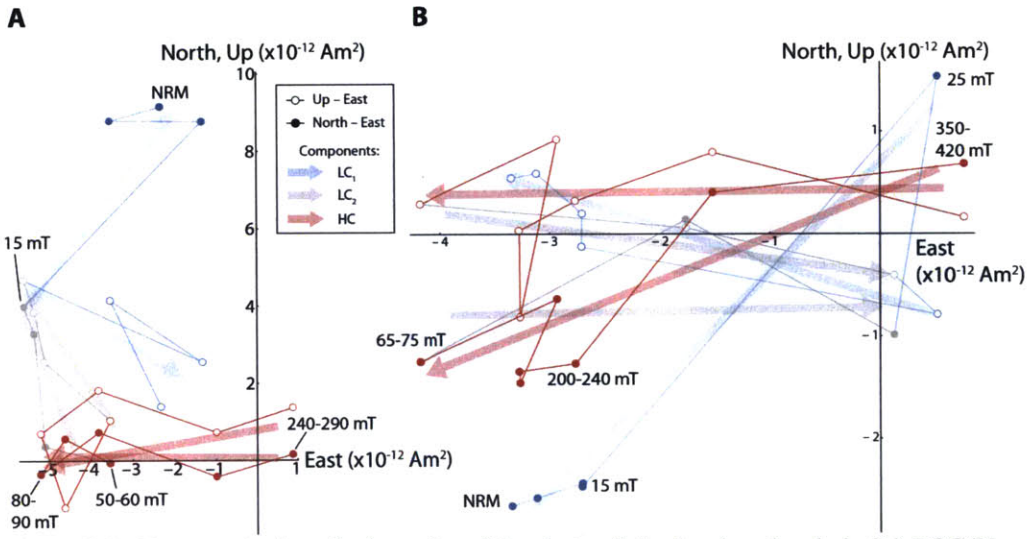

Figure 2.9. Demagnetization of subsamples of the dusty olivine-bearing chondrule (**A**) DOC4N and (**B**) DOC4S. Orthogonal vector endpoint diagrams show the evolution of the NRM vector during AF demagnetization. Open and closed circles indicate the projection of the magnetization vector onto the vertical (up-east) and horizontal (north-east) planes, respectively. We attribute the non-unidirectional LC components to spontaneous magnetizations acquired during metamorphic recrystallization. In contrast, the unidirectionality of the HC components suggests a TRM origin.

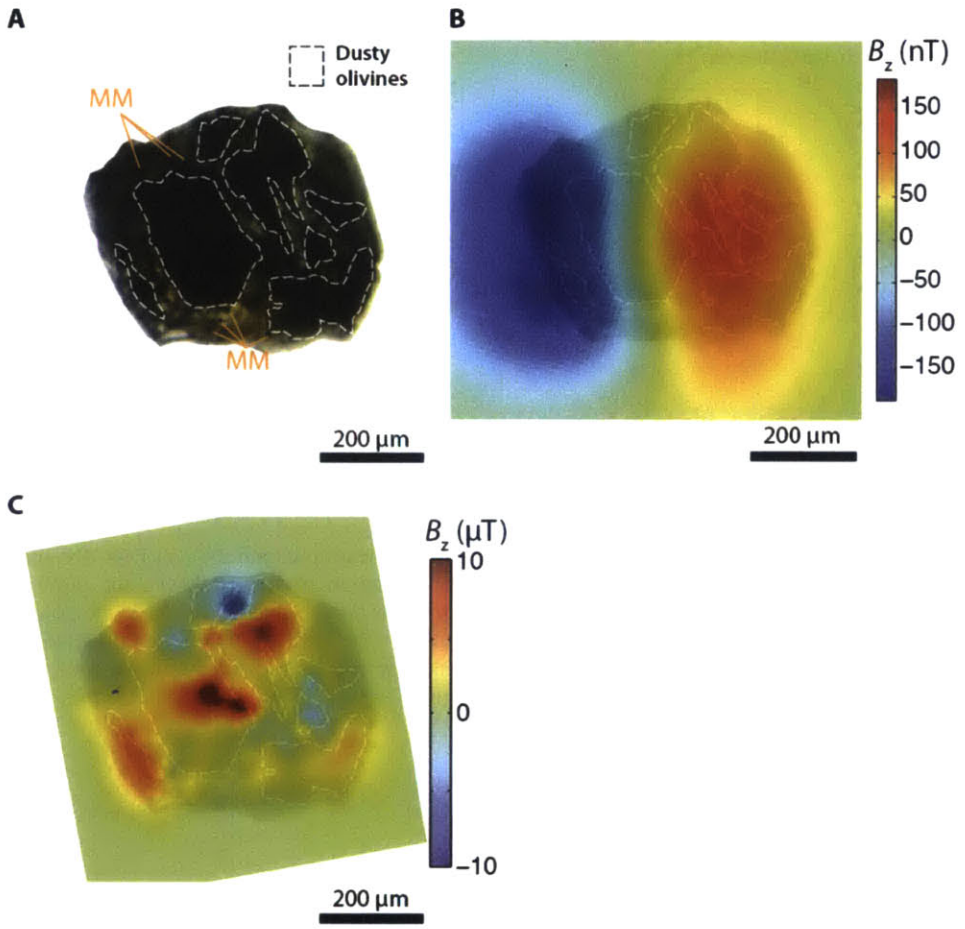

Figure 2.10. (**A**) Transmitted light optical photomicrograph of sample DOC1, (**B**) overlay of the magnetic field map of the NRM upon AF demagnetization to 50 mT and the optical image in part (A), and (**C**) overlay of the magnetic field map of an AF cleaned laboratory ARM and the optical image in part (A). In both magnetic maps, positive B_z corresponds to the out of the page direction. White dashed outlines in part (A) denote the location of dusty olivine grains, which are optically opaque. Orange line segments point to mesostasis metal grains (MM). Magnetic fields generated by the NRM shown in part (B) were mapped with the MIT SQUID Microscope. Laboratory ARM in part (C), which was mapped using an NV quantum diamond magnetometer, consists of a 290 mT AC field with a 600 µT bias field that was AF demagnetized to 100 mT to simulate part of the coercivity range of the HC component. The ARM bias field was applied in the positive z direction, implying that locations with strong positive B_z correspond to those of magnetic remanence carriers. Note the spatial correspondence between the largest concentration of dusty olivines in part (A), the center of the dipolar source in part (B), and the strongest magnetic sources in part (C).

The LC component. All dusty olivine-bearing chondrules except DOC5 and DOC8 carry at least one unique low coercivity (blocked up to between 15 and 87.5 mT depending on the sample) component of magnetization oriented in random directions relative to components found in other chondrule and bulk samples. Because these are not directionally consistent with the identified overprint directions LCa, LCb, and MCa, we

generically refer to these magnetizations as LC components. All dusty olivine-bearing chondrules carry only one LC component except for the subsamples of DOC4, which carry two randomly oriented LC components (denoted LC_1 and LC_2; Fig. 2.9 and Table 2.1). Analogous LC components are also present in some non-dusty olivine-bearing chondrules (NDOC), strongly suggesting that LC magnetizations are carried by recrystallized Ni-rich metal grains, which are present in the mesostases of all chondrules. Furthermore, the low coercivity range of these components is consistent with their presence in MD mesostasis metal grains (Gattacceca et al. 2014). As discussed above, the plessitic unmixing of kamacite and Ni-rich taenite phases in such grains during metamorphism on the LL parent body in a weak field likely resulted in the loss of any pre-accretional remanence and the acquisition of randomly oriented, spontaneous magnetizations. Similar secondary magnetizations have been observed in other ordinary chondrites (Gattacceca et al. 2003; Uehara et al. 2011; Morden & Collinson 1992).

The HC/HT component. Five of seven dusty olivine-bearing chondrules subjected to AF demagnetization carry an HC component of magnetization blocked above any LC components and up to 240-380 mT. The high coercivities above 170 mT indicate that SD kamacite grains are responsible for carrying part of the HC magnetizations (Lappe et al. 2013). The field geometry observed in SQUID Microscope and NV diamond magnetometer maps confirm that high coercivity magnetization is carried by dusty olivine grains (Fig. 2.10).

In contrast to these chondrules that carry HC magnetization, DOC7 carries no directionally stable component above 37.5 mT while DOC6 carries a possible HC component blocked between 100 and 240 mT. However, given that the latter putative component consists of only four averaged demagnetization steps and that an ARM in DOC6 (see below) is fully demagnetized by 100 mT, we do not consider this magnetization to be a reliable HC component. In any event, inclusion of this component's direction in the conglomerate test does not affect the outcome of the test. The absence of a reliable HC component in samples DOC6 and DOC7 may be due to the presence of a higher abundance of unextracted mesostasis metal grains which have very low coercivities and contribute significant noise during AF demagnetization (Tikoo et al.

2012). Alternatively, these chondrules may have tumbled, possibly due to the loss of angular momentum, during their cooling process and thereby never acquired a unidirectional TRM. Finally, the rotation axis of these chondrules may have been nearly perpendicular to the ambient magnetic field during cooling, resulting a very weak effective bias field that did not impart an identifiable remanent magnetization.

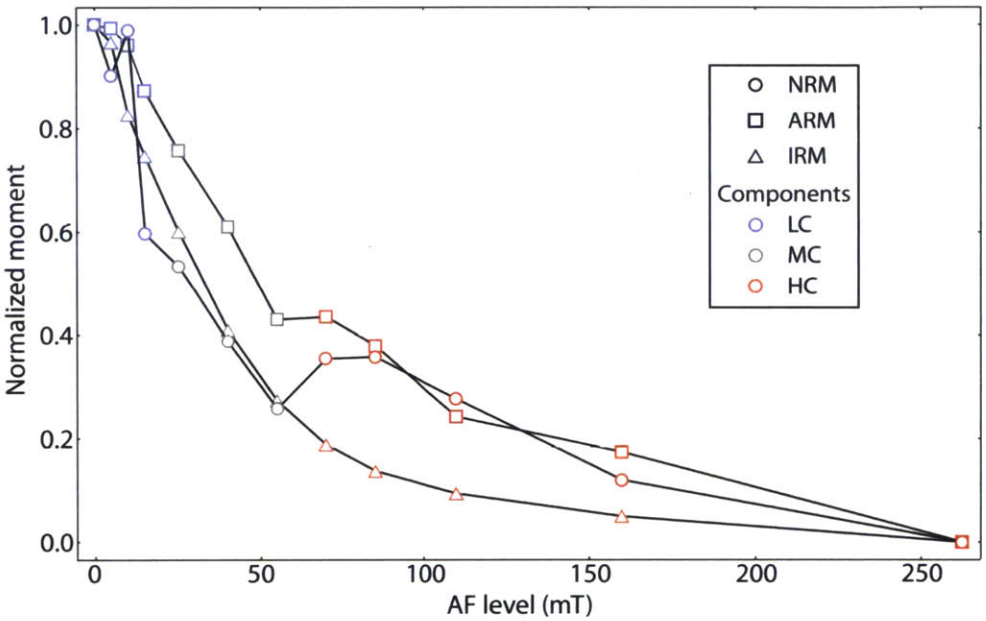

Figure 2.11. Comparison of the coercivity spectrum of an NRM, ARM, and IRM between 0 and 262.5 mT for dusty olivine-bearing chondrule sample DOC4N. The NRM coercivity spectrum in the HC component range is more similar to the ARM (AC field 290 mT; bias field 100 μT) than the 420 mT IRM, suggesting a TRM origin for the HC magnetization. For the NRM, we corrected for the non-parallel directions of the LC, MC, and HC components by computing the moment at a given AF level using the vector difference with the moment at the highest AF level of the corresponding component.

All HC components are origin-trending as confirmed by the comparison between the maximum angular deviation (MAD), which describes the uncertainty in the component direction as determined using PCA, and the deviation angle [DANG; (Tauxe & Staudigel 2004)], which is the angular difference between the best-fit direction of the HC component according to PCA and the vector from the origin to the centroid of data points that make up the HC component (i.e., the best-fit direction of the HC component, assuming that it passes through the origin). If DANG < MAD, then the component's decay is origin-trending to within the uncertainty of the component's direction (Shea et al. 2012). The rate of HC component decay over its coercivity range is similar to that of an

ARM but not to that of an IRM (Fig. 2.11), providing evidence that the HC component was acquired as a TRM (Stephenson & Collinson 1974).

The NRM of DOC8 remained stable in both direction and intensity during thermal demagnetization up to 400°C (Fig. 2.4). Rapid decay towards the origin commenced upon heating to 400-450°C and continued until the loss of directional stability at ~750°C. The survival of this HT component up to above ~550°C shows that tetrataenite cannot be its primary carrier (Nagata 1983). The blocking temperature range of this HT component and the lack of component decay below ~400°C are fully consistent with that expected for a pre-accretional TRM in the chondrule that had been thermally demagnetized in a null field on the LL parent body during 5 My of metamorphism at 200°C (Uehara & Nakamura 2006). The thermal demagnetization sequence of DOC8 therefore offers strong evidence that pre-accretional remanence is preserved in dusty olivine-bearing chondrules.

Because the precise relative directions of the HC/HT components are critical for paleomagnetic tests for a pre-accretional origin, we conducted ARM acquisition experiments to compute the anisotropy tensor for all dusty olivine-bearing chondrule samples except DOC8 after the completion of their NRM demagnetization. In the case of DOC8, possible sample alteration during partial TRM acquisition experiments may have affected the anisotropy of the sample. For other samples, we isolated the anisotropy tensor most relevant to the HC component by first imparting an ARM in a 290 mT AC field with a 200 μT bias field and then AF demagnetizing the ARM up to the lower bound of the coercivity range of the HC component (Jackson 1991). We imparted two such AF-cleaned ARMs to each of three orthogonal axes, measured the resulting remanence using the SQUID Microscope after each application, and averaged the moments from the two applications to compute all six independent elements of the anisotropy tensor. For the dusty olivine-bearing chondrule samples that carry an HC component, the anisotropy ratio P, defined as the ratio between the greatest and smallest eigenvalues of the anisotropy tensor, spans a range between 1.4 and 2.5, implying moderate to high degrees of anisotropy (Selkin et al. 2000).

We find no evidence of gyroremanent magnetization (GRM) acquired during our AF demagnetization experiments (Stephenson 1993). The magnitude of GRM associated

with a certain orientation of the AF axis and sample is expected to increase with the application of higher AF levels, as more high coercivity magnetic grains would be magnetized by the AF application. In all cases, the HC magnetization decays uniformly to the origin (see above) without detectable increase in moment in an identifiable direction.

Statistical analysis of dusty olivine-bearing chondrule data. The relative directions of the HC/HT magnetizations provide critical clues regarding their origin. To test the hypothesis that the HC/HT components are pre-accretional, we perform the paleomagnetic conglomerate test on all dusty olivine-bearing chondrules and the unidirectionality test on subsamples of two individual chondrules. In the conglomerate test, mutually random chondrule magnetization directions support a pre-accretional origin since chondrules likely accreted onto the parent body in random orientations (Watson 1956). In contrast, magnetizations that are unidirectional among different chondrules were acquired after accretion of the meteorite. In the unidirectionality test, coherent magnetization directions found in subsamples of the same chondrule provide evidence for the acquisition of magnetization in a uniform ambient magnetic field [e.g., (Sugiura & Strangway 1983; Usui et al. 2009)]. A sample that passes both paleomagnetic tests must have chondrules with mutually random but internally unidirectional magnetizations.

Passing both tests provides strong evidence that the chondrule magnetizations are pre-accretional. Samples that pass the conglomerate test alone may have suffered post-accretional remagnetization in a weak-field environment that randomized magnetization at small scales, resulting in a false-positive outcome (Uehara et al. 2011). Application of the unidirectionality test eliminates this possibility, as subsamples of weak-field remagnetized chondrules would show mutually random magnetizations. Furthermore, chondrules that pass both paleomagnetic tests likely acquired magnetization as a TRM during cooling in the nebula. Although a CRM can potentially record pre-accretional magnetic fields, no evidence for recrystallization exists in dusty olivine metals, precluding a CRM origin for their magnetization.

To perform the conglomerate test, we use the anisotropy-corrected HC/HT component directions recovered from all six dusty olivine-bearing chondrules found to

contain these magnetizations. For chondrules DOC3 and DOC4, each of which has two subsamples, we take the mean of the unit vectors representing each subsample's magnetization direction. Because of the close agreement between the magnetization directions within each pair of subsamples (see below), the choice of averaging technique does not affect the result of the conglomerate test. The resulting set of six HC/HT directions passes the conglomerate test at the 95% significance level (Watson 1956). Specifically, a set of six randomly oriented vectors has a 38% probability of showing more unidirectionality than the set of six HC/HT directions, implying that these directions are fully consistent with a random distribution and do not tend toward an identifiable direction.

We use two approaches to evaluate the unidirectionality of HC/HT components found in subsamples of DOC3 and DOC4. First, we test whether the directions for each subsample are consistent with a single magnetization direction in each chondrule given the uncertainties on the component directions. As above, we adopt the mean between the HC component unit vectors for each pair of subsamples as the mean HC direction of each chondrule. For all four subsamples, the angular separation between the subsample HC direction and the mean HC direction of the chondrule is smaller than the MAD of the subsample HC component, implying that the subsample and mean directions agree at the 1σ level (Kirschvink 1980). All subsample HC directions are therefore consistent with the sampling of a single true HC direction in each chondrule.

Second, we compute the probability that the apparent alignment between the HC directions of subsamples from each chondrule occurred randomly. If the HC directions in all subsamples are independent and randomly distributed over the unit sphere, the probability density function (P) for the angular separation (θ) between the HC directions of two subsamples from a single chondrule is given by (Weisstein):

$$P(\theta) = \frac{1}{2}\sin\theta \tag{2.3}$$

over the domain $0^\circ \leq \theta \leq 180^\circ$. Because we took two subsamples each from two separate chondrules, we must evaluate the probability that randomly oriented magnetizations resulted in the observed degree of unidirectionality in both chondrules simultaneously. The probability density function (Q) of the sum of the separations between HC directions

in both chondrules ($\theta_1+\theta_2$) may be derived from the convolution of Eq. 2.3 with itself [p. 136 of Papoulis (2002)]. The result is a piecewise function that is given by:

$$Q(\theta_1+\theta_2)=\frac{1}{8}[\sin(\theta_1+\theta_2)-(\theta_1+\theta_2)\cos(\theta_1+\theta_2)] \tag{2.4}$$

over the restricted domain $0^\circ\leq\theta\leq180^\circ$. The measured separations of subsample HC directions in DOC3 and DOC4 are 32.8° and 17.7° (Table 2.1), respectively, resulting in $(\theta_1+\theta_2)=50.6^\circ$. Integrating Eq. 2.4, the probability of two pairs of random directions yielding $(\theta_1+\theta_2)<50.6^\circ$ is 0.0060. We therefore reject the hypothesis that the unidirectionality of the HC component in both subsampled chondrules occurred randomly at the 99% confidence level. A simpler but more restrictive calculation of the joint probability, multiplying the individual probabilities that the angular separation observed in each chondrule is less than the observed value, yields an even lower joint probability of 0.0019.

Because the unidirectionality test is critical to our interpretation of a pre-accretional origin for the HC magnetization, we verify the above calculations by performing Monte Carlo simulations using Mathematica. In each instance of the simulation, we choose four random directions from a uniform distribution on the unit sphere and sum the angular separations between the first pair and between the second pair. In a simulation of 10^6 instances, 5901 or 0.59% resulted in a sum of separations of less than 50.6°, fully corroborating our theoretical calculations. In summary, our statistical analysis of HC/HT directions shows that (1) the mean magnetization directions of the six dusty olivine-bearing chondrules represent a random distribution, (2) the directions of chondrule subsamples from DOC3 and DOC4 are consistent with unidirectional magnetization in each chondrule, and (3) the unidirectionality of these subsample magnetization is non-random at the 99% confidence level. We therefore conclude that the HC/HT components pass both the conglomerate and the unidirectionality test with high confidence, providing strong evidence for a pre-accretional TRM origin of these magnetizations.

As an additional test for pre-accretional origin of the HC/HT magnetizations, we evaluate the correspondence between the direction of magnetization and the inferred spin axis of the chondrules. The shortest principal axis of oblate chondrules may represent the spin axis of the chondrules during cooling near the solidus (Miura et al. 2008;

Tsuchiyama et al. 2003). Because spinning objects cooling in a magnetic field acquire a magnetization parallel to the spin axis (Suavet et al. 2011), pre-accretional magnetization may be parallel to the shortest physical dimension of the chondrule. We note that our following analysis assumes that the chondrule morphology is indeed a result of rotation instead of, for example, the presence of unmolten relic grains near the surface or to aerodynamic effects (Miura et al. 2008). Furthermore, we assume that the chondrules are rotationally symmetric spheroids although we cannot confirm this given the effectively two-dimensional (2D) sections available to us.

Because we extracted all chondrules from 150 μm thick slices of Semarkona, our samples cannot uniquely define the three-dimensional (3D) orientation of the chondrules' short axis. However, approximating chondrules as oblate ellipsoids of rotation, the section of the chondrule that appears on our sample slice is an ellipse whose orientation constrains the direction of the true, 3D short axis. Specifically, the 3D short axis must lie in a plane that is perpendicular to that of the sample slice and that passes through the short axis of the sectioned ellipse [i.e., the 2D short axis; (Gendzwill & Stauffer 1981; Ferguson 1979)]. Close alignment between the magnetization direction and the 3D short axis would therefore imply a correspondence between the azimuth of the magnetization and that of the 2D short axis of the chondrule section.

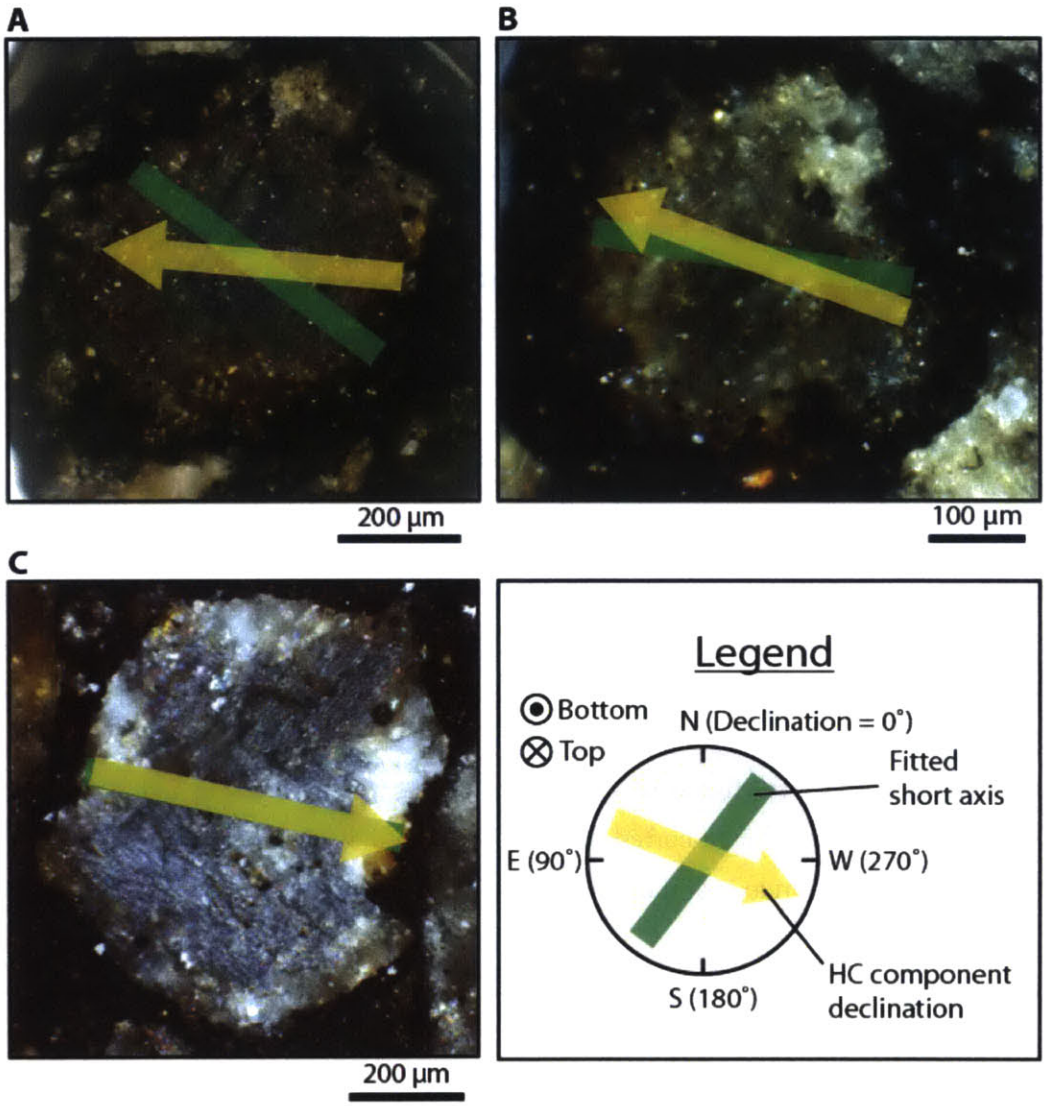

Figure 2.12. Reflected light photomicrographs of dusty olivine-bearing chondrule (**A**) DOC1, (**B**) DOC2, and (**C**) DOC4 showing the correspondence between the physical short axis and the horizontal projection of the HC magnetization. To obtain the best-fit ellipses and the short axis orientation, we used images of the bottom side of the sample slice due to the availability of higher quality photographs. Note the resulting reversed (counter-clockwise) sense of the declination scale.

Because the plane of the sample slice corresponds to the horizontal plane (i.e., the inclination (i) equals zero plane) in our coordinate system, we compare the anisotropy-corrected declination of the HC/HT components and that of the chondrules' 2D short axes (Fig. 2.12). To objectively determine the orientation of the latter, we select the Cartesian coordinate of 12 points evenly spaced points on the boundary of the chondrule and use the MATLAB routine fitellipse to compute the short axis orientation of the best-

fit ellipse (Brown 2007). Following the preceding analysis for the unidirectionality of DOC3 and DOC4 subsamples, we evaluate the unidirectionality of the component declinations and the 2D short axis orientations by calculating the probability that the observed angular discrepancies occurred by chance. If the declinations of the magnetization and short axis are mutually independent, their separation for each chondrule would be uniformly distributed between 0° and 90° [the short axis has no preferred sense; (Weisstein)]. Out of six dusty olivine-bearing chondrules that carry an HC/HT component, only three are available for this analysis. Two chondrules are incomplete due to their location at the edge of the sample slices, which precludes an accurate assessment of their shape. One chondrule, DOC3, carries an HC component oriented nearly normal to the slice plane and therefore does not have a well-determined declination. For a sample size of three, the probability density function of the sum of all three separation angles ($\phi_1 + \phi_2 + \phi_3$) may be found by the convolution of the uniform distribution that describes each separation angle [(Papoulis 2002), p. 136]. Analogously to Eq. 4, the result is a piecewise function given by:

$$P(\phi_1 + \phi_2 + \phi_3) = \frac{4}{\pi^3}(\phi_1 + \phi_2 + \phi_3)^2 \tag{2.6}$$

over the restricted domain $\phi_1 + \phi_2 + \phi_3 \leq 90^\circ$. For our chondrules, $\phi_1 + \phi_2 + \phi_3 = 44.0^\circ$. Integration of Eq. 6 shows that the probability of mutually random directions resulting in $\phi_1 + \phi_2 + \phi_3 \leq 44.0^\circ$ is 1.9%. We therefore reject the hypothesis that the HC/HT component directions and the chondrule 2D short axes are unrelated at the 98% level, implying that the two directions are mutually aligned. We conclude that HC/HT magnetizations in the dusty olivine-bearing chondrules were likely acquired during spinning and cooling in the solar nebula. Future 3D tomographic imaging combined with paleomagnetic measurements would permit comparison between the magnetization and the true short axis of the chondrule.

NRM of non-dusty olivine-bearing chondrules. We extracted a total of seven samples from five NDOCs from our Semarkona slices to compare their magnetization to that of dusty olivine-bearing chondrules. Because most non-dusty metal grains in Semarkona have been subject to recrystallization during parent body metamorphism (Kimura et al.

2008), NDOCs are not expected to retain pre-accretional magnetization. We test this hypothesis by performing the same conglomerate test and unidirectionality tests on our NDOC samples.

We subjected all NDOC samples to three-axis AF demagnetization up to 290 mT in steps of 5 mT below 90 mT and in steps of 10 to 50 mT between 90 and 290 mT. We applied AF demagnetization three times at each level ≥85 mT to reduce noise. Furthermore, we averaged the magnetizations of each two adjacent AF steps above 20 mT and each three adjacent steps above 40 mT.

Six out of seven NDOC samples carry two components of magnetization while one sample, C4b, carries a single component (Table 2.3). The NRM components of NDOC samples exhibit a greater diversity of coercivity ranges than dusty olivine-bearing chondrules. Two samples, C2 and C4b, have no stable magnetization above 32.5 mT while C4a loses directional stability by 140 mT. These maximum coercivities are lower than those of dusty olivine-bearing chondrules, suggesting that the main carrier of these magnetizations is mesostasis metal grains, which are much larger than dusty olivine metals and exist in the magnetically soft MD state (Gattacceca et al. 2014). In contrast, the remaining four NDOC samples are not fully demagnetized by 290 mT, possibly due to the presence of fine FeNi grains in the mesostasis.

Table 2.3: Summary of paleomagnetic results from non-dusty olivine-bearing chondrules

Sample	Mass (mg)	NRM moment (10^{-4} A m^2 kg^{-1})	Component	AF range (mT)	*N*	Dec, Inc (°)	MAD (°)	DANG (°)
C1	0.14	0.37	LC	0-22.5	9	63.6, 28.2	11.5	11.9
			HCa	22.5->290	8	196.5, -21.6		
C2	0.27	0.89	LCa	0-5	3	66.5, -48.8	22.0	17.5
			HCa	5-32.5	8	325.1, 72.2		
C3	0.60	1.2	LC	0-10	5	23.1, 45.9	14.5	11.6
			HCa	10->290	12	233.5, 21.7		
C4a	0.14	0.42	LCa	0-15	7	157.7, -53.3	20.4	4.7
			HCa	15-140	9	274.8, 25.8		
C4b	0.18	0.20	HCa	0-12.5	6	38.1, -12.0	18.8	8.3
C5a	0.22	0.72	LCa	0-10	5	251.4, -53.6	17.2	23.2
			HCa	12.5->290	11	300.8, 25.4		
C5b	0.07	1.5	LC	0-12.5	6	60.0, 0.9		
			HCa	12.5->290	11	237.1, -72.7	8.9	19.2
LCa					20	92.4, -83.3	8.9	
MCa					14	109.9, -2.0	11.7	
LCb					5	183.9, -9.2	19.2	

Note: All samples in table are mutually oriented to within ~5°. All samples were subjected to AF demagnetization. The first column gives the sample name; the second column give the mass; the third column gives the mass-normalized NRM moment; the fourth column gives the component name; the fifth column gives the coercivity range of the component; the sixth column gives the number of AF or thermal steps in each component or the number of samples in a mean direction; the seventh column gives the direction of the component as calculated from PCA or mean direction; the eighth column gives the maximum angular deviation (MAD) of the component or the 95% confidence interval (α_{95}) of the mean direction; the ninth column gives the deviation angle (DANG).

For the six NDOC samples that carry two magnetization components, the softer LC components of magnetization are blocked between 0 and up to 22.5 mT. In samples C2, C5a, and C4a, this LC component may correspond to the LCa overprint. The HCa magnetizations, so named to avoid confusion with the internally unidirectional HC components found in dusty olivine-bearing chondrules, are found in all NDOC samples and are blocked between the end of the LC component, if one exists, and up to >290 mT. Comparing the values of DANG and MAD, only the HCa components found in samples C3, C4a, and C4b are origin-trending, although continued demagnetization of the remaining samples may alter the relative magnitudes of DANG and MAD. The HCa components of magnetization are mutually randomly oriented and pass the conglomerate test at the 95% confidence level (Watson 1956).

Among the five extracted NDOCs, C4 and C5 have been further divided to yield two subsamples each. Unlike dusty olivine-bearing chondrules, subsamples of individual NDOCs have mutually random HCa magnetizations, as the sum of the angular

separations between chondrule subsamples is 232°, which corresponds to P value of 0.82 according to Eq. (2.4). Such internally non-unidirectional magnetization is consistent with acquisition during plessitic exsolution on the LL parent body but inconsistent with a pre-accretional origin (Morden & Collinson 1992).

We therefore conclude that, as predicted by the petrography of metal, Ni-rich, mesostasis metal grains in Semarkona carry randomly oriented secondary magnetization due to metamorphic recrystallization in a weak field while the Ni-poor dusty olivine metals retain pre-accretional magnetization. The results of these subsampling experiments on both dusty olivine-bearing chondrule and NDOC samples highlight the importance of the unidirectionality test as a complement to the conglomerate test in identifying pre-accretional magnetization. Although the HC/HT/HCa magnetizations in both sets of chondrules pass the conglomerate test, the unidirectionality test supports a pre-accretional origin for only the magnetization in dusty olivine-bearing chondrules.

In summary, we argue based on seven lines of evidence that these HC/HT components are pre-accretional TRMs. First, HC/HT components decay to the origin upon demagnetization, which is the expected behavior of primary magnetization (Fig. 2.4). Second, the HC/HT magnetization directions in the six chondrules are collectively random, passing the conglomerate test at the 95% confidence level [Fig. 2.13; (Watson 1956)]. No HC/HT component is oriented in the direction of any of the post-accretional overprints. Third, the HC magnetizations in chondrules DOC3 and DOC4, which were each partitioned into two subsamples, are unidirectional within each chondrule and inconsistent with random magnetizations at the 99% confidence level. Such uniformity is expected of a TRM acquired by individual chondrules cooling in the solar nebula because the field should be uniform across the submillimeter scale of each sample (Fu, Lima, et al. 2014). Fourth, the blocking temperature range of the HT component (350-750°C) agrees closely with that expected of a pre-accretional magnetization that was partially demagnetized for ~5 My at ~200°C [Fig. 2.4B; (Uehara & Nakamura 2006; Garrick-Bethell & Weiss 2010)], which is the estimated metamorphic temperature for Semarkona on the LL parent body (Uehara & Nakamura 2006; Cody et al. 2008). Fifth, magnetic field maps of dusty olivine-bearing chondrules confirm that the HC magnetization is carried by dusty olivines, which formed in the nebula and are expected to retain pre-

accretional magnetization as outlined above. Sixth, the magnetization direction acquired during cooling for a spinning chondrule is expected to be parallel to its rotation axis (Suavet et al. 2011). The close alignment between the HC directions and the short axes of our chondrules, which are likely related to the rotation axis (see below), are non-random at the 98% confidence level, suggesting that HC/HT magnetizations were indeed acquired parallel to the spin axis. Seventh, the coercivity spectrum of the HC component of dusty olivine-bearing chondrules is very similar to that of an ARM and dissimilar to that of an IRM, which suggests that the HC component was acquired as a TRM (Lappe et al. 2013). We therefore conclude with high confidence that the HC/HT magnetizations observed in dusty olivine-bearing chondrules are TRMs acquired in the solar nebula.

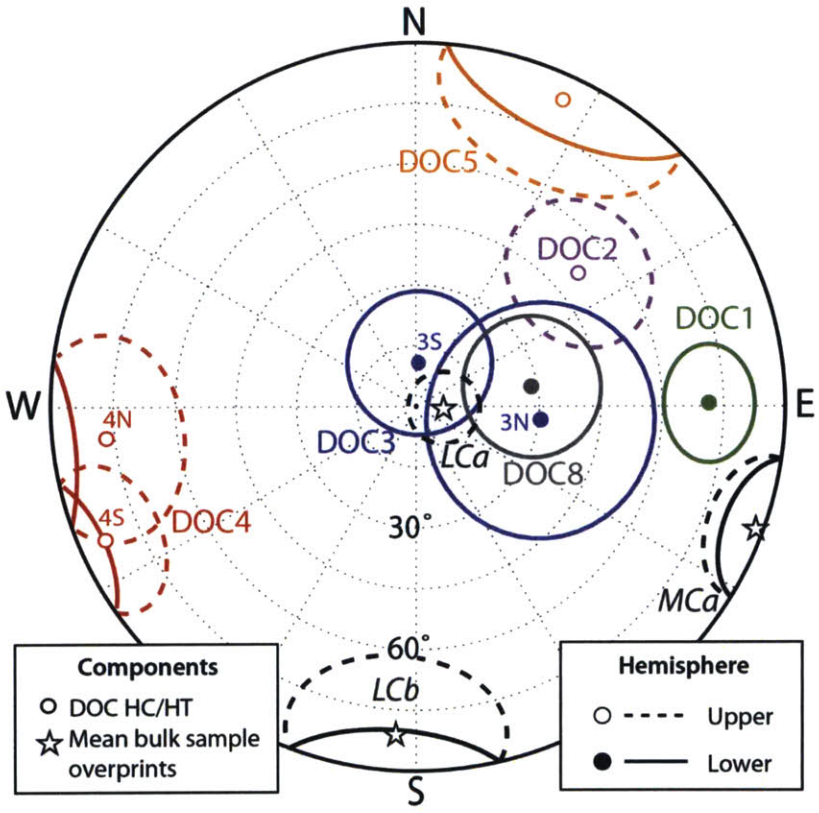

Figure 2.13. Magnetization directions in Semarkona chondrules and bulk samples. Equal area stereonet projection diagram where colored points and circles denote high coercivity or high temperature (HC/HT) magnetization in individual dusty olivine-bearing chondrule samples or subsamples and the associated maximum angular deviation (MAD) obtained from principle components analysis. Each color represents a single chondrule with chondrules DOC3 and DOC4 having two subsamples each. Black stars

and associated ovals represent the mean directions of the three post-accretional overprints identified from bulk samples and their 95% confidence intervals. Open symbols represent the upper hemisphere; solid symbols represent the lower hemisphere. The wide scatter of the HC/HT magnetizations, the unidirectionality of subsamples from DOC3 and DOC4, and their non-correspondence to the directions of post-accretional overprints provide strong evidence for a pre-accretional origin of the HC/HT magnetizations in dusty olivine-bearing chondrules.

2.4. Paleointensities of dusty olivine-bearing chondrules

As discussed above, HC/HT components of dusty olivine-bearing chondrules represent pre-accretional TRMs acquired during cooling in the solar nebula. The paleointensities derived from these components therefore constrain the strength of magnetic fields in the nebular gas, likely during the late cooling stage of chondrule formation.

Experiments on laboratory TRMs imparted on synthetic dusty olivine grains show that the ARM normalization method potentially yields paleointensity estimates accurate to within ~20% (1σ) of the true value for samples whose magnetization is dominated by SV states similar to our dusty olivine-bearing chondrules (Lappe et al. 2013). The best-fit calibration factor f for such samples is 1.87 [see Eq. (2)]. This ARM calibration is most applicable in the coercivity range 100-150 mT. All HC components found in dusty olivine-bearing chondrules are blocked across this coercivity range. Furthermore, the ratio of ARM to NRM loss does not show significant variation across the coercivity range of the HC component (Fig. 2.14). We therefore use the ARM calibration inferred from the 100-150 mT range to calculate the paleointensity for the full HC component. Finally, our applied bias field of 100 μT for the ARM acquisition experiments is well within the range where ARM intensity varies linearly with the bias field. For these reasons, we expect similar performance of the ARM normalization method for our dusty olivine-bearing chondrules compared to the SV grains dominated synthetic dusty olivine grains used by Lappe et al. (2013), implying that 1σ uncertainty due to the ARM calibration factor is ~20%.

Due to its well determined calibration, we use the ARM normalization method to infer paleointensities for all dusty olivine-bearing chondrule samples that carry an HC component except DOC4S (see below). We first imparted an ARM with an AC field of

290 mT and a bias field of 100 μT. We then subjected the ARM to AF demagnetization using the same sequence of steps as during AF demagnetization of the NRM for each sample. Finally, we averaged multiple measurements at the same AF level and across adjacent AF levels as was done for the NRM.

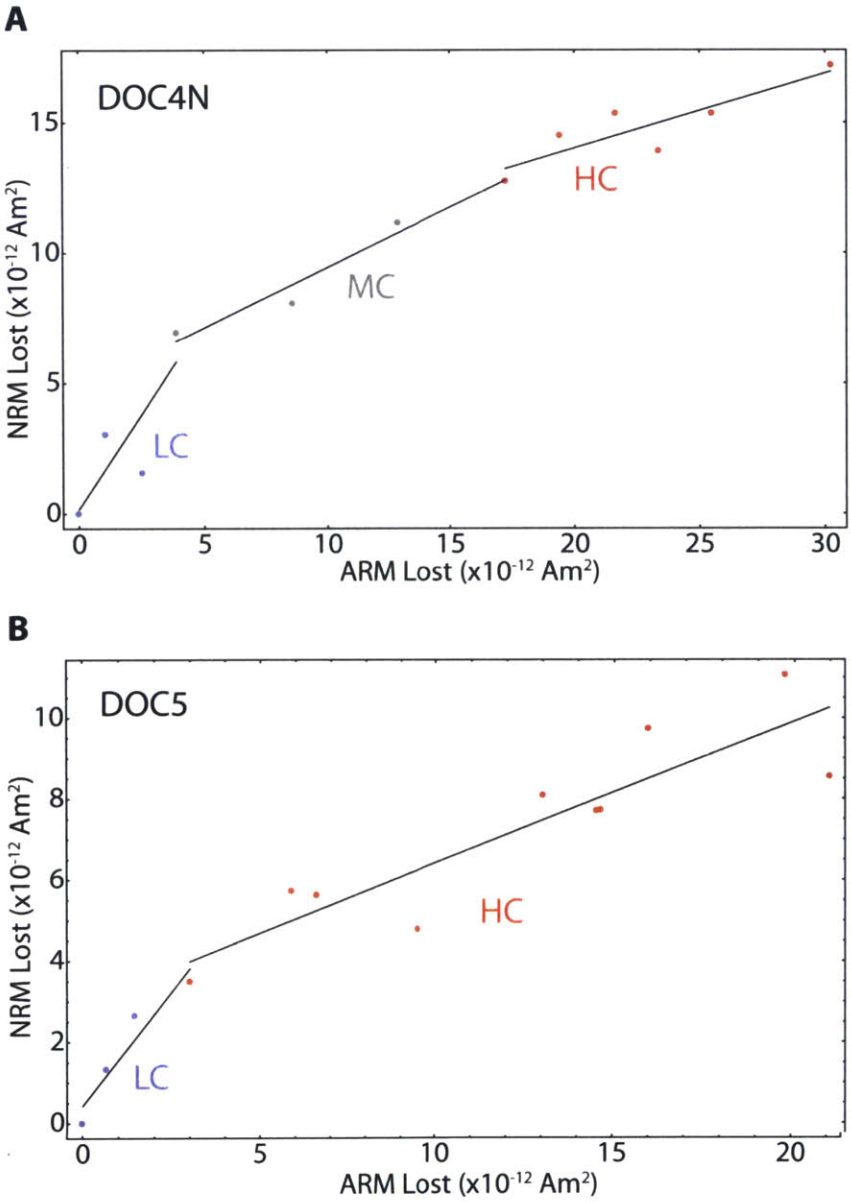

Figure 2.14. Representative ARM paleointensity experiments on dusty olivine-bearing chondrule samples (**A**) DOC4N and (**B**) DOC5.

To derive paleointensities, we then compared the vector change in NRM with that of ARM for AF levels in each component and used a linear least-squares fit to obtain the ratio $\Delta NRM / \Delta ARM$ (Fig. 2.14). We then applied Eq. 2.2 and corrected the resulting raw paleointensities for effect of sample anisotropy (Selkin et al. 2000), which may be a significant effect for samples whose HC component direction was offset from that of the ARM bias field (Table 2.4). For DOC3 and DOC4, we averaged the paleointensities derived from each subsample to obtain the representative paleointensity for the whole chondrule. In the case of DOC4S, the coercivity range of the HC component extends to 420 mT, which is above the maximum AC field level available for an ARM. We therefore use the IRM normalization method for this sample by imparting a 400 mT IRM followed by stepwise demagnetization up to 420 mT. Similar to our ARM normalization procedure, we ratio the vector change in NRM and IRM for each component and calculate the paleointensity using Eq. (2.1). To derive the IRM calibration factor a, we performed an identical IRM paleointensity experiment on the subsample DOC4N, which originates from the same chondrule and for which we also have ARM normalized paleointensities. Assuming that the IRM normalized paleointensity for DOC4N equals the ARM normalized value, we find that a=3100 μT, which is similar to typical values for iron-bearing lunar samples (Cisowski et al. 1983).

Table 2.4: Summary of dusty olivine-bearing chondrule paleointensities

Sample	Fitted paleointensity (μT)	Anisotropy-corrected paleointensity (μT)	Total sample uncertainty (2σ; μT)	Rotation corrected paleointensity (μT)	Rotation-corrected total uncertainty (2σ; μT)
DOC1	29	37	22		
DOC2	22	40.	27		
DOC3	17 (N), 31 (S)	17 (N), 32 (S)	13 (N), 21 (S)		
DOC4	15 (N), 18 (S)	13 (N), 10 (S)	8.9 (N), 10. (S)		
DOC5	19	21	11		
Mean	22.1	27		54	21

Note: The first column gives the sample name; the second column gives the raw ARM paleointensity from a comparison NRM and ARM loss in a given coercivity range with the exception of DOC4S, which has an IRM-based paleointensity; the third column gives the paleointensity after correction for anisotropy using measured anisotropies of ARM acquisition; the fourth column gives the uncertainty in the paleointensity accounting for the statistical uncertainty from linear regression and the uncertainty in the ARM calibration factor f; the fifth column gives the paleointensity for the ambient field after correction for the rotation of chondrules during cooling; the sixth column gives the uncertainty in the rotation-corrected paleointensity, taking into account the uncertainty in column four and the uncertainty of the rotation correction (see Section 4).

We consider two sources of uncertainty in the paleointensity of each dusty olivine-bearing chondrule. First, the linear fit to determine the ratio $\Delta NRM / \Delta ARM$ or $\Delta NRM / \Delta IRM$ carries uncertainties of typically 20-30% (1σ). Second, the ARM

calibration factor, where used, is subject to uncertainty of ~20% (see above). We assume that the two sources of errors are independent for each chondrule. Further, we assume that the uncertainties in ARM calibration factor for each subsample of DOC3 and DOC4 are also mutually independent. Total 1σ uncertainties in the ARM and IRM normalized paleointensity of each chondrule derived from the combination of these two sources range between 26% and 50% (Table 2.4).

One final source of uncertainty arises due to the rotation of chondrules during remanence acquisition. Tomographic studies of chondrule morphology imply that, above the solidus [~1000°C; (McCoy et al. 1999)], chondrules rotated with angular velocities 50-350 s^{-1} around the chondrules' symmetry axis (Miura et al. 2008; Tsuchiyama et al. 2003). Upon cooling across the solidus, chondrules would have retained rotation around the same spin axis unless perturbed by external torques, which may have led to precession of the spin axis.

We first address the correction to the measured paleointensity assuming that negligible precession occurs and the chondrule maintains spin around its axis of highest moment of inertia. The magnetic field intensity recorded by a spinning chondrule (B_{rec}) is the projection of the true ambient field (B_{amb}) onto the chondrule spin axis. Assuming that the orientation of the spin axis is independent of the local magnetic field, the probability distribution function of B_{rec} is a simple uniform distribution [(Feller 1966), p. 30]:

$$P(B_{rec}) = \frac{1}{B_{amb}}. \tag{2.7}$$

over the domain $0 \leq B_{rec} \leq B_{amb}$. Given a finite number of measurements, the probability density distribution of the mean of the chondrule paleointensities ($\overline{B}_{rec}$) may be found by the repeated convolution of Eq. (7) with itself. By the central limit theorem, the probability distribution function of $\overline{B}_{rec}$ approaches a Gaussian distribution centered on $\frac{1}{2}B_{amb}$ [(Feller 1966), p. 252]. For a sample size of five, we find that the probability distribution function of $\overline{B}_{rec}$ very closely approximates a Gaussian distribution with standard deviation $0.13B_{amb}$. In summary, for the non-precessing case, the best guess ambient field strength is twice our mean paleointensity while the additional 1σ

uncertainty due to rotation and our finite sample size is 0.13 of the true field. Applying this, we find a true ambient field strength of 54±21 μT (2σ).

We now address the correction to the paleointensity assuming that precession of the chondrule was significant. If the uniform rotation of the chondrule is disturbed after cooling below the solidus, the elastic nature of the solid chondrule implies that the damping timescale of precession is much longer than the cooling timescale of chondrules [(Peale 1977), p. 92], implying that once a chondrule is precessing, it would continue to do so over the course of remanence acquisition. The precession rate of the instantaneous rotation axis in the body frame of the chondrule is a function of its oblateness and rotation rate [(Morin 2008), pp. 396-399]. For a chondrule with an aspect ratio ~1.3 (e.g., DOC4; Fig. 2.1) spinning at 140 s^{-1}, the precession frequency is 36 s^{-1}, implying that precession occurs on much shorter timescales than that of chondrule cooling. Azimuthal (i.e., perpendicular to the chondrule's symmetry axis) components of remanence therefore average to zero during remanence acquisition. The magnetization acquired by a precessing chondrule is then parallel to the symmetry axis, which is consistent with the observed alignment between HC direction and chondrule short axes, although this alignment is also consistent with non-precessing rotation.

We therefore calculate the expected intensity of magnetization acquired in an ambient field B_{amb} by finding the time-averaged projection of $\vec{B}_{amb}$ onto the chondrule symmetry axis. We adopt a fixed frame where the angular momentum vector ($\vec{L}$) is aligned with the positive z axis, $\vec{B}_{amb}$ is offset from $\vec{L}$ by angle θ_B, and the symmetry axis ($\hat{c}$) of the chondrule is offset from $\vec{L}$ by angle θ_c. Due to its precession around $\vec{L}$, $\hat{c}$ is given by $(\sin\theta_c \cos\omega_p t,\ \sin\theta_c \sin\omega_p t,\ \cos\theta_c)$, where ω_p is the precession frequency [(Morin 2008); pp. 396-399]. Assuming no significant external torques, $\vec{B}_{amb}$ is constant in this reference frame and can be denoted by $B_{amb}(\sin\theta_B,\ 0,\ \cos\theta_B)$. The time average of the dot product $\vec{B}_{amb} \cdot \hat{c}$ is then given by:

$$\vec{B}_{amb} \cdot \hat{c} = B_{amb} \cos\theta_B \cos\theta_c . \tag{2.8}$$

Assuming that the orientation of $\vec{L}$ is independent of $\vec{B}_{amb}$, the expectation value of the recorded paleointensity ($\overline{B}_{rec}$) can be found by integrating Eq. (2.7) weighted with the

probability distribution function of θ_B, which is $P(\theta_B) = \sin\theta_B$ on the relevant domain $0 \leq \theta_B \leq \pi/2$. We then arrive at the equation:

$$\overline{B}_{rec} = 1/2 B_{amb} \cos\theta_c, \tag{2.9}$$

which is identical to the non-precessing case except for the factor $\cos\theta_c$. For weak precession (i.e., $\theta_c \approx 0$), we recover the previous relationship $\overline{B}_{rec} = 1/2 B_{amb}$. If we assume that θ_c is randomly distributed (i.e., strong precession, implying frequent processes that disturb the rotational axis of the chondrule from the original non-precessing direction), the expectation value of $\overline{B}_{rec}$, found by again integrating Eq. (2.9) weighted by $P(\theta_c)$, yields the relationship $\overline{B}_{rec} = 1/4 B_{amb}$, implying a maximum true ambient field intensity 4 times our measured paleointensity.

However, we argue that the amplitude of precession was likely small in chondrules (i.e., $\theta_c \approx 0$), which would imply that $\overline{B}_{rec} \approx 1/2 B_{amb}$ as in the non-precessing case. To impart significant precession to a chondrule, external processes must contribute angular velocities not negligible compared to the 50-350 s^{-1} values for chondrules within the several hour timespan of chondrule cooling.

Collisions with gas molecules may perturb the original spin axis of the chondrule. The contribution to the angular momentum of the chondrule from a single gas molecule collision is $dL \approx mvr_c$ where m is the mass of the gas molecule, v is its velocity, and r_c is the chondrule radius. Because the gas molecules arrive from random directions, the total contribution to the angular momentum can be described by a random walk and is given by $\Delta L \approx \sqrt{N} dL$ [(Reif 1985); p. 34], where $N = 4\pi v n r_c^2 t$ is the number of collisions in time t and in a gas with number density n. Approximating a chondrule as a uniform sphere with 0.6 mm diameter and assuming a gas environment with v = 3000 m s^{-1} and n = 1.8×10^{21} m^{-3} (Desch & Connolly 2002), the associated angular velocity acquired in one hour is only ~0.01 s^{-1}, which is negligible compared to the original chondrule angular velocity.

We next consider collisions with dust particles as the source of external torque. Assuming collision velocities of 1 m s^{-1} between chondrules and 1 μm dust grains and a dust to gas ratio of 0.01 (Ciesla et al. 2004), we find that 2500 collisions occur in each hour, imparting an angular velocity of ~0.02 s^{-1}.

Finally, we consider collisions with other chondrules. Such collisions can impart large angular velocities to chondrules (Fu & Weiss 2012). The frequency of compound chondrules is 5%, which represents a lower bound to the frequency of collisions during cooling between approximately 1500 and 1100°C (Ciesla et al. 2004; Connolly et al. 1994). Assuming that the rate of cooling did not change at the lower temperatures relevant to remanence acquisition, this implies that few chondrules should have been affected by such collisions. In summary, precession can lead to a discrepancy of up to a factor of 4 between B_{amb} and our measured mean paleointensity while rotation around a single spin axis would imply a factor of 2. We find that known processes are unlikely to have induced significant precession of chondrules within the cooling timescale. We therefore regard rotation around a single spin axis as the most likely state of motion for a cooling chondrule, leading to a discrepancy factor of 2 and an inferred ambient field strength of 54±21 μT (2σ).

Summarizing this Section, TRM acquisition experiments on analogs of dusty olivine chondrules have shown that the ARM normalization method potentially produces paleointensities accurate to ~40% [2σ; Lappe et al. (2013)]. Assuming that the five chondrules with recovered paleointensities formed in similar magnetic field conditions in the nebula, our nominal ARM paleointensities for six dusty olivines yielded a mean value of 27 μT. The morphology of chondrules (Miura et al. 2008) and the apparent correspondence between HC magnetization directions and the short axes of our chondrule samples (see above paragraph) strongly suggest that chondrules were rotating during remanence acquisition in the solar nebula. In the case of rotation around a single axis, which is the expected motion inherited from cooling of a viscous droplet, the true mean field intensity should have been greater than our experimental paleointensity by a factor of 2 (see below). Meanwhile, precession of the chondrule's rotation axis would imply a multiplicative factor of up to 4. However, given the high inferred rotation rates of chondrules (>50 s^{-1}), the magnitudes of effects that may lead to precession are comparatively small. Therefore, we adopt non-precessing rotation as the most likely state of cooling chondrules and recommend a value of 54 ± 21 μT (2σ) for the ambient nebular field strength. Although unlikely, if chondrules did not rotate or precessed strongly

during remanence acquisition, the corresponding estimated ambient field strength would be 27 ± 8 μT or 108 ± 42 μT (2σ), respectively.

2.5. Comparison with theoretically predicted field strengths

The above paleointensity constrains the magnetic field environment during the last time the chondrule cooled through the 765-350°C blocking temperature range of the HC/HT component, which likely was the chondrule forming event. Our recommended paleointensity is significantly lower than the >80-400 μT expected for chondrules purportedly formed in the x-wind model (Shu et al. 1996). Furthermore, mechanisms that invoke intense electric currents such as magnetic reconnection flares and current sheets predict strong fields in excess of 500 μT during chondrule heating (Levy & Araki 1989). The short circuit instability may also imply similarly strong fields at high temperature (McNally et al. 2013), although the decay of field strength below 765°C has not been studied in detail. In contrast, given that magnetic fields inherited from the collapsing molecular cloud were likely on the order of 10 μT (Desch & Mouschovias 2001), nebular shocks, which may enhance the ambient magnetic field by a factor of <10, would result in paleointensities of <100 μT (Desch & Connolly 2002). Meanwhile planetesimal collisions would likely not perturb the background field. Therefore, nebular shocks and planetesimal collisions are the chondrule formation models most consistent with our measured paleointensities.

Adopting nebular shocks and planetesimal collisions as the most likely origins of chondrules, background magnetic fields in the nebula may have been amplified by a factor between 1 and 10 during chondrule formation. We therefore infer that background magnetic fields in the solar nebula were between 5 and 54 μT (Desch & Connolly 2002). Assuming Semarkona chondrules formed near 2.5 AU, which is the present day location of S-type asteroids (Bus & Binzel 2002), the vertical distribution of dust in the nebula strongly suggests that chondrule formation took place in the weakly ionized "dead zone", which contains gas poorly coupled to local magnetic fields and occurs within ~3 gas scale heights of the midplane (Bai 2011). Our measurements therefore indicate that a substantial magnetic field [yet still well below the ~400 μT equipartition field strength

Wardle (2007)] existed in the dead zone, potentially due to fields inherited from the collapse of the solar system's parent molecular cloud. Given our measured field strengths, mass accretion driven by the MRI or magnetic braking at 2.5 AU would have been $<0.04\text{-}3.5\times10^{-8}$ M_{sun} yr^{-1}, where M_{sun} is the Sun's mass (see below). Meanwhile, the MCW model would predict mass accretion rates of $0.3\text{-}30\times10^{-7}$ M_{sun} yr^{-1} or less. The inferred age of Semarkona chondrules is 2-3 My after the first calcium alunimum-rich inclusions (Mostefaoui et al. 2002). Given that protoplanetary disks are observed to have accretion rates of 10^{-9}-10^{-7} M_{sun} yr^{-1} at 2-3 My after collapse of their parent molecular clouds (Hartmann et al. 1998), both magnetic mechanism could fully account for the expected accretion rates. This suggests that magnetic fields govern the observed rapid transformation of protoplanetary disks into planetary systems around sun-like stars.

Previous theoretical work on nebular fields. Magnetic mechanisms are a promising solution to the problem of rapid gas accretion in the solar nebula and other protoplanetary disks (Turner et al. 2014), which have typical observed accretion rates between 10^{-9} and 10^{-7} M_{Sun} y^{-1} where M_{Sun} is the sun's mass (Herczeg & Hillenbrand 2008). In this section we summarize the relationship between magnetic field strength and mass accretion rate, thereby deriving the accretion rate given our experimental nebular paleointensities. We then compare these inferred accretion rates with observational constraints.

Accretion disk magnetic fields may transport angular momentum in two fundamental ways. The first is to transport angular momentum radially outward by the $R\phi$ component of the Maxwell stress tensor, given by $T_{R\phi}=-B_R B_\phi/4\pi$, where R and ϕ are the radial and azimuthal coordinates, respectively. This can be achieved either from turbulent magnetic fields, most plausibly from the MRI (Hawley & Balbus 1991; Balbus & Hawley 1991) or contributions from the large-scale field via magnetic braking, especially when the disk is threaded by external magnetic flux (Bai & Stone 2013; Bai 2014; Lesur et al. 2014). Assuming the $R\phi$ Maxwell stress is exerted through a layer with thickness comparable to the disk scale height $H=c_s/\Omega$, where c_s is the isothermal sound speed [given by $(kT/\mu m\text{-}_H)^{1/2}$ where k is the Boltzmann constant, T is the local disk temperature, m_H is the mass of hydrogen, and μ=2.34 describes the mean particle mass of the nebular gas] and Ω is the

local angular velocity, the steady-state accretion rate is given by (Wardle 2007; Bai & Goodman 2009):

$$\dot{M} \approx \frac{|B_R B_\phi| H}{2\Omega}. \tag{2.10}$$

Since $B^2 \geq B_R^2 + B_\phi^2 \geq 2|B_R B_\phi|$, the above equation yields a lower limit on the total magnetic field strength at a given accretion rate, which can be expressed as [see (Bai & Goodman 2009) for complete derivation]:

$$B \geq 1.0 \times 10^2 \dot{M}_{-8}^{1/2} R_{AU}^{-11/8} \ \mu\text{T}, \tag{2.11}$$

where $R_{\rm AU}$ is the disk radius is AU, $\dot{M}_{-8}$ is the accretion rate normalized to $10^{-8}\ M_{\rm Sun}\ {\rm y}^{-1}$, and we have assumed that $T = 280\ R_{\rm AU}^{-1/2}$ K (Hayashi 1981).

The second way is to transport angular momentum vertically and outward via the $z\phi$ component of the Maxwell stress tensor, given by $T_{z\phi} = -B_z B_\phi / 4\pi$. This can be achieved by the magnetocentrifugal wind (Blandford & Payne 1982). Accretion is driven by the torque $RT_{z\phi}$ exerted at the disk surface, which leads to an accretion rate:

$$\dot{M} \approx \frac{2|B_z B_\phi| R}{\Omega}. \tag{2.12}$$

Similarly, a lower limit on the total magnetic field strength in this scenario can be estimated to be [see ref. (Bai & Goodman 2009) for complete derivation]:

$$B \geq 10 \dot{M}_{-8}^{1/2} R_{AU}^{-5/4} \ \mu\text{T}, \tag{2.13}$$

which is largely independent of assumptions about disk model. We see that given similar level of stress, disk wind is more effective in driving accretion than the radial transport of angular momentum by a factor of $R/H \sim 30$ in the inner disk. Therefore, the disk wind requires weaker magnetic fields to achieve a given accretion rate.

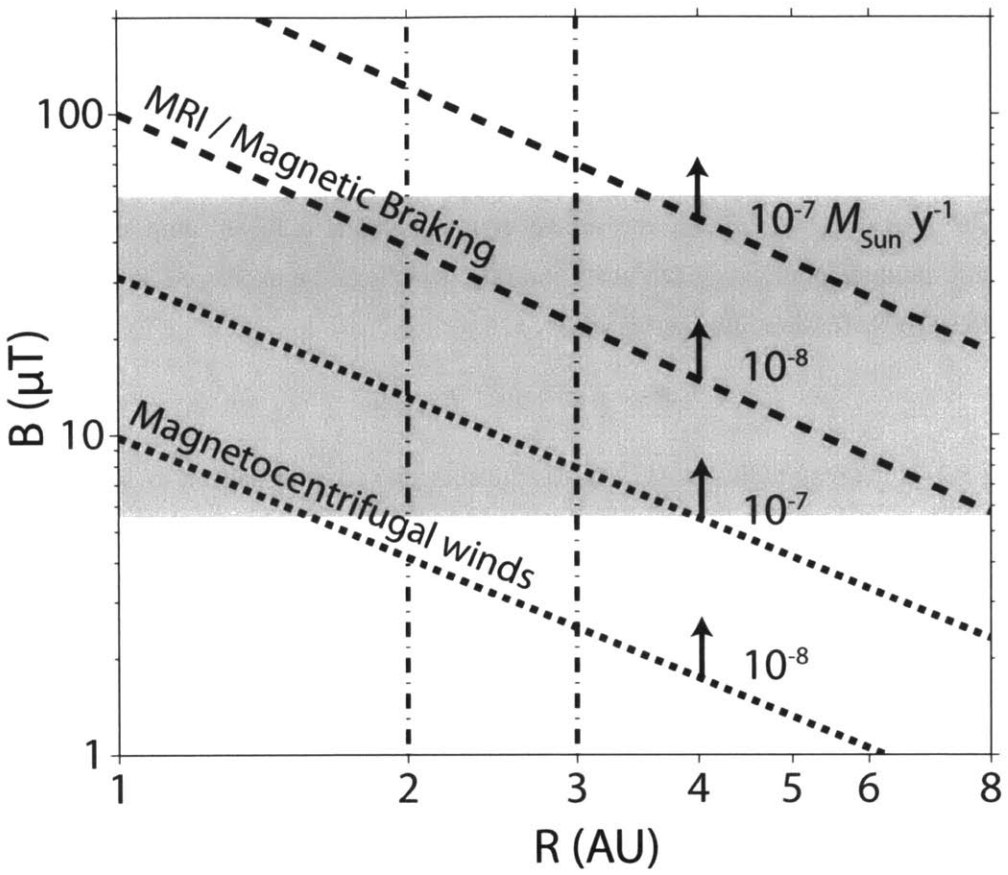

Figure 2.15. The minimum magnetic field strength as a function of disk radius at a given accretion rate. Dashed and dotted lines correspond to accretion driven by radial transport of angular momentum (due to MRI or magnetic braking) and by vertical transport of angular momentum (due to magnetized disk wind), respectively. The range of background disk magnetic field strength from our experimental results is denoted in gray (5-54 μT). The 2-3 AU region between the dot-dashed lines represent the probable source region of Semarkona based on the distribution of S-type asteroids, which are associated with ordinary chondrites such as Semarkona. Note that dashed and dotted lines represent lower bounds for the magnetic field strength expected for a given mechanism, orbital radius, and accretion rate.

Comparing these results with the inferred our experimental paleointensities (Fig. 2.15), we see that for a typical accretion rate of 10^{-8} M_{Sun} y^{-1} at the expected radius of R~2.5 AU, radial transport of angular momentum via the MRI or magnetic braking is possible if the disk magnetic field is ≥30 μT. In the case of wind-driven accretion, any disk field strength ≥3 μT would drive accretion at $>10^{-8}$ M_{Sun} y^{-1}. Given our recovered paleofield intensity during chondrule formation of 54±11 μT, the MRI or magnetic braking would drive sufficient mass accretion in the solar nebula if background fields were amplified by less than a factor of ~2 during chondrule formation. For wind-driven

accretion, even field amplification of 10× during chondrule formation, which is the highest amplification factor expected in the nebular shock (Desch & Connolly 2002), would imply sufficient background magnetic fields strength to drive disk accretion. Therefore, regardless of the type of chondrule formation mechanism, our experimental magnetic fields imply that magnetic mechanisms can readily account for the bulk of mass and angular momentum transport in the solar nebula.

Comparison with recent simulations. One uncertainty about the general discussion above is that our sample most likely records the magnetic field near disk midplane, while the lower limit of magnetic field strength in the two scenarios (2.11) and (2.13) only applies to regions where the $R\phi$ and $z\phi$ Maxwell stress is exerted. In particular, the wind stress $T_{z\phi}$ is exerted at the disk surface, which does not necessarily have the same field strength as that at the midplane. Therefore, comparison with detailed models of protoplanetary disks is necessary.

The gas dynamics and magnetic field structure in protoplanetary disks/solar nebula are strongly controlled by non-ideal magnetohydrodynamic effects including Ohmic resistivity, Hall effect and ambipolar diffusion (Turner et al. 2014). While the effect of Ohmic resistivity has been studied for over a decade (Gammie 1996), systematic exploration of ambipolar diffusion and the Hall effect began only recently. It has been found in simulations that, in the inner region of protoplanetary disks up to 10 AU, the MRI is suppressed and accretion is instead driven by the magnetocentrifugal wind (Bai & Stone 2013; Bai 2013). Inclusion of the Hall effect makes gas dynamics and magnetic field structure depend on the polarity of the net vertical magnetic field with respect to the angular momentum vector (rotation axis) of the disk. This polarity leads to markedly different behaviors especially in the inner disk (Desch 2004; Salmeron & Wardle 2003).

Full discussion about these effects is beyond the scope of this paper, and there remain several unresolved issues particularly concerning the wind geometry and kinematics. In brief, when the external vertical field is aligned with disk rotation, we expect amplification of the R and ϕ magnetic field components around disk midplane due to the Hall-shear instability (Kunz 2008). In this case, estimates based on Eq. (2.11) are relatively reliable if magnetic braking is the only mechanism operating. For the wind

scenario, Eq. (2.13) is likely an underestimate since the midplane field can be much stronger than the surface field [but still lower than that in Eq. (2.9)]. When the external vertical field is anti-aligned with disk rotation, current simulation results suggest wind-driven accretion with stress exerted at the disk surface, while the midplane field is mostly vertical whose strength is of the order 1 μT for typical accretion rates, which are too weak to be consistent with our experimental results. Therefore, our results may further suggest that the solar system was formed with its large-scale poloidal magnetic field aligned with disk rotation.

Chapter 3: Accretional detrital remanent magnetization

3.1. Introduction

As discussed in Chapter 1, one of the key unresolved problems in planet formation is the so called meter size barrier where decimeter and larger solid aggregates tend to disintegrate instead of accrete during mutual collisions. Turbulent instability models represent a promising solution to this problem, although direct experimental confirmation of their role in planet formation remains elusive.

Remanent magnetization in primitive materials provides one of the few direct records of magnetic fields present during the accretion stage of the solar system. Magnetic fields coupled to conducting nebular gas have been proposed as the principle mechanism responsible for outward angular momentum transport and inward mass transport in the accretion disk (Hawley & Balbus 1991). In this process, known as the magnetorotational instability (MRI), infalling material in the accretion disk is weakly coupled to material at greater orbital radii via magnetic fields in the 10 to 100 μT range. The nebular field therefore may have played a key role in establishing the large scale radial mass distribution in the solar system. Heating events associated with reconnection of nebular fields may have also formed chondrules and melted calcium-aluminum-rich inclusions (CAIs), the lithic constituents of chondritic meteorites (Levy & Araki 1989; Joung et al. 2004). However, reliable direct constraints on the strength and morphologies of solar nebular magnetic fields have proven elusive, and the precise role of magnetic fields in the accretion process remains uncertain.

At the same time, the process of growth for particles between 1 cm and 1 km in size in the solar nebula remains an open question. Unlike smaller particles, which efficiently form agglomerates during mutual collisions, particles at the centimeter scale or larger may undergo non-sticking collisions (Paraskov et al. 2007; Zsom et al. 2010). As a result, several competing hypotheses exist to facilitate the accretion of such particles into kilometer-sized planetesimals, at which size gravitational attraction accelerates the accretion process (Johansen et al. 2007; Cuzzi et al. 2008).

Remanent magnetism in primitive solar system materials could provide records of the magnetic fields in the early solar system. It may also constrain the nature and timing of

early remagnetization events such as thermal metamorphism and aqueous alteration in the nebular environment and on planetesimals (Weiss et al. 2010). In the latter case, remanence acquired on primitive parent bodies may record fields generated by interior metallic core dynamos, thereby constraining the timing and extent early planetesimal accretion and differentiation (Carporzen et al. 2011). Furthermore, relationships between the magnetization of different components in meteorites (e.g., between chondrules or between chondrules and matrix) can potentially distinguish amongst the various proposed accretional processes.

Records of ancient fields have been observed in meteorites and possibly via spacecraft flybys of primitive bodies (Weiss et al. 2010; Weiss et al. 2008; Richter et al. 2001). Most such remanence has been identified as thermoremanent magnetization (TRM) or crystallization remanent magnetization (CRM) that formed during thermal and crystallization events in the nebula or following accretion on planetesimals. However, during accretion, there are at least two additional ways by which ferromagnetic particles may form magnetized materials at larger scales.

Firstly, strongly ferromagnetic particles with sizes of ~10 nm may accrete as a result of their mutual magnetic attraction, thereby forming chain-like structures with increasingly larger net magnetic moments. This possibility, which we refer to as accretional attractive remanent magnetization (AARM), was addressed in detail by several numerical (Nübold & Glassmeier 2000; Dominik & Nübold 2002) and laboratory studies (Nübold et al. 2003; Wang et al. 2010). These studies found that AARM acting upon Fe metal and magnetite-rich particles with strong magnetizations can form "fluffy" aggregates of low fractal dimensions with sizes ranging from 0.1 μm to 1 mm. Beyond this limit, the specific moment of the aggregates becomes insufficient for the particles' mutual magnetic attraction to be the dominant factor in further aggregation. AARM may therefore have played an important role in the formation of the first macroscopic grain aggregates in the solar nebula.

AARM is not the focus of the present study. Rather, we describe a second process whereby both weakly and strongly ferromagnetic particles accreting in a background magnetic field may become mutually aligned to produce even larger structures with significant net magnetic moment. Unlike in AARM, the magnetic field in the latter

process is ambient (i.e., is not generated by the particles themselves) and serves to align the grains rather than act as an attractive force that enhances accretion (such that other forces like gravity and electrostatic attraction are relied upon for accretion). On Earth, the effect of such a process is ubiquitously observed in sedimentary rocks and is termed detrital remanent magnetization (DRM). Here we show how an analogous process that we call accretional detrital remanent magnetization (ADRM) should have operated during the accretional phase of the solar nebula. We also demonstrate that ADRM may be preserved in primitive meteorites, interplanetary dust particles (IDPs), asteroids, and comets. As described below, it may even have already been observed in some chondritic meteorites. Identification and characterization of ADRM may yield new constraints about the magnetic and dynamic environment of the early solar system as well as the accretion process of solid particles.

In ADRM, ferromagnetic grains are aligned such that their magnetic dipole moment is parallel to the background field. Such a "compass needle" alignment mechanism was also proposed as an explanation for the polarization of light passing through interstellar dust aligned to the interstellar magnetic field (Spitzer & Tukey 1951). This mechanism has since been shown to be implausible in the interstellar medium (ISM) given the weak intensity (~0.3 to 0.4 nT) of interstellar fields (Draine & Weingartner 1997). Instead, most observed grain alignment in the ISM is likely caused by a combination of radiative torque due to impinging light and paramagnetic dissipation. In the latter process, also known as the Davis-Greenstein effect, the rotation axis of rapidly spinning grains align to the ambient magnetic field over timescales of up to 10^6 yr. Other alignment mechanisms, such as interaction with interstellar gas flow fields, have also been proposed (Gold 1952).

However, as shown Section 3.2, several conditions should have favored compass needle alignment over these other mechanisms for ferromagnetic particles in the solar nebula. Firstly, observations of chondrites indicate there should have been significant quantities of highly ferromagnetic material present in the nebula. Magnetic minerals including magnetite, pyrrhotite, and Fe-Ni metals are present in both meteorite components such as CAIs and chondrules (Zolensky et al. 2006). FeNi metals and sulfides have also been identified in cometary grains and glassy pre-solar inclusions in interplanetary dust particles (IDP) (Bradley 1994; Nakamura et al. 2008). Secondly, the

much denser gas medium of the nebula (by a factor of ~10^9 relative to that of the ISM) causes rapid decay of angular velocity on a timescale far shorter than that of the Davis-Greenstein effect. Thirdly, the magnetic fields in protoplanetary disks are expected to be more than 10^3 times stronger than those of the ISM: direct observations of star-forming regions suggest that the ambient magnetic field in a protoplanetary disks is >1 μT (Wardle 2007). Finally, the larger particle sizes in the solar nebula relative to the ISM reduce the relative importance of processes that lead to rapid rotation of particles such as radiative torque, which has been proposed to operate only on small particles (< 100 μm) in the outer portions (10-100 AU) of T Tauri disks (Cho & Lazarian 2007).

Ferromagnetic particles will align with the background field when 1) the timescale of magnetic alignment is short compared to that of periodic, disruptive processes and 2) the dominant torque on the particle is magnetic. In Section 3.2, we describe a set of models used to constrain the range of particles and locations in the disk where alignment to a background field is expected. These models address seven distinct processes that affect the orientations of magnetic particle in the solar nebula:

1. Mutual collisions between dust grains
2. Rotational gas drag
3. Larmor-type precession around the background field direction
4. Rotational Brownian motion
5. Aerodynamic torque on non-spherical grains
6. Accomodation torque due to variations in momentum transfer efficiency on grain surface during gas molecule collisions
7. Radiative torque on irregular grains
8. Purcell torque due to H_2 formation at enhanced surface sites.

We quantify the effect of each of these processes and evaluate the likelihood of ferromagnetic grain alignment and formation of ADRM over a range of particle and nebula parameters. The results of our models are presented in Section 3.3.

In Section 3.4, we qualitatively address other relevant processes. We first use the results of recent dust collision experiments to identify the classes of collisions that would lead to the preservation of grain alignment in accreting dust agglomerates. We then discuss and evaluate the degradational effects of post-accretional impacts and parent

body alteration processes of ADRM. The requirements on temporal and spatial uniformity of the background field are outlined. We identify several observations from past chondrite paleomagnetism that may be attibuted to ADRM. Finally, we discuss the possibilities for future observations and their potential implications for our understanding of the early solar system.

3.2. Model description

Overview. Before delving into the physics of grain alignment, we provide a qualitative overview of the processes involved. In the solar nebula, solid particles composed of rock, ice, and metals with sizes ranging from 1 μm to many meters orbited the sun embedded in a tenuous gas environment ($\sim 10^7$ times less dense than air at sea level, but still $\sim 10^{14}$ times denser than interstellar space). Many of these particles should have contained ferromagnetic grains, which should have experienced a torque that could lead to alignment with the local magnetic field. For magnetic alignment to successful, it must proceed more rapidly than the timescale of mutual collisions beween solid particles, which disrupt alignment by imparting random, fast angular velocities to the grains. Rapidly spinning grains lose their angular velocity due to gas drag. If a grain spins down quickly before the occurrence of the next interparticle collision, it is free to align to the local magnetic field in the absence of another, stronger torque acting on the grain. These other possible effects include thermal excitation, aerodynamic torque, radiative torque, and several other processes.

If the conditions are satisfied such that grains align to the local magnetic field, further agglomeration of these coherently aligned particles may form a net magnetic moment pointing in the direction of the local magnetic field. The net moment of the agglomerate grows until it reaches a regime where the agglomerate's orientation is no longer controlled by magnetic torques. Therefore, the accretion of small, magnetically aligned agglomerates onto a nascent planetesimal, perhaps due to a local dynamical instability, may form large regions of uniform magnetization.

The solar nebula. We begin with a brief description the of the solar nebula environment. Although there is uncertainty regarding the evolution of the nebula during the time of

planet formation, it is likely that the accretion of sub-micrometer dust particles into kilometer-sized planetesimals took place over a timescale of order one million years (Weidenschilling & Cuzzi 2006). Most workers assume that the total initial mass of solid particles is equal to the combined mass of solids in the present-day solar system disk and that the total initial mass of gas is greater than that of solids according to the observed solar relative abundances. A disk with this assumed property is known as the minimum mass solar nebula (MMSN). The initial distribution of both gas and dust is expected to be in a flared disk up to 50 AU in radius. With time, solid particles settle to the midplane, creating a dust sub-layer whose height is determined by the amount of turbulence in the gas, which acts to suspend solid particles away from the disk midplane.

Due to the radial pressure gradient in the disk, gas molecules experience a slightly smaller centripetal acceleration than dust particles at the same location and therefore orbit more slowly. Larger dust particles are less coupled to the gas and feel a stronger "headwind." This effect, in conjunction with turbulent gas motion, generates relative velocities between dust particles, allowing them to collide and accrete. Such "hit and stick" agglomeration is an efficient method of forming particles of up to several centimeters in size (Zsom et al. 2010) in the standard MMSN and may be an important factor in accretional growth at even larger sizes. Growth by mutual collisions may be aided by local enhancements of density, leading to gravitational instabilities that form km-size planetesimals (Cuzzi et al. 2008). These objects in turn grow rapidly via gravity-enhanced collisions to form planetary embryos and planets.

Here we are most interested in the earlier stages of this process, wherein "hit and stick" collisions between micrometer to centimeter-sized objects is the dominant growth mechanism. The lifetime of the gas disk is between 5 and 10 million years and so is much longer than the timescale of planetesimal accretion. We therefore adopt a simple, time-independent temperature and density radial profile for gas in a minimum mass solar nebula following structure (Hayashi 1981):

$$T_{gas} = 280\, R^{-1/2}\,\mathrm{K} \tag{3.1}$$

$$\rho_{gas} = 1.36 \times 10^{-6} R^{-11/4} \,\mathrm{kg\,m^{-3}} \tag{3.2}$$

where R denotes distance from the sun in AU. We first consider a time-independent, locally uniform background magnetic field and discuss this assumption further below.

Particle-particle collisions. Solid particles in the nebula periodically encounter each other in non-sticking collisions. Such collisions impart high rotational velocities to the participating grains (e.g., (Wurm et al. 2005)). In order for magnetic alignment to overcome the effect of mutual collisions, two conditions much be met. First, the timescale of mutual particle collisions must be much longer than the timescale for a particle to come to rotational rest via gas drag. In the solar nebula, gas drag is the primary process by which particle angular momentum may be dissipated. Second, the strength of the background magnetic field must be sufficiently strong to align the particles within the timespan between successive collisions.

We constrain the collision timescale t_{coll}, which can be estimated simply: $t_{coll} = (\sigma n v_{rel})^{-1}$, where σ is the interaction cross-sectional area of the particles, n is their number density, and v_{rel} is a typical relative velocity. Because most particles are relatively weakly magnetized, there should be little magnetic enhancement of their interaction cross-sectional area such that σ is $\pi(2r_p)^2$, where r_p is the particle radius. If we assume a uniform size distribution of spherical particles, we obtain:

$$t_{coll} = \frac{\rho_p}{3 v_{rel} \rho_s} r_p \tag{3.3}$$

where ρ_p is the density of the particle and ρ_s is the volume density of solids at the specified radius in the solar nebula. We adopt a single grain density of $\rho_p = 2000$ kg m^{-3} as representative of a mix of compact particles such as CAIs and chondrules with highly porous dust agglomerates. The value of σ_s for a given particle size and location depends on the assumed surface density (σ_s, in kg m^{-2}) and the scale height (H_{dust}) of the dust sub-layer:

$$\rho_s = \frac{\sigma_s}{H_{dust}} \tag{3.4}$$

We adopt a simple model for the surface density based on the present-day radial distribution of solid matter in the solar system (Hayashi 1981):

$$\sigma_s = 300 R^{-3/2} \,\mathrm{kg\,m^{-2}} \tag{3.5}$$

The scale height of the dust sub-layer depends on the assumed degree of turbulence, since a more turbulent nebula stirs the solid particles into a thicker sublayer. Its value can be estimated for a given scale height of the entire gas disk and an assumed degree of turbulence, which can be parameterized by the dimensionless quantity α. We combine a simple power law for the gas disk scale height (Nakagawa et al. 1986)n with the considerations on turbulence given in Dubrulle et al. (1995) to obtain:

$$H_{dust} = 0.0472 \left(\frac{1}{3}\right)^{1/4} \sqrt{\frac{\alpha}{\Omega_k t_f}} \left(\sqrt{1 + \frac{\alpha}{\sqrt{3}\Omega_k t_f}}\right)^{-1} R^{5/4}\,\mathrm{AU}. \tag{3.6}$$

where R is given in AU, Ω_k is the Keplerian orbital frequency, and t_f is the timescale in which a particle slows to $1/e$ of its original translational velocity due to gas drag. For particles smaller than the mean free path of gas molecules, this is given by (Weidenschilling 1977):

$$t_f = \frac{\rho_p r_p}{\rho_{gas} \bar{c}} \tag{3.7}$$

where c is the mean velocity of gas molecules in the gas center of mass frame.

We assume a uniform particle size based on results from recent numerical simulations of bouncing dust collisions (Zsom et al. 2010). When compared to a size distribution heavily skewed towards smaller agglomerate sizes such as in the dust collision simulations of (Weidenschilling 1984), equation (3.3) underestimates t_{coll} for all but the

largest particles (those within one order of magnitude of the maximum particle size assumed in the distribution). Finally, the characteristic particle-particle velocity (v_{rel}) for a give particle size and location depends on the state of nebular turbulence. We adopt an analytic estimate valid for small particles with $t_f<\Omega_k$ [(Cuzzi & Hogan 2003), equation 22].

The rotational gas damping timescale. The decay of rotation due to gas damping plays two key roles. Firstly, as mentioned in the previous section, some damping is necessary to bring particles to near rotational rest. Compass needle alignment is possible only when the particle has no appreciable rotational energy retained from the most recent mutual collision. This is because if the particle is spinning sufficiently quickly, the magnetic torque will lead to precession of the rotation axis around the field direction instead of alignment. Secondly, the magnitude of gas drag determines the timescale of magnetic alignment, which must be shorter than the collisional timescale for magnetic alignment to proceed to completion. To calculate the timescale of angular deceleration of a particle, we evaluate rotational gas drag in the free molecular (FM regime, $Kn > 1/8$) and the low Reynolds number continuum (LR, $Kn < 1/8$, $Re < 1$) regimes, where the Knudsen number Kn is the ratio of the mean free path of gas molecules to the diameter of a solid particle (Lord 1964). The Reynolds number is defined as $Re = r_p^2 \rho_{gas} \omega/\eta$. is the angular velocity and η is the viscosity of the gas medium. Physically, the FM flow regime corresponds to an extremely rarefied gas where the mean free path length of gas molecules is long compared to the particle size. Molecules can therefore be thought of as independent impactors onto the particle surface. By comparison, the gas particles in the continuum regime will interact with each other within the vicinity of the particle, thereby leading to boundary layer formation. The torques due to gas drag in these two regimes are given by the following expressions (Lord 1964):

$$\tau_{FM} = \frac{2\pi}{3} f \rho_{gas} \bar{c} r_p^4 \omega \tag{3.8}$$

$$\tau_{LR} = 8\pi\eta r_p^3 \omega \tag{3.9}$$

where f is the efficiency factor of momentum transfer that we assume to be 1. The equations of motion governing the decay of angular velocity over time are of the form:

$$\omega' + \frac{\tau_{FM,LR}}{I}\omega = 0 \tag{3.10}$$

where $\tau_{FM,LR}$ denotes either τ_{FM} or τ_{LR} as appropriate for the particle, and I is the moment of inertia of the particle (approximated to be a uniform sphere). The solutions to the equations of motion are given by exponential functions:

$$\omega_{FM}(t) = \omega_0 e^{-(\tau_{FM}/I)t} \tag{3.11}$$

$$\omega_{LR}(t) = \omega_0 e^{-(\tau_{LR}/I)t} \tag{3.12}$$

where ω_0 is the initial angular velocity immediately after a particle-particle collision. The angular velocity in both regimes decreases by $1/e$ in the timescale I/ $\tau_{FM,LR}$ (Weidenschilling 1977):

$$t_{FM} = \frac{4\rho_p}{5f\rho_{gas}\bar{c}}r_p \tag{3.13}$$

$$t_{LR} = \frac{\rho_p}{15\eta}r_p^2 \tag{3.14}$$

In the sections below, we use the generic variable t_{drag} to denote this timescale of particle spin down, which is equal to t_{FM} or t_{LR} as appropriate for the particle and its environment. The values of t_{drag} for chondrule-sized particles are on the order of 10^2 to 10^4 seconds. This is consistent with the results of (Tsuchiyama et al. 2003).

Precession around the background field direction. In a macroscopic analog to the Larmor precession of atomic nuclei and electrons, dust grains with significant angular

velocity will precess around the axis parallel to the background magnetic field. As a result, a grain that has undergone a recent particle-particle collision will precess around rather than directly align to the magnetic field. Precession is the dominant motion of the grain until its angular velocity has slowed sufficiently such that the magnetic torque can alter the particle's rotation axis in a timescale less than the rotational period of the particle. Equivalently, the rotational energy of the grain must be on the order of, or smaller than, the work done by the magnetic torque over an angle of one radian (Davis & Greenstein 1951):

$$\tau_B \gtrsim \frac{1}{2} I \omega^2 \tag{3.15}$$

where τ_B is the torque due to the magnetic field and ω is the remaining angular speed of the particle from the most recent disruption event. We have shown above that, regardless of the initial angular velocity of a particle after collision, ω decays according to an exponential function with timescale t_{FM} or t_{LR} depending on the appropriate drag law. The condition on τ_B in equation (3.15). becomes:

$$\tau_B \gtrsim \frac{1}{2} I \omega_0^2 e^{-2t/t_{drag}} \tag{3.16}$$

where ω_0 is the initial angular velocity of the particle imparted in a collision and t is the time elapsed after the collision. A maximum value of ω_0 can be estimated by equating the energy of the colliding particles to the rotational energy of one of the particles immediately after the collision, which yields the approximation:

$$\omega_0 \approx \frac{v_{rel}}{r_p} \tag{3.17}$$

We find that, under turbulent conditions ($\alpha = 10^{-2}$), ω_0 is on the order of several times 10^3 s^{-1} for millimeter-sized particles and several times 10^2 s^{-1} for centimeter-sized particles.

Direct observations of particle rotation as observed in high speed dust collision experiments broadly agree with these estimates. One pair of photographs from Wurm et al. (2005) shows two 1 mm grains each rotating half a revolution in 0.5 ms ($\omega_0 \approx 6000$ s^{-1}), although it is conceivable that one or both grains rotated an odd multiple of that number. These values are also roughly consistent with the angular velocities inferred by (Tsuchiyama et al. 2003), who estimated chondrule angular velocities of between 300 and 2000 s^{-1} from their oblate shapes that formed during solidification.

The rotational kinetic energy of a particle immediately after collision is much larger than any reasonable estimate of magnetic torque in the solar nebula. Magnetic alignment is therefore not possible for the first several gas drag timescales until the rotational kinetic energy decays to the requisite levels. Whether a particle can align to the background field hinges on whether this angular velocity decay occurs quickly compared to the timescale between successive collisions.

Torque and timescale of magnetic alignment. The torque on a magnetic particle with mass-specific magnetic moment j in a background field with strength B_u is approximately:

$$\tau_B = \frac{4\pi}{3}\rho_p r_p^3 j B_u. \tag{3.18}$$

Laboratory measurements of the magnetic properties of natural and simulated early solar system material constrain the value of j. The value of ~220 Am^2 kg^{-1} adopted by (Nübold & Glassmeier 2000) is certainly an upper limit because idealized single-domain crystals of pure iron were assumed. Experimental studies with metallic iron and oxides reacting under simulated conditions of the hot early solar nebula produced sub-micron sized spherules with specific moments on the order of 10 Am^2 kg^{-1} (Wang et al. 2010). A more conservative estimate is given by the natural remanent magnetization (NRM) of chondrules. Laboratory measurements of chondrules and CAIs in the Allende CV carbonaceous chondrite show a range of magnetizations from 10^{-5} to 10^{-1} Am^2 kg^{-1}. The lower end of this range is consistently lower than analogous values for fine-grained

chondritic matrix, which may have been magnetized in post-accretionary processes (Carporzen et al. 2011). We adopt the value of $j = 10^{-5}$ Am^2 kg^{-1} as a reasonable, conservative estimate in our calculations. Furthermore, we adopt a value of 10 μT for the background field strength, consistent with measurements of midplane magnetic field strengths in the solar nebula (Fu, Weiss, et al. 2014).

We can now show that the magnetic torque is small compared to the rotational energy of a particle immediately after collision and is therefore unable to cause alignment until particle rotation has decayed [equation (3.16)]. For a 1 mm chondrule in a strong 100 μT field, the magnetic torque is 10^8 times smaller than the initial rotation energy given $\omega_0 \approx 10^3$ s^{-1}.

We will compare the magnitude of magnetic torque to that of other torques on the grain in the sections below. However, dominance of the magnetic torque over other effects alone is insufficient for successful grain alignment: the alignment must also occur quickly before grain orientation is disrupted by particle-particle collisions. We therefore calculate the timescale of compass needle alignment in a background field of a given strength and proceed to establish a minimum field strength necessary to bring a particle into alignment given a limiting timescale.

We are only interested in particles with t_{coll} much larger than the angular velocity decay timescale (t_{FM} or t_{LR}); otherwise precession would preclude alignment. Therefore, the particles may be treated as having essentially no initial angular velocity. Defining θ_t to be the angle between the direction of the uniform magnetic field and the dipole moment of the particle, the angular equation of motion is:

$$\theta'' + I^{-1}[\tau_{FM,LR}\theta' + B_u J_p \sin\theta] = 0 \tag{3.19}$$

where the second term is due to rotational gas drag and the third term is the magnetic torque. Here J_p is the total dipole moment of the particle and is given by the product of j and particle mass. We can approximate this system as a damped harmonic oscillator by setting $\sin\theta \approx \theta$. In the critical and overdamped cases, the timescale of rotation from an arbitrary initial orientation to the background field is on the order of the timescale of rotational gas damping (t_{drag}). Rotation of a ferromagnetic particle to the background field

cannot occur faster than this timescale; even in the presence of an arbitrarily strong magnetic field, the particle would oscillate around the field orientation, coming into alignment only after gas drag has dampened the amplitude of its oscillation. The background field strengths above which particle rotation occurs on the order of t_{drag} can be found by finding the value of B_u such that the grain is critically damped [e.g., (Taylor 2005)]:

$$B_{FM} = \frac{5f^2\rho_g^2\bar{c}^2}{32\rho_p^2 j} \tag{3.20}$$

for particles in the FM regime of rotational gas drag and

$$B_{LR} = \frac{45\eta^2}{2\rho_p^2 r_p^2 j} \tag{3.21}$$

in the LR regime. Note that in all damping scenarios, as long as the particle belongs to the free molecular rotational drag regime, the value of B_{FM} does not depend on the size of the particle, whereas in the low Reynolds number regime, larger particles become critically damped in weaker magnetic fields. Under solar nebula conditions, critical field strengths B_{FM} and B_{LR} are very weak, below 1 μT for all locations outside of 0.5 AU. Exact numerical solutions of equation (3.19) corroborate these findings and validate the approximation of simple harmonic motion. Therefore, all grains under consideration in this work are in the underdamped regime, in which rotation from rest into alignment with the background field takes place in a timespan of approximately t_{drag}.

We can now define t_{align}, which is the time required for alignment to the magnetic field after a mutual particle collision. This quantity is the sum of contributions from both the decay time of the angular velocity to the requisite levels and the time of rotation to the magnetic field. The former contribution t_{prec} can be found by combining equations 3.16 and 3.18:

$$t_{prec} = -\frac{1}{2} \ln \frac{5B_u j}{r_p^2 \omega_0^2} t_{drag}. \tag{3.22}$$

Because the subsequent rotation of the magnetic particle to the background field takes place in the timescale t_{drag} in the underdamped regime, the total time of alignment is:

$$t_{align} = \left(1 - \frac{1}{2} \ln \frac{5B_u j}{r_p^2 \omega_0^2}\right) t_{drag}. \tag{3.23}$$

Under solar nebula conditions, the precession term in equation (3.23, second term) is typically one order of magnitude greater than the magnetic rotation term.

Brownian motion. The orientations of very small magnetic grains are subject to the randomizing effects of rotational Brownian motion. Grains behave in this regime when the rotational component of thermal energy ($kT/2$) is comparable to the magnetic energy of alignment. Assuming thermal equilibrium, the grain size at which this occurs (r_{Br}) can be estimated conservatively as (Collinson 1965; Tauxe et al. 2006):

$$\frac{4\pi}{3} \theta_{crit}^2 \rho_p B_u j r_{Br}^3 \approx kT_{gas} \tag{3.24}$$

where k is the Boltzmann constant, B is the strength of the background field, and θ_{crit} is the allowed angular deviation from perfect alignment. We adopt a value of $\theta_{crit} = \pi/10$ as our threshold for an "aligned" particle. This simple analysis neglects the inertia of the grain and viscous drag forces, which decrease the effect of random thermal rotations. Therefore, our estimate for r_{Br} should be regarded as an upper bound, and some particles smaller than this threshold may not be strongly affected by rotational Brownian motion.

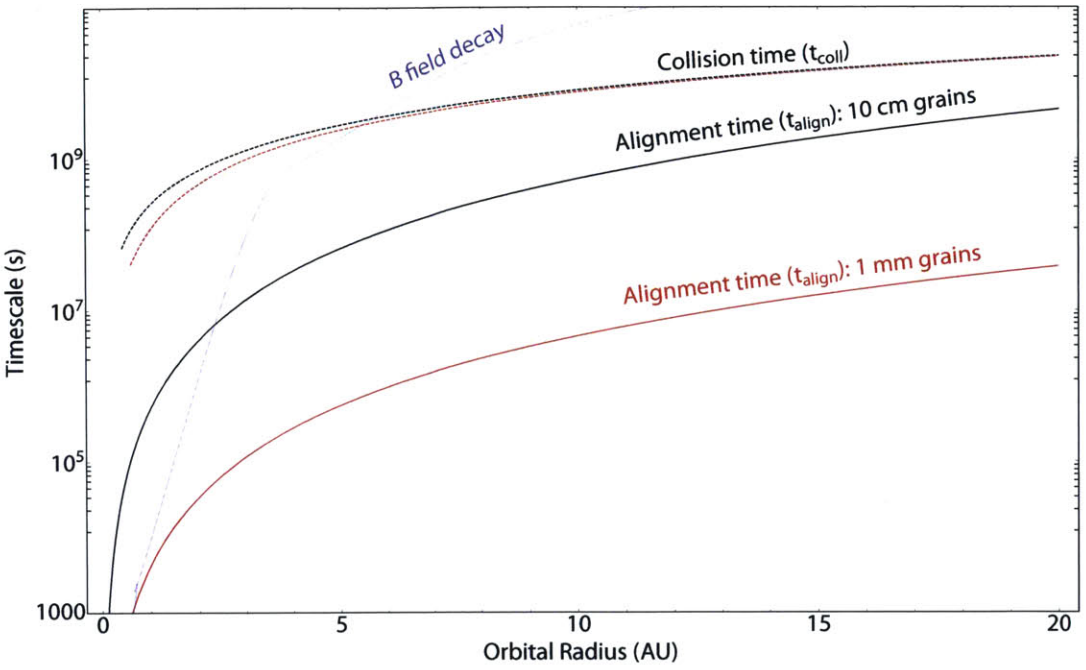

Figure 3.1: The expected timescales of successive particle to particle collisions (dotted curves, t_{coll}) compared to timescales of alignment to the local magnetic field of strength 10^{-5} T (solid curves, t_{align}). The alignment timescale includes contributions from both the spin down in angular velocity and the rotation of a particle at rest to the magnetic field direction. The spin down contribution is 8-11 times that of magnetic rotation for particles between 100 μm and 10 cm in size in the solar nebula. The blue curve indicates the expected timescales of magnetic field diffusion in a late-stage solar nebula with large accreted particles 1 cm in size (Stepinski 1992). ADRM may be active where these diffusion timescales are longer than those of magnetic alignment.

Aerodynamic torque. Non-spherical particles with Reynolds number greater than about 0.1 tend to align their long axis perpendicular to their direction of motion within laboratory timescales of a few seconds [e.g. McNown & Malaika (1950)]. This mechanism has been proposed as a key factor limiting the maximum particle size that is able to participate in terrestrial DRM (Heslop 2007). Particles in water on Earth tend to align to their hydrodynamically preferred orientation when they are larger than about 10 μm for ellipsoidal particles with aspect ratios (ratio of major to minor axes) of $\chi = 1.1$. As the timescale available for alignment is long in the solar nebula (Figure [fig:timescales]), particles with Reynolds numbers smaller than 0.1 may also align to the wind direction unless the magnetic torque is greater in magnitude. We therefore evaluate the magnitude of the aerodynamic torque in both FM and LR regimes. In both cases, for the sake of simplicity, we consider prolate ellipsoidal particles of homogenous density

where r_p now refers to the minor axis radius and χ equals 1.1 and 2 to simulate a range of non-sphericities.

In the FM regime, the overall torque is found by a sum of contributions from individual gas molecule collisions on all parts of the body. We use the expression for torque from each surface element as derived in [Ivanov & Yanshin (1980), equation (3.3)], who assumed a Maxwellian velocity distribution of gas molecules and thermal equilibrium with the solid particle.

For torque due to Stokes flow in the LR regime, we follow Galdi & Vaidya (2001) and Heslop (2007). The aerodynamic torque τ_a on a symmetrical prolate ellipsoid with semi-minor axis radius r_p and eccentricity $e = (1-\chi^{-2})^{1/2}$ is:

$$\tau_{asym,LR} \approx \frac{16\chi^4 r_p^4 \rho_{gas}^2 v_{gas}^3 |G|}{\eta} \sin(2\phi)\sqrt{\frac{\sin^2\phi}{Y^2}+\frac{\cos^2\phi}{X^2}} \tag{3.25}$$

$$\left\{\cos(2\phi)\left[\left(\frac{\cos\phi}{X}\right)^2-\left(\frac{\sin\phi}{Y}\right)^2\right]-\frac{\cos(4\phi)}{2XY}\right\}$$

where

$$X = \frac{8}{3}e^3\left[-2e+(1+e^2)\ln\left(\frac{1+e}{1-e}\right)\right]^{-1}$$

$$Y = \frac{16}{3}e^3\left[2e+(3e^2-1)\ln\left(\frac{1+e}{1-e}\right)\right]^{-1}$$

The torque coefficient $|G|$ varies between 0 and 1 and is a function of e, Φ is the angle between the long axis of the particle and the plane perpendicular to the flow axis, and v_{gas} is the relative velocity between the particle and surrounding gas. The angle Φ is estimated as $\pi/4$ to yield a value of torque close to the maximum. The velocity v_{gas} is estimated with a combination of systemic drift (due to different orbital velocities of solids and gas) and turbulence contributions. The former contribution is calculated explicitly by

simultaneously solving equations 15 and 20 in Weidenschilling (1977). The latter velocity component due to turbulence is estimated for two scenarios. First, we assume a quiescent nebula with zero turbulent velocity (Zsom et al. 2010) in order to find a lower bound on the aerodynamic torque. Second, we assume a highly turbulent turbulent nebula [$\alpha = 10^{-2}$; Dubrulle et al. (1995)]. To simulate the instances of maximum particle-gas velocity we add the drift and turbulent contributions of velocity (as opposed to adding in quadrature). Following the notation of (Cuzzi & Hogan 2003), the turbulent component of particle-gas velocity, v_{turb}, is:

$$v_{turb} = v_g \left[\frac{St_L^2 (Re^{1/2} - 1)}{(St_L + 1)(St_L Re^{1/2} + 1)} \right]^{1/2} \tag{3.26}$$

where v_g is the root mean square local velocity of gas relative to its own center of mass frame given by $v_g = c\alpha^{1/2}$. The Stokes number St_L is defined as the ratio of the translational gas stopping timescale (t_f) to the overturn timescale of the largest eddy, which is on the order of the local orbital period. The flow Reynolds number Re is defined as:

$$Re \equiv \frac{L v_g \rho_{gas}}{\eta} \tag{3.27}$$

where L is the size scale of the largest eddy, which is equal to the local scale height of the gas in the accretion disk (Nakagawa et al. 1986). Employing the derived velocities, we calculate the aerodynamic torque and compare it to the torque of the background magnetic field, τ_B.

In addition, we note Gold (1952) proposed that supersonic flow of a dilute gas across an ensemble of elongated particles would produce dust grain angular momentum vectors in the plane perpendicular to the direction of gas flow. The reasoning is that each impact between a grain and a molecule in a unidirectional stream contributes a small angular momentum that is described by a vector confined to the perpendicular plane. Given a large number of such collisions, a significant net angular momentum vector will result.

This effect is only valid for fast, rarified, and unidirectional gas flows such that the angular momentum contribution from each gas molecule collision is independent of the orientation and angular velocity of the grain. Specifically, the gas flow velocity across the grain must be supersonic so that only the faces of the grain oriented towards the flow direction receive momentum from the gas (Lazarian 2007). However, the gas environment within the solar nebula is sufficiently dense and warm such that grain motion is dominated by gas molecule collisions on all faces of the grain both towards and away from the wind direction. The mean gas particle velocity at 20 AU, for example, is c = 745 m s^{-1}, while particle drift velocities relative to the wind are no higher than several times 10 m s^{-1}. The Gold mechanism therefore cannot be a significant source of angular momentum for dust grains in the inner solar nebula.

Accomodation torque. Random heterogeneities in the momentum transfer coefficient (f, or the accommodation coefficient) on the surface of grains can result in a small net torque due to the bombardment of many gas molecules. Purcell (1979) first studied this effect and showed that the rotational energy from this source compared to the thermal excitation is:

$$\frac{E_{accom}}{kT_{gas}} \approx 7 \times 10^{6} \left(\frac{S\delta}{r_p}\right)^2 \tag{3.28}$$

where S is the characteristic size scale of surface heterogeneities and δ represents the magnitude of contrast in the accommodation coefficient. The latter quantity is estimated to range between 0.01 and 0.1, while S can be estimated by the mineral grain size observed in primitive materials. We therefore follow (Purcell 1979) and adopt 10^{-7} m as our estimate for S. We use δ = 0.1 to simulate a high degree of variability in the accommodation coefficient.

Radiative torque. Incident radiation can result in a torque on irregularly shaped grains. This effect was first proposed by [dolginov1976orientation], who considered the case of polarized incident radiation. The full magnitude of radiative torque due to a general

radiation field was not appreciated until the numerical simulations of Draine & Weingartner (1996), who showed that this effect may be the primary source of grain angular momentum in the ISM for particles of size greater than ~0.1 μm. Torque on a grain in a radiation field with volume energy density u_{rad} and mean wavelength λ can be estimated by:

$$\tau_{rad} \approx \frac{1}{2} r_p^2 u_{rad} \bar{\lambda} Q_\Gamma \tag{3.29}$$

where Q_Γ is the radiative "torque efficiency," which is specific for each grain shape and orientation with respect to any anisotropic radiation field. The value of Q_Γ generally varies by within a factor of a few for a variety of distinctly shaped irregular particles (Lazarian & Hoang 2007). A representative value of Q_Γ can be estimated as a function of the size of the particle and the characteristic wavelength of the impinging radiation. For particles larger than the typical wavelength ($r_p/\lambda \geq 1$), Q_Γ is on the order of unity, while $Q_\Gamma \approx (r_p/\lambda)^3$ for $r_p/\lambda < 1$ (Cho & Lazarian 2007). We adopt this approximation for our analysis. In reality, Q_Γ is suspected to decrease for particles much larger than the wavelength of radiation ($r_p/\lambda \geq 10$) due to the mutually incoherent torque contributions from a large number of grain facets. Numerical simulations for such large grains have not yet been carried out due to the computational costs involved. Radiation in the dust sub-layer of the solar nebula is dominated by in situ blackbody radiation in the far infrared, peaking at ~100 μm. Therefore, our values for τ_{rad} represent an upper bound for grains larger than about 1 mm.

Radiation with wavelengths shorter than the above peak value is expected to be reradiated from dust that is exposed to sunlight at the top and bottom surfaces of the disk. However, this reradiated light is greatly attenuated in the deep interior of the disk within the dust sub-layer (Chiang & Goldreich 1997). The radiation energy density is therefore a function of the interior temperature of the disk (equation 3.1). The energy density inside a blackbody emission region at temperature T integrated over all wavelengths is given by Planck's Law:

$$u_{rad} = \frac{8\pi^5 k^4}{15c^3 h^3} T^4 \tag{3.30}$$

where k is Boltzmann's constant, h is Planck's constant, and c is the speed of light.

Purcell torque. Purcell torque arises from heterogeneities on grain surfaces that result in variations in the rate of H_2 formation. Molecular hydrogen (H_2) formation in the ISM occurs primarily when individual H atoms are adsorbed onto the surface of dust grains where they encounter each other and depart as newly formed H_2. This recombination process occurs preferentially at "enhanced sites" where the binding energy between the grain and H atom is anomalously high. At such locations, H atoms are prevented from leaving the grain surface for a timespan longer than from other locations, thereby increasing the probability of an H_2 formation reaction (Hollenbach & Salpeter 1971). Because these sites are not uniformly distributed across the surface of the grain, unbalanced reaction forces from the departure of H_2 molecules result in a net torque on the grain. Purcell (1979) estimated this torque to be:

$$\tau_{Purcell} \approx \sqrt{\frac{32}{3\pi}} \gamma r_p^3 n_H \sqrt{\frac{kTE_{H_2}}{\nu}} \tag{3.31}$$

where γ is the fraction of H atoms that leave the grain as H_2 molecules, n_H is the number density of atomic hydrogen, E_{H2} is the kinetic energy of an ejected H_2 molecule, and ν is the number of "enhanced sites" on the grain. For the elevated temperatures in the solar nebula, γ is approximately 0.2 (Cazaux et al. 2005). The relative abundance of atomic to molecular hydrogen (n_H/n_{H2}) in protoplanetary disks is less than 10^{-4} at 1 AU (Glassgold et al. 2009). Willacy et al. (1998) showed that this ratio decreases with increasing orbital radius, although they did not present the values that support this. We use the approximation $n_H/n_{H2} = 10^{-4}$ for all radii. Purcell (1979) estimated E_{H2} to be 3×10^{-20} J and ν to be on the order of 100 for a grain with radius 10^{-7} m. We adopt Purcell's figure for E_{H2} and estimate ν for all grain sizes by scaling with the grain surface area: $\nu(r_p) = 100(r_p/10^{-7})^2$.

3.3. Results

The analysis in the preceeding section allows us to evaluate the likelihood of magnetic alignment for particles of different sizes and at distinct locations in the solar nebula. The following conditions are necessary for alignment between the grain magnetic moment and the background field:

1. Sufficient gas damping to bring a particle to near rotational rest in between successive collisions
2. Sufficient background field strength to bring a particle to alignment between successive collisions
3. Sufficient temporal stability of the background magnetic field direction
4. Negligible effect of Brownian motion
5. Small aerodynamic torque due to non-spherical particle shape compared to magnetic torque
6. Small torques due to variations in accomodation coefficient on grain surface
7. Small radiative torque compared to magnetic torque
8. Small Purcell torque compared to magnetic torque

Note that these conditions can be divided into dynamical (1, 2, and 3) and equilibrium (4, 5, 6, 7, and 8) requirements. The former requirements ensure that alignment occurs quickly between disruptive events (either mutual collisions or changes in the background field) while the latter establish magnetism as the dominant source of torque on the grain. Both sets of requirements must be met in order for a ferromagnetic grain to align successfully to the background field. We refer to the grains that satisfy the dynamical requirements as "stationary" and ones that satisfy both dynamical and equilibrium requirements as "aligned."

Dynamical requirements. Grains satisfying the dynamical requirements of magnetic alignment orient to the background field quickly before another event disrupts their alignment. As discussed above, gas drag must slow the angular velocity of grains

sufficiently such that their rotational energy is on the order of the magnetic work over one radian of rotation. This spin down occurs over the timescale t_{prec}. In addition to the time required for grain spin down due to gas drag, an additional timespan is required for the magnetic field to rotate the grain from an arbitrary orientation into alignment. For fields stronger than the critical strength indicated in equations (3.20) and (3.21), this rotation timescale is on the order of t_{drag}. Under solar nebula conditions, this critical field strength is very weak, below 1 μT for all locations outside of 0.5 AU. Therefore, the total time elapsed between a particle-particle collision and magnetic alignment (t_{align}) is the sum of these two contributions ($t_{prec} + t_{drag}$) and is given in equation (3.23).

At the same time, the expected time between particle-particle collisions (t_{coll}) for a given r_p and R can be estimated by combining equations (3.3) through (3.7). Particles of a given size and at a given radius in the disk spend some fraction of time at rotational rest (i.e., they are stationary particles) if $t_{coll} > t_{align}$. Mutual collisions between solid particles do not prevent magnetic alignment for such particles. In the inner 10 AU of the disk, most grains smaller than 1 m in diameter in a 10^{-5} T field are stationary (Figure 3.2).

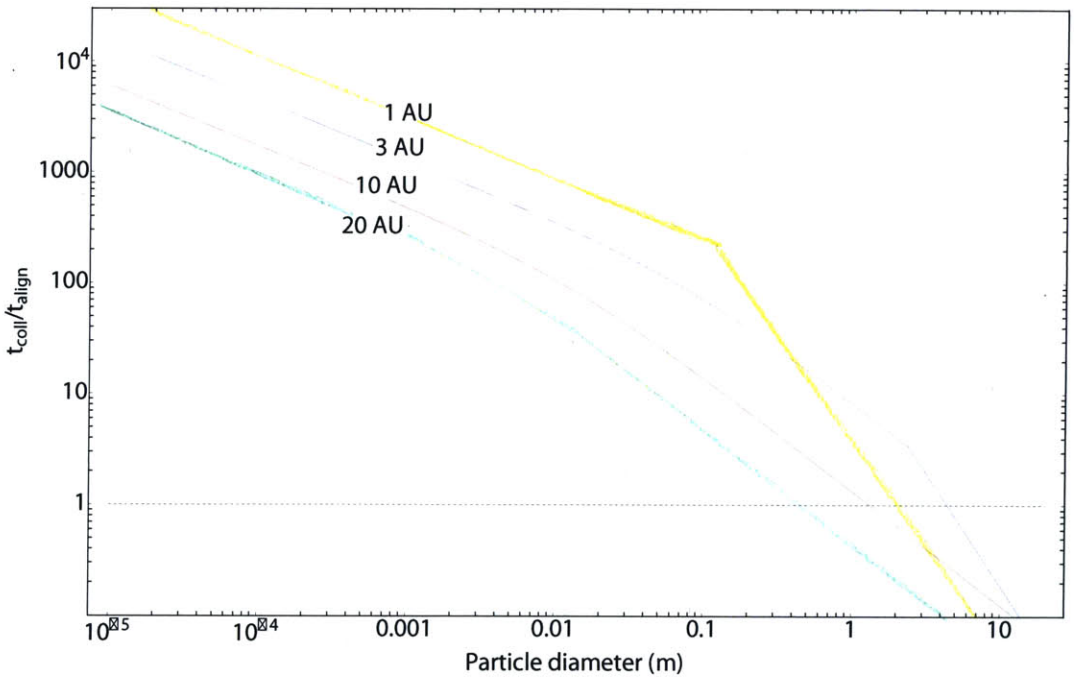

Figure 3.2: The ratio of average time between mutual collisions (t_{coll}) and minimum time necessary for particles to spin down and align to the background field following a mutual collision (t_{align}) for a range of particle sizes and locations in the solar nebula. Assumed background field is 10^{-5} T. Particles with the ratio $t_{coll}/t_{align} >> 1$ have negligible angular velocity at most times and would align to the magnetic field if no

stronger torque acts on them. The discontinuity in the curves at 1 and 3 AU is due to transition of the rotational drag law from the FM to LR regime.

A maximum in the possible size range of stationary particles occurs at about 4 AU (Figure 3.3, black curve). The existence of this maximum can be explained as follows. At this orbital radius, the gas drag law governing the largest stopped particle transitions from the LR regime at smaller orbital radii to the FM regime. The stopping time of particles of a given size in the LR regime is relatively insensitive to orbital radius ($t_{LR} \sim R^{1/4}$). On the other hand, at all orbital radii, t_{coll} increases quickly for particles farther from the sun ($t_{coll} \sim R^{3/2}$). Therefore, as one moves innerward from 4 AU, t_{coll} decreases faster than t_{align}, making stopping more difficult. As such, only smaller particles, which always have shorter values of t_{align} at the same orbital radius than larger particles, are able to stop, resulting in the decreasing range of stopped particle sizes at $R < 4$ AU. On the other hand, due to the more rarified gas environment, the largest stopped particles at $R > 4$ AU are in the FM regime, where t_{align} is very sensitive to orbital radius ($t_{align} \sim R^3$). As one moves away from the sun beyond 4 AU, t_{align} increases more rapidly than t_{coll}, resulting in more difficult stopping and therefore a smaller range of stationary particle sizes.

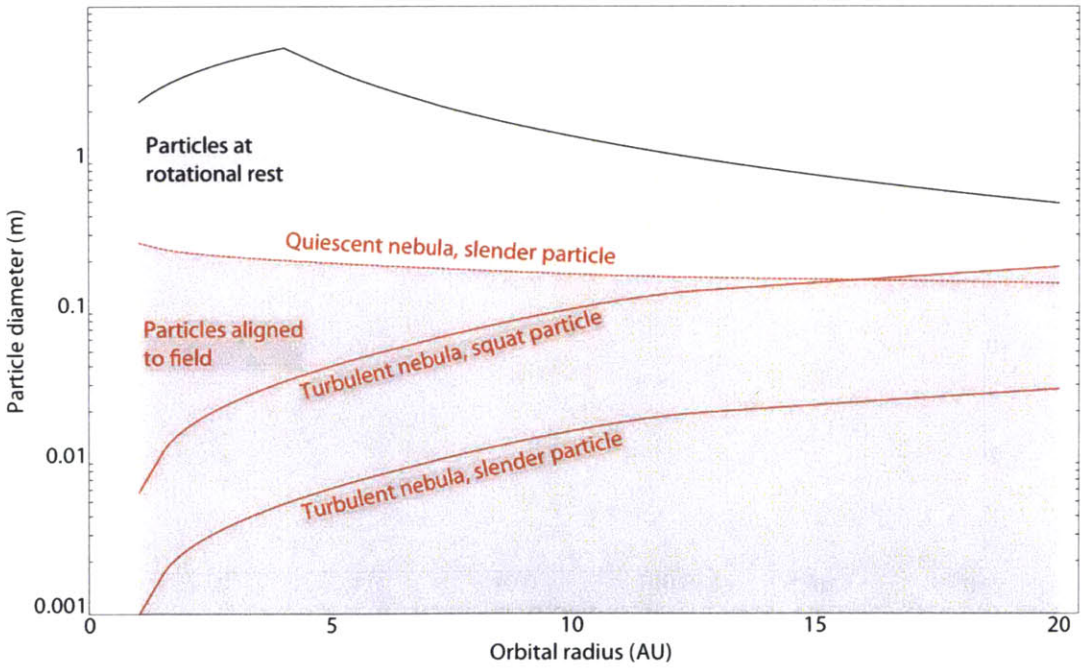

Figure 3.3. Expected maximum particle sizes to reach magnetic alignment. The solid black curve shows the maximum size of a particle that can be efficiently brought to rotational rest within the timescale of successive collisions ($t_{coll} = t_{align}$) for a background field strength of 10^{-5} T. The set of three red curves show

the maximum semi-minor axis diameter of an elongated particle (χ = 2 for "thin" and χ = 1.1 for "squat" particles) for which magnetic torque is greater than aerodynamic torque. The "Quiescent Nebula" case assumes relative velocity due to only radial drift while the "Turbulent Nebula" case assumes $\alpha = 10^{-2}$. Dark grey zone delineates particle sizes that reach alignment with the field between successive collisions, light grey zone delineates particles that come to rotational rest between collisions but do not align with the background field between successive collisions, and white zone delineates particles that remain continuously in motion between successive collisions.

Equilibrium requirements. Grains satisfying the dynamical requirements in the previous section have sufficient time between successive disruptive events to come to alignment in response to the strongest torque acting on the particle. Of the six candidate phenomena evaluated here (magnetic, thermal, aerodynamic, accomodation, radiative, and Purcell), we find that magnetic torque controls the orientation of spherical ferromagnetic grains within a range of sizes spanning several orders of magnitude (30 μm to several cm; Figures 3.4 and 3.5). Between \sim 1.5 and 20 AU in the dust sub-layer of the disk, aerodynamic torques dominate for larger, non-spherical grains while thermal excitation (i.e., rotational Brownian motion) prevents the alignment of very small grains. Radiative torque is stronger than magnetic torque for small grains ($\leq$ 500 μm) in the innermost nebula ($\leq$1.5 AU).

Non-spherical particles experience an aerodynamic torque based on their shape and direction of motion. For most locations in the solar nebula ($\geq$0.2 AU), this effect imposes the upper limit on the size range of magnetically aligned particles (Figures 4 and 5). This size threshold is provided by equating the aerodynamic and magnetic torques for a range of locations in the solar nebula and for an assumed field strength. We constrain the effect of turbulence by evaluating the aerodynamic torque for a quiescent (α = 0) and highly turbulent ($\alpha = 10^{-2}$) nebula. The lower size limit for magnetic alignment is defined by Brownian motion, except for the innermost nebula (<1.5 AU), where radiative torques dominate the alignment of grains on the order of 100 μm in size or smaller. Grains in this size range are most susceptible to radiative torque since they are close to the characteristic wavelength of the radiation field.

Due to the low abundance of atomic H and the large grain sizes in the solar nebula, Purcell torque is weaker than its magnetic counterpart for grains larger than the micrometer scale. For such small grain sizes, rotational Brownian motion inhibits successful magnetic alignment in any case. With respect to torque due to heterogeneities

in the accommodation coefficient, we find that this contribution to rotational kinetic energy is on the order of or less than 0.1 times the magnetic torque at the transition around 50 μm above which magnetic torques overwhelm thermal excitation. Magnetic torque increases quickly with respect to accommodation torque for larger grains. Therefore, this effect is not the dominant effect for grains of any diameter. Note that accommodation torque is greater in magnitude than Purcell torque (Figs. 3.4 and 3.5), which is opposite of the situation in the ISM, where Purcell torque are dominant. This is due to the much lower ratio of atomic H to molecular H_2 in the solar nebula.

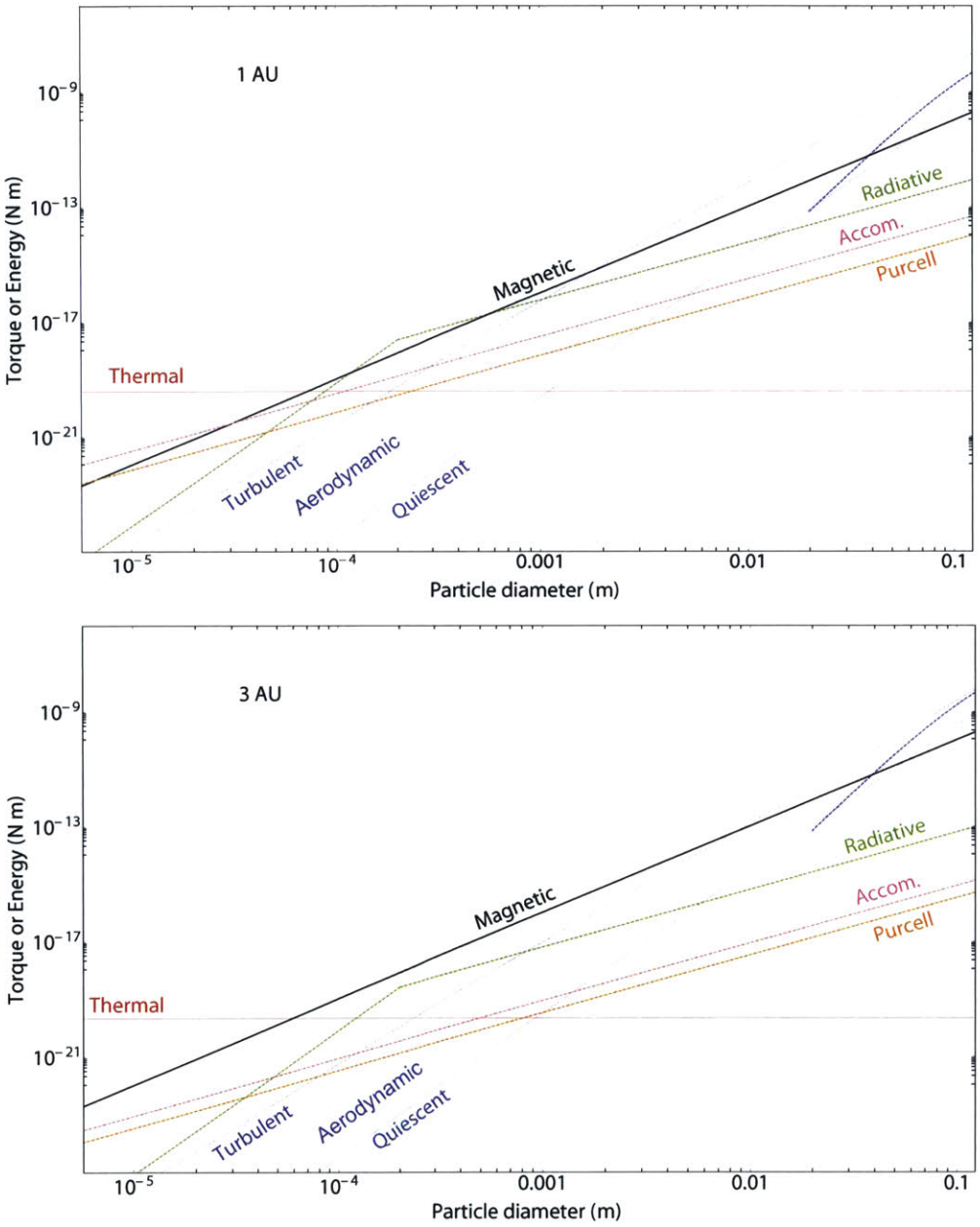

Figure 3.4. A comparison of the magnitudes of static and thermal excitation as a function of particle size for a background field of 10^{-5} T. The upper and lower solid blue lines were calculated for prolate ellipsoids in the FM regime with 1:2 and 1:1.1 aspect ratios, respectively. The dashed blue line represents torque in a turbulenton a 1:2 ellipsoid in the LR regime, which applies for particle sizes of >7 cm. Particles in the size range where the magnetic torque is dominant are expected to come to alignment with a uniform magnetic field. "Accom." is short for accomodation torque.

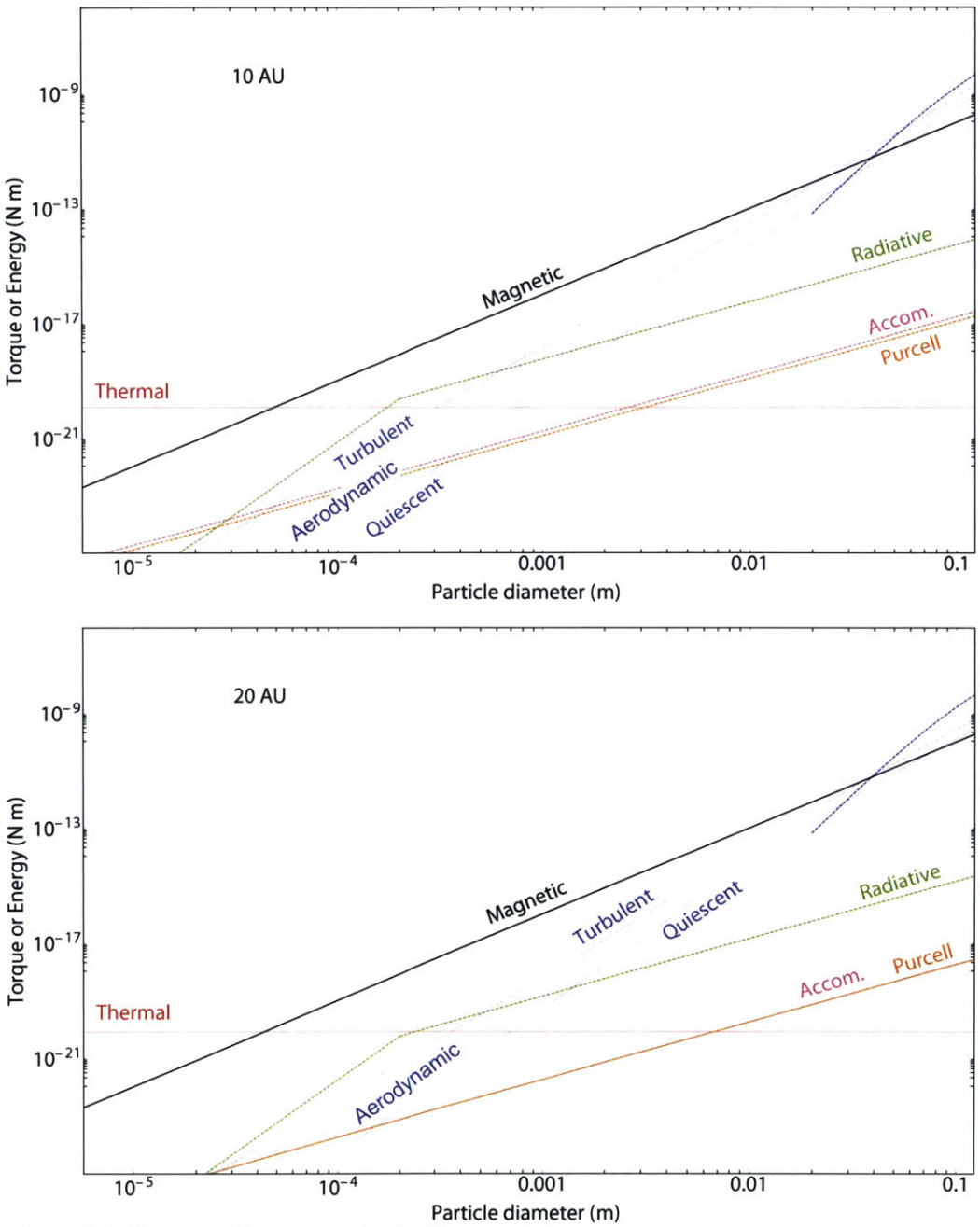

Figure 3.5: As Fig. 3.4 for greater orbital radii.

Taken together, our models show that, in a stable, uniform 10 μT field in a turbulent nebula, non-spherical magnetic particles with sizes from several tens of μm to several cm and aspect ratios between 1.1:1 and 2:1 are expected to be aligned with the background

field (Figure 3.3). Even larger particles greater than a meter in size may be aligned for nearly spherical particles, although the production of extremely spherical particles may be unlikely. Particles larger than these sizes are oriented primarily due to aerodynamic torque such that further mutual accretions will no longer efficiently preserve a net dipole moment. This size range includes significantly larger particles than those aligned in terrestrial DRM, which is thought to align grains up to just several tens of μm in size (Tauxe et al. 2006). This difference is due to a combination of a much more rarefied environment (hence less gas drag and aerodynamic torque) and longer timescales of accretion compared to settling in a water column (hence allowance for longer timescales of magnetic alignment). Our predictions for ADRM also contrast with the predicted alignment of small (0.01 – 100 μm) grains in T Tauri disks due to radiative torque (Cho & Lazarian 2007). However, Cho & Lazarian (2007) did not address the effect of magnetic fields on ferromagnetic grains, for which magnetic torques dominate over radiative torques under most circumstances (Figs. 3.4 and 3.5).

We note that some fraction of grains may be oriented such that radiative torques induce sustained suprathermal rotation, (i.e., their rotational energy is much greater than kT) (Lazarian & Hoang 2008). In such a case, the radiative torque, although weaker than the magnetic torque in magnitude, can sustain fast rotations in dust grains, which do not undergo compass needle alignment if their rotational energy is greater than the magnitude of magnetic torque. However, such suprathermal rotation is not likely to be a significant source of grain misalignment limiting ADRM for two reasons. Firstly, using the formalism in Lazarian & Hoang (2008), the suprathermal rotation state is not always stable even for ferromagnetic particles. This is mainly due to the high density of gas in the solar nebula (compared to the ISM), which makes for very short gas damping timescales. Ferromagnetic particles (with a typical susceptibility enhancement of 10^3 over paramagnetic grains) larger than ~40 μm at 3 AU (2 μm for 1 AU, 1 mm for 10 AU, 1 cm for 20 AU) have $t_{DG}>t_{drag}$. Most such particles, like paramagnetic particles, have a single stable rotational configuration with subthermal velocity (Lazarian & Hoang 2007).

Secondly, even if there is a stable high rotational velocity configuration for the grains, only some small fraction of grains are in the high rotational velocity state at any given time [Lazarian & Hoang (2008), Figure 2b]. Therefore, although this effect may be

responsible for preventing some grains from undergoing magnetic compass needle alignment, some population of grains will still be rotating slowly and therefore subject to magnetic torque. Unfortunately, we do not have access to the numerical simulations of Lazarian & Hoang (2008) to quantify the exact proportion of fast grains, and doing such a simulation is beyond the scope of this paper. We therefore regard suprathermal rotation as a possible means of decreasing the efficiency of alignment for a limited range of particle sizes, but cannot prevent the alignment of such grains altogether.

3.4. Discussion

Origin of ferromagnetic grains. With the size range of magnetic alignment constrained (Figs. 3.3, 3.4, and 3.5), we now discuss the likelihood of forming ferromagnetic particles within this size. In order for ADRM to operate, particles smaller than about 30 μm must grow into the size range in which ADRM is active while preserving an appreciable net magnetic moment. Specifically, the per unit mass magnetic moment must be greater than or equal to 10^{-5} Am^2 kg^{-1} to be consistent with our assumption. This may be achieved in three ways. Firstly, magnetic aggregates up to ~1 mm may be formed due to AARM if some of the magnetic grains in the agglomerate are made of strongly ferromagnetic minerals like kamacite or magnetite (Nübold & Glassmeier 2000; Wang et al. 2010). Secondly, millimeter-scale igneous particles such as chondrules and CAIs, which may have formed in great abundance in the early hot nebula (Bockelée-Morvan et al. 2002), would carry a significant magnetization if they formed in the presence of a magnetic field. Thirdly, even fully random assemblages of micrometer-scale grains can maintain a significant dipole moment into the size range where alignment to a background field is expected. Monte Carlo simulations of such flocs of magnetic grains show that the specific magnetization of a 10 μm aggregate is decreased by a factor of 40 compared to that of its constituent 1 μm grains (Heslop 2007). Therefore, if individual grains are magnetized to the mid- to upper- range of values as observed in the chondrules and CAIs of the Allende CV carbonaceous chondrite (j = 10^{-4} – 10^{-3} Am^2 kg^{-1} or 10^{-6} to 10^{-5} times the saturation magnetization of iron), our conservative estimate of j = 10^{-5} Am^2 kg^{-1} is reasonable.

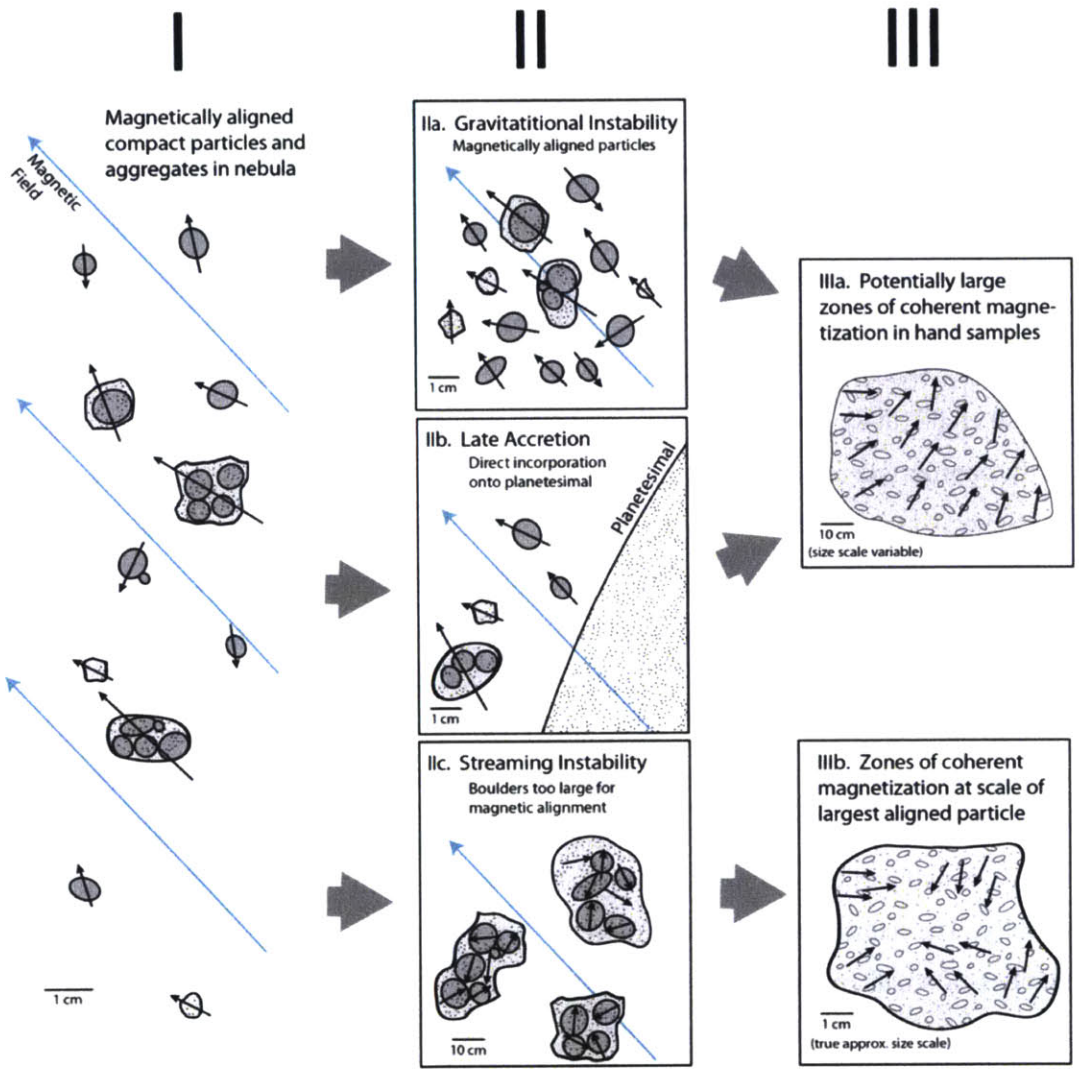

Figure 3.6: Three possible pathways for the accretionary growth of solid particles in the solar nebula and predicted ADRM zones. In Panel I, particles, including chondrules, CAIs, lithic clasts, and porous dust aggregates, grow or are formed in the size range in which magnetic alignment is active (up to several centimeters, see Fig. 3.3). Magnetic moments of particles are shown by black arrows and background magnetic field is shown by blue arrows. In the gravitational collapse scenario for small particles [Panel IIa, Cuzzi et al. (2008)], the gentle accretion of magnetically aligned particles may produce large (tens of centimeter or larger) ADRM zones in hand samples (Panel IIIa). Late accretion of aligned particles onto planetesimals may produce the same result (Panel IIb). On the other hand, streaming instabilities [Panel IIIc, Johansen et al. (2007)] require larger boulders that have already outgrown the size range of magnetic alignment, resulting in final ADRM zones no larger than the maximum size of magnetic alignment (typically centimeter-sized). In this case the ADRM zones formed when the particles and agglomerates were incorporated into the boulders before onset of the streaming instability.

Accretion and subsequent processing. In the preceding sections, we defined the size range of particles that are expected to align to a stable background magnetic field in the

solar nebula. We now discuss the subsequent growth of such particles into planetesimals and the necessary conditions for the preservation of ADRM on planetary bodies.

Solid particles in the solar nebula took the form of compact particles (CAIs, chondrules, lithic fragments), porous dust aggregates, or a mixture of the two. Melting or condensation produced directly compact particles up to 1 cm in size (more typically $\leq$1 mm). Although the agglomeration of dust and compact particles is a poorly understood process, most models and experiments suggest that growth into the millimeter or even centimeter scale is possible solely due to mutual, sticking collisions (Beitz et al. 2012; Ormel et al. 2008). Particles in these size ranges should be subject to magnetic alignment in the appropriate regions of the nebula (Fig. 3.6, panel I).

Several hypotheses exist regarding the subsequent evolution of such millimeter or centimeter-sized particles. The first class of models involve the incremental growth of particles via mutual collisions. Some fraction of these collisions result in the creation of larger solid aggregates. This process continues throughout the nebula until dust aggregates reach the km size scale, whereupon gravitational attraction becomes the driving force between further agglomeration. The second class of models call on some form of instability that enhance the density of a solid particles in a localized region of the nebula. Small particles within these high-density zones then accrete to form planetesimals directly. The nature of the instability may be solely due to the mutual gravity of a large number of small particles (Cuzzi et al. 2008) (Fig. 3.6, panel IIa) or may invoke local flow fields (i.e., streaming instabilities) of the nebular gas initially to concentrate particles (Johansen et al. 2007) (Fig. 3.6, panel IIc). In the former scenario, solid particles of millimeter size are able to form gravitational instabilities directly while in the latter scenario "boulders" at least several decimeters in size are required to participate in the streaming instabilities. A third possible fate of free particles in the solar nebula is late accretion directly onto the surface of an already-formed planetesimal (Figure 3.6, panel IIb).

ADRM operates differently on particles that accrete via these distinct pathways. In the incremental growth scenario, agglomeration of particles within the size range in which ADRM is active should form structures with larger and larger net magnetic moment. This process should continue until the dust aggregates have grown larger than

the maximum size for effective ADRM, which may be from several millimeters to several centimeters in size, depending on the sphericity of the aggregate. Further agglomeration of larger dust aggregates, which are oriented to the direction of gas flow, no longer preserve a net magnetic moment. Ultimately, the accreted planetesimal would be composed of zones of uniform magnetization with a range of sizes up to the upper size limit of active ADRM. Adjacent ADRM zones may show some coherence in direction if the rate of accretion was rapid compared to the timescale of local magnetic field change (e.g., due to rotation of the parent body).

In the gravitational collapse scenario, the participating particles may be in the appropriate size regime for magnetic alignment (Fig. 3.6, panel IIa). In such a case, the resulting planetesimal may contain large ADRM zones. Portions of the planetesimal that accreted in a stable magnetic field may show coherent magnetic moment directions. Although the high density of solids in the gravitational instability tends to make magnetic alignment more difficult, relative velocities in such concentrated clumps may be much slower than those typical in the solar nebula, resulting in more efficient magnetic grain alignment (Cuzzi et al. 2008). On the other hand, the streaming instability requires solid boulders too large for magnetic alignment. In this scenario, the boulders, and therefore the planetesimals they form, may contain ADRM zones near the upper size limit of magnetic alignment (Fig. 3.6, panel IIc). The ADRM zones in these boulders would therefore remain at the cm-size. Finally, in the case of late accretion directly onto formed planetesimals, we may expect to see zones of coherent magnetization whose size depends on the rate of accretion compared to that of planetesimal rotation or local magnetic field change (Fig. 3.6, panel IIb).

Can the orientation of solid particles be preserved during accretional collision? In the case of porous aggregates, some coherent grain orientations are likely preserved upon accretion. Dust collision experiments at high relative velocities of several tens of meters per second (Wurm et al. 2005; Paraskov et al. 2007; Teiser & Wurm 2009) have shown that sticking collisions between a small porous (80-90% porosity) "projectile" and a "target" of lower porosity (but still as high as 66%) preserve a nearly intact core of the porous body accounting for between 30% and 70% of the original projectile mass. Collisions of dust aggregates may therefore result in zones of unidirectional

magnetization bordered by zones of randomized grain orientations and low net magnetic moment (Fig. 3.6, panel IIIa). The zones of unidirectional magnetization represent the intact cores of the impactor, while the interstitial regions of low magnetization represent particles whose orientations were scrambled upon impact. Disruption of particle orientations in the larger participating aggregate ("target") is more severe when it is also highly porous (80-90% porosity). On the other hand, compacted aggregates (<66% porosity) are much more resistant to such catastrophic excavation (Paraskov et al. 2007; Teiser & Wurm 2009). In the case of chondrules and CAIs, sticking collisions may or may not result in the rolling of one object across the surface of another (Ormel et al. 2008). In the former case, magnetic coherence is preserved.

Subsequent impacts of compact and porous particles onto the planetesimal body likely led to significant compaction (Weidenschilling & Cuzzi 2006). Compaction of an accreted magnetic aggregate will affect the preservation of its ADRM. Studies of terrestrial DRM formation (Anson & Kodama 1987) have found that compaction alone should not erase ADRM, although its magnitude can be modestly reduced (e.g., 20% reduction after 50% volume change). A later study using a wider variety of minerals showed that magnetization reduction ranged from 0.2% to 48.5%, with most samples in the 30% to 40% range (Deamer & Kodama 1990). Major impacts on the parent body may also cause short-term heating that remagnetize material near the impact site.

Aqueous alteration in the nebular gas or on the planetesimal may further erode any preaccretional remanence. Several common magnetic phases found in chondrites (e.g., magnetite, pyrrhotite, and Ni-rich Fe-Ni alloys) are suggestive of metasomatic activity, although it is not entirely clear whether this occurred before or after planetesimal accretion (Brearley 2003). Reheating in the nebula or due to thermal metamorphism on the planetesimal may also cause partial demagnetization and/or magnetic overprinting (Carporzen et al. 2011), although metamorphic temperatures sufficient for complete demagnetization are not observed except for high petrologic type chondrites (Scott 2007).

In summary, the physics of small particle collisions and the origin and alteration of magnetic mineral phases in the solar nebula are not well-known, and the discussion above describes plausible scenarios where uniform magnetization in accreting particles may become preserved on a planetesimal object.

Stability of background magnetic field. The orientation and intensity of the magnetic field in the solar nebula can be changed by shear in the ionized gas medium and diffusive decay due to ohmic losses. Magnetic coherence of particles may be destroyed if the direction of the field changes faster than the timescale of magnetic grain rotation. The latter timescale is equal to t_{drag} instead of t_{align} (which includes the contribution from t_{prec}) because particles traveling from one region of uniform field into another do not need to spin down. The diffusive decay timescale of magnetic fields is controlled by the local gas conductivity, which requires a source of ionization energy, and the size and abundance of grains, which deionize the gas by acting as sites for charge recombination. Larger dust grains are less efficient at depleting gas ions than smaller grains. During all phases of the solar nebula, the surface layers of the gas disk are subject to ionization by cosmic ray bombardment, and the interior of the disk is also partly ionized due to radioactive decay of its constituents. Furthermore, in the initially hot solar nebula, thermal excitation is sufficient to produce similarly high ionization fractions within about 1 AU (Stepinski 1992). During the early stages of the nebula, the small characteristic size of dust grains (< 1 μm) reduces the conductivity of the gas such that the disk within ~20 AU of the sun is unable to sustain strong magnetic fields by the shear motion of the gas (i.e., it is magnetically inactive) (Sano et al. 2000). However, by the time dust grains have coagulated into the size range where ADRM is active (up to several cm), the dust-rich midplane outside of 5 AU is magnetically active. Furthermore, even the region within 5 AU may be magnetically active due to turbulent mixing of strong magnetic fields from near the surfaces of the disk (Turner et al. 2007). Magnetic fields in the midplane of the disk are expected to be stable on the order of the Keplerian orbital period (Turner & Sano 2008), which is at least one order of magitude greater than t_{drag} for all particles less than 10 cm in diameter at all radii less than 20 AU. Anticipated field strengths in the 1-5 AU zone range between 10^{-5} and 10^{-4} T, consistent with the lowest assumption of field strength made in the this work.

Even in the presence of a time-invariant magnetic field, solid particles may simply move in and out of zones of uniform fields if the spatial extent of uniform fields is small. To address this possibility, we take the simple approach of comparing the characteristic

length scale of uniform magnetic fields to the distance traversed by a particle relative to the gas in t_{drag}. We assume that solid particles travel through the gas at their systemic drift velocity. Turner et al. (2007) find that the magnetic field is mostly unidirectional on scales smaller than ~1/4 the gas disk scale height with $R < 5$ AU. At these orbital radii, the length scale of homogeneous magnetic fields is much longer than the path traveled by particles smaller than 10 cm within their t_{drag}. We therefore find that variations of nebular magnetic fields in both time and space do not pose a challenge for magnetic alignment within 5 AU. However, coupling between the magnetic fields and turbulent gas is stronger in the outer disk and the size scale of the smallest features in the magnetic field may be much smaller than the gas disk scale height if R is much greater than 5 AU. Therefore, it is possible and small field domains can interfere with particle alignment within 20 AU, although the precise size scale of field heterogeneities has yet to be studied at these radii. The observation of ADRM in primitive materials would constrain the minimum size of magnetic field heterogeneities in the region of accretion.

Detection of ADRM. Two methods for the detection of ADRM are available: paleomagnetic studies of samples of small bodies (meteorites and returned samples) and in situ magnetometry of small bodies. The following characteristics of ADRM may aid in its positive identification in both the laboratory and on small bodies:

1. Depending on the accretion scenario, ADRM may be manifested in meteorites as millimeter to centimeter-scale zones of uniform magnetization, with intermediate regions of suppressed magnetization formed by the scrambling of surface grain orientations upon accretionary impact (Figure 3.6, Panel IIIa). Even larger zones of coherent magnetization may be observed depending on the nebular mechanisms for accretionary growth (i.e., Figure 3.6).
2. The ADRM component is likely to be blocked to the Curie temperatures (the temperature above which no remanent magnetization can exist for a given magnetic mineral) of the constituent magnetic minerals, although it may be unblocked at lower temperatures if individual grains in the sample have been subjected to a partial thermal remagneization event prior to agglomeration.

3. Studies of terrestrial DRM, the intensity of ADRM magnetization is likely to be one to two orders of magnitude les efficient than TRM, possibly on the order of 10^{-4} of the saturation isothermal remanent magnetization of the same sample (Stacey 1972). Even if a slab of meteoritic material carries a bulk ADRM, the magnetic moments of individual components (chondrules, CAIs, lithic clasts) should not be precisely unidirectional; each would be misaligned from the net moment direction while the overall the magnetization would tend towards one direction. This stands in contrast to a TRM, which would produce well-aligned magnetizations down to much finer scales (within the limits of magnetic anisotropy within each component).
4. On unheated bodies such as comets, ADRM may be the most likely explanation for any detected remanence.

ADRM may have already been observed in meteorite hand samples, although the available data are ambiguous. In a detailed study of the Abee enstatite chondrite, (Sugiura & Strangway 1983) found that NRM directions from subsamples taken from a single ~1 cm clast ("Clast C") fell into two groups, with each group corresponding to a distinct section of the clast. To explain this observation, the authors proposed a partial TRM event prior to accretion in which the clast was not uniformly heated, but the plausibility of a large temperature contrast on a one centimeter body is uncertain. In any case, Abee is estimated to have experienced peak metamorphic temperatures of ~640° C on the parent body, which should have limited preservation of magnetization acquired prior to and during accretion (Fogel et al. 1989).

A later study of 17 mutually oriented chondrules in the Allende CV carbonaceous chondrite identified clustering of magnetic moment orientations in a direction dissimilar from that of the matrix. The authors conjectured that the chondrules' coherent orientations may reflect "depositional or accretional remanence" (Sugiura & Strangway 1985). More recently, Carporzen et al. (2011) detected the existence of several distinct zones of remanence direction in the matrix of Allende. After removing a mid-temperature unidirectional overprint (the authors' "MT" component), high-temperature remanence (the "HT" magnetization) of adjacent subsamples generally showed concordant directions

while subsamples taken with separations of several millimeters or greater showed distinct moment orientations. This HT magnetization might be a manifestation of ADRM, while the MT component cannot be an ADRM because it is only blocked up to 290 C (see Point 2 above). On the other hand, even the identification of the HT component as ADRM is suspect because Allende has been extensively metasomatized such that few ferromagnetic minerals present during accretion remain (Carporzen et al. 2011).

Despite these intriguing observations, no unambiguous detection of ADRM has been made in hand specimen. Further laboratory work is required for the positive identification and characterization of ADRM. This should consist of the mapping of remanent magnetization on the millimeter or greater scale in a range of meteorite groups. Characterization of blocking temperature, mineralogy, and local porosity will aid in ruling out CRM and inhomogeneous partial TRM as alternative sources of magnetic heterogeneity. Furthermore, the observation of demagnetized (i.e., "scrambled") zones between adjacent ADRM zones would argue strongly in favor of ADRM (Figure 3.6, Panel IIIa). Observations of consistency between magnetization and accretional textures, such as uniform magnetization in the dusty rims of CM chondrules (Metzler et al. 1992), would also provide strong evidence for ADRM.

Strong net dipole moments may have been detected during spacecraft flybys of the asteroids Gaspra and Braille (Kivelson et al. 1993; Richter et al. 2001). However, a large number of mutual non-unidirectional ADRM zones at the meter scale or smaller is unlikely to result in a strong net dipole when observed from an orbiting spacecraft. Magnetic zones of the sizes expected from ADRM can only be detected in situ by measurements directly on the surface of a body. Although no such remanent crustal fields were detected on the one asteroid surfaces that has been visited (Acuña et al. 2002), in 2015 the Rosetta orbiter and Philae lander are scheduled to measure the magnetic field of comet 67P/Churyumov–Gerasimenko. Because comets have not been globally heated since their accretion, they should not have a TRM. Other alternatives for the origin of cometary remanence are isothermal remanent magnetization (IRM) acquired in a strong external field, shock remanent magnetization (SRM), and CRM. IRM requires a strong, stable field of presently unknown origin, while SRM should be highly localized near impact features. Furthermore, modern interplanetary fields (order 0.5 nT) are likely two

weak to be recorded as SRM and CRM. As discussed in Section [sub:Accretion-and-subsequent], certain accretional histories such as gravitational instabilities and late accretion can potentially form large ADRM zones. The resulting magnetic fields may be detectable from a magnetometer such as the one onboard the Philae lander, which will make measurements ~1 m above the comet's surface (Auster et al. 2007; Bibring et al. 2007; Glassmeier et al. 2007).

Implications of ADRM. What can observations of ADRM tell us about the accretional phase of the solar nebula? With respect to nebular structure, the detection of ADRM would set a lower bound on the size scale of magnetically coupled eddies, as ADRM requires that regions of uniform field be large enough such that particles passing through them can align to the field before they pass into another eddy.

The identification of ADRM would represent the first unambiguous detection of magnetic remanence acquired in solar nebular magnetic fields during the accretion process [although not during chondrule formation (Fu, Weiss, et al. 2014)]. Its preservation would therefore constrain the intensity of nebular fields and the extent of subsequent demagnetization processes (e.g. recrystallization, thermal metamorphism, shock events) and overprinting episodes acting in the nebular gas and on the parent body. Coherence of magnetization on scales of larger than a few centimeters within a sample would provide evidence of formation via a quickly-accreting gravitational instability or thorough late accretion. It may be possible for a large fraction or even all of a planetesimal to be uniformly magnetized. The hypothetical detection of small ADRM zones on the centimeter scale or smaller would suggest that solids agglomerated past the maximum size of magnetic alignment before their incorpoation into a planetesimal. This is consistent with a streaming instability scenario involve decimeter to meter-sized boulders or with incremental growth. In such cases, large scale coherence among ADRM zones may be due to rapid accretion of particles onto a parent body. The rate of accretion onto the parent body surface must be quick compared to the timescale of the parent body's rotation with respect to a background field. Alternatively, the presence of strong surface fields on the parent body, possibly due to an internal dynamo, may be able to align incoming particles quickly and lead to coherent orientations upon accretion.

The size of ADRM zones would indicate that particles were aggregated to at least the size scale of the zones before final accretion. Therefore, observation of millimeter-centimeter scale zones suggests that particle agglomeration was possible at these size scales, despite high velocity collisions. As seen in Figure [fig:The-maximum-size], the size of expected magnetic zones is rather insensitive to solar nebula location but is a strong function of particle shape, turbulent gas velocity, and background field strength. Given the similar effects of these three parameters, a precise estimate of ancient field intensity may remain elusive. On the other hand, the presence of ADRM provides a lower bound on the possible strength of solar nebula magnetic fields. Furthermore, we can find a lower bound of the size scale of magnetic fields in the solar nebula as the alignment of particles requires regions of unidirectional field above a minimum size.

3.5. Conclusion

In this work, we have introduced a theoretical framework to judge the plausibility of accretional detrital remanent magnetization (ADRM) and predict its possible manifestations in primitive solar system material. We have shown that ferromagnetic particles between ~30 μm and several cm in size may align with the background field in the solar nebula and subsequently accrete to form ADRM, which is potentially observable in primitive meteorites and small bodies. We have considered a series of processes that govern the efficiency of ADRM acquisition and estimated the particles sizes that are subject to forming ADRM. Factors that may interfere with particle alignment in the nebular gas include mutual particle collisions, rotational Brownian motion, aerodynamic torque, radiative torque, and magnetic field instability in time and space. Using plausible values for the magnetic field strength (>1 μT), rotational gas drag is not sufficient to hinder alignment within the timescale of successive particle collisions and in fact aids particle alignment by quickly damping random rotations of particles. This is distinct from DRM on Earth, where viscous drag prevents rapid alignment of larger particles. For most orbital radii <20 AU, rotational Brownian motion and aerodynamic torque provide the lower and upper size limits on particles that can be successfully aligned to the background field. Meanwhile, radiative torques play a significant role for

small particles in the inner nebula (<1.5 AU). The necessary condition of temporal field stability appears to be satisfied for the solar nebular outside of about 2 AU and for all distances from the central plane. The size scale of magnetic field heterogeneity must not be small such that solid particles can traverse them faster than their alignment timescale.

The upper size limit for magnetic alignment in the solar nebula (Fig. 3) is ~1000 times larger than that for terrestrial DRM. Magnetic particles within the size range of efficient alignment that accrete with another such particle will grow while maintaining their net magnetic moment until they reach the upper end of this size range. Gravitational instabilities or rapid accretion in a slowly changing field may lead to coherence among the magnetic orientations of accreted particles at larger scales of >1 m. Although the degree of preservation of grain orientations upon accretionary collision beyond this stage cannot be quantified, grain collision experiments suggest that a significant portion (>30%) of the projectile's material becomes compressed but is otherwise left intact. Further metasomatism and impacts on the planetesimal body may weaken the magnitude of the remanence, but a pathway by which the uniform magnetic remanence in nebular agglomerates may be preserved in larger bodies is established.

Zones of unidirectional magnetization (Fig. 3.6, panels IIIa and IIIb) may potentially be observed in primitive samples, such as chondritic matrices. These zones are likely separated by regions of low magnetic coherence among grains. Monolithic particles such as CAIs and chondrules may also show mutually coherent magnetic orientations, resembling those observed by Sugiura & Strangway (1985). Along with CRM, ADRM represents a plausible origin for observed magnetic coherence on the millimeter to centimeter scale observed in in some chondrites [e.g., the HT magnetization studied by Carporzen et al. (2011)]. Other possible detections of ADRM in meteorite samples and by spacecraft measurements exist, but so far the interpretation of all of these observations as ADRM remains ambiguous.

If detected, the characterization of ADRM would have important implications for the structure of the solar nebula turbulence, the nature of early magnetic fields, and the thermal, chemical, and impact history of primitive bodies. Furthermore, structure of ADRM zones would constrain the formation process of the sample, distinguishing between the various hypothesized accretion scenarios. ADRM zones could be identified

by conducting detailed mapping of magnetization directions in primitive meteorite samples. A true ADRM may be distinguished from other forms of remanence by its characteristic larger-scale (centimeters or larger) non-unidirectionality, low intensity, and the fact that it is blocked up to the Curie temperature. ADRM may also be detected by spaceborne magnetometry measurements of small bodies such as comets and primitive asteroids. We hope that this work will encourage further experimental studies to detect this new form of remanent magnetization.

Chapter 4: Magnetization of the Allende CV carbonaceous chondrite

4.1. Introduction

This Chapter represents a transition between my work on nebular magnetic fields to those potentially generated by the core dynamos of differentiated planetesimals. Here I perform paleomagnetic experiments on the Allende CV carbonaceous chondrite, which has previously been cited as a recorder of nebular magnetic fields. I show that this interpretation is inconsistent with new experiments that recover remanence at finer spatial scales and that the most likely origin of the magnetization in this meteorite is during and after aqueous alteration in the presence of a core dynamo that persisted for <40 My.

During the first several million years of planet formation, dust in the solar nebula accreted to form 100 to 1000 km-scale planetesimals (Chambers 2004). Theoretical models strongly suggest that magnetic fields played a critical role in the dynamics of the nebular gas and the evolution of solid particles. In particular, large-scale mass and angular momentum transfer in the nebula may have relied on magnetocentrifugal winds and/or turbulence generated by the magnetorotational instability (MRI) (Bai & Stone 2013; Balbus 2003). Magnetically-induced turbulence may have also facilitated mutual collisions and local concentration of solid matter, thereby allowing for the accretion of solid bodies (Cuzzi & Hogan 2003; Johansen et al. 2007).

The first known macroscopic solids to form in the solar nebula were chondrules and CAIs, millimeter-sized inclusions now found in chondritic meteorites. Chondrules are igneous spherules that melted and cooled quickly in the solar nebula, while CAIs are nebular condensation products often subjected to subsequent reheating (MacPherson 2007). Because they were heated and cooled in the solar nebula, these objects may have recorded the nebular magnetic field. Therefore, paleomagnetic studies of chondrules and CAIs can potentially provide direct constraints on the strength of nebular magnetic fields and their role in solar system formation. Fields in the midplanes of the terrestrial planet-forming region in protoplanetary disks are currently inaccesible to astronomical measurements (Crutcher 2012).

Paleomagnetism of chondrite inclusions such as chondrules and CAIs may also have important implications for the setting and mechanism of chondrule formation (Desch et al. 2012). Chondrule formation hypotheses often predict very different magnetic field environments (Desch & Connolly 2002; McNally et al. 2013). Knowledge of the magnetic field intensity in the chondrule-forming environment would therefore provide new constraints on this enigmatic process.

However, paleomagnetic studies of primitive inclusions face the challenge that chondrules and CAIs in all meteorites have been subject to a combination of secondary alteration and metamorphic reheating after their accretion onto their parent body. These processes may have compromised any pre-accretional natural remanent magnetization (NRM). Furthermore, many meteorite samples experienced remagnetization in strong artificial magnetic fields on Earth following their collection. Such strong fields, if not properly identified and removed, can lead to misinterpretation and severe overestimates of ancient magnetic field strengths (Weiss et al. 2010).

Paleomagnetic tests can aid in distinguishing between pre-accretional and post-accretional NRM in chondrites. In the *conglomerate test*, mutually random magnetization directions in chondrules and other inclusions provide evidence for magnetization predating the final assembly of the rock. This is because if the chondrules were completely remagnetized in a spatially uniform field following accretion, they should be magnetized in the same direction within a given meteorite. A second, *unidirectionality test* examines the direction of magnetization in subsamples of individual chondrules and CAIs. A pre-accretional thermoremanent magnetization (TRM) is expected to be unidirectional across subsamples. Both paleomagnetic tests require analysis of mutually oriented samples.

The Allende CV carbonaceous chondrite is probably the most extensively analyzed chondrite using paleomagnetic methods. Measurements of individual, unoriented chondrules (Acton et al. 2007; Emmerton et al. 2011; Lanoix et al. 1978) have inferred magnetic field paleointensities of between 10 and 1600 μT. However, these studies could not establish a pre-accretional origin for the magnetization or rule out artificial isothermal remanent magnetization (IRM) contamination. The latter almost certainly accounts for the paleointensity values >200 μT (Cisowski 1987; Wasilewski

1981). Neglecting those affected by IRM, bulk Allende samples and some isolated chondrules carry a strong unidirectional overprint that unblocked below ~300°C acquired on the CV parent body (Carporzen et al. 2011; Nagata 1979a; Sugiura & Strangway 1985). Carporzen et al. (2011) interpreted this post-accretional magnetization, which they called the middle temperature (MT) component, as evidence for a past magnetic core dynamo on the CV parent body, implying that this body underwent igneous differentiation while preserving a relatively unheated chondritic crust.

Nevertheless, paleomagnetic studies by Sugiura et al. (1979) and Sugiura & Strangway (1985) showed that, after removal of the low temperature overprint at ~300°C, individual, mutually-oriented chondrules in Allende had widely scattered magnetization directions that pass the paleomagnetic conglomerate test at the 95% significance level (Watson 1956). Sugiura & Strangway (1985) concluded that this non-unidirectional component is a pre-accretional TRM acquired in a nebular magnetic field.

However, a major source of subsequent confusion has been that no paleointensities were reported for this non-unidirectional HT component. As a result, many later studies have mistakenly cited paleointensities derived for the other magnetization components in Allende as constraints on nebular fields. In particular, many theoretical studies (Levy & Araki 1989; Stepinski 1992; Rozyczka et al. 1996; Shu et al. 1996; Nübold & Glassmeier 2000; Desch & Connolly 2002; Johansen 2009) have cited the ~100 μT paleointensity values derived from unoriented chondrules or bulk samples (which should be dominated by the post-accretional MT overprint) or even the high paleointensities of 100-1600 μT from a set of unoriented chondrules likely contaminated by IRMs on Earth (Wasilewski 1981).

Adding to the uncertainty, the paleomagnetic conglomerate test alone, as performed by Sugiura & Strangway (1985), is in fact insufficient for establishing the pre-accretional origin of the HT chondrule magnetization. Post-accretional recrystallization of magnetic phases in a near-zero magnetic field can also produce randomized magnetization directions (Uehara et al. 2011), potentially leading to a false-positive conglomerate test. In fact, the weak intensity of the HT magnetization and its non-origin trending behavior during higher temperature thermal demagnetization are all characteristics of such null field remanence (see Section 4.4).

Here we report new paleomagnetic analyses on mutually-oriented Allende chondrules and subsamples of individual chondrules with the goal of determining whether the HT component in Allende chondrules is in fact pre-accretional. We find that, although the HT magnetizations of individual chondrules pass the conglomerate test, *subsamples* of individual chondrules also have statistically random magnetization directions, thereby failing the unidirectionality test. Coupled with petrographic observations and modeling of TRM acquisition in the solar nebula, we argue that all observed magnetization components in Allende chondrules are post-accretional. Finally, we discuss the implications of these results for the CV parent body core dynamo hypothesis and the lifetime of such a dynamo.

4.2. Samples and methods

We performed two kinds of paleomagnetic measurements. The bulk of our analyses employed classic moment magnetometry using a 2G Enterprises Superconducting Rock Magnetometer (2G SRM) 755 at the MIT Paleomagnetism Laboratory. These were supplemented with magnetic field maps acquired with the MIT SQUID Microscope (Weiss et al. 2007).

Samples analyzed using the 2G SRM were extracted from a slab of Allende provided by the American Museum of Natural History called AMNH5056, which is a ~10 × 10 × 0.8 cm piece previously studied by Carporzen et al. (2011). All samples taken from AMNH5056 are mutually oriented with respect to samples in Carporzen et al. (2011).

Carporzen et al. (2011) conducted a fusion crust baked contact test (Nagata 1979c; Weiss et al. 2010) on AMNH5056 and showed that the fusion crust, which was melted during atmospheric entry, carries magnetization distinct from that in samples taken ≥1 mm in the interior. This systematic change in magnetization direction and intensity indicates that AMNH5056 escaped significant remagnetization after its arrival on Earth and that the interior magnetization is extraterrestrial in origin. Because AMNH5056 had been stored in the magnetically shielded room at the MIT Paleomagnetism Laboratory (DC field <150 nT) since the experiments in Carporzen et al. (2011), their demonstration

of extraterrestrial magnetization in AMNH5056 applies to our samples extracted from this parent piece.

We used nonmagnetic dental tools to extract twenty-one chondrules and six matrix-rich samples from thin (0.5 – 1.0 mm) slices of Allende cut using a diamond wire saw. Because the Allende matrix is on average 2-4 times more magnetic per unit mass than typical chondrules and CAIs (Emmerton et al. 2011; Nagata & Funaki 1983), we carefully removed all visible traces of matrix material adhered to chondrules. When possible, we subsampled individual chondrules using either a diamond wire saw or dental tools. Seven of the twenty-one chondrules were partitioned into at least two mutually oriented pieces. All chondrule and matrix samples were mutually oriented to better than 5° accuracy. Samples were numbered before extraction, resulting in unused numbers among the successfully extracted and measured samples. We mounted all samples on GE 124 quartz disks with cyanoacrylate or non-magnetic silver paste (SPI Silver Paste Plus). All sample mounts and adhesive had moments less than $\sim 5 \times 10^{-12}$ Am^2, which is the effective noise level of our 2G SRM measurements.

Twelve chondrule samples from six distinct chondrules and four matrix-rich samples were subjected to stepwise thermal demagnetization in air up to the point when the magnetization direction became incoherent or the sample moment spontaneously increased due to alteration of magnetic phases, which occurred ≤420°C. An additional two matrix-rich samples and thirteen chondrule subsamples from eleven distinct chondrules were subjected to three-axis alternating field (AF) demagnetization up to 85 mT. Samples mapped using SQUID microscopy include one 30 μm thin section from AMNH5056 and the five isolated chondrules from a second Allende slab called AMNH4889. The thin section was prepared without any heating using cyanoacrylate and bronze saw blades. Non-magnetic alumina-based polishing agents were used during thin section preparation to minimize contamination.

The MIT SQUID Microscope acquires maps of the vertical component of the magnetic field produced by geological samples with 100-200 μm spatial resolution and ultra-high sensitivity (Fong et al. 2005; Weiss et al. 2007). We first measured the magnetic field of the AMNH5056 thin section at a sensor-to-sample distance of ~200 mm with a step size of 80 mm. It is usually not possible to calculate uniquely the fine-scale

(<200 μm) non-unidirectional magnetization distribution from raw field measurements (Baratchart et al. 2013). Instead, we enhanced the magnetic field map using potential field techniques. Following (Lima, Weiss, Baratchart, et al. 2013), we first performed a bilinear interpolation of the field map by a factor of 2 in each horizontal direction. We then downward continued the field map to obtain an effective sensor-to-sample distance of 100 mm with a step size of 40 mm. Finally, we computed the full three-component vector field using the procedure described in Lima & Weiss (2009) and used this to obtain the total field map. The thin section was subjected to stepwise three-axis AF demagnetization up to 39 mT to remove any possible low-coercivity overprints due to sample preparation. The close agreement between NRM directions recovered from the 2G SRM samples and the thin section confirms the lack of contamination. Finally, to characterize the magnetic mineralogy of Allende material, we performed electron microprobe analyses on two isolated chondrules and one matrix-rich sample using a JEOL-JXA-8200 Superprobe in the MIT Experimental Petrology Laboratory.

4.3. Results

The Allende matrix carries a strong, unidirectional magnetization. Isolated matrix-rich samples carry a strong unidirectional NRM oriented in the same direction as that of the bulk samples measured by Carporzen et al. (2011) (Fig. 4.1A). Among our samples, the matrix, which composes ~40% of bulk material (Weisberg et al. 2006), has an average mass-normalized NRM intensity for millimeter-sized samples that is ~4 times higher than that of chondrules. Furthermore, the NRMs of most chondrules are randomly oriented, which further reduces their combined contribution to the net magnetization of bulk material compared to the unidirectionally magnetized matrix. Therefore, matrix magnetization dominates that of bulk Allende material, explaining the similarity in NRM directions of matrix-rich and bulk samples. The highly uniform NRM intensity varies <40% among the seven matrix samples.

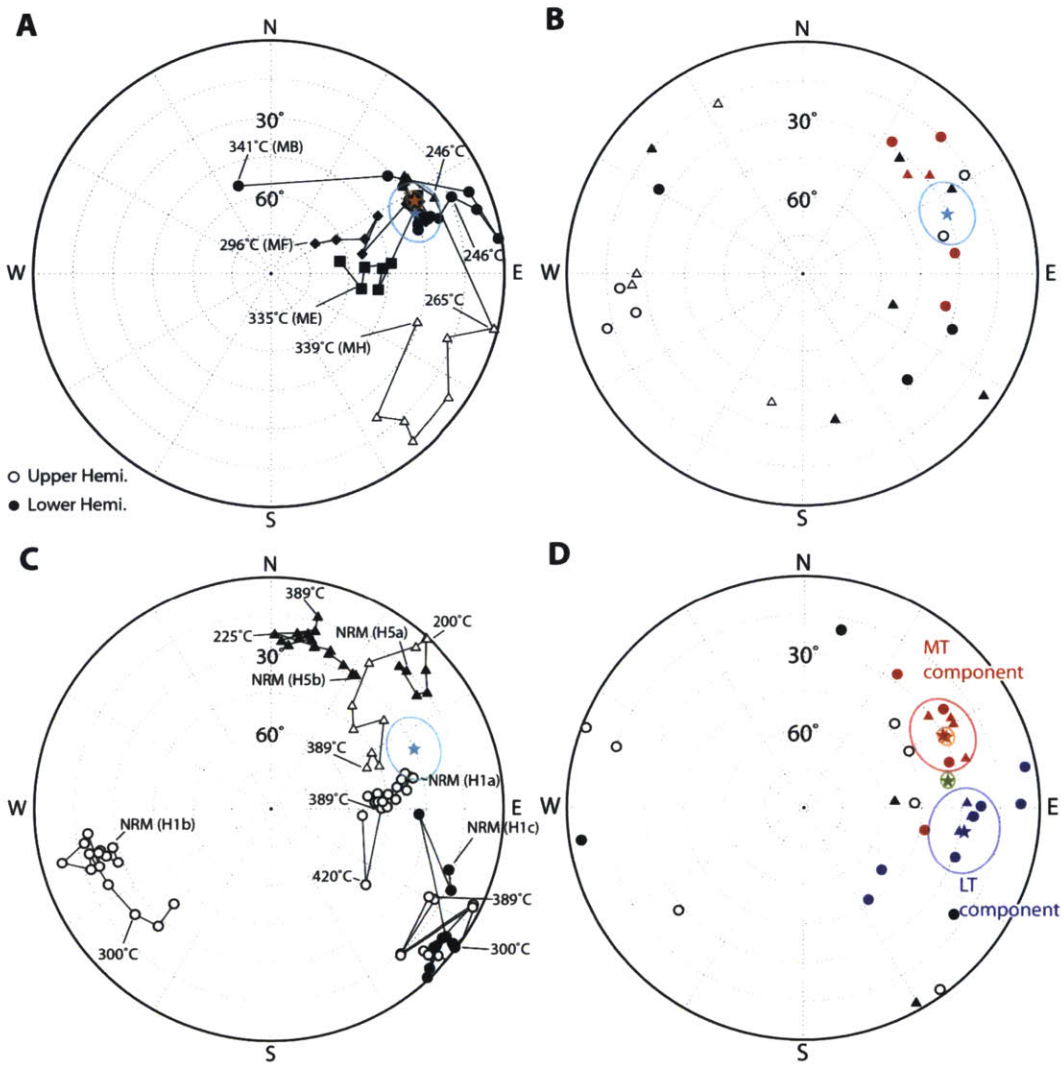

Figure 4.1. NRM directions in Allende chondrules and matrix-rich samples. Shown are equal area stereographic projections with solid (open) symbols representing lower (upper) hemisphere. (**A**) Thermal demagnetization of four isolated Allende matrix-rich samples (MB, ME, MF, and MH). Light blue star and circle correspond to the MT component direction and associated 95% confidence interval of matrix-rich samples from this study. Orange star and circle indicate the average MT component direction and associated 95% confidence interval for bulk Allende samples measured by Carporzen et al. (2011). Each subsample is assigned a different symbol (i.e., circle, square, diamond, and triangle). NRM directions for all four subsamples lie within the 95% confidence interval of the mean (i.e., within light blue circle). Selected demagnetization temperatures are labeled. (**B**) NRM directions of all chondrule samples. Triangles denote samples subjected to AF demagnetization and circles denote samples subjected to thermal demagnetization. Red symbols correspond to class A chondrule samples (which have strong MT overprints and are stable upon AF demagnetization), and black symbols correspond to class B chondrule samples (which have no MT overprint and are unstable upon AF demagnetization). As in panel (A), light blue star and circle correspond to MT component direction of matrix samples from this study. Note the clustering of class A chondrule sample NRM directions around the matrix MT component direction. (**C**) Thermal demagnetization of subsamples from a class A (H2; triangles) and a class B (H1; circles) chondrule. As in panel (A), light blue star and circle correspond to MT component direction of matrix samples from this study. Selected demagnetization temperatures are labeled. (**D**) Directions of LT, MT, and HT

magnetization components obtained using principal components analysis. Shown are the LT (blue), MT (red), and HT (black) magnetization directions from all thermally demagnetized chondrule (circles) and matrix (triangle) samples. Blue and red stars and ellipses indicate the average directions and 95% confidence intervals of the LT and MT components in chondrules from this study while the green and orange stars and ellipses correspond to the LT and MT components in bulk samples from Carporzen et al. (2011). Note the non-unidirectionality of the HT component directions.

Thermal demagnetization of four matrix-rich samples reveals two unidirectional components of magnetization (Fig. 4.2A) similar to those observed by Carporzen et al. (2011) for bulk samples. A weak (~5×10^{-5} Am^2kg^{-1}) low temperature (LT) component is blocked between room temperature and 100°C. A stronger (~2×10^{-4} Am^2kg^{-1}) MT component is blocked between 100°C and 260–280°C. Finally, we observe a much weaker (~1×10^{-5} Am^2kg^{-1}), non-unidirectional HT magnetization in two of the four matrix-rich samples. The HT magnetization does not decay to the origin for most subsamples during thermal demagnetization and remains stable in direction until ~325–420°C, at which point it loses directional coherence. Such unstable demagnetization behavior at higher temperatures is likely due to chemical alteration of magnetic phases, as significant alteration during heating in air has been observed for Allende material at as low as 320°C (Carporzen et al. 2011). To test this hypothesis, we conducted stepwise heating on matrix-rich sample MC while performing IRM acquisition after each heating step. We observed that the saturation IRM intensity of the sample increased by a factor of 1.7 between 360°C and 390°C, indicating the alteration of magnetic phases. Therefore, 325–420°C represents a lower bound on the true upper unblocking temperature of the HT magnetization.

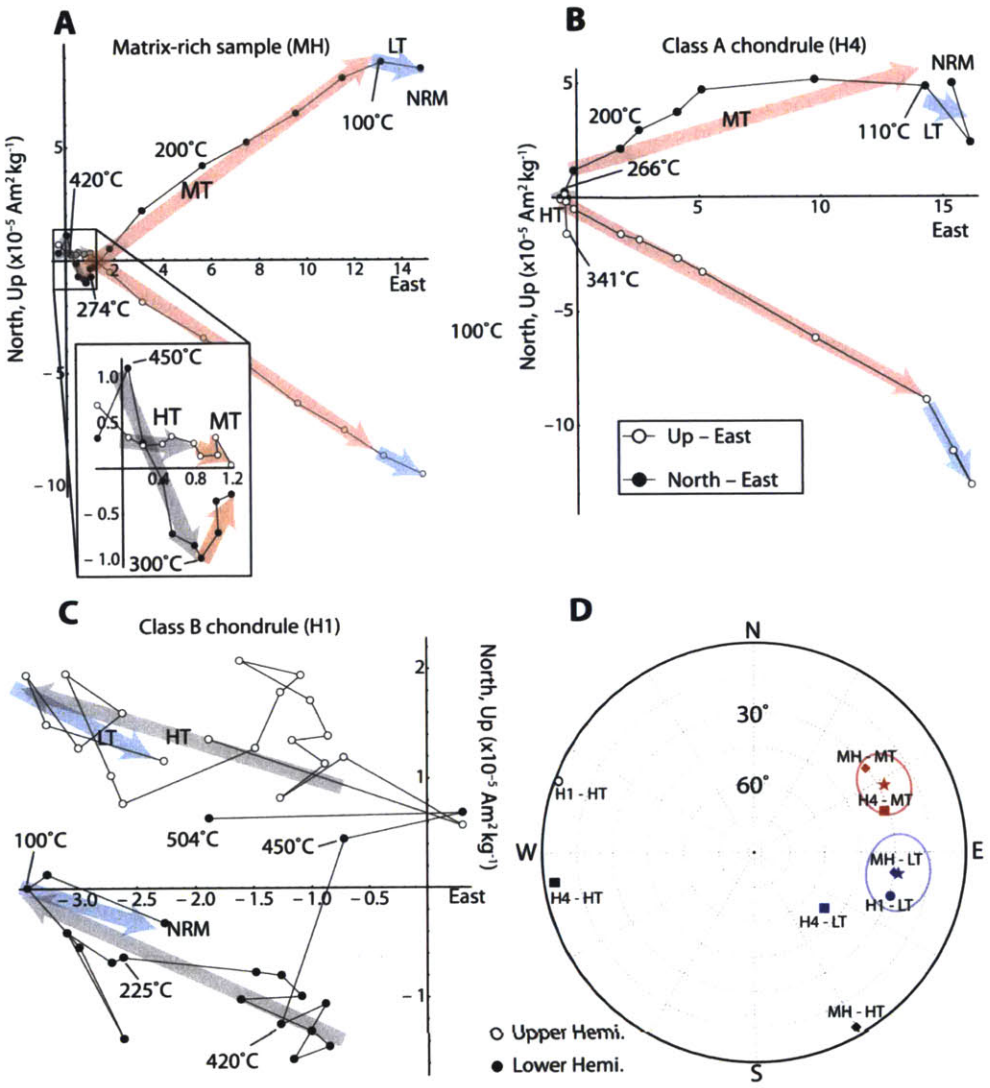

Figure 4.2. Thermal demagnetization of (**A**) matrix-rich sample MH, (**B**) class A chondrule sample H4a, and (**C**) class B chondrule sample H1d. Open and closed circles indicate the projection of the magnetization vector onto the vertical (up-east) and horizontal (north-east) planes, respectively. Inset to panel (A) has same units as main plot. (**D**) Equal area stereonet showing the component directions for each sample in panels A-C. All three samples carry a unidirectional low temperature (LT) and non-unidirectional high temperature (HT) component, but only the matrix-rich and class A chondrule samples carry the strong, unidirectional MT component. As in Fig. 4.1D, blue and red stars and ellipses indicate the average direction and 95% confidence intervals of the LT and MT components in chondrules, respectively. Open (closed) symbols denote upper (lower) hemisphere.

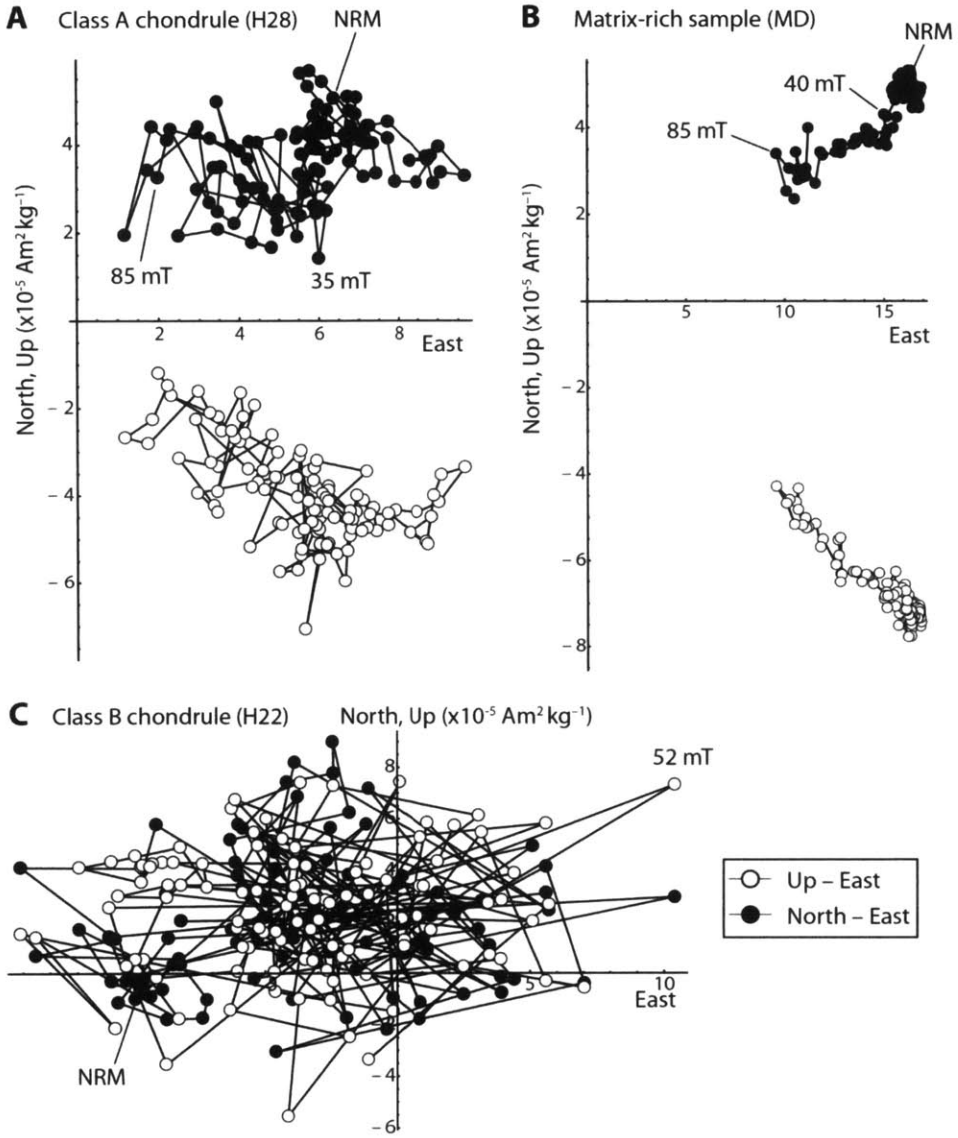

Figure 4.3. AF demagnetization of Allende chondrules and matrix-rich samples. Open and closed circles indicate the projection of the magnetization vector onto the vertical (up-east) and horizontal (north-east) planes, respectively. (**A**) Class A chondrule H28. (**B**) Matrix-rich sample MD. (**C**) Class B chondrule H22. Note the dramatic difference in stability of the class A (panel A) and class B (panel C) chondrules.

The MT component direction is indistinguishable from those observed for bulk samples from AMNH5056 (Fig. 4.1D) (Carporzen et al., 2011). The small offset between our mean LT component direction and that of Carporzen et al. (2011) is likely due to small (5°) errors in the mutual orientations between our samples and the ones used

in Carporzen et al. (2011). Likewise, the non-unidirectional HT component observed in our matrix samples was also previously observed in bulk samples from AMNH5056. During AF demagnetization, two matrix samples exhibited single-component, unidirectional magnetization whose intensity decayed by only 38-42% by 85 mT (Fig. 4.3), again consistent with previous measurements of bulk samples (Carporzen et al., 2011).

Isolated chondrules carry mutually and internally non-unidirectional magnetization. In contrast to the uniform magnetization of matrix samples, NRM intensities for chondrule samples vary across two orders of magnitude. We assign all Allende chondrules to one of two classes with systematically different magnetic properties (Table 4.1). Class A chondrules carry the same strong MT component of magnetization as in matrix material. As with the matrix-rich samples the MT component in class A chondrules is unblocked between ~100°C and 274-286°C (Fig. 4.1D; Fig. 4.2B) and has intensities of 1.1×10^{-4} Am^2kg^{-1}or higher. In contrast, class B chondrules do not carry this overprint and therefore have much lower NRM intensity (Fig. 4.2C).

Due to the high intensity of their MT overprint, the NRM directions of class A chondrules cluster around the mean MT component direction similar to bulk and matrix-rich samples (Fig. 4.1B). Upon the demagnetization of the MT component, matrix and class A chondrule samples have lost ~90% of their initial NRM intensities (Fig. 4.4). In contrast, because class B chondrules do not carry the MT overprint, their magnetic moments exhibit limited decay below 300°C.

Table 4.1: Summary of characteristics of Class A and Class B chondrules.

Class A chondrules	Class B chondrules
Carry MT component of magnetization also found in all matrix samples	Lack the MT component of magnetization
NRM directions close to the MT overprint direction	Random NRM directions
NRM intensities between 2.0 and 21.6×10^{-5} Am^2kg^{-1}	NRM intensities between 0.2 and 10.4×10^{-5} Am^2kg^{-1}
Subsamples of single chondrules carry unidirectional magnetization below ~280°C and non-unidirectional magnetization above	Subsamples of single chondrules carry stable, non-unidirectional magnetization between room temperature and ~400°C
Stable, unidirectional magnetization upon AF demagnetization	Unstable magnetization upon AF demagnetization
Higher abundance of FeNi sulfides relative to awaruite	Higher abundance of awaruite relative to FeNi sulfides

Seven out of thirteen chondrule samples from both classes A and B subjected to thermal demagnetization carry a weak (~3×10^{-5} Am^2kg^{-1}) LT component unblocked below 110°C and nearly parallel to the LT component of matrix samples. After the removal of any LT and MT overprints at or below 280°C, all chondrules carry an HT magnetization. As with the HT magnetization in matrix-rich samples, the HT magnetization in chondrules exhibits random directions (Figs. 4.1D and 4.2D), and is consistent with the HT chondrule remanence described in Sugiura and Strangway (1985). This HT magnetization is directionally stable until at least 314-420°C, at which point mineralogical alteration occurs.

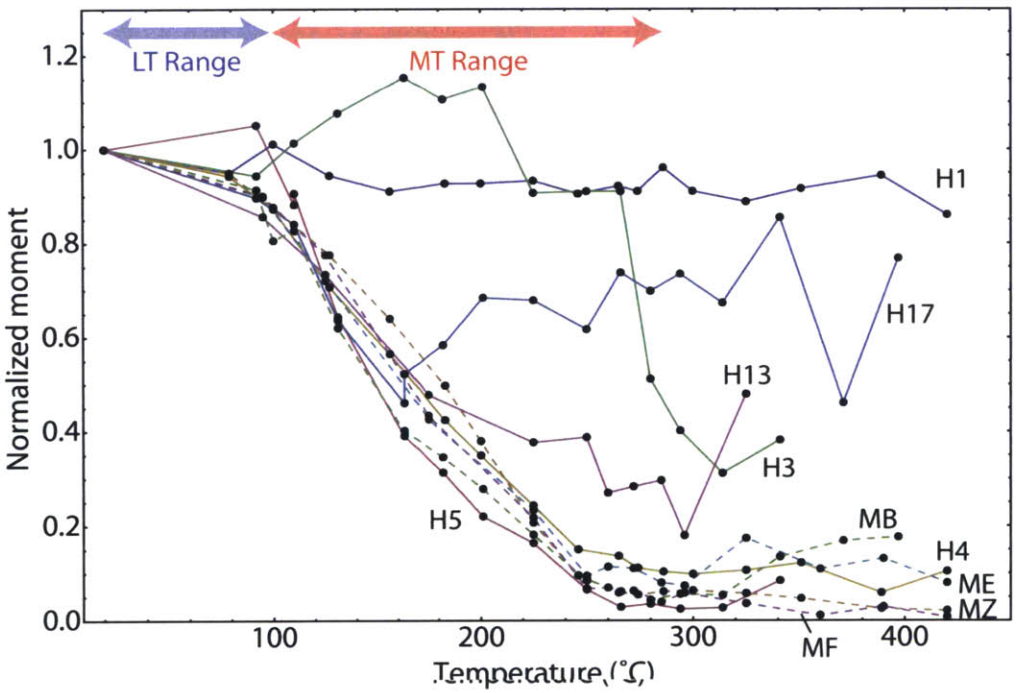

Figure 4.4. Normalized moments of chondrule and matrix-rich samples during thermal demagnetization. Solid and dashed curves represent chondrules and matrix-rich material, respectively. Demagnetization was halted when samples no longer exhibited directional stability or when sample moments increased dramatically. Chondrules H4 and H5 are of class A while H1, H3, H13, and H17 are of class B.

Class A and B chondrules also show systematically different behaviors during AF demagnetization. The NRMs of class A chondrules remain directionally stable during AF demagnetization up to 85 mT, which is similar to the behavior of matrix-rich samples (Fig. 4.3A,B). In contrast, class B chondrule samples exhibit highly unstable NRM

during AF demagnetization at all AF levels (Fig. 4.3C). We therefore identify class A and class B chondrules with the "AF stable" and "AF unstable" chondrules described by Wasilewski & Saralker (1981), respectively. As further support of this correspondence, Wasilewski & Saralker (1981) reported that 14 out of 20 chondrules are "AF unstable," which is similar to our proportion of class B chondrules (17 out of 21).

Importantly, optical microscopy suggests that the major ferromagnetic phases in "AF unstable" (class B) chondrules are sulfides, metal, and magnetite while those in "AF stable" (class A) chondrules are predominantly just sulfides (Wasilewski and Saralker, 1981). This is consistent with other previous studies showing that the magnetic phases in Allende consist of iron sulfides, high-Ni FeNi metal (awaruite), and magnetite (Butler 1972; Carporzen et al. 2011; Emmerton et al. 2011; Funaki & Wasilewski 1999; Nagata & Funaki 1983; Wasilewski & Saralker 1981). Our electron microprobe studies of one class A and one class B chondrule show that sulfides are indeed the dominant opaque phase in the former, occurring in both the interior and in a highly sulfidized rim. Meanwhile, awaruite is the most abundant opaque phase in the class B chondrule (Fig. 4.5).

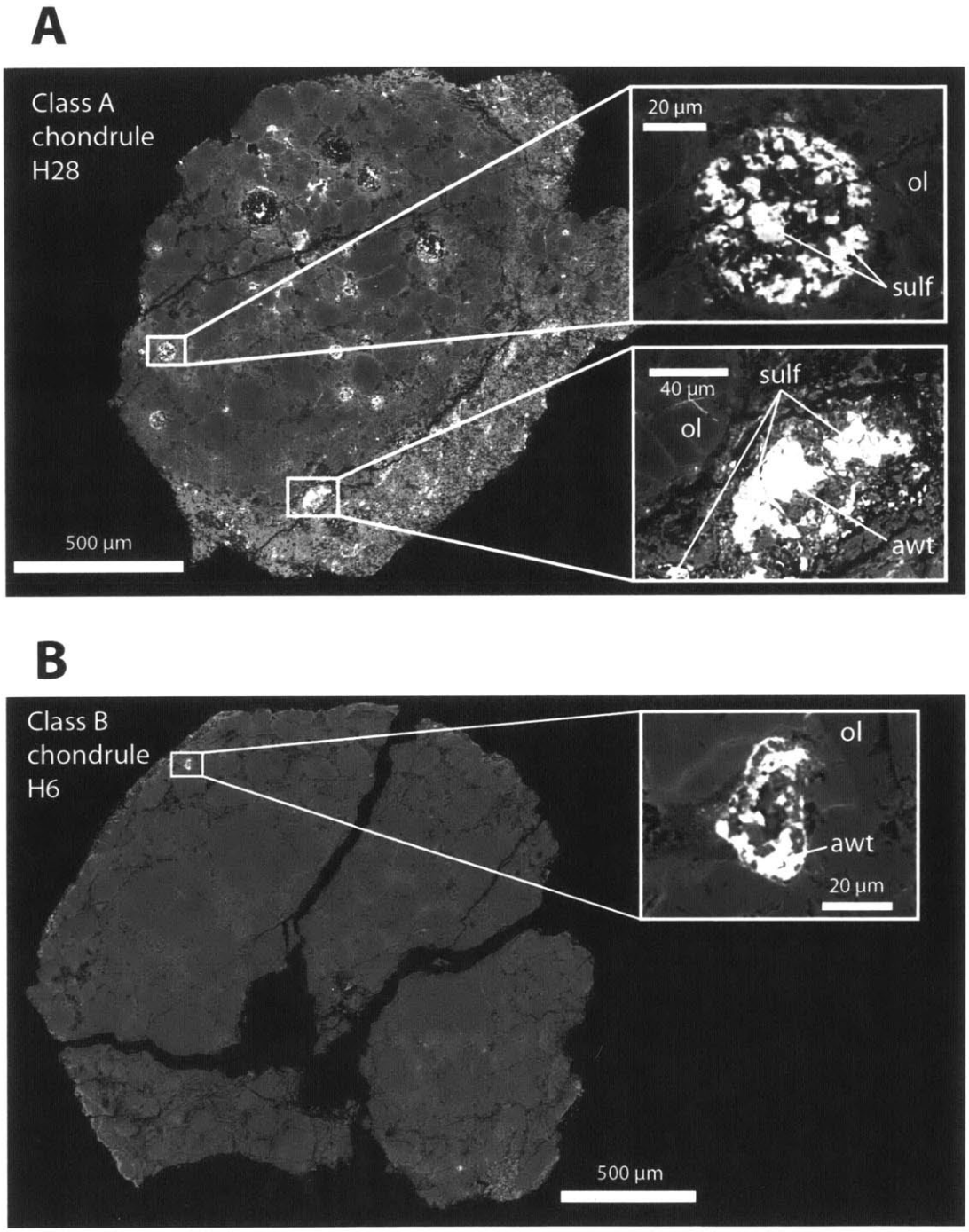

Figure 4.5. Backscatter scanning electron microscopy image of (A) a class A chondrule H28 and (B) a class B chondrule H6. Insets show the composition of opaque phases in each chondrule. Abbreviations "sulf", "awt", and "ol" refer to FeNi sulfides, awaruite, and olivine, respectively. The higher relative abundance of sulfides in class A chondrules and of awaruite in class B chondrules is consistent with optical microscopy observations and coercivity spectra Curie temperatures (Wasilewski and Saralker, 1981).

The composition of the sulfides is homogeneous among the chondrules and matrix. Six quantitative wavelength dispersive spectroscopy (WDS) analyses using a ~2 μm resolution beam yielded a mean composition of $Fe_{6.1}Ni_{2.8}S_{8.0}$. Assuming a low temperature formation significantly below 400°C (Carporzen et al., 2011), this composition corresponds to an equilibrium assemblage consisting of troilite, pentlandite, and hexagonal pyrrhotite (Vaughan & Craig 1978), the last of which is magnetic and may account for the rapid decay in the moment of a saturation IRM in our samples below 270°C upon thermal demagnetization. Further, pentlandite is commonly observed in other oxidized CV chondrites where it may be intergrown with pyrrhotite at the <2 μm scale (Brearley & Krot 2012; Krot, Petaev, Zolensky, et al. 1998; Krot, Petaev, Scott, et al. 1998; Krot et al. 1997).

We note that the dichotomy between class A and B chondrules is not clearly related to the FeO content (i.e., type I and type II chondrules) or the textural classification. Both class A and B chondrules subjected to electron microprobe analyses (Fig. 4.5) are type I porphyritic olivine chondrules, which are the most common classification of chondrules in Allende (McSween 1977).

The differences between class A and B chondrules cannot be explained by the retention of contaminating matrix material on class A chondrules. The mass-normalized magnitude of the MT component in class A chondrules is $5\text{-}18\times10^{-5}$ Am^2kg^{-1} (Fig. 4.2). Given that class B chondrule materials carry no MT component and that the MT component in matrix samples is $\sim20\times10^{-5}$ Am^2kg^{-1}, class A chondrule samples, if they are in fact a mixture of class B chondrule material and contaminating matrix, must consist of between 25 and 90 wt% matrix material to produce the observed MT component intensities. Such extensive contamination would be readily observed.

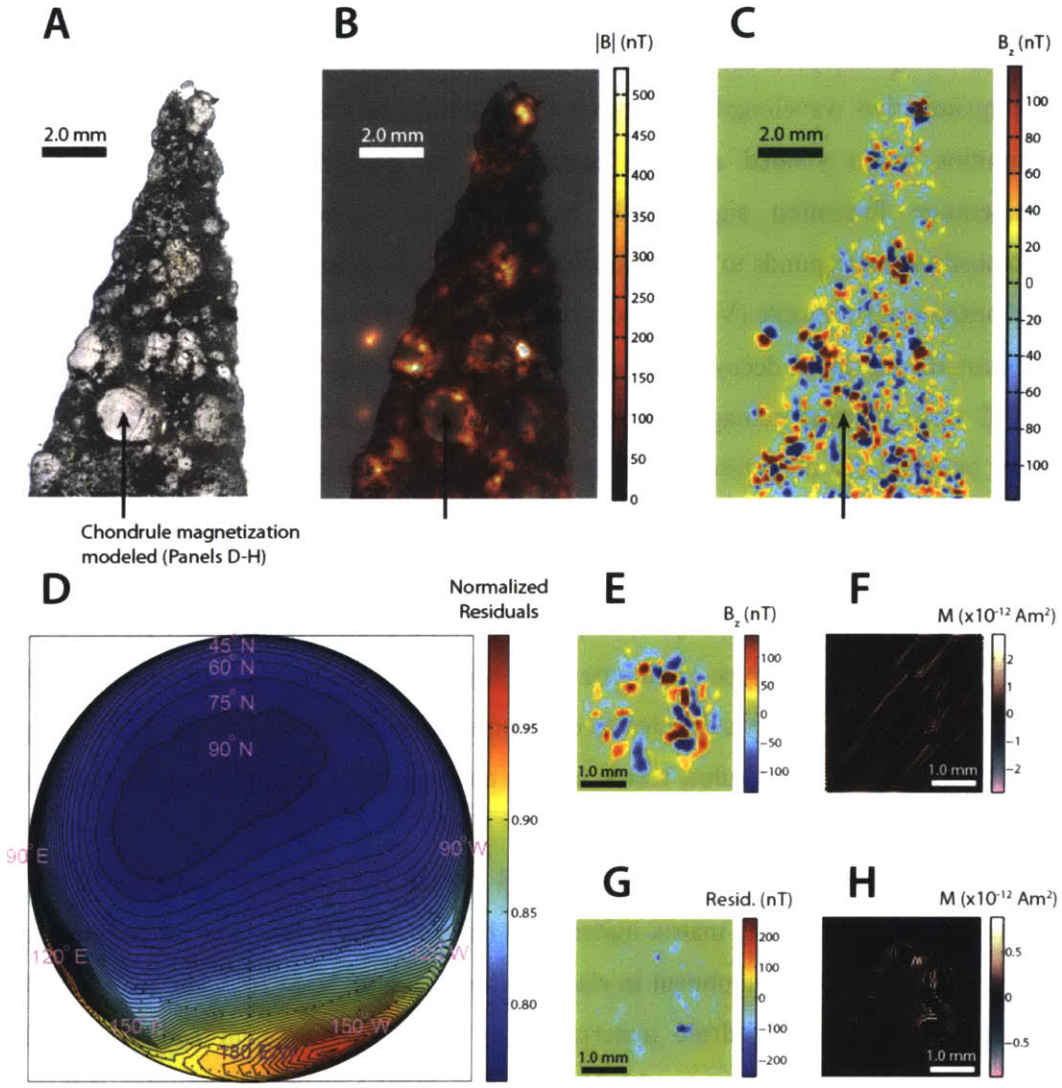

Figure 4.6. SQUID Microscope measurement of a 30 μm thin section of the Allende meteorite and inversion calculations of a single chondrule. (**A**) Reflected light photomicrograph, (**B**) magnitude of the total magnetic field 100 μm above the thin section superimposed over the optical photomicrograph, and (**C**) vertical component of the magnetic field 100 μm above the thin section. For a single chondrule (black arrow), we fit for the three-dimensional magnetization intensity pattern assuming unidirectional magnetization oriented in 600 trial directions. The residuals (**D**) between the model and observed vertical fields (**E**) show a weak minimum (i.e., best-fit direction). However, the magnetization distribution corresponding to the best-fit direction is non-physical (**F**). Restricting the location of magnetization to within just the surface of the chondrule results in high residuals between the observed and model magnetic fields (**G**) and likewise non-physical magnetization (**H**). Therefore, the magnetization in this chondrule cannot be unidirectional, corroborating our results from isolated chondrule samples.

The directions of the HT magnetization in subsamples of individual chondrules are randomly oriented (Fig. 4.1C). In the case of chondrule H1, which is the only chondrule that yielded more than two subsamples, subsample HT directions are statistically non-unidirectional [$P = 0.77$, where P is the probability that four random unit vectors shows greater unidirectionality; Watson (1956)]. In contrast, the MT component in four total subsamples from two class A chondrule is unidirectional ($P = 0.0015$).

SQUID microscopy of the Allende thin section confirms and extends our conclusion that class B chondrules have non-unidirectional magnetization (Fig. 4.6). To quantitatively test chondrule non-unidirectionality, we solved for the unidirectional magnetization model that best fits the magnetic field above a single chondrule in the thin section and evaluated whether such a model is physically plausible (Fig. 4.6D-H). The greater abundance of awaruite compared to FeNi sulfides in the chondrule interior, observed via reflected light optical microscopy, suggests that this is a class B chondrule. We applied a spatial window to taper off contributions from adjacent sources outside of the chondrule. Following Weiss et al. (2007), we then computed the best fit magnetization intensity distribution in the chondrule for 600 uniformly distributed assumed magnetization directions. The peak magnitude of residuals for the best-fit direction is ~100 nT, which is 10^2 times the expected noise limit, meaning that a unidirectional solution can be rejected. Additional strong evidence for non-unidirectional magnetization is that this computed best-fit magnetization solution is nonphysical: it exhibits strong streaking, which is inconsistent with the expected distribution of ferromagnetic minerals (Fig. 4.6F). Thin section SQUID microscopy therefore supports the conclusion from 2G SRM measurements that class B chondrules are not unidirectionally magnetized. Although AF demagnetization of the thin section to 39 mT may have altered the magnetization, the MT component in class A chondrules and matrix material is still directionally stable at this AF level. Therefore, the non-unidirectional chondrule magnetization mapped using SQUID microscopy confirms that this chondrule belongs to class B and never carried the MT component.

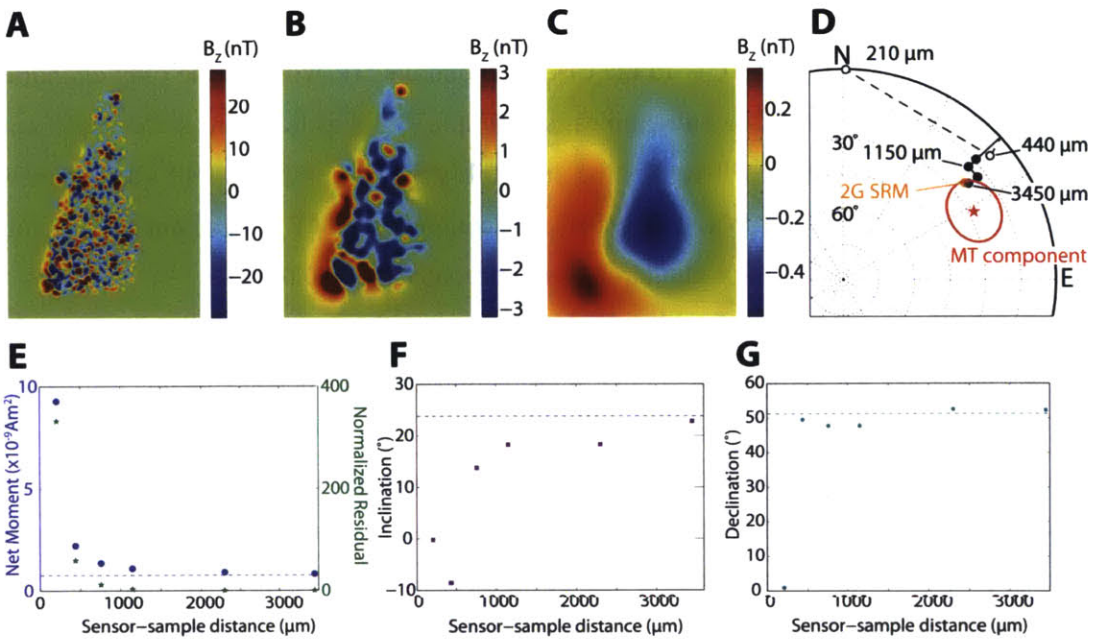

Figure 4.7. Recovery of the NRM magnetization of bulk Allende material via SQUID microscopy at increasing sensor-to-sample distances. SQUID Microscope map of the vertical component of the magnetic field (**A**) ~200 µm, (**B**) ~750 µm, and (**C**) ~3450 µm above the Allende thin section. The map in (C) was obtained by upward continuation of the magnetic data shown in (B). (**D**) Equal area stereonet diagram showing the best-fit magnetization direction of the thin section assuming a unidirectional magnetization model (black points). For increasing sensor-to-sample distances, the best-fit direction approaches the net magnetization direction of the sample as measured in the 2G SRM (orange) and the mean MT component direction (red star; red circle represents the 95% confidence interval). (**E**) Recovered net moment (blue circles) as a function of sensor-to-sample distance assuming a unidirectional magnetization distribution model. The dashed line indicates the net moment strength measured by the 2G SRM for the thin section. Also shown is the normalized residual (i.e., the norm of the difference between the model and experimental magnetic field maps divided by the norm of the experimental field map) as a function of sensor-to-sample distance (green stars). (**F**) Recovered inclination as a function of the sensor-to-sample distance assuming a unidirectional magnetization distribution model. The dashed line represents the inclination measured by the 2G SRM for the thin section. (**G**) Recovered declination as a function of the sensor-to-sample distance assuming a unidirectional magnetization distribution model. The dashed line indicates the declination of measured by the 2G SRM for the thin section. The convergence of the net magnetization recovered from the SQUID map using a unidirectional magnetization model for sensor-to-sample distances greater than ~1 mm confirms that the magnetization of Allende material is heterogeneous at scales less than ~1 mm and that the strong unidirectional MT magnetization dominates the NRM direction of bulk Allende material.

To demonstrate that the non-unidirectional magnetization in Allende at sub-chondrule scales is consistent with the unidirectional NRM of bulk samples, we mapped the thin section using the SQUID Microscope at different sensor-to-sample distances (approximately 200 µm, 450 µm, and 750 µm; Fig. 4.7A-B). We computed the upward continuation of the map taken 750 mm above the sample for three sensor-to-sample distances (1150 mm, 2300 mm, and 3450 mm; Fig. 4.7C). We then used a two-step

inversion procedure on each map to find its best unidirectional magnetization representation. The first step consists of computing the magnetization intensity distribution in the thin section for 200 uniformly distributed assumed magnetization directions and selecting the one that best fits the measured map. In the second step, we refined this result by computing inversions on a ~40 point fine grid spanning ± 15° around both the inclination and declination found in the first step (Fig. 4.7 F-G). A net moment estimate was directly obtained by integrating the best-fit unidirectional magnetization intensity distribution (Fig. 4.7E).

The uniform magnetization model is a poor representation of the Allende magnetization for sensor-to-sample distances smaller than 1000 μm. It becomes increasingly accurate for maps with larger sensor-to-sample distances, which show small normalized residuals and accurately reproduce the net moment measured by the 2G SRM (Fig. 4.7 D-G). We stress that this progression toward a unidirectional behavior does not stem from a transition to the far-field, dipole-dominated regime given that the thin section has dimensions of ~17 x 7 mm, which is much larger than the ≤3.45 mm sensor-to-sample distance. Instead, the non-unidirectional magnetic fields produced by class B chondrules, although they are of a comparable intensity as those produced by the matrix at the 100 μm scale (Fig. 4.6), fall off much more rapidly with distance than the unidirectional MT component carried by the matrix and class A chondrules. Thus, Allende exhibits non-unidirectional behavior at sub-chondrule scales and unidirectional behavior at larger scales. Moreover, at such large spatial scales the magnetization direction converges to the direction measured for the strong, unidirectional MT component (Fig. 4.7D). This experiment demonstrates that SQUID microscopy can measure the spatial scale at which a sample is unidirectionally magnetized.

To characterize the magnetic recording limit and rock magnetic properties of Allende material, we conducted a suite of anhysteretic remanent magnetization (ARM) and IRM acquisition experiments. We imparted laboratory ARMs as an analog for TRM on three class B chondrules to find the lowest ambient magnetic field that can be reliably recorded. Because we identified magnetization components based on the existence of a coherent magnetization direction across different samples, we define an ARM bias field level as "recordable" if the set of five ARMs acquired in the field is non-random at the

95% confidence interval and their mean direction is consistent with the bias field direction at the 95% confidence level (Watson, 1956). By this definition, two out of the three chondrules gained a unidirectional ARM in a 2 μT bias field and one chondrule recorded a 1 μT bias field. No chondrule reliably acquired an ARM in a 0.7 μT bias field. This ~0.7 μT ARM recording limit implies that some class B chondrules should have acquired a 280°C partial TRM (pTRM) in a >2 μT field given a pTRM/ARM ratio of 0.373, which is well below the 60 μT paleointensity found for the MT component (Carporzen et al., 2011). Furthermore, the 60 μT value is likely an underestimate since the earlier authors did not account for the lack of MT magnetization in chondrules, resulting in higher intensities of laboratory pTRM, ARM, and IRM used to calculate paleointensities. Assuming that chondrules have similar mass-normalized saturation IRM intensities as matrix material and that Allende contain 40% chondrules by mass, removal of the chondrule contribution to the laboratory remanences results in revised MT component paleointensities of ~100 μT

For possible chemical remanent magnetization (CRM) in Allende chondrules (see Section 4.4) the ~0.7 μT threshold for ARM corresponds to a CRM recording limit of <8 μT. Furthermore, thermal demagnetization of a near-saturation IRM showed that ~30% of remanent magnetization in class B chondrules unblock between room temperature and 280°C, implying that the lack of the MT component in these chondrules cannot be explained by their unblocking temperature spectrum.

Finally, progressive IRM acquisition up to 0.9 T shows that matrix material has the hardest coercivity spectrum followed by class A and then class B chondrule samples. The lower coercivities of class B chondrules are consistent with their more unstable behavior during AF demagnetization (Tikoo et al. 2012). FeNi metals, including awaruite, are typically found in the multi-domain state and exhibit low coercivities (Gattacceca et al., 2014; Weiss et al., 2010). The lower coercivities of class B chondrules therefore provide further evidence that they contain a higher ratio of awaruite to pyrrhotite compared to class A chondrules and matrix material.

4.4. Discussion

The non-unidirectional HT magnetization is most likely a parent body chemical remanent magnetization (CRM). Earlier studies have documented randomly oriented HT magnetization among whole Allende chondrules and used this observation to argue for a pre-accretional TRM origin (Sugiura et al., 1979; Sugiura et al., 1985). However, our measurement of non-unidirectional HT magnetization among *subsamples* of single chondrules places further strong constraints on its origin. A non-unidirectional TRM in single chondrules requires that each sector of the chondrule cooled across the >300°C HT blocking temperature range independently. However, the small size of chondrules implies that they cannot sustain large internal temperature contrasts for more than ~2 seconds while chondrules cooled across their blocking temperature spectrum over much longer timescales. Therefore, temperatures in a single chondrule would have homogenized before any one sector could have acquired a TRM in a unique direction; the HT magnetization cannot be a pre-accretional TRM. The HT magnetization is also not a post-accretional TRM because no heat source is likely to result in temperature contrasts of >300°C at such fine scale. Impact heating, if it had a significant effect on Allende, is predicted to result in the preferential heating of the matrix instead of chondrules (Muxworthy et al. 2011).

We consider a CRM or thermochemical remanent magnetization (TCRM) origin for the HT magnetization. As described above, magnetic phases in Allende consist of iron sulfides, magnetite, and high-Ni FeNi metal (awaruite). All of these phases likely formed due to sulfidization and oxidation of primary low-Ni FeNi metal (Brearley & Krot 2012; Haggerty & McMahon 1979; Krot, Petaev, Scott, et al. 1998). Sulfides in Allende, which include ferromagnetic pyrrhotite, show higher S excess compared to those of less altered CV chondrites such as Vigarano, suggesting an origin due to low temperature sulfidization of FeNi metal and Fe-rich sulfide phases such as troilite (Krot et al., 1998a). The oxygen isotopic composition of Allende magnetite is distinct from that of primary olivine, indicating a secondary origin (Choi et al., 1997). The Ni-rich composition observed for FeNi metal in Allende (~70 wt% Ni) is consistent with formation due to Fe-removal in a secondary oxidation event (Haggerty and McMahon, 1979) and is broadly consistent with an observed 600-610°C Curie point reported in previous Allende rock magnetic studies (Butler, 1972; Nagata and Funaki, 1983; Wasilewski and Saralker,

1981), which corresponds to a composition of 61-64 atomic percent (at%) Ni (Swartzendruber et al. 1991). In contrast, the primary low-Ni FeNi metal found in less altered CV chondrites (e.g., Leoville) has a nickel content of ~5 at% (Krot et al., 1998a) and an expected Curie temperature of 753°C. Previous rock magnetic studies of Allende have not identified a magnetic phase with Curie temperature >610°C, suggesting the complete removal of the primary low-Ni FeNi metal in Allende by alteration.

Alteration in Allende likely occurred on the CV parent body; veins of alteration minerals that crosscut chondrule-matrix boundaries strongly suggest post-accretional formation (Brearley 1997; Kojima & Tomeoka 1996; Krot, Petaev, Scott, et al. 1998). Summarizing these lines of petrographic and rock magnetic evidence, all magnetic minerals in Allende likely formed during metasomatism on the CV parent body. No evidence exists for the survival of primary low-Ni FeNi phases from which the observed magnetic phases were altered.

CRM or TCRM due to recrystallization of magnetic phases in weak ambient fields may give rise to non-unidirectional magnetization at small scales. For example, CRM acquired in a <1 μT field is likely responsible for the non-unidirectional magnetization at the <5 mm scale carried by tetrataenite in the Bensour LL chondrite (Gattacceca et al. 2003).

Analogous to the HT magnetization in Allende and non-unidirectional magnetization in Bensour, randomly oriented magnetizations in the L6 chondrite ALH-769 that pass the paleomagnetic conglomerate test may also be due to post-accretional recrystallization instead of pre-accretional heating as previously argued (Funaki et al. 1981). In the case of ALH-769, the high metamorphic temperatures [>1000°C (Bennett & McSween 1996)] precludes the retention of any pre-accretional magnetization.

Although in some cases secondary minerals may inherit the magnetization direction of its precursor mineral phases, such a process is usually important for reactions that do not involve a change in lattice structure (Dunlop and Ozdemir, 1997). The formation of magnetite, pyrrhotite, and awaruite (fcc lattice) from 5% Ni metal (bcc lattice) in Allende would have led to rearrangement of the parent mineral structure, consistent with these minerals acquiring a spontaneous non-unidirectional CRM instead of inheriting pre-existing magnetization.

Given the pervasive alteration observed in Allende magnetic phases and the potential for recrystallization to result in non-unidirectional magnetization at the sub-chondrule scale, we conclude that CRM or TCRM acquired in a weak magnetic field during alteration is the most likely origin for the non-unidirectional HT magnetization observed in Allende chondrules. As such, although the HT magnetization passes the conglomerate test, Allende chondrules carry no discernible recording of ancient magnetic fields. We therefore do not refer to it as a magnetization "component," in contrast to the unidirectional MT and LT components. Despite widespread practice, paleomagnetic results from Allende should not be used to constrain solar nebula magnetic fields or the chondrule-forming process. Future studies of pre-accretional magnetization in chondrules should conduct both the conglomerate test and the single chondrule unidirectionality test to establish the pre-accretional origin of magnetization.

Any dynamo on the CV parent body had declined before the end of metasomatism. The non-unidirectionality of the HT magnetization can constrain the strength of ambient magnetic fields during its acquisition. The background field strength must have been below the recording limit for a CRM/TCRM; otherwise, Allende samples would carry a unidirectional HT magnetization corresponding to the magnetic field during alteration (Fig. 4.8). The capacity for secondary minerals to acquire a CRM parallel to the direction of the ambient field depends on the specific alteration reaction (Dunlop and Ozdemir, 1997). CRM acquisition during oxidation and sulfidation of low-Ni FeNi metal has not been experimentally studied. However, secondary formation of pyrrhotite and magnetite on Earth leads to recording of the ambient field direction (Dinarès-Turell & Dekkers 1999; Haigh 1958; Weaver et al. 2002). The strength of the ambient magnetic field during the acquisition of the HT magnetization was therefore likely significantly weaker than Earth-strength (i.e., $<<50$ μT). Furthermore, assuming that the efficiency of CRM acquisition is ~0.09 times that of an ARM, the 0.7 μT recording limit from our ARM acquisition experiments implies that the ambient field strength during the acquisition of the HT magnetization was likely <8 μT. We evaluate the implications of this constraint on the magnetic evolution of the CV parent body given two hypotheses for the origin of

the MT overprint, which is found in class A chondrules and matrix material but is absent from class B chondrules.

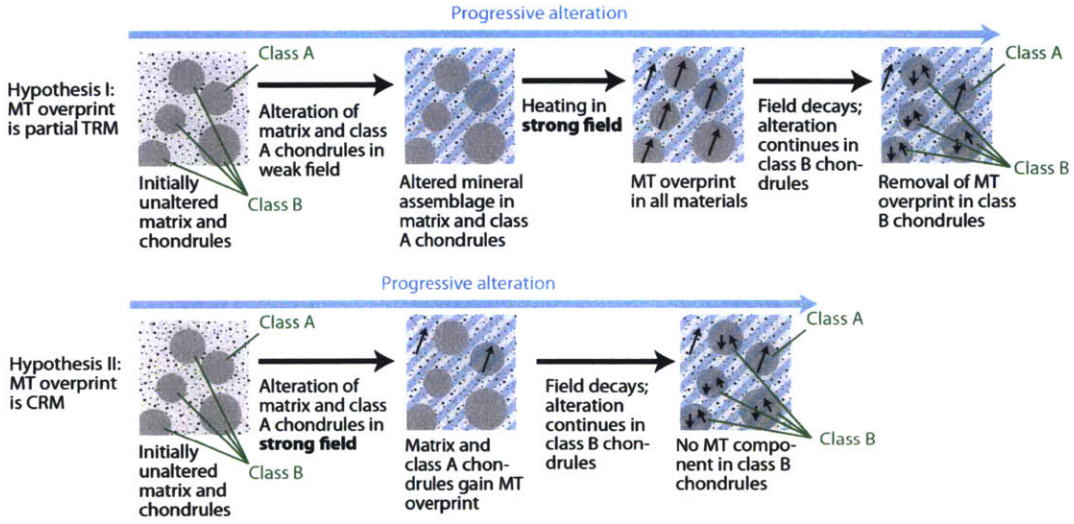

Figure 4.8. Two possible alteration and magnetic histories for the Allende meteorite. Dark grey circles represent chondrules, speckled light grey surrounding represents matrix, and small black arrows represent magnetization. Light blue stripes denote chondrule and matrix materials that have undergone metasomatism, resulting in the recrystallization of all magnetic phases. (Top) Assuming that the MT overprint is a partial TRM (Carporzen et al., 2011), a late alteration event is required to remove this overprint from class B chondrules. Because there is no unidirectional magnetization blocked to the Curie temperature, the first episode of metasomatism must have occurred in a near-zero field. Heating in a strong field (such as from a core dynamo) then imparted the MT component in all Allende materials. This MT magnetization was erased by late alteration in class B chondrules. This sequence of events can explain the presence of the MT component in class A chondrules but not in class B. (Bottom) Assuming that the MT overprint is a CRM or TCRM, the field could have been present from the beginning of alteration. Progressive alteration first altered the matrix and class A chondrules in the presence of a strong field (such as from a core dynamo), followed by alteration of class B chondrules in near-zero field. The field must have likewise decayed after the alteration of class A chondrules but before that of class B chondrules.

Hypothesis I: The MT overprint is a partial TRM. Owing to its 290°C maximum blocking temperature, which is distinct from the Curie points of ferromagnetic minerals in Allende, Carporzen et al. (2011) argued that the MT overprint is most likely a partial TRM acquired in a ~60 μT field (Fig. 4.8 top). Since class B chondrule samples are likely capable of recording a 290°C partial TRM in magnetic fields stronger than ~2 μT, the absence of the MT overprint in class B chondrules requires a late remagnetization event that removed the previously recorded MT overprint but did not affect the overprint in class A chondrules and the matrix. No known heating mechanism can lead to the

localized heating of only a subset of chondrules to >290°C. Impact shock may lead to localized heating, but is expected to cause greater heating in the more porous matrix instead of chondrules (Muxworthy et al., 2011).

On the other hand, ongoing alteration or a late alteration event is capable of affecting a subset of chondrules while preserving the MT overprint in the adjacent material. As discussed above, such alteration in a <8 μT field may lead to the non-unidirectional NRM observed in class B chondrules. The early timing of metasomatism in the matrix and class A chondrules before the heating event that created the MT overprint would have led to the preservation of the MT magnetization (Fig. 4.8 top).

Hypothesis II; MT overprint is a CRM or TCRM. Alternatively, we assume that the MT overprint is a CRM or TCRM (Nagata & Funaki 1983)(Fig. 4.8 bottom). If class A chondrules and matrix material acquired the MT component in this fashion, then class B chondrules, which also contain secondary magnetic minerals [see Section 4.3 and Wasilewski and Saralker (1981)] should have acquired the same overprint if the alteration occurred concurrently. The metasomatism of magnetic phases in class B chondrules therefore must have taken place in a magnetic field weaker than both that of class A chondrules and matrix material and the CRM recording limit. I-Xe dating of the formation of secondary phases suggests that matrix material in Allende underwent alteration 0.5-3.2 My before chondrules (Swindle et al. 1983). Therefore, if class A chondrules and matrix material acquired a CRM in the same strong field environment, this strong field epoch must have predated the weak field epoch during which alteration occurred in class B chondrules.

Synthesis. In the case of either a partial TRM or CRM/TCRM origin for the MT overprint, alteration in class B chondrules must have occurred later than in the matrix and class A chondrules in the absence of a <8 μT magnetic field. In further support of these hypotheses, petrographic observations alteration minerals suggest that the matrix underwent the earliest alteration while chondrules were altered at a range of ages, with the cores of chondrules experiencing the least extensive and likely latest alteration (Brearley and Krot, 2012). Because in both cases alteration in class B chondrules

occurred after the post-accretional MT overprint, the setting of this alteration must have been on the CV parent body. Furthermore, the difference in the mineralogies of the dominant opaque phases (Fig. 4.5), which are all secondary in origin, for the two chondrule classes suggests that alteration in the two classes took place in distinct events or under progressively changing conditions.

Previous paleointensity estimates found that the unidirectional MT magnetization was likely acquired in a Earth-strength magnetic field [~60 μT; Carporzen et al. (2011)]. Due to the high paleointensity, unidirectionality, and inferred stability of this field, Carporzen et al. (2011) concluded that it is most likely due to a core dynamo in the CV parent body. The low field environment in which class B chondrule material altered would correspond to after the cessation or decline of the dynamo. The alteration age of class B chondrule material would therefore provide an upper bound to the age of the purported magnetic core dynamo in the CV parent body.

Radiometric dating using the $^{129}I/^{129}Xe$ system may directly constrain the timing of alteration in Allende due to the high I content of sodalite, an abundant secondary mineral found in all Allende components (Kirschbaum 1988). $^{129}I/^{129}Xe$ dates for individual Allende components suggest that sodalite formation continued during a span of up to ~10 My, with the latest major resetting occurring at 10-15 My after CAIs (Pravdivtseva et al. 2003; Swindle et al. 1988) when adopting an absolute age of 4562.3 Ma for Shallowater enstatite (Gilmour et al. 2009). Furthermore, limited alteration may have continued to cause Xe loss until up to 40 My after CAIs (Carporzen et al., 2011). Based on the I-Xe data, we propose that, assuming the ^{129}I carrier in Allende chondrules formed concurrently with the secondary magnetic phases, any core dynamo in the CV parent body had likely declined within 40 My of CAIs. This is broadly consistent with some theoretical models predicting a 10 to several 10s My lifetime for planetesimal dynamos (Elkins-Tanton et al. 2011; Sterenborg & Crowley 2013).

4.5. Conclusion

We find that, after the removal of unidirectional, post-accretional overprints blocked up to ~290°C (the LT and MT components), all Allende chondrules carry an HT magnetization. This magnetization is non-unidirectional across chondrules and

subsamples of the same chondrule. Due to its stability over a range of blocking temperatures and its heterogeneity on <1 mm scales, we rule out a pre-accretional TRM origin for the HT magnetization and conclude that it was most likely acquired during metasomatic replacement of primary magnetic phases in a low field (<8 μT) environment during alteration on the CV parent body. Allende chondrules therefore contain no discernable preaccretional magnetization. Despite widespread practice, documented magnetization in Allende should not be used to constrain early protoplanetary disk fields and their possible roles in mass and angular momentum transfer, chondrules formation, and planetary accretion and migration [e.g., Levy and Araki (1989); Stepinski (1992); Rozyczka et al. (1996); Shu et al. (1996); Nübold and Glassmeier (2000); Desch and Connolly (2002); Johansen (2009)].

We found that all chondrule samples fall into one of two classes based on their remanent magnetization and rock magnetic properties. Class A chondrules, which make up ~20% of the sampled chondrules, carry the MT overprint and exhibit random magnetization directions after demagnetization of this component at ~290°C. Class B chondrules show non-unidirectional NRM and absence of the post-accretional MT overprint. Given that the magnetic minerals in Allende are of secondary origin and that alteration in Allende was a heterogeneous process spread across several My, late alteration in a weak field environment is the most plausible explanation for the lack of the MT overprint in Class B chondrules. This scenario requires that any purported magnetic core dynamo had decayed before the end of alteration. Assuming that the I/Xe system records the last phases of magnetic mineral formation, then the lifetime of the CV parent body dynamo was ≤40 My.

Chapter 5: Retention of chondritic crusts on differentiated bodies

5.1. Introduction

The diversity of achondritic meteorites indicates that a significant population of asteroid-sized bodies underwent internal melting and differentiation during the first several million years (My) of the solar system. The iron meteorites alone originate from more than 50 distinct parent bodies (Wasson 1990). Inclusion of other achondrite groups and all ungrouped iron meteorites brings the total number of differentiated bodies represented in our meteorite collection to over one hundred (Burbine et al. 2002).

However, telescopic observations of asteroids have found relatively few objects with spectral properties indicative of differentiated material (Burbine et al., 2002). As many as 500 asteroids display spectra potentially consistent with a basaltic surface, which implies past igneous activity (Duffard 2009; Roig & Gil-Hutton 2006). However, because most such bodies are dynamically associated with the large basaltic asteroid 4 Vesta, these candidate basaltic asteroids may represent as few as three distinct differentiated parent bodies (Carruba et al. 2007).

One possible explanation for this discrepancy between the number of differentiated bodies inferred from meteorite studies and spectral observations is that some planetesimals may have undergone internal melting and differentiation while preserving a primitive chondritic surface (Weiss & Elkins-Tanton 2013; Wood 1959). In this hypothesis, early accreting planetesimals retained sufficient short-lived radiogenic isotopes to partially or fully melt the interior except for a conductively cooled crust with thickness between a few and several 10s km (Elkins-Tanton et al. 2011; Šrámek et al. 2012). Material near the surface of this crust would have undergone minimal metamorphic heating and would become the source region for chondritic meteorites of low petrologic type (i.e., 1-3). Deeper material from the crust would experience increased degrees of metamorphism and eventually undergo partial melting and differentiation.

In support of this hypothesis, isotopic and petrologic evidence suggests that some low petrologic type chondrites may originate from the same parent bodies as highly metamorphosed or igneous meteorites. Chondrites that experienced minimal parent body heating in the CV, CR, and CM groups have been associated with metachondrites that experienced heating at up to 1000°C (Bunch et al. 2008; Greenwood et al. 2010; Nakato et al. 2013; Righter & Neff 2007). At the same time, trace element and oxygen isotope compositions show evidence for a genetic relationship between H chondrites and IIE iron meteorites (Teplyakova et al. 2012). As further evidence, paleomagnetic studies suggest that the CV and CM parent bodies harbored magnetic core dynamos, necessitating the co-presence of a molten core and chondritic crust on the same body (Carporzen et al. 2011; Cournède et al. 2012).

The preservation of a chondritic crust on a differentiated body likely requires that silicate melts produced at depth were negatively buoyant with respect to the overlying crust. Pervasive melt ascent to the surface would introduce achondritic spectral features and widespread contact metamorphism of the chondritic crust. In cases of extensive interior melting, a denser, gravitationally unstable crust would be subject to foundering into the interior in the event of structural failure due to, for example, early impacts that breach the crust. Melts on some planetesimals have been hypothesized to be positively buoyant due to the high volatile content of their chondritic precursors (Muenow et al. 1995; Muenow et al. 1992; Wilson & Keil 2012). However, progressive heating of the chondritic protolith may result in extensive devolatilization before mobile silicate melts are formed. Furthermore, lithostatic pressures at the base of the crust result in finite volatile solubilities. Both effects can hinder bubble formation and volatile-driven eruption.

In this work we consider the progressive heating and devolatilization of a chondritic protolith. We show that volatiles are efficiently lost via Darcy flow from the melt region before the onset of partial melting. The first silicate melts are therefore generated at the dry solidus and are too volatile-depleted to ascend driven by gas-phase exsolution (Fig. 5.1). We then calculate the densities of these volatile-poor melts based on experimental partial melt compositions for the H, LL, CV, CM, and EH chondrite groups. We find that

the silicate melts on the CV and CM parent planetesimals were likely negatively buoyant, thereby permitting the retention of a primitive chondritic crust on these bodies.

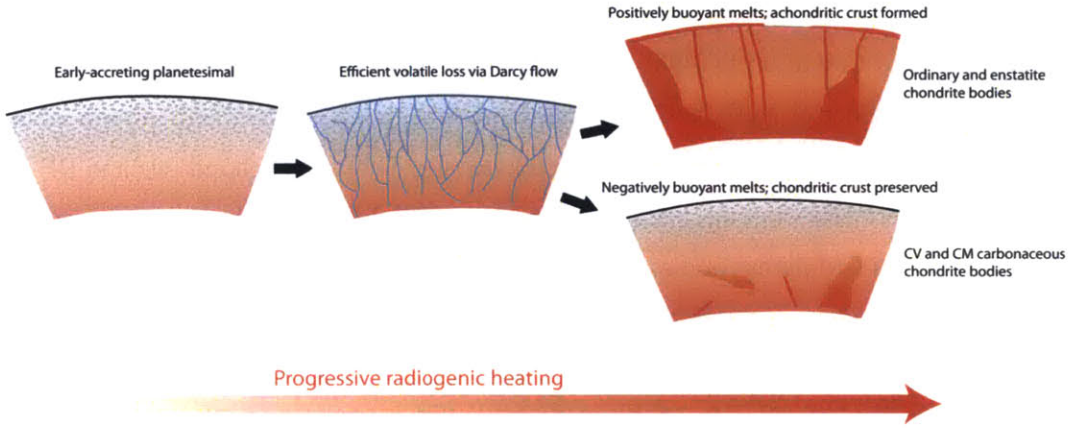

Figure 5.1. Schematic illustration of silicate melt ascent in planetesimals. Moderate radiogenic heating leads to formation of free volatile phases. Most volatiles are efficiently removed via Darcy flow, resulting in volatile-poor silicate melts, whose buoyancy depends on bulk composition. Melts of CV and CM chondrites are negatively buoyant, leading to preservation of a chondritic crust. On the other hand, enstatite chondrite melts are likely to breach the surface and ordinary chondrites are an intermediate case.

5.2. Models and methods

Radiogenic heating led to sub-solidus devolatilization. Volatile release from solution into bubbles is one of the primary drivers of eruptions on the Earth and may have also driven fire-fountaining eruptions on the Moon. Cold chondritic materials on early planetesimals were volatile-rich. However, for these volatiles to drive magma ascent, they must have been present during the formation of the first mobile silicate melts.

We first consider the fate of water, which was an abundant component of early carbonaceous and ordinary chondrite parent bodies (Alexander et al. 1989; Grimm & McSween 1989). On the Earth, the highest water content magmas are found in subduction zones. At the pressures relevant to terrestrial subduction zones, hydrous phases are stable at temperatures immediately below the solidus, which ensures that water is present during melting. The resulting silicate melts are H_2O-rich and the exsolution of H_2O in the upper crust drives explosive eruptions [e.g., Lambert & Wyllie (1968)]. Further, water and other volatiles are fluxed into hot mantle material, which is the trigger for wet melting (Hamilton et al. 1964).

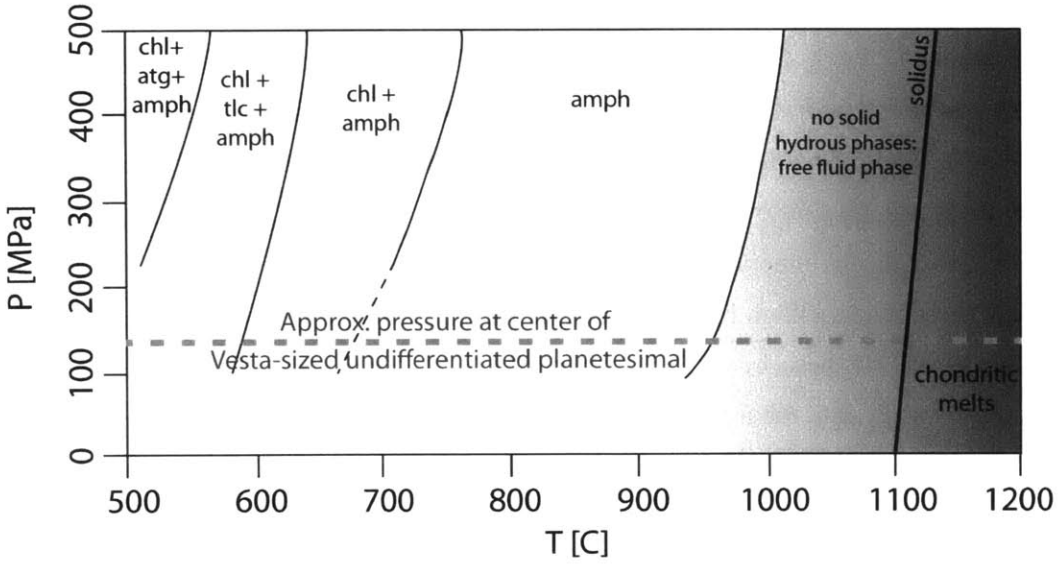

Figure 5.2. Stability of hydrous silicate phases in a peridotitic bulk composition. At low pressures, a wide temperature range exists in which there is no stable hydrous silicate phase, but silicate melting has not yet begun. In that temperature range, fluids in large planetesimals percolate out of the melting region before melting begins. Low temperature phase assemblages after Till et al. (2012). High temperature boundary of the amphibole stability field from Niida & Green (1999). Solidus based on Agee et al. (1995) and McCoy et al. (1999). Key: chl = chlorite, atg = antigorite, amph = amphibole, tlc = talc.

In contrast, lithostatic pressures in planetesimals are much lower than those of subduction zones on the Earth. Previous experimental results show that the stability fields for hydrous mineral phases are very different at the lowest pressures (Fig. 5.2). For water-saturated peridotitic compositions at pressures up to 1 GPa, talc and chlorite are the hydrous phases stable below about 600-700°C. Upon progressive heating, talc is replaced by amphibole. Above 700-800˚C, water or hydroxyl can be held in amphibole alone (Ohtani et al. 2004; Schmidt & Poli 1998; Till et al. 2012). At ~100 MPa, which corresponds to the center of a Vesta-sized planetesimal, amphiboles are unstable above ~950˚C (Niida and Green, 1999), which is more than 100˚C lower than the experimentally determined dry solidus of chondritic silicates at 1,050-1,150 °C (Agee et al., 1995; McCoy et al., 1999). Amphiboles in smaller planetesimals are expected to be stable only up to substantially lower temperatures. Corroborating these phase relations found from experiments on terrestrial mantle compositions, progressive heating of the Murchison and Semarkona chondrites showed that the most stable hydrous phases

decomposed by 800-900°C and 600-750°C, respectively (Akai 1992; Muenow et al. 1995).

As such, the hydrous metamorphic progression in a planetesimal heated by ^{26}Al involves both a hydration and dehydration stage before silicate melting temperatures are reached. Radiogenic heat first melts ice to water. As evidenced by the abundance of alteration minerals in low-grade chondrites, these hydrous fluids react into a progressive series of hydrous minerals. Eventually, as temperatures rise above some temperature ≤950°C, depending upon bulk composition, water and other volatiles (see below) exist as a free phase. If these free volatiles migrates away, the resulting dry chondritic material would not melt until the dry solidus at 1,050-1,150 °C.

Besides water, other volatiles in chondrites consist of several hundred ppm or less CO_2, N_2, and Cl. Furthermore, a smelting reaction between C and ferrous silicates may produce CO (Walker & Grove 1993). Accounting for both primordial trapped CO and that potentially produced in the smelting reaction, the total CO release for most samples ranges between 1000 and 4000 ppm (Muenow et al., 1995; Muenow et al., 1992). However, CO_2 and N_2 are released from the host chondrite below ~800°C, well before the onset of silicate melting. CO and Cl may be trapped in microvesicles in silicates and djerfisherite, respectively. The release of these volatiles corresponds to the onset of melting and their release may not be complete until 1255°C for CO and >1300°C for Cl (Muenow et al., 1995; Muenow et al., 1992). However, the bulk of CO and Cl are released below 1250°C, at which temperature the first silicate melts are mobilized (see Section 5.3). In summary, nearly all volatiles are found as free phases and not incorporated into hydrous minerals at temperatures below the generation of mobile silicate melts.

Volatile migration in igneous planetesimals occurred rapidly. If the free volatiles migrate away before silicate melt migration begins, then magmas on planetesimals would have very low volatile contents. The ability for the free volatiles to migrate away and leave a dry melting region depends upon a competition between the upward flow velocity of the volatiles and the rate of heating of the body.

Upon progressive heating in the pressure regime relevant to planetesimal interiors, water would exist in the gas phase or as a supercritical fluid above the critical temperature of 374°C or lower temperatures at lower pressures. For planetesimals with radius smaller than 107 km (with a uniform density of 3,700 kg m^{-3}), all water in the heated interior would be converted to vapor, while supercritical fluids would form in the center of larger planetesimals. Other volatiles such as CO_2 and CO are also expected to exist in the gas or supercritical fluid phase.

While the water is in the liquid phase, the upward, buoyancy-driven Darcy flow is limited by the fluid viscosity. Once water passes into the gas or supercritical fluid phases, upward migration becomes much more efficient. We estimate the flow rate of water as a supercritical fluid to place a lower bound on the efficiency of transport. Darcy flow calculations indicate that supercritical fluids at 900°C would move upward through the planetesimal at speeds in excess of 1 km per year. For this calculation, the permeability k of the solid material is expressed as

$$k = \frac{b^2 \Phi^2}{72\pi} \tag{5.1}$$

where grain size b is 0.001 to 0.01 m, and dimensionless porosity F is 0.1 to 0.3. The Darcy flow velocity relative to the stationary solid matrix (v_{Darcy}) is then given as (Turcotte & Schubert 2002):

$$v_{Darcy} = \frac{kg\pi\Delta\rho}{\eta\Phi} \tag{5.2}$$

with difference in density Dr between the fluid and the matrix of 3,650 kg m^{-3} (Smits et al. 1994) and fluid viscosity η of 5×10^{-5} Pa s (Sengers & Kamgar-Parsi 1984). The gravitational acceleration g decreases with increasing depth, thereby limiting the flow rate near the center the of body. However, even within 1 km of the center, the flow rate is in excess of 1 km per year. The delivery of volatiles to the surface therefore requires no more than ~100 years.

At the same time, the timescale of heating of a planetesimal can be calculated by assuming an initial ^{26}Al composition and a time of accretion. Accretion must have occurred within ~1.5 My of the first calcium-aluminum inclusions (CAIs) for heating to be sufficient to melt the silicate portion of the body (Elkins-Tanton et al. 2011; Ghosh & McSween 1998; Hevey & Sanders 2006; Sahijpal & Gupta 2011; Šrámek et al. 2012). We use the techniques from Hevey and Sanders (2006) and Elkins-Tanton et al. (2011) to model the evolution of the interior temperature in early-accreting planetesimals (Fig. 5.3). Using these models, we constrained the time interval between accretion and the production of the mobile silicate melts at ~1250°C (see Section 5.5), which occurred for all 100 km radius planetesimals that accreted before 1.4 My after CAIs. We find that even in the fastest possible case (instantaneous accretion at the time of first CAIs), the planetesimal's interior reaches 1250°C approximately 0.1 My years after accretion (Fig. 5.3A).

Thus, water and other volatiles are liberated and percolate upward via Darcy flow efficiently long before the melting point of the silicates is reached. If these percolated volatiles are lost to space or trapped in a near-surface layer, the planetesimal's interior would be volatile-depleted due to heating before silicate melting ever begins, and the resulting melt will be correspondingly volatile-poor (Fig. 5.1). The lack of primordial volatiles on igneous asteroids such as Vesta and in highly metamorphosed meteorites strongly suggests that volatile loss to space occurred efficiently on planetesimals (Prettyman et al. 2012).

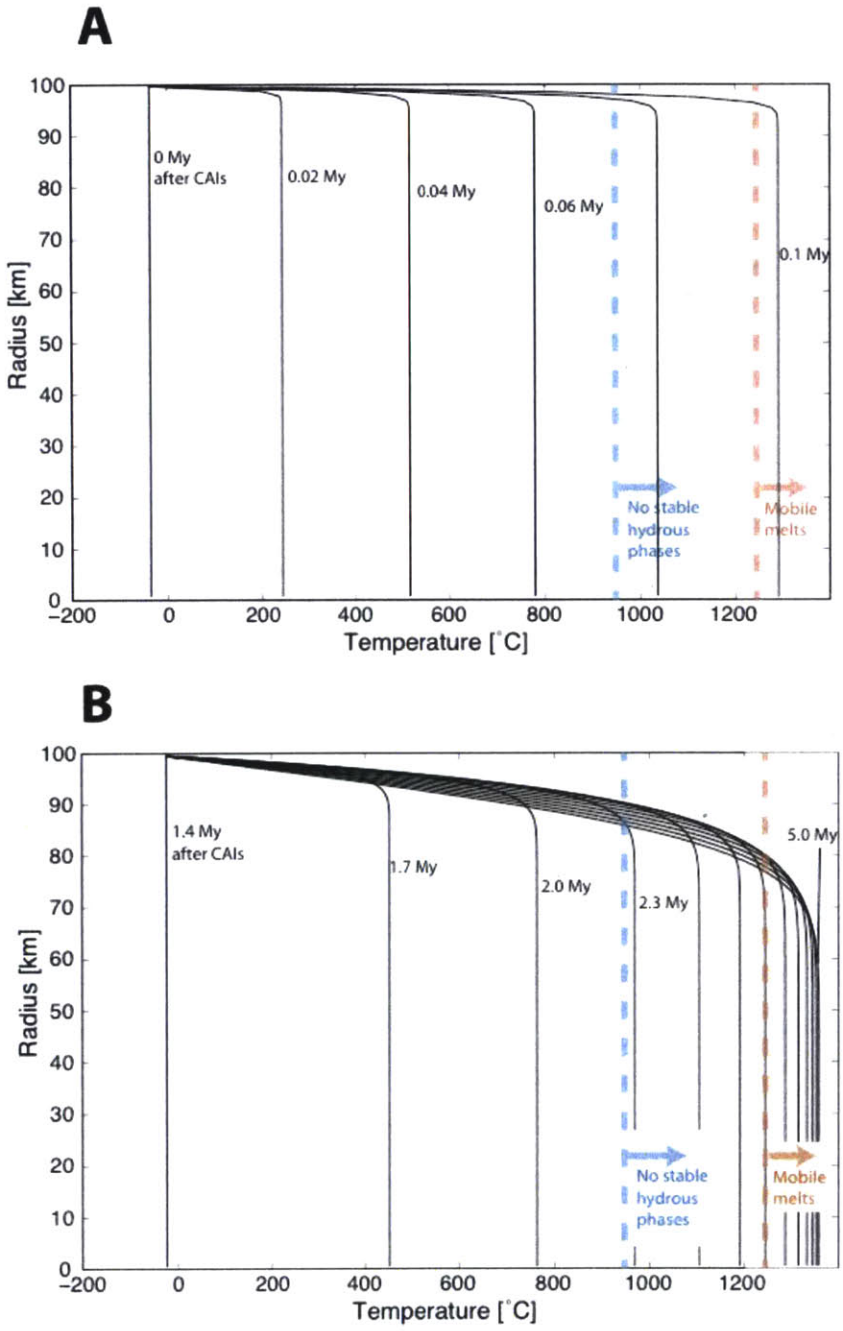

Figure 5.3: Thermal evolution of planetesimals for the end-member cases of instantaneous accretion at (**A**) 0 My and (**B**) 1.4 My after CAIs. In the former case, melting occurs <0.1 My throughout the planetesimal except for a thin crust while in the latter case, the interior of the planetesimal undergoes partial melting beneath a 20-30 km crust.

The rapid rate of volatile loss from the above analysis is consistent with the works of Young (2001) and Young et al. (2003) for large planetesimals. In contrast, the analysis of Young et al. (2003) further concluded that smaller bodies (<40-60 km radius) may be unable to efficiently lose fluids via porous flow. However, their calculation considered the balance between buoyancy and viscous forces appropriate for liquid water. While this is the relevant regime for the low metamorphic grade carbonaceous chondrites parent bodies they considered (<374°C), water heated further into the gas or a supercritical fluid phase is much more easily mobilized and ascends efficiently through the planetesimal (see above). Finally, we note that the expansion of water vapor during its ascent through the planetesimal may have contributed to the porosity of the surrounding chondritic matrix. Although local porosity would be closed viscously at ~900°C (see Section 3.2), planetesimals that did not reach such temperatures while experiencing sufficient heating to generate ascending water vapor may contain high porosity due to this effect.

Residual volatiles in igneous planetesimals are unlikely to affect melt density. Although free volatiles released upon heating in large planetesimals are efficiently removed, a finite amount of volatiles still remains in the nominally anhydrous protolith even upon heating. Small abundances of water can be accommodated in olivine and pyroxene structures. However, the solubility of H in these minerals drops precipitously at low pressures. Although no measurements have been made below 300 MPa, at pressures of <1 to ~100 MPa relevant to planetesimals, olivine holds <<20 ppm equivalent H_2O (Bai & Kohlstedt 1993). Pyroxenes hold up to 10 times more water per unit mass at low pressures (Hirschmann et al. 2005). We therefore estimate the residual water content in the chondritic protolith to be <<200 ppm upon mobile melt generation. Water trapped in olivine and pyroxene at such concentrations continues to be stable in olivines and pyroxenes upon the initiation of partial melting (Aubaud et al. 2004; Hauri et al. 2006).

Other volatiles in chondrites are likewise unlikely to survive in sufficient abundances to affect the density of mobile melts at >1250°C. As discussed above, heating of carbonaceous and enstatite chondrites releases up to several hundred ppm N_2 and CO_2 below 800°C (Muenow et al., 1995; Muenow et al., 1992). Further release between 800 and 1250°C is below the detection threshold of ~100 ppm, suggesting that the abundance

of these volatiles remaining at >1250°C would be <<100 ppm. Likewise, no additional release of CO is measured above 1255°C, and its residual abundance would be similar to that of N_2 and CO_2. Both ordinary and enstatite chondrites can retain Cl up to >1300°C. However, only a fraction (<25%) of the initial ~450 ppm still remains above 1250°C. In summary, upon the generation of the first mobile silicate melts, the residual abundance of H_2O is likely <<200 ppm, that of Cl ~100 ppm, and that of other volatiles <<100 ppm. We note that the CO release observed in ordinary and enstatite chondrites occurred at lower temperatures than in heating of lodranite and acapulcoite samples (McCoy et al. 1997), likely due to the greater role of the C-FeO smelting reaction in the latter case. Our estimates of residual volatile abundances should therefore be regarded as specific to the meteorite classes in question.

To inhibit gas phase exsolution, the solubility of these volatiles in silicate melts at the base of the unmolten crust must be higher than the residual concentrations. The solubility of Cl (~1000 ppm) remains much higher than expected Cl concentrations for a wide range of pressures (Webster 1997). Meanwhile, at comparable pressures, the solubility of H_2O in melt is a factor of 100 greater than the expected residual abundances in olivine and pyroxene as discussed above (Papale 1997). Residual volatiles are therefore not expected to undergo exsolution at the onset of silicate melting.

Without gas phase exsolution, residual volatiles at the level found in chondrite melts have a small effect on melt density. Using the experimental results of Ochs & Lange (1999), H_2O at the <200 ppm level decreases the melt density by only <0.1%. Therefore, we find that volatile contents likely do not enhance melt buoyancy on planetesimals.

For bodies with radius larger than 100 km, our result is in agreement with the previous work of Wilson and Keil (2012), who concluded that magmas on such planetesimals are unlikely to be volatile-saturated. However, in contrast to Wilson and Keil (2012), we predict likewise volatile contents for smaller planetesimals due to the efficient loss of free volatiles via porous flow as modeled above, which was not included in the earlier work.

Without volatile exsolution as a driving force, the likelihood of silicate melt ascent is controlled by the relative densities of dry melts and the overlying crust. Specifically, because we are most interested in the likelihood of melt ascent through the crust and

surface eruption, we find the density of the lightest mobile silicate melts for a range of chondritic protoliths. We calculate the density of partial silicate melts using the composition of the melt and the formalism described in Kress & Carmichael (1991) and used previously in (Elkins-Tanton et al. 2003). We assume that the silicate melt consists of SiO_2, TiO_2, Al_2O_3, FeO, MgO, CaO, Na_2O, and K_2O. The proportion of each component in the melt is determined by existing partial melting experiments. We calculate the dry melt densities for at least one sample from the ordinary, carbonaceous, and enstatite chondrite classes. Based on the availability of partial melting data, we consider the melts of the Lost City (H4), St. Severin (LL3), Allende (CV3), Murchison (CM2), and Indarch (EH4) meteorites (Jurewicz et al. 1995; Jurewicz et al. 1993; McCoy et al. 1999).

5.3. Results

Buoyancy of dry melts depends on bulk composition. Mobile silicate melts on planetesimals were likely dry (Section 5.2). The density of such melts is a function of the bulk composition, the degree of melting, and the oxygen fugacity. In general, the lowest temperature Al-rich melts are less dense than the Mg-rich high degree melts (Fig. 5.4). At the same fO_2, the density of intermediate melts at 1300°C are between 3% and 13% denser than the initial melts at 1100°C.

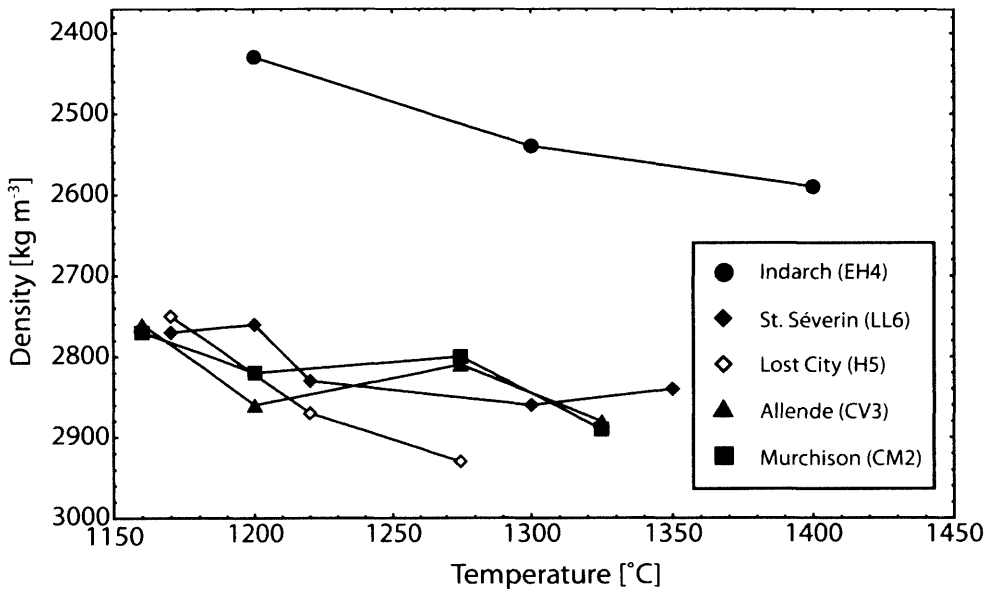

Figure 5.4: Density of silicate melts from chondritic starting compositions as a function of temperature. The high Al and low Mg content of low temperature melts leads to lower densities. Ordinary and carbonaceous chondrite melts are calculated for fO_2 = IW-1. The much lower density of the enstatite chondrite melt is primarily due to its oxidation state (fO_2 ~ IW-2.5). At such reduced conditions, almost no Fe partitions into the silicate melt, leading to very low densities.

Even though the first melts are the most buoyant, they may be incapable of migration and therefore irrelevant for melt ascent through the crust. The first silicate melts of a chondritic protolith occur at between 1050°C and 1150°C (Agee et al. 1995; McCoy et al. 2003) and are not mobilized until a higher degree of partial melting in silicates is achieved. The amount of partial melting required for melt mobilization to occur depends on a range of factors, including the melt composition, the fO_2, and the local stress state [e.g., Rubie et al. (2007)]. Broadly however, observations of melt vein formation in lodranites and acapulcoites show that low degree melting between 5 and 10% is sufficient for efficient melt migration, which corresponds to a temperature of ~1250°C (McCoy et al. 1997). Melting experiments on enstatite chondrites show melt separation at ~1300°C (McCoy et al. 1999). Based on these data, we adopt 1250°C as the temperature above which silicate melts can freely migrate. Only melts above this temperature are considered for possible ascent in planetesimal crusts. Inferences from the decay of U-series elements in terrestrial lavas show that melt fractions of <1% can be mobilized beneath mid-oceanic ridges (Lundstrom et al. 1995; Spiegelman & Elliott 1993). The higher melt fractions required for mobility in meteorite parent bodies may be due to

differing phase assemblages or pressure conditions in the melts are generated. We note that lowering the degree of melting required for silicate melt migration may result in more volatile-rich melts, since volatiles may not be as completely degassed at the correspondingly lower temperatures.

Oxygen fugacity can have an even greater effect on density than melt degree. Observations of achondrites show that igneous planetesimals spanned a wide range of fO_2 from IW+2 for angrites to IW-2.5 for pallasites, where IW refers to the native iron-wüstite buffer (Brett & Sato 1984; Greenwood et al. 2005). Higher fO_2 leads to the increased partitioning of Fe into the silicate melt, resulting in higher density. Increasing the fO_2 from IW-1 to IW+2 for the ordinary and carbonaceous chondrites in our selection results in between 1 and 7% increase in density (Jurewicz et al., 1993, 1995). At the other extreme, enstatite chondrite melts [fO_2~IW-2.5 (Brett and Sato, 1984)] are essentially devoid of FeO and have very low densities (Fig. 5.4). An accurate estimate of the melt oxygen fugacity is therefore important for determining the correct melt density. For the ordinary and enstatite chondrites, we assume oxygen fugacities similar to that of the unmolten chondrite. We therefore use experimental melt compositions at fO_2=IW-1 (Brett and Sato, 1984) for the ordinary chondrites. For the enstatite chondrite, the melting experiments of McCoy et al. (1999) did not impose a single fO_2 but buffered the experimental charges to maintain the intrinsic reduced state of the meteorite. The enstatite chondrite melt compositions used here therefore have an fO_2 close to IW-2.5 as measured for another EH chondrite (Hvittis; Brett and Sato (1984)).

The appropriate oxygen fugacities for the CV and CM carbonaceous chondrites are less constrained due to the diverse redox histories of their components. The wide range of inferred fO_2 values for components in Allende and Murchison reflect unaltered refractory inclusions formed in the solar nebula (fO_2~IW-5) and minerals aqueously altered on the parent bodies (fO_2~IW+5) (Ihinger & Stolper 1986). Measurement of the bulk oxygen fugacity of a CO chondrite yielded an intermediate estimate of fO_2~IW+1 (Brett and Sato, 1984). We adopt a lower oxygen fugacity of IW-1 for Allende and Murchison melts to account for reduction at high temperatures and to provide a probable lower bound on the melt densities (Nakamura 2005).

Table 5.1: Densities of lightest mobile silicate melt for four chondrite groups.

Chondrite group	Silicate melt density at 1250°C (kg m^{-3})	Reference for partial melt composition
H	2907*	Jurewicz et al. (1995)
LL	2843*	Jurewicz et al. (1995)
CV	2808*	Jurewicz et al. (1993)
CM	2827*	Jurewicz et al. (1993)
EH	2486	McCoy et al. (1999)

*Linear interpolation of densities at two bracketing temperatures

In summary, the lightest mobilized silicate melts for each chondritic starting composition are generated at ~1250°C in the most reducing condition likely for the given chondrite class. The density of such melts varies significantly between the chondrite groups (Fig. 5.5; Table 5.1). H chondrite melts are denser than those of LL and carbonaceous chondrites due to its higher bulk Fe content. Meanwhile, enstatite chondrite melts are the least dense due to their low oxygen fugacity and the nearly complete loss of FeO to the Fe-FeS melts.

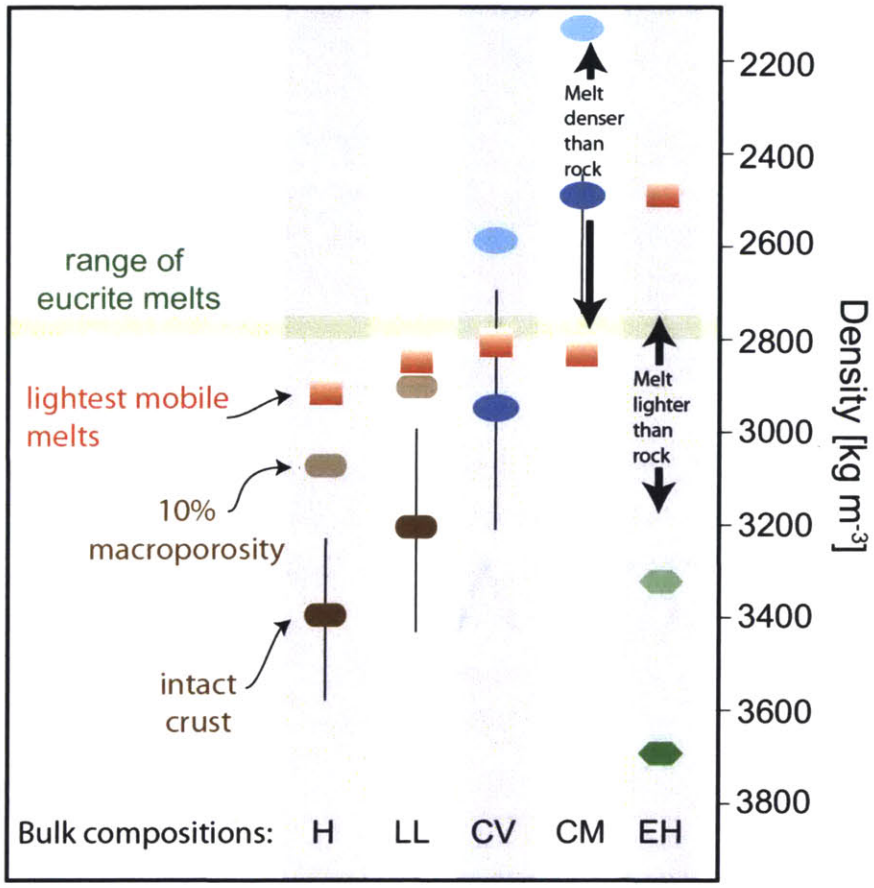

Figure 5.5: Densities of meteorites, their porous equivalents (expected in planetesimals' unsintered lids), and their melts (see text). The lightest mobile melts refer to the first mobilized silicate melts at ~1250°C. More advanced melts, although also mobile, become progressively denser. CV and CM compositions produce melts likely too dense to erupt through buoyancy alone. These planetesimals may internally differentiate without any surface expression. Intact crust (no macroporosity) densities are from Britt and Consolmagno (2003). Crustal densities for CM chondrites have been corrected for dehydration during metamorphism.

The bulk density of the chondritic crust varies with composition. Comparison of these melt densities with chondrite hand samples shows that ordinary, enstatite, and CV chondrites melts are less dense than the intact rock. However, the near-surface material of planetesimals likely had high macroporosity due to frequent early meteoroid bombardment (Davison et al. 2013). Small asteroids in the present day solar system have ~20% macroporosity (Consolmagno et al. 2008). Furthermore, recently accreted material at the surface of planetesmals may have higher porosities due to the absence of heating, aqueous alteration, and compaction. On the other hand larger, including Vesta-sized, planetesimals likely had smaller near-surface macroporosities than modern small

asteroids due to their higher surface gravity. For reference, the lunar crust has a bulk porosity of 12% (Wieczorek et al. 2013). We therefore conservatively assume 10% macroporosity for the bulk crust overlying the melt region.

Metamorphic heating of the lower crust may lower the effective porosity of the bulk crust. Porosity closure through this mechanism is due to the viscous creep of rock under lithostatic pressure (Wieczorek et al., 2013). Because viscous creep is a strong function of temperature, the thermal profile and the rheology of the crust control the depth below which the crust becomes non-porous. The closure timescale of porosity ($\tau_{closure}$) due to viscous creep is given by $\tau_{closure} \approx \eta/P$, where P is the lithostatic pressure and η is the viscosity, which is a function of temperature (Wieczorek et al., 2013). Therefore, for a given timescale and pressure, we can find the viscosity and, in turn, temperature required for pore space closure to occur. Adopting a dry olivine viscosity and a characteristic timescale of 1 My (Chopra & Paterson 1984), the lower crust of a 100 km radius planetesimal (~10 km depth; 4 MPa pressure) is expected to be non-porous below the 900°C critical isotherm. Given a temperature of -73°C at the surface and 1250°C in the melting region and a nearly linear conductive temperature gradient in between, porosity closure occurs in only the lowermost ~25% of the overlying 10 km crust. Different crustal thicknesses would imply different driving pressures for porosity closure. However, the effect on the critical isotherm is minimal due to the exponential dependence of viscosity on temperature. Therefore, metamorphic heating does not significantly affect the column integrated porosity of the crust.

At the same time, contact metamorphism of the bottom of a chondritic crust can lead to the dehydration of crustal material and a corresponding increase in density. This effect is significant only for CM chondrite compositions as the densities of the other chondrite classes used in this study are based on already fully dehydrated samples (Jarosewich 1990). For CM chondrites, dehydration reactions in the abundant phyllosilicates begin between 400 and 650°C, at which point the water content of the meteorite falls rapidly (Nakamura 2005). Assuming once again that the surface of the crust is at -73°C and that the mobile melt-generating region is at 1250°C, a conductive temperature profile in the crust implies that ~45% of the thickness of the crust would be un-dehydrated. The overall density of the crust is therefore approximately the average of the un-dehydrated

and dehydrated densities. Because metamorphosed CM chondrites are a relatively rare group, no direct measurement of their densities has been published. We adopt the density of anhydrous CV chondrites as an upper bound on that of the metamorphosed CMs. CM chondrites contain more matrix and anomalously high microporosity and are therefore likely less dense than CVs even when dehydrated (Akai 1994). The bulk density of such a partially dehydrated crust is still ~2500 kg m^{-3}, not considering the additional effect of macroporosity. The true crustal density would therefore be well below the expected melt density of 2827 kg m^{-3} (Fig. 5.5).

On Earth, seafloor hyaloclastite deposits, similar to the porous and hydrated sections of chondritic crusts, also decrease the bulk density of the oceanic crust. However, hyalocastite layers are less dense than MORB melts by ~300 km m^{-3} (Moore 2001; Niu & Batiza 1991), while an unmetamorphosed CM crust is ~600 km m^{-3} less dense than their respective melts [Table 5.1; (Britt & Consolmagno 2003)]. Furthermore, hyaloclastites compose a small percentage (17%) of the total volume at shallow depths and are found in small proportions deeper than 2-3 km (Stolper et al. 2008), which is less than 5% of the depth of melt source regions (Hirschmann & Stolper 1996). Therefore, unmetamorphosed chondritic lids have a much greater effect on bulk crustal density than these terrestrial analogs.

Based on these estimates for bulk crustal densities, dry melts on the CV and CM parent bodies are too dense to ascend in the planetesimal crust. For the ordinary chondrites, melts may be marginally buoyant (Fig. 5.5). However, since the newly accreted, unsintered material at the very surface of planetesimals likely had higher porosity, the rise of melts to the surface of planetesimals of ordinary chondrite composition would depend on the efficiency of processes that reduce porosity such as hydrothermal alteration and compaction.

In the case of enstatite chondrites, melts would ascend even in a planetesimal crust with much higher than 10% macroporosity. Provided that the degree of interior melting is advanced enough to permit melt migration and that there is sufficient melt to avoid freezing during the ascent, melts in enstatite chondrite planetesimals are likely to rise to the surface of the parent body.

5.4. Discussion

We have shown that the buoyancy of silicate melts on planetesimals depends on the bulk composition of the body. Melts of CV and CM carbonaceous chondrites are negatively buoyant and not expected to breach the chondritic crust while enstatite chondrite melts are positively buoyant and readily ascend. Melts of H and LL ordinary chondrites represent an intermediate case and are expected to be marginally buoyant.

Our results imply that a primitive chondritic crust on the CV and CM parent bodies would have been protected from foundering and is likely to survive even in the case of pervasive interior melting and differentiation. Paleomagnetic evidence suggests that material from the Allende CV chondrite, which originated from the unmelted crust of the planetesimal, was not heated above 290°C during the time of an active dynamo (Carporzen et al., 2011). Similarly, unidirectional magnetization in CM chondrites also suggests low degree metamorphism in the presence of a dynamo magnetic field (Cournède et al., 2012). These observations also suggest that the radii of these parent bodies were greater than 100 km (Weiss et al., 2010), leading to high confining pressures that prevent volatile exsolution as described in Section 5.2. Our predictions for chondrite crust preservation on these bodies are therefore fully consistent with paleomagnetic results.

Remote sensing observations of the surface compositions of modern asteroid can also constrain their early igneous activity. Dynamical simulations of the evolution of the asteroid belt size-frequency distribution suggests that most asteroids larger than ~100 km in diameter escaped catastrophic disruption during the history of the solar system (Bottke et al. 2005; Morbidelli et al. 2009). The low macroporosities of some large asteroids provide further support that many such bodies have not been shattered by a large impact (Britt et al. 2002). Finally, the eucritic composition of the Vestan surface and the saturated crater densities and nearly hydrostatic figure of Vesta's northern hemisphere indicate that Vesta has not been significantly resurfaced dues to impacts aside from two large craters in the southern hemisphere (De Sanctis et al. 2012; Fu, Hager, et al. 2014; Marchi et al. 2012). If melt ascent and eruption occurred during their early history, the

surface spectra of a fraction of such large asteroids are expected to indicate achondritic materials.

The asteroid 21 Lutetia is ~100 km in diameter and therefore likely escaped catastrophic disruption (Sierks et al. 2011). Furthermore, its high density rules out a reassembled rubble pile structure (Pätzold et al. 2011). The surface of Lutetia may therefore retain its primodial composition from the early solar system. Lutetia has been hypothesized to have undergone interior heating based on its high density (Weiss et al. 2012). Depending on the macroporosity, Lutetia's observed density is consistent with full or partial differentiation (Neumann et al. 2013). However, spacecraft observations suggest that the surface consists mainly of CV-like material (Coradini et al. 2011), which is consistent with our prediction that melts from CV compositions are too dense to breach the surface. However, partial melting is not required to explain the high density of Lutetia as sub-solidus closure of pore space can produce the same effect. Furthermore, the surface spectra of Lutetia may also be consistent with chondrites of other groups, including enstatite chondrites. In the latter case, the lack of surface melts would imply that the internal heating of Lutetia was insufficient to produce mobile melts; otherwise, the low density melts would readily ascent to the surface.

The low density of enstatite chondrite melts implies that, if their parent bodies underwent advanced internal melting, silicate melts should have ascended to the surface. These parent bodies, if their primordial surfaces are retained, are then expected to show achondritic surface spectra. However, if the parent bodies represent broken fragments of a once larger body, then melt ascent is not required for achondritic surface compositions.

Spectroscopic studies have linked the E-type asteroids with aubrites (Gaffey et al. 1992), which share the same oxygen isotopic composition as enstatite chondrites and originate from the melting of enstatite chondrites or enstatite chondrite-like protoliths (Keil 2010). Most E-type asteroids are small and are therefore likely to be fragments from earlier impacts. Even so, 44 Nysa, the largest E-type asteroid, has a diameter of ~80 km and may have escaped catastrophic disruption (Bottke et al. 2005). The largest E-type asteroid or asteroids may therefore represent remnants of a differentiated planetesimal or planetesimals made of enstatite chondrites or enstatite chondrite-like material on which light aubritic melts have ascended to the surface. Future telescopic

and spacecraft observations of possibly igneous asteroids of all spectral types such as 44 Nysa and 20 Massalia can potentially resolve heterogeneities in surface composition, thereby providing clues to the extent of surface eruption of melts, if any.

Although we have considered so far only ascent of primary chondritic partial melts, secondary silicate melts could have also potentially breached an overlying crust. Eucrites are believed to represent lava flows from the surface of Vesta, the largest and best-studied basaltic asteroid (Binzel & Xu 1993; McCord et al. 1970). Major element compositions of eucrites indicate that they formed from the partial melting of an already differentiated protolith (Stolper 1977) or that they are products of fractional crystallization of the last melts of a Vestan magma ocean (Mandler & Elkins-Tanton 2013; Righter & Drake 1997). Given sufficient heating, the chondritic parent bodies considered here may have also generated secondary melts analogous to eucrites. The densities of eucritic melts, as represented by experimental melts of the Juvinas, Stannern, Bereba, Pasamonte, and Sioux County meteorites (McCarthy et al. 1973), span a very narrow range between 2764 and 2800 kg m^{-3} at 1250°C (Table 5.1). Such eucritic melt would have been marginally negatively buoyant in a primordial Vestan crust with 10% macroporosity consisting of 2/3 H and 1/3 CM chondrite material (Toplis et al. 2012). However, remote sensing from the NASA Dawn spacecraft indicates that primitive chondritic material does not survive on the surface of Vesta while eucritic material is abundantly exposed (De Sanctis et al. 2012; Reddy et al. 2012). As one possible explanation for this observation, Vesta's primordial crust may have consisted of denser material than the proposed H and CM chondrite mixture. Alternatively, internal heating may have thinned unmelted lid to <<10 km, in which case moderate impacts events or hydrostatic readjustment may have destroyed Vesta's primitive chondritic crust.

Large impacts into differentiated planetesimals can drive melt to the surface via deep excavation (Davison et al. 2012). Impacts that breach the chondritic crust can therefore lead to the surface exposure of melt even in cases where buoyant ascent is otherwise unlikely (i.e., CV and CM chondrite parent bodies). However, a single impact results in melt surfacing in a local area, and a large number of impact is likely necessary to destroy a significant fraction of a buoyant primitive crust. Molten interiors persist in planetesimals for only a short time window, as the conductive cooling timescale for a 100

km radius planetesimal is only ~40 My given a thermal diffusivity of 8×10^{-7} m^2 s^{-1} (Šrámek et al. 2012). Coupled with the low probability of disruptive impacts on planetesimals larger than 50 km in radius (Bottke et al. 2005; Morbidelli et al. 2009), most planetesimals would not experience a sufficient number of large impact to drive melt ascent on a global scale.

Although we have shown that silicate melts on planetesimals are likely volatile undersaturated, volatile content of magmas on some may be increased if they contain higher concentrations of trapped volatiles at high temperatures than the experimentally determined values from fourteen ordinary and enstatite chondrites (Muenow et al., 1995; Muenow et al., 1992). Heating experiments on more samples of chondrites from a range of groups can better constrain the diversity of residual volatile contents. Furthermore, observations of achondrites and heating experiments such as perform in McCoy et al. (1997) and McCoy et al. (1999) can constrain the temperature necessary for silicate melt migration in a wider range of chondritic parent bodies. If higher residual volatiles concentrations are present in planetesimals of other compositions, exsolution-driven melt ascent as modeled by Wilson and Keil (2012) may occur. Whether these ascending melts can reach the surface would then depend on additional factors. The ascent of bubbles can potentially outpace that of the melt, releasing volatiles to the planetesimal surface while melts, now free of exsolved gases, remain below. The retention of gas bubbles in the melt would depend on the viscosity of the latter (Phillips & Woods 2002). At the same time, unconsolidated surface material may have significantly lower bulk density, hindering surface eruption of the melt. Lastly, low volumes of melt may freeze during ascent. Future theoretical studies, coupled with new experiments as described above, can lead to stronger constraints on the fate of melts on a wider range of bodies.

Finally, volatiles mobilized during interior heating would affect the composition of the planetesimal crust, which may lead to both spectroscopic and meteoritic observables indicative of past igneous activity. Future modeling may address the freezing of these volatiles and their loss to space via sublimation or impact ejection, thereby explaining the lack of volatiles on the surface of igneous asteroids such as Vesta.

5.5. Conclusion

The preservation of primitive chondritic material on differentiated planetesimals depends on the ability of silicate melts to ascend and breach the chondritic crust. In general, melt ascent in planetary bodies may be driven by volatile exsolution or positive buoyancy of the dry silicate melt itself. Based on the stability field of hydrated minerals at low pressures and experimental observations of volatile release during heating, chondritic volatiles exist as free gases and supercritical fluids at temperatures in a range of one to several hundred degrees immediately below the silicate solidus. Darcy flow calculations show that these volatiles are expected to ascend efficiently to the surface of planetesimals. The efficient rise of these volatiles leaves behind a dry interior.

The abundance of volatiles in the protolith at the time of the first silicate melt mobilization is therefore expected to be low. Water, Cl, and other volatiles are expected to be present at the $<<200$, ~100, and $<<100$ ppm levels, respectively. At such concentrations, volatiles are unlikely to exsolve and drive melt ascent in the lower crust of planetesimals. Densities of volatile-poor melts based on partial melting experiments show that ordinary and enstatite chondrite melts are likely to ascend in a moderately porous crust. On the other hand, CV and CM partial melts are denser than the overlying crust, leading to preservation of low metamorphic grade chondritic material on these bodies. These predictions support paleomagnetic evidence for the survival of primitive chondritic material on the CV and CM parent bodies during differentiation. Furthermore, our calculations show that enstatite chondrite or enstatite chondrite-like parent bodies, if differentiated, should exhibit achondritic surfaces. This prediction provides support for the correspondance between the E-type asteroids and aubrites.

Chapter 6: Magnetic fields and dynamo generation on asteroid Vesta

6.1. Introduction

The terrestrial planets are thought to have formed from the successive growth and accretion of protoplanetary objects <1000 km in diameter (Chambers 2004). A fraction of these protoplanets have survived to the present day and include 4 Vesta, the second most massive asteroid (525 km mean diameter). In particular, Vesta's high density, primordial basaltic crust, and large size suggest that it is an intact remnant of the early solar system that escaped catastrophic collisional disruption (Russell et al. 2012). Vesta therefore provides a unique opportunity to characterize the building blocks of the terrestrial planets and to study processes of planetesimal accretion and differentiation.

Meteorites of the howardite-eucrite-diogenite (HED) clan likely sample the crust and upper mantle of Vesta (Binzel & Xu 1993). Geochemical studies of HED meteorites suggest that Vesta has a fully differentiated structure with a metallic core ranging from 5 to 25% of the total planetary mass (Righter & Drake 1997) that formed within ~1-4 million years (My) of the first CAIs (Kleine et al. 2009). Recent volume and mass constraints from the NASA Dawn mission, in orbit around Vesta since July 2011, provide evidence of a metallic core between 107 and 113 km in radius (Russell et al. 2012).

Vigorous advection in a molten metallic core may generate a dynamo magnetic field. Paleomagnetic studies of meteorites suggest that past dynamos may have existed on other asteroidal objects such as the angrite and the CV carbonaceous chondrite parent bodies (Weiss et al. 2008; Carporzen et al. 2011). These data offer the possibility of studying the physics of dynamo action in a small body regime not represented by active dynamos in the solar system today, in which Mercury is the smallest body with a known active dynamo (Stevenson 2010). However, there has been no meteorite group for which evidence of dynamo action has been confidently established and that has been directly associated with a known, intact asteroidal parent body.

Previous paleomagnetic studies have shown that many HED meteorites are low-fidelity recorders of magnetic fields due to their coarse grained mineralogy (which tends to produce low-coercivity ferromagnetic grains) (Cisowski 1991). Furthermore, these

paleomagnetic studies generally lacked radiometric ages and thermochronometry. As a result, they came to no firm conclusions about the origin of magnetization identified in HED meteorites. Although dynamo-generated fields were considered, other potential sources such as recent magnetic contamination and impact-generated fields could not be ruled out (Cisowski 1991; Collinson & Morden 1994; Weiss et al. 2010).

Most relevantly, Cisowski (*10*) alternating field (AF) demagnetized two mutually oriented subsamples of ALHA81001 up to 100 mT. Unfortunately, the relatively low peak AF levels used in their study did not allow them to isolate a primary thermoremanent magnetization (TRM), as indicated by divergent magnetization directions for their mutually oriented samples and an observed lack of origin-trending magnetization [likely due to spurious anhysteretic remanent magnetization (ARM) noise from their AF system (Weiss et al. 2010), as indicated by variability during repeat AF applications with the same peak field]. As a result, they were apparently unable to isolate the HC component that we observe to be blocked from 60 to >290 mT (Fig. 2). Instead Cisowski (*10*) inferred weak (~6 μT) paleointensities using the isothermal remanent magnetization (IRM) method for natural remanent magnetization (NRM) blocked below 50 mT and ~10-16 μT for NRM blocked at higher AF levels (calculated using the same ratio of TRM to IRM as that used in this study; see Section 6.3). However, the Cisowski study (1991) did not estimate separate paleointensities for each component of the magnetization and instead obtained a single paleointensity for a coercivity range that included up to 3 directionally distinct components, resulting in systematically underestimated paleointensities. Paleointensities obtained using our data without separation of components differ by less than 20% from those of Cisowski (1991) over the same coercivity ranges (see Section 6.3), suggesting that the mixing of NRM components is indeed the cause of his underestimated paleointensities. In part due to these low paleointensity values, Cisowski (1991) considered an early Vestan dynamo to be an unlikely source of HED magnetization.

In contrast, Morden's study of the polymict eucrite Millbillillie found strong paleointensities ranging between 6 and 37 μT and argued for a dynamo-generated field on Vesta (Morden 1992). However, this study analyzed a piece of Millbillillie with fusion crust, which the author apparently did not remove before performing the

measurements. Morden's reported mass-specific NRM intensity values ranged from $5-20\times10^{-6}$ Am^2kg^{-1}, which is one to two orders of magnitude stronger than recent measurements of deep interior Millbillillie material not containing fusion crust (Fu & Weiss 2011). Furthermore, Fu & Weiss (2011) found that Millbillillie subsamples composed of a mixture of fusion crust and interior samples carried mass-specific NRM intensities consistent with the values in Morden's study. The predominantly single-component magnetizations found in Morden's study are also consistent with fusion crusted material. In contrast, non-fusion crusted subsamples in the experiments of Fu & Weiss (2011) were found to carry three distinct components of NRM. For these reasons, the samples in Morden's study were very likely contaminated with fusion crust. The relatively strong paleointensities from the Morden study therefore probably reflect at least partly a TRM acquired in the Earth's magnetic field during atmospheric passage.

Collinson and Morden (1994) also found evidence for extraterrestrial magnetism in HED meteorites, which they tentatively suggested was the product of a dynamo-generated field. However, with the exception of the eucrite Pecora Escarpment 82502, all the meteorites samples in their study did not exhibit unidirectional magnetization or stable AF demagnetization behavior. On the other hand, Pecora Escarpment 82502, which showed the most promising magnetic properties, was recently found to have an oxygen isotopic composition anomalous with respect to most other HEDs, indicating that it is likely not from Vesta (Li et al. 2011).

In the present work, we aim to resolve the ambiguities of previous studies by performing a detailed study of a single meteorite with exceptionally high magnetic recording fidelity, ALHA81001. Compared to that of magnetometers used in most previous studies the moment sensitivity of our system is better by a factor of >10. We conducted AF demagnetization up to ~3 times the maximum field level used in previous studies, allowing us to identify and characterize high-coercivity components of magnetization. We also obtained the first radiometric ages for ALHA81001, which allow us to constrain when and how its NRM was acquired. Finally, we performed detailed petrographic and geochemical analyses that allow us to further constrain its thermal history and mode of magnetization.

6.2. Description of samples

Origin of sample. ALHA81001 was found in the Allan Hills of Antarctica as a part of the US Antarctic Search for Meteorites (ANSMET) Program in 1981. Its original mass was 52.9 g. The meteorite is classified as weathering stage Ae, indicating "minor" rustiness with the presence of surface evaporates (Gooding 1986; Velbel 1988), although weathering stages may be underestimated for eucrites due to their low metal content.

We received two non-mutually oriented samples of ALHA81001,48 from Johnson Space Center (JSC) with masses of 748.2 and 221.9 mg in April, 2011 in a nonmagnetic shielded container, which was opened in our magnetically shielded room (DC field <150 nT). With the exception of viscous remanent magnetization (VRM) acquisition experiments described below, all samples were subsequently kept in the MIT Paleomagnetism Laboratory magnetically shielded, class ~10,000 clean laboratory until the demagnetization of the NRM.

We subsampled the two parent pieces of ALHA81001 using a diamond wire saw with a 220 μm diameter diamond impregnated wire. Measurements of subsamples before and after cutting show that the cutting process did not affect the NRM of the meteorite material by more than 5% of the magnetic moment. We obtained nine mutually oriented subsamples from the larger piece of ALHA81001 and four from the smaller piece. Subsamples from the larger piece are denoted by A1 - A6 and B1 - B3 while those from the smaller piece are denoted by C1 - C4. To subsample meteorite material near the fusion crust, we cut 4 slices of thickness 0.4-1.0 mm, each parallel to the plane of the fusion crust.

The main-HED group oxygen isotopic composition of ALHA81001 suggests that it originated on Vesta (Scott et al. 2009). As a eucrite, ALHA81001 has a basaltic composition and likely samples the asteroid's upper crust. Our petrographic observations show that ~99 vol. % of ALHA81001 has a fine-grained texture. A previous paleomagnetic study found that ALHA81001 has one of the most stable NRM records observed for any main-oxygen isotope group HED (Cisowski 1991). This is likely due to its fine grain size, which has led to the formation of unusually high coercivity ferromagnetic crystals [kamacite and iron sulfide]. In particular, the width of plagioclase

phenocrysts in the groundmass ALHA81001 indicates that the primary crystallization of the meteorite above 1150°C took place over the course of ~1 hour (Walker et al. 1978). However, the presence of ~0.4 μm-wide augite exsolution lamellae in host pigeonite grains suggests that the meteorite was reheated to between 1100°C and 800°C, possibly due to burial in a hot ejecta blanket, and then cooled slowly over several hundred years (Grove 1982). Because these temperatures are above the Curie point of FeNi minerals, any remanent magnetization in ALHA81001 must have been acquired during or subsequent to this slow-cooling episode. Furthermore, we observed no undulatory extinction in plagioclase phenocrysts in the groundmass, indicating that the meteorite escaped impact shock pressures above 5 GPa following this slow-cooling (Bischoff & Stoffler 1992).

Thermal history of ALHA81001. To infer the timing of NRM acquisition in ALHA81001, we conducted $^{40}Ar/^{39}Ar$ and $^{38}Ar/^{37}Ar$ thermochronometry on three ~1 mg whole-rock aliquots (a, b, and c) of ALHA81001 subsample ,48. The experimental methods involved neutron irradiation for 50 hours in the Oregon State University TRIGA reactor in the Cadmium-Lined In-Core Irradiation Tube (CLICIT) facility, followed by sequential degassing experiments under high vacuum and mass spectrometry under static vacuum conditions at the Noble Gas Thermochronometry Lab at Berkeley Geochronology Center [see Shea et al. (2012) for complete analytical details]. Temperatures were controlled and measured to within ± 10°C at each extraction. Apparent $^{40}Ar/^{39}Ar$ ages were calculated relative to the Hb3gr fluence monitor (1081 million years (My) old) using decay constants and standard calibration (Renne et al. 2011; Renne et al. 2010) and isotope abundances of Steiger & Jager (1977). Cosmic ray exposure ages were calculated from the ratio of cosmogenic ^{38}Ar ($^{38}Ar_{cos}$) to reactor-produced ^{37}Ar ($^{37}Ar_{Ca}$) (Shea et al. 2012; Cassata et al. 2010; Levine et al. 2007).

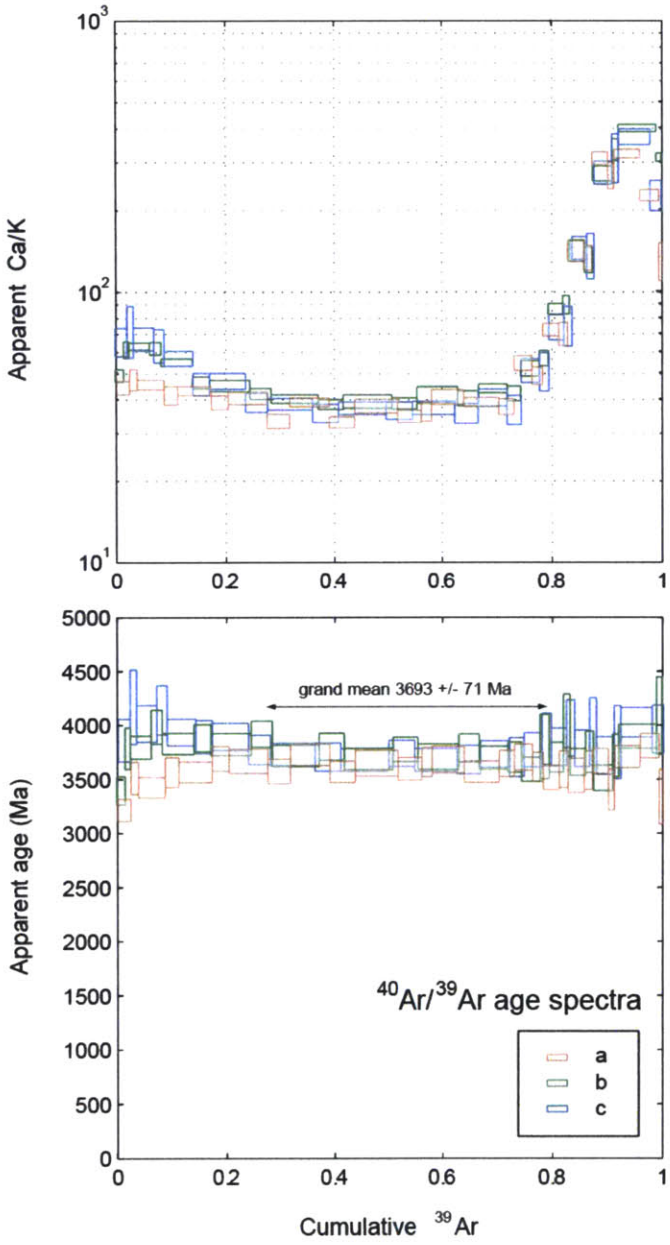

Figure 6.1. $^{40}Ar/^{39}Ar$ chronometry of ALHA81001. Apparent Ca/K (**A**) and $^{40}Ar/^{39}Ar$ age (**B**) spectra for three aliquots (a, b and c) of whole-rock sample ALHA81001. Each spectrum is plotted against the cumulative release fraction of ^{39}Ar. Dimensions of boxes indicate ± 2 SD (vertical) and the fraction of ^{39}Ar released (horizontal). Ca/K ratios were calculated from the $^{37}Ar_{Ca}/^{39}Ar_K$ ratio assuming the relative production ratio for Ca to K is 1:1.96. A mean plateau age of 3693 ± 71 Ma (1 SD) is shown, calculated from sub-selected steps for each analysis between 622˚C and 931˚C as indicated by the arrow.

The $^{40}Ar/^{39}Ar$ age spectra and apparent Ca/K spectra of all three aliquots are in good agreement with one another (Fig. 6.1). Uniform Ca/K ratios observed in the initial 19 heating steps indicate that the first 80% of the gas, corresponding to extraction temperatures of <933°C, was dominantly extracted from a single mineral with uniform composition, whereas the final 20% was derived from a different phase with much higher Ca/K ratio. We interpret this transition in Ca/K ratio as a threshold beyond which the Ar was extracted from the more retentive phase. Since we ultimately seek an upper bound on permissible thermal conditions of ALHA81001, in our subsequent analysis we focus on the least retentive portion of the sample as observed in the initial 19 steps. The mean plateau $^{40}Ar/^{39}Ar$ age of the three aliquots, calculated from subsets of the initial 19 steps, indicates that ALHA81001 experienced a major, probably complete Ar degassing event at 3693 ± 71 million years ago (Ma).

The higher measured $^{40}Ar/^{39}Ar$ ratios for the lowest temperature releases from aliquots b and c (Fig. 6.1) are likely due to ejection of ^{39}Ar during sample irradiation (i.e., recoil loss). This is consistent with the small, ~1 μm characteristic grain size of plagioclase, which is likely the primary ^{40}K-bearing phase in ALHA81001 (Mayne et al. 2009). Recoil loss of ^{39}Ar from such small grains during the irradiation interval can result in over-estimation of the age by several percent (Jourdan et al. 2007).

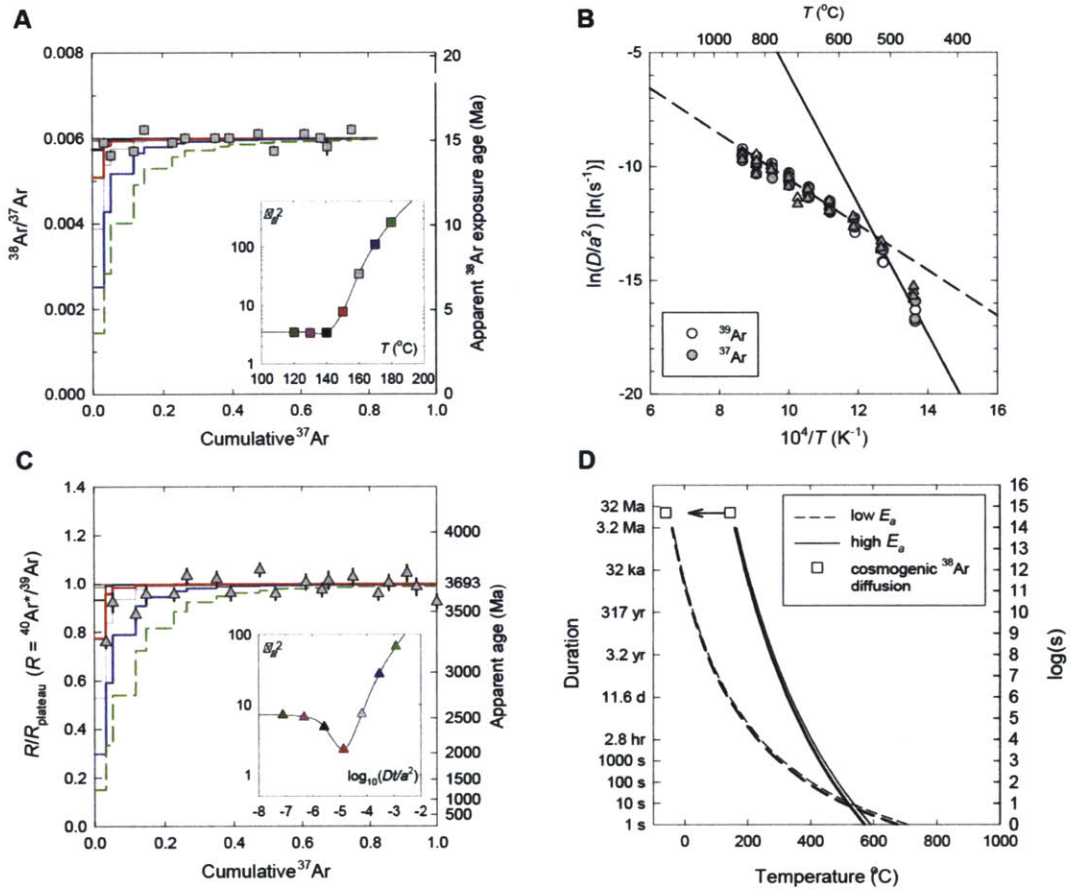

Figure 6.2. ^{40}Ar and ^{38}Ar thermochronometry of ALHA81001. (**A**) Cosmogenic ^{38}Ar. Squares are observed ^{38}Ar/^{37}Ar ratios ± 1 standard deviation (SD) versus the release fraction of ^{37}Ar. Colored steps are synthetic release spectra calculated for production and diffusion of cosmogenic ^{38}Ar over the apparent exposure duration of 15 My, assuming the Ar diffusion kinetics with maximum activation energy (E_a) in (B) (solid line) and isothermal temperatures ranging from <120 to 180°C. Inset shows reduced chi-squared (χ^2) fit statistics of each model compared to filled points, identifying the best-fit temperatures to be ≤140°C. (**B**) Diffusivity as a function of temperature calculated (Fechtig & Kalbitzer 1966) from ^{37}Ar and ^{39}Ar released during the first 19 heating steps of two degassing experiments; points are diffusion coefficients (D) divided by the square of the effective domain radius (a). Solid line quantifies kinetics with the apparent E_a determined from regression to the initial 4 extractions of each experiment; dashed line gives the apparent E_a determined from the subsequent 16 extractions. The difference in these values of E_a may be due to a change in a or non-uniform spatial distribution. We take the values of E_a for the first 4 extractions and the subsequent extractions as upper and lower bounds on the true value. (**C**) Production and diffusion of radiogenic Ar (^{40}Ar*). Triangles are measured ^{40}Ar*/^{39}Ar ratios (R) normalized to the mean ratio of the apparent plateau ($R_{plateau}$) versus the cumulative ^{37}Ar release fractions. Colored steps are model release spectra for heating conditions, as in (A), normalized to a mean plateau age of 3.693 ± 0.071 Ga (1 SD); inset identifies $\log_{10}(Dt/a^2)$ = -5 as the best-fit solution. (**D**) Duration and temperature constraints on possible thermal excursions experienced by ALHA81001. Solid curves are upper bounds on permissible thermal events at 15 million years ago (Ma) (bold curve) and at 1.0 Ga (thin curve) that would best predict the observed ^{40}Ar*/^{39}Ar spectrum shown in (C) using the maximum apparent E_a in (B); dashed curves are calculated from models using the minimum apparent E_a in (B) for thermal events at 15 Ma (bold curve) and 1.0 Ga (thin curve). The squares are upper bounds from (A) for

maximum and minimum values of E_a. Solar heating since ~15 Ma to mean effective temperatures between −50 and 140°C provides an internally consistent prediction of the entire Ar dataset.

From the fractional release of ^{39}Ar and ^{37}Ar (i.e., the nuclides produced via neutron irradiation that are most likely to be spatially uniform) observed in the first 19 steps of all three analyses, we calculated values of the apparent Ar diffusion coefficient (D) normalized to the effective radius of a spherical diffusion domain (a) at each step according to (Fechtig & Kalbitzer 1966). When plotted against extraction temperatures, calculated values of D/a^2 for both isotopes from all three aliquots are in excellent agreement with one another in an Arrhenius plot (Fig. 6.2B). This agreement indicates systematic Ar diffusion in each. However, the experiments do not reveal a single linear Arrhenius relationship, but rather two approximately linear relationships separated by a break in slope at ~550°C. Possible explanations for this pattern include a range in diffusion domain sizes (i.e., a) within each aliquot, or a slightly non-uniform spatial distribution of ^{37}Ar and ^{39}Ar due to diffusion during production in the nuclear reactor. Although we cannot *a priori* distinguish between these scenarios, we take linear regressions to data collected below and above ~550°C to be upper and lower bounds on the activation energy, hence bounds on the effective kinetics of Ar diffusion from plagioclase.

Under the assumption that the kinetics of Ar diffusion observed at laboratory conditions also apply to natural conditions, we test various thermal histories through geologic time that would result in the apparent spatial distribution of radiogenic ^{40}Ar ($^{40}Ar^*$) or cosmogenic ^{38}Ar ($^{38}Ar_{cos}$), as constrained by observed $^{40}Ar^*/^{39}Ar$ and $^{38}Ar_{cos}/^{37}Ar$ stepwise release spectra (e.g., Fig. 6.2). We describe below a number of thermal modeling strategies to constrain permissible thermal conditions of sample ALHA81001 from the observed $^{40}Ar/^{39}Ar$ datasets.

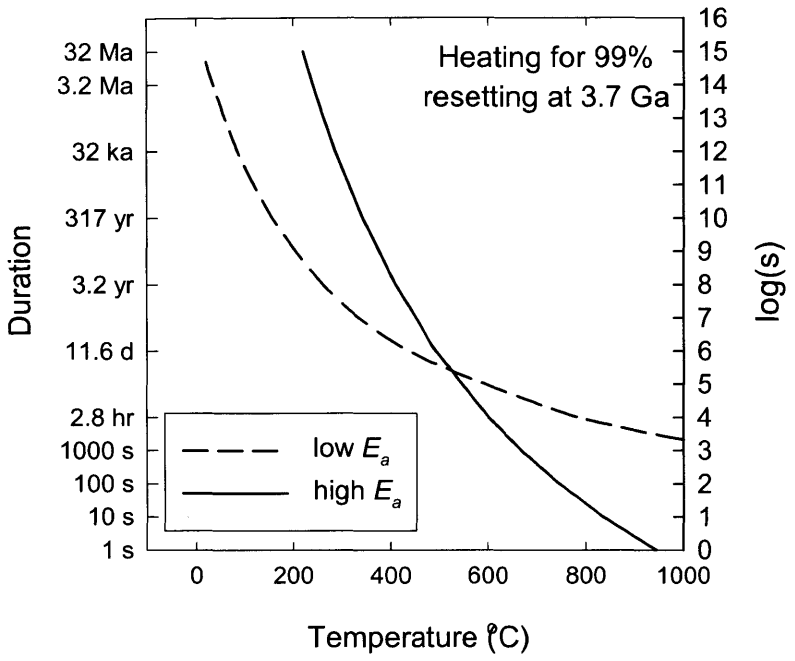

Figure 6.3. Thermal constraints on ALHA81001 at ~3700 Ma. Assuming that the "high E_a" and "low E_a" models shown in Fig. 6.2B provide bounds on the kinetics of ^{40}Ar diffusion in ALHA81001 at 3.7 Ga, the solid and dashed curves, respectively, are the reheating conditions that would be required to diffuse 99% of the radiogenic ^{40}Ar accumulated between 4500 Ma and 3700 Ma.

Although the simplest explanation of the datasets is that ALHA81001 experienced complete degassing of ^{40}Ar at 3693 Ma, ALHA81001 may have been incompletely degassed at 3693 Ma and the elevated ^{40}Ar/^{39}Ar ratios from aliquots b and c at low temperature steps are due to retention of radiogenic ^{40}Ar produced prior to that age. Incomplete degassing at 3693 Ma may suggest a lower temperature thermal event and thereby complicate determination of the age of the NRM (Fig. 6.3). At high temperatures above ~1200°C, the diffusivity of Ar in pyroxene increases dramatically. Therefore, extremely short duration, high temperature thermal excursions can theoretically lead to more complete degassing of pyroxenes compared to plagioclase and silica glass, even if the latter phases degas at lower temperatures during progressive laboratory heating (Cassata et al. 2010). However, the lower Ca/K ratio measured for the initial 80% of the ^{39}Ar extracted at lowest temperature releases suggest that plagioclase, instead of pyroxene, is the dominant ^{40}K-bearing phase with the lowest retentivity. Therefore, the

higher $^{40}Ar/^{39}Ar$ ratios for aliquots b and c are more likely due to recoil and the 3693 Ma degassing event was likely complete.

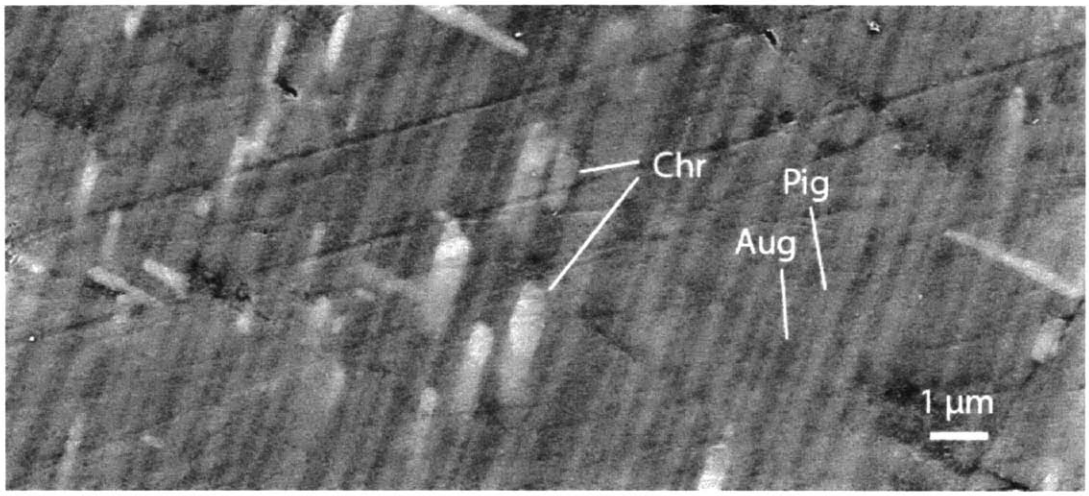

Figure 6.4. Electron microscopy image showing augite-pigeonite (Aug-Pig) exsolution lamellae and associated chromite (Chr) grains in interior subsample A4. Image obtained with in-lens detector, which responds to both backscattered and secondary electrons, on a Zeiss NVision40 SEM.

The co-presence of ~1 µm wide plagioclase grains and pigeonite-augite exsolution lamellae suggests that although ALHA81001 underwent rapid primary crystallization, it was later reheated to >800°C and subsequently cooled slowly (Fig. 6.4). The latter reheating event would have been sufficient to fully degas ^{40}Ar in the meteorite (Fig. 6.3). Because magmatism on Vesta likely lasted for no longer than ~100 My (Yamaguchi et al. 1996), the degassing of ALHA81001 at 3693 Ma must be impact-induced. An impact melt origin for ALHA81001 is also supported by our finding of a minor fraction (~1 vol. %) of relict, mosaicized pyroxene grains indicating that the precursor material for ALHA81001 underwent shock above 30 GPa (Fig. 6.5) [although after crystallization ALHA81001 was not shocked to >5 GPa (Bischoff & Stoffler 1992) as indicated by the low shock stage (S0-S1) groundmass]. The two thermal episodes, rapid quenching followed by slow cooling, may have occurred during the same impact event which could have involved impact-melting followed by crystallization and then burial in a hot ejecta blanket.

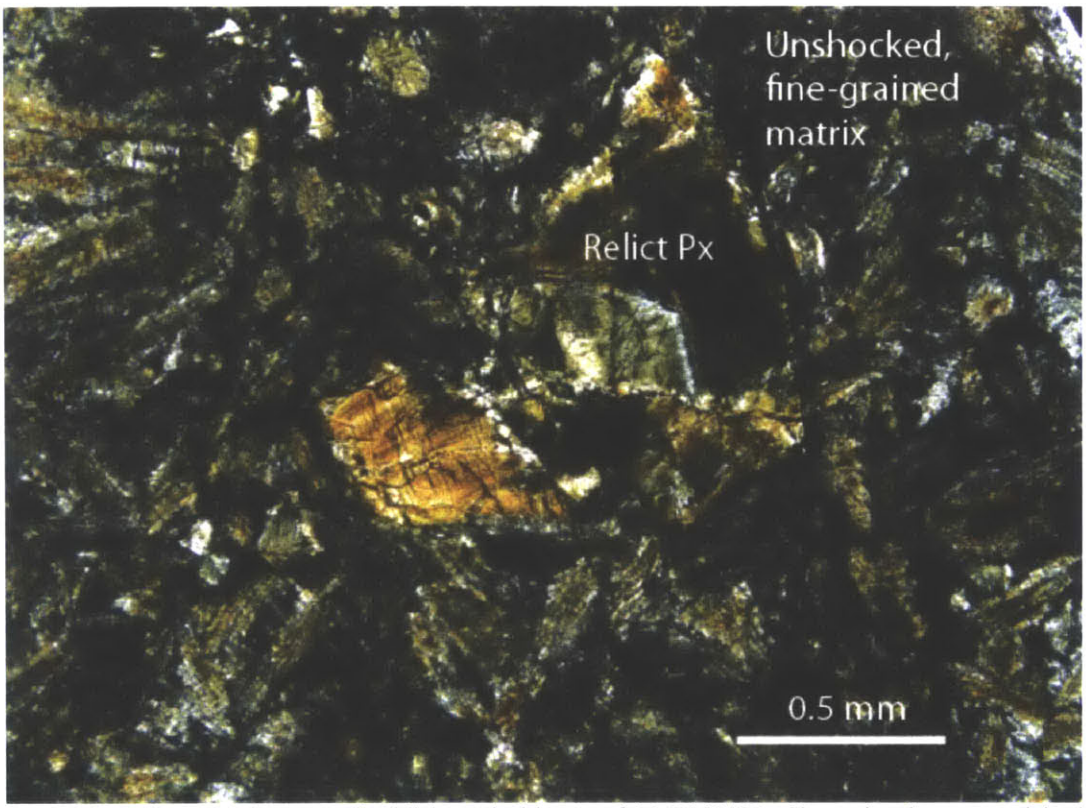

Figure 6.5. Crossed polar transmitted light optical image of ALHA81001. Shown is a large, mosaicized relict pyroxene clast that has experienced shock to >30 GPa surrounded by unshocked matrix. Such relict pyroxene clasts make up ~1% of ALHA81001 by volume.

Alternatively, ALHA81001 may have crystallized as an impact melt before 3693 Ma and the $^{40}Ar/^{39}Ar$ age represents slow cooling after a second impact-induced thermal event, either from direct shock heating or from conductive heating in a hot ejecta blanket. However, the high maximum coercivity of the HC component (>290 mT) suggests that it is a total TRM (see Section 6.3), which requires heating to above the 780˚C Curie point of kamacite. If these temperatures were directly produced by a shock, this would require pressures in excess of 30 GPa (Stöffler et al. 1991). The unshocked groundmass in ALHA81001 (see above) therefore excludes the direct shock heating scenario. On the other hand, burial at 3693 Ma by a hot ejecta blanket may have led to high-temperature reheating of ALHA81001 without high-pressure shock. However, assuming a flat contact surface, an ejecta blanket can only heat the underlying material to the mean temperature of the ejecta sheet and the original surface. Assuming an original surface temperature of 180 K, thermal diffusion calculations show that the ejecta blanket must

have been at a temperature of >1650°C to heat the surface to 780°C (Crank 1975). Formation of a large deposit of such high temperature ejecta is unlikely given the slow impact velocities typical on Vesta (Pierazzo et al. 1997). Most likely, ALHA81001 is an impact melt that was quenched, buried, and slowly cooled in a single large impact event at 3693 Ma. The several hundred years cooling timescale inferred from the width of pigeonite-augite exsolution lamellae therefore corresponds to the 3693 Ma age and to the acquisition of TRM at that time.

Subsequent thermal processing of ALHA81001 was insufficient to affect significantly the remanent magnetization of the meteorite. Using the bounds on Ar diffusion kinetics described above, we modeled the expected ^{40}Ar loss upon heating at 1000 Ma, the probable age of ejection from Vesta (Schenk, Marchi, et al. 2012), and 15 Ma, the measured minimum cosmic ray exposure (CRE) time for ALHA81001 (see Fig. 6.2A). The true duration of the meteorite's residence on a small meteoroid may have been longer if it was buried at sufficient depth to attenuate the effects of cosmic ray bombardment. Assuming that the ALHA81001 meteoroid was a rapidly rotating blackbody, residence for 15 My at a solar orbital distance between 1 and 2.36 AU (equilibrium temperatures between -5 and -92°C) is sufficient to explain the full extent of ^{40}Ar loss, assuming that the true Ar diffusivity is closer to the lower end member of our derived range of permissible values. Such temperatures are too low to cause full thermal remagnetization. Therefore, the HC magnetization, whose demagnetization characteristics suggest that it is a total TRM (see Section 6.6), was most likely acquired during the 3693 Ma ^{40}Ar resetting event.

Ferromagnetic mineralogy and grain size. We utilized low and high temperature (5-1073 K) thermomagnetic analyses, superconducting quantum interference device (SQUID) microscopy, vibrating sample magnetometer (VSM), IRM acquisition and demagnetization, and electron microprobe analyses to constrain the magnetic mineralogy of ALHA81001. Low temperature thermomagnetic data were acquired on a Quantum Design MPMS-XL system with maximum field of 7 T and minimum temperature of 5 K in the MIT Center for Materials Science and Engineering. Using the SQUID Microscope in the MIT Paleomagnetism Laboratory (Weiss et al. 2007), we mapped the magnetic

field above a 8 mm × 9 mm × 30 μm thin section of ALHA81001 that was given a saturation IRM. The magnetic field was measured at a vertical distance of 195 μm above the thin section surface and was downward continued to a height of 145 μm (Lima et al. 2006), resulting in horizontal spatial resolution of ~150 μm. Electron microprobe analyses were performed on a JEOL-JXA-8200 Superprobe in the MIT Experimental Petrology Laboratory and a Zeiss NVision40 scanning electron microscope (SEM) in the Harvard Center for Nanoscale Systems (CNS) using secondary electron, backscattered electron, in-lens electron, election dispersive spectroscopy (EDS), and wavelength dispersive spectroscopy (WDS) detectors. The maximum spatial resolution achieved with secondary electron imaging was ~10 nm. Although the strong paramagnetic response of ALHA81001 prevented a high-fidelity measurement of its ferromagnetic hysteresis, we estimated its hysteresis parameters using a Princeton Micromag VSM at CEREGE. IRM acquisition and demagnetization experiments were conducted with the 2G Enterprises Superconducting Rock Magnetometer (SRM) 755 in the MIT Paleomagnetism Laboratory.

Analysis of the ferromagnetic hysteresis of ALHA81001 yielded an average ratio of saturation remanence to saturation magnetization (M_{rs}/M_s) of 0.081 and an average ratio of remanent coercive force to coercive force (H_{rc}/H_c) of 2.71. Assuming shape-anisotropy-dominated grains, the calculated hysteresis parameters indicate predominantly single-domain/pseudo-single-domain behavior with a possible superparamagnetic component (Dunlop 2002). Given these hysteresis properties, ALHA81001 exhibits distinctly more single-domain behavior than other HED meteorites, consistent with its uniquely fine-grained, quenched texture.

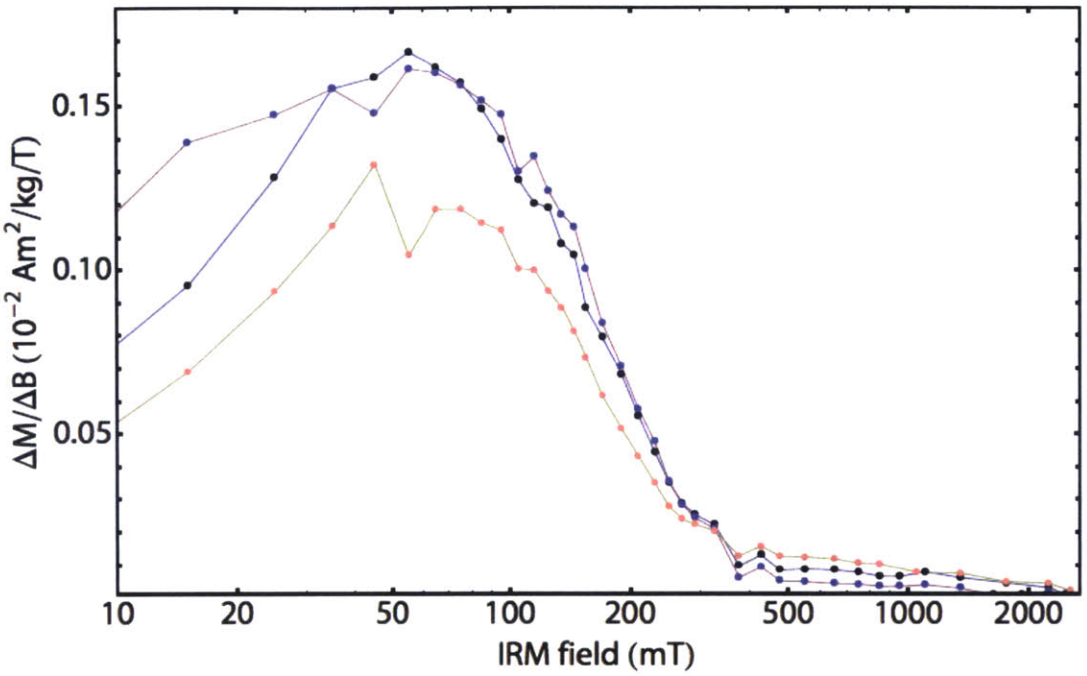

Figure 6.6. Derivative of remanence gained during acquisition of a near-saturation IRM. Experiment performed on three interior subsamples A4 (black), A6 (pink), and C4 (blue) in fields up to 2.7 T. Note the high degree of homogeneity among the subsamples.

Stepwise acquisition of a near-saturation IRM up to 2.7 T revealed two probable magnetic phases (Fig. 6.6). The first is fully saturated by ~0.4 T and the second is not fully saturated by 2.7 T in two of three subsamples. We performed the Lowrie test [thermal demagnetization of IRMs of different strengths applied perpendicularly (Lowrie 1990)] on one subsample, which showed two probable Curie points at 320-350°C and >700°C (Fig. 6.7). The phase with the lower Curie temperature is carried by high-coercivity grains blocked above 2.7 T. We interpret the low coercivity, high Curie temperature phase to be an FeNi mineral and the high coercivity, low Curie temperature phase to be an iron sulfide phase (see below).

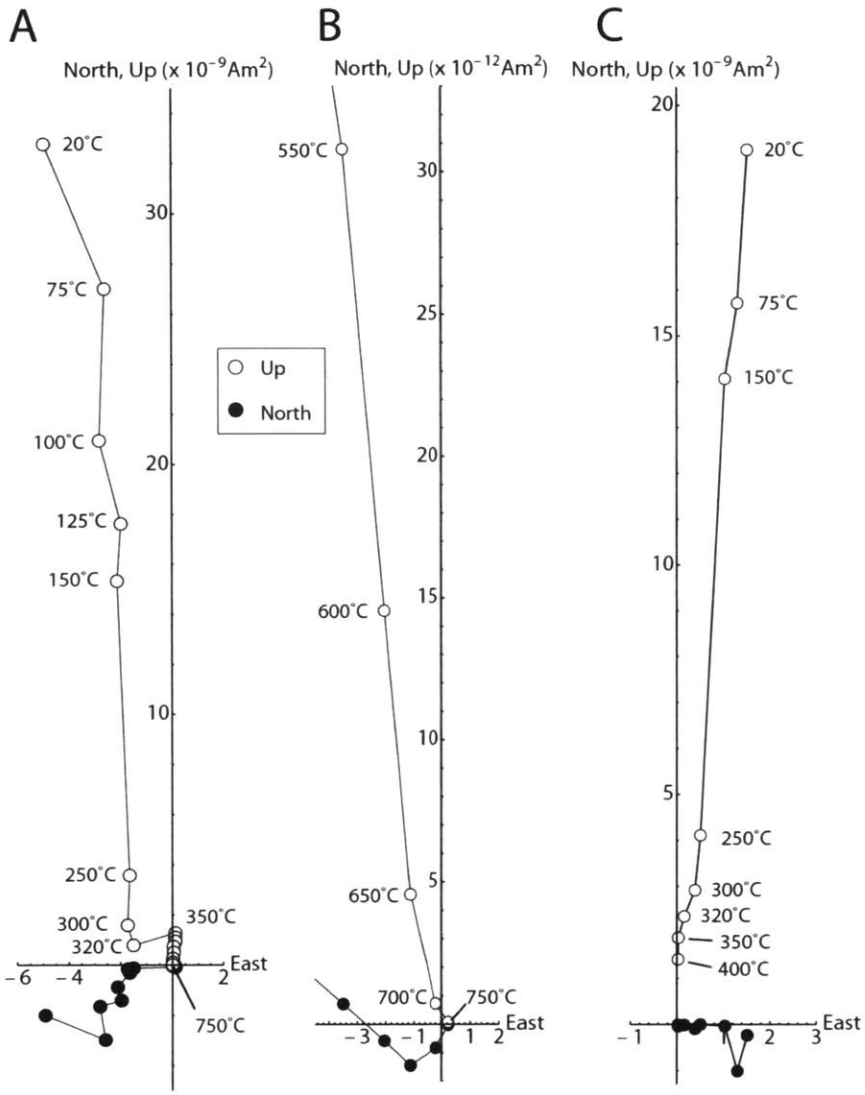

Figure 6.7. Thermal demagnetization of saturation IRM. **(A)** Orthographic projection for full thermal demagnetization sequence of a 7 T saturation IRM acquired in the West direction followed by a 2.7 T IRM acquired in the Up direction for interior subsample A6. Note the removal of westward (2.7 - 7 T) magnetization between 320 and 350°C. **(B)** Close up orthographic projection of the final steps in the thermal demagnetization of a 2.7 T IRM acquired in the Up direction for interior subsample A4. (**C**) Orthographic projection for thermal demagnetization of a 2.5 T saturation IRM acquired in the East direction followed by a 1.05 T IRM acquired in the Up direction for subsample M3 from the Millbillillie eucrite, which is an observed fall. As in the case of Panel A, note decay of high-coercity magnetization between 320°C and 350°C.

We conducted electron microscopy analyses in an effort to characterize the ferromagnetic mineralogy of ALHA81001. Characteristic x-rays analyzed using EDS

and WDS detectors (resolution ~1 μm) revealed that the meteorite contains 1 to 3 μm diameter grains of ilmenite and iron sulfide and 100 nm to 2 μm diameter grains of Al-bearing chromite (Fig. 6.8). Our quantitative WDS analyses on 11 iron sulfide grains (up to 3 μm diameter) showed that all measured grains have composition within error of that of stoichiometric troilite (FeS), which is nominally antiferromagnetic. However, stoichiometric troilite may still be able to carry defect remanence and may be responsible for the observed Curie point at 320-350°C (Pearce et al. 2006; Strangway et al. 1967). At the same time, due to the small sizes of some iron sulfide grains, the uncertainty in composition for several analyses is up to several atomic percent in each element, allowing the possibility of remanence-carrying Fe-deficient sulfide (Vaughan & Craig 1978). Although stoichiometric chromite ($FeCr_2O_4$) has a Curie temperature of ~90 K, iron-rich chromites can have higher Curie temperatures of up to 580°C [for the magnetite end member (Francombe 1957)]. Electron microprobe analysis shows that ALHA81001 contains Al-bearing chromite, which likely has a Curie temperature equal to or less than that of stoichiometric chromite (Gattacceca et al. 2011). Ilmenite in ALHA81001 has a near-stoichiometric composition of $Fe_{1.0}Ti_{0.96}Mn_{0.04}O_3$, which is weakly ferromagnetic below its Curie temperature of ~60 K (Dunlop & Ozdemir 1997a).

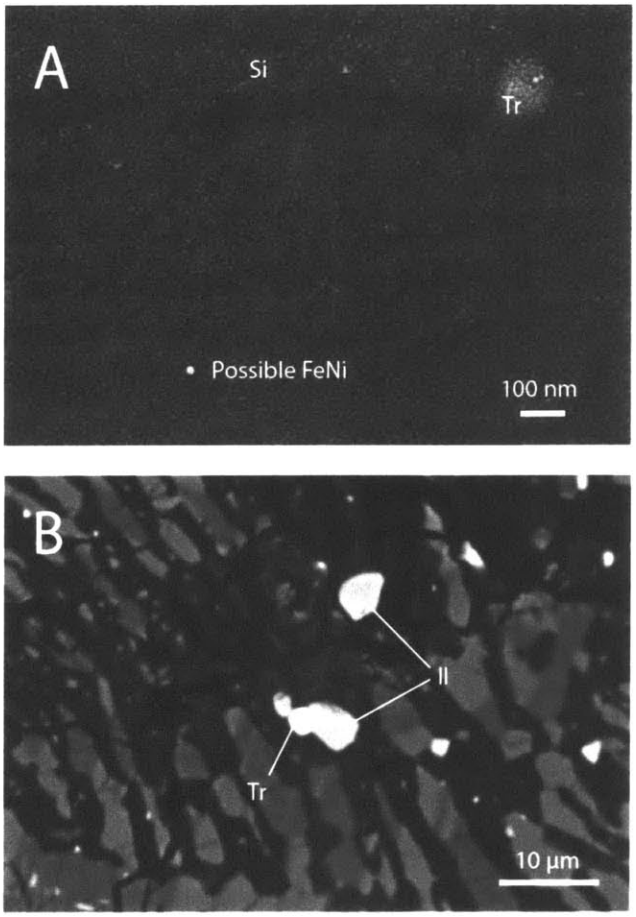

Figure 6.8. High-resolution electron microscopy image of probable ferromagnetic phases. **(A)** Troilite (Tr) and possible FeNi metal particles embedded in a silica-rich phase (Si) in interior subsample A4. Image obtained with in-lens detector on a Zeiss NVision40 SEM. **(B)** Troilite (Tr) and ilmenite (Il) in thin section ALHA81001,48 showing a lack of weathering textures. Backscattered electron microscopy image acquired with JEOL-JXA-8200 microprobe.

These electron microprobe results are consistent with our low temperature magnetic data. Thermal demagnetization of a saturation IRM acquired at 5 K (Fig. S8A) shows a distinct Curie point between 80 and 90 K, which likely reflects a mixture of ilmenite and chromite magnetization. The lack of transitions at ~120 K and 258 K suggest that magnetite (Fe_3O_4) and hematite (Fe_2O_3), which can form due to terrestrial weathering, are not significant contributors to the magnetization of ALHA81001 (Uehara et al. 2012). The lack of a 35 K transition suggests the absence of stoichiometric monoclinic pyrrhotite (Fe_7S_8), although non-stoichiometric composition, small sulfide grain size and the presence of other phases often render the transition inconspicuous.

Although our low resolution (~1 μm) compositional analyses using EDS and WDS identified no phase that can account for the high Curie temperature ferromagnetic phase in ALHA81001, high resolution (<20 nm) secondary electron imaging revealed the presence of a small population of apparently high atomic number objects with diameters <20 nm in the silica-rich portions of the mesostases found between larger pyroxene phenocrysts (Fig. 6.8). The size range of these bright objects is consistent with single-domain FeNi metal. Smaller single-domain and superparamagnetic (<8 nm) FeNi grains may also be present but would be difficult to identify due to the resolution limits of the SEM. The lack of larger, multidomain (>20 nm) high atomic number objects is consistent with the strongly single-domain and superparamagnetic state of the magnetic phase in ALHA81001 as indicated by low temperature demagnetization and viscous remanent magnetization (VRM) acquisition experiments (see below). We therefore interpret these objects as the FeNi grains responsible for carrying high temperature remanence in ALHA81001, although particulate contamination and topography on the surface of the thin section may account for some of the apparent high atomic number objects. In any case, the high Curie temperature (>700°C) of the low coercivity phase strongly suggests the presence of FeNi in ALHA81001.

Assuming that the nanometer-scale, high-atomic-number grains are FeNi metal, they can exist in three different ferromagnetic phases: kamacite (α-FeNi), taenite (γ_2-FeNi), or tetrataenite (γ"-FeNi) (Yang & Williams 1996). While both kamacite and taenite are capable of recording a primary TRM, tetrataenite forms due to Ni diffusion through the taenite lattice during slow annealing below 320°C. During this process, the material develops strong magnetocrystalline anisotropy, which may lead to remagnetization of any pre-existing remanence (Uehara et al. 2011). Although the maximum size of the inferred FeNi grains in ALHA81001 is too small to allow quantitative constraints on composition, we infer that they are most likely kamacite or taenite instead of tetrataenite for three reasons. First, the unidirectionality of NRM in ALHA81001 across 0.9 cm is inconsistent with the observed incoherence of tetrataenite magnetization at the millimeter scale (Uehara et al. 2011). Second, heating of a subsample to 550°C, at which temperature tetrataenite transforms to taenite, did not induce a dramatic transformation from single-

domain to multidomain magnetization as is observed in tetrataenite-bearing samples (Wasilewski 1988).

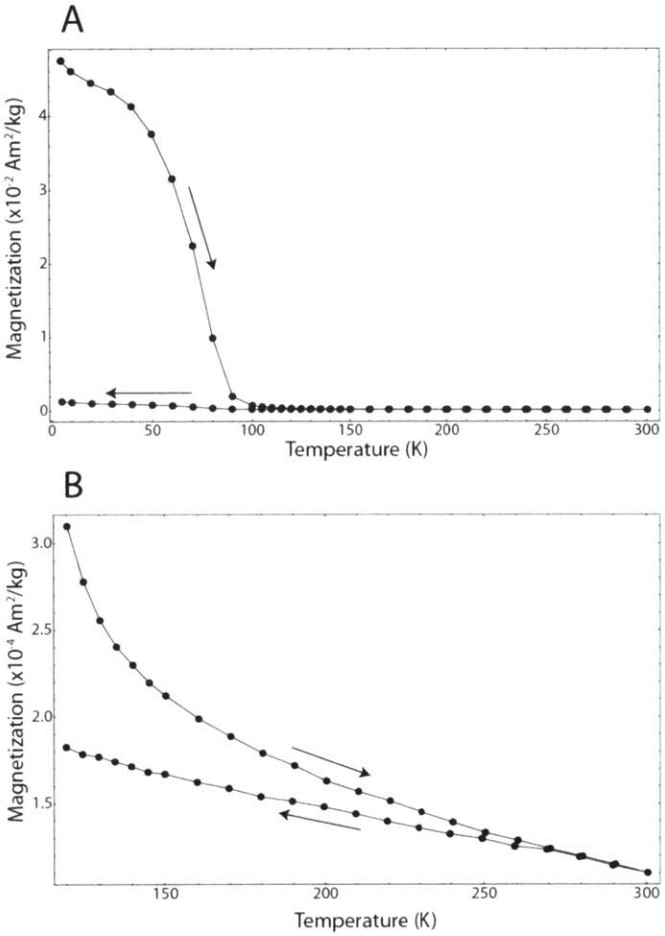

Figure 6.9. Low temperature thermal demagnetization of interior subsample A6. Thermal cycling (from 5 K to 300 K and back to 5 K) of a 5 K saturation IRM (7 T field). The background field during cycling was <0.2 mT. (**A**) All data from 5 to 300 K. A Curie point at ~90 K is clearly observed. (**B**) Data above 120 K to emphasize superparamagnetic grains.

A third argument against the presence of tetrataenite and in favor of kamacite in particular is that previous paleomagnetic studies of eucrites have found kamacite to be the main room temperature ferromagnetic mineral (Cisowski 1991; Collinson & Morden 1994; Nagata 1980), consistent with the reduced oxidation state and low nickel composition of eucrites (Kitts & Lodders 1998; Duke & Silver 1967). FeNi phases with high Ni content such as taenite and tetrataenite have been found in very few unbrecciated eucrites (e.g., NWA 011, EET 92023, and EET 92004), all of which either have

anomalous oxygen isotopic compositions (suggesting that they are from a different parent body than Vesta) or are suspected to be clasts from mesosiderites (Mayne et al. 2009; Yamaguchi et al. 2002).

Due to the small size range for single-domain grains (~10-20 nm) and the high metal content of most extraterrestrial rocks, most kamacite-bearing samples are dominated by multidomain grains. In contrast, the fast cooling rate and low metal content in ALHA81001 have resulted in the apparent absence of multidomain grains and the presence of a population of superparamagnetic grains. Thermal demagnetization of a saturation IRM acquired at 5 K shows that grains blocked between 150 and 300 K carry a magnetization of 5×10^{-5} Am^2kg^{-1}, which is equivalent to ~17% of the saturation IRM at room temperature and indicates the presence of a significant population of superparamagnetic grains (Fig. 6.9). Further evidence for the presence of superparamagnetic grains comes from the high efficiency of VRM acquisition, measured to be ~0.03% of the saturation IRM per decade of time (see Section 6.3). Such a high rate of VRM acquisition is a factor of ~5-15 greater than has been observed for multidomain kamacite-bearing lunar rocks (Gose et al. 1972) but is similar (to within 10%) to the glassy lunar regolith breccia 14313 (Dunlop et al. 1973). Similarly, the ratio of low field susceptibility to saturation magnetization (χ_0/M_s), for which a high value indicates single-domain and superparamagnetic magnetization, is 8.6×10^{-7} T^{-1} for ALHA81001, a high value for kamacite-bearing lunar rocks but nearly identical to that of regolith breccia 14313 (Fuller 1974). This lunar sample has been shown to contain a mixture of mostly single-domain and some superparamagnetic kamacite. Furthermore, its ferromagnetic mineralogy has a similar impact melt origin as that of ALHA81001 (Meyer 2011). These affinities between the magnetic and petrographic properties of ALHA81001 and lunar regolith breccia 14313 suggest that the latter may serve as a close analog to the ferromagnetic mineralogy of ALHA81001. The significant superparamagnetic component of ALHA81001 suggests the presence of fine ferromagnetic grains with low blocking temperatures that may explain the relatively large loss of moment below ~300°C.

The remanence-carrying iron sulfide phase in ALHA81001 may be stoichiometric troilite with defect moment or iron-deficient sulfide in small grains with unconstrained

composition. We argue for a preterresterial origin of these minerals using six lines of evidence. First, troilite is ubiquitously observed in HED meteorites, while primary Fe-deficient sulfide (pyrrhotite) has also been observed in a number of unweathered HED falls (Mostefaoui et al. 2004; Beck et al. 2011). Second, although terrestrial oxidation is known to affect sulfides, the principal products of the process are iron oxides and oxyhydroxides (e.g., maghemite, magnetite, and goethite) instead of ferromagnetic iron sulfides (Bland et al. 2006; Buchwald & Clarke 1989; Uehara et al. 2012). We do not observe these phases in ALHA81001 (see below). Third, textures produced by this weathering process, such as oxide- and clay-filled microfractures and staining of silicates surrounding iron sulfide grains (Gooding 1986; Delaney et al. 1984), are not observed in our optical petrographic or electron microscopy analyses, even at ~20 nm resolution. Fourth, the stoichiometric or near-stoichiometric troilite compositions from our quantitative WDS measurements are inconsistent with terrestrial weathering, which produces sulfides with Fe content as low as $Fe_{0.46}S_{0.54}$ (Lorand et al. 2005). Fifth, the relatively flat rare earth element (REE) abundances of ALHA81001 compared to CI chondrites, particularly the lack of Ce enrichment, suggests the lack of oxidation in the metal and sulfide phases (Warren & Jerde 1987; Shimizu et al. 1983). In contrast, weathered Antarctic eucrites show overall depletion of REEs, large variations in the relative abundances of REEs, and large, usually positive Ce anomalies (Mittlefehldt & Lindstrom 1991).

Sixth, we observe a similar remanence-bearing sulfide phase in Millbillillie, an unweathered eucrite fall. We extracted three small subsamples consisting of pure interior material from a large sample of Millbillillie provided by the Western Australia Museum. The three subsamples, called M1, M2, and M3, have masses of 382.5 mg, 227.9 mg, and 126.8 mg, respectively. Similar to our thermal demagnetization of saturation IRM experiment for ALHA81001, we imparted a 2.5 T remanence to each sample in the East direction followed by a 1.05 T remanence in the Up direction. All kamacite grains, which have maximum coercivities of ~1.05 T (Dunlop et al. 1973), should have been magnetized in the Up direction, while a portion of sulfide grains, which may have higher coercivities (Martín-Hernández et al. 2008), were magnetized in the East direction. During stepwise thermal demagnetization, the high coercivity (>1.05 T) component of

magnetization shows a distinct Curie point at 320°C - 350°C, which is identical to the demagnetization behavior of ALHA81001. Given that Millbillillie is a highly shocked eucrite containing impact melt veins with potentially similar petrography as ALHA81001 (Yamaguchi et al. 1994), the similarity between the magnetic mineralogy of the two eucrites may be expected. Summarizing these six lines of evidence, we observe no signs of terrestrial weathering in ALHA81001 and find that the magnetic mineralogy of ALHA81001 is fully consistent with that of an unweathered eucrite.

Other weathering phases such as maghemite, magnetite, goethite, and hematite are also unlikely to be present in ALHA81001. As mentioned above, there is no SEM or optical petrographic evidence for iron oxides or corrosion textures around sulfides. Furthermore, the high maximum coercivities, even for the low coercivity phase (~0.4 T), are inconsistent with maghemite and magnetite (Lowrie 1990). Furthermore, the low coercivity phase has a Curie temperature of >700°C (Fig. 6.7), which is higher than the inversion or Curie temperatures of maghemite and magnetite. Hematite requires a very high degree of weathering and is very rarely observed in Antarctic meteorites (Bland et al. 2006). Furthermore, both observed Curie temperatures of ALHA81001 are inconsistent with that of hematite. The high coercivity of goethite is consistent with that of the high coercivity phase in ALHA81001. However, a Curie temperature at 120°C is not clearly observed in our data (Fig. 6.7). More importantly, given that the blocking temperature of the HC component is above 150°C, any presence of goethite does not change our interpretation of this magnetization.

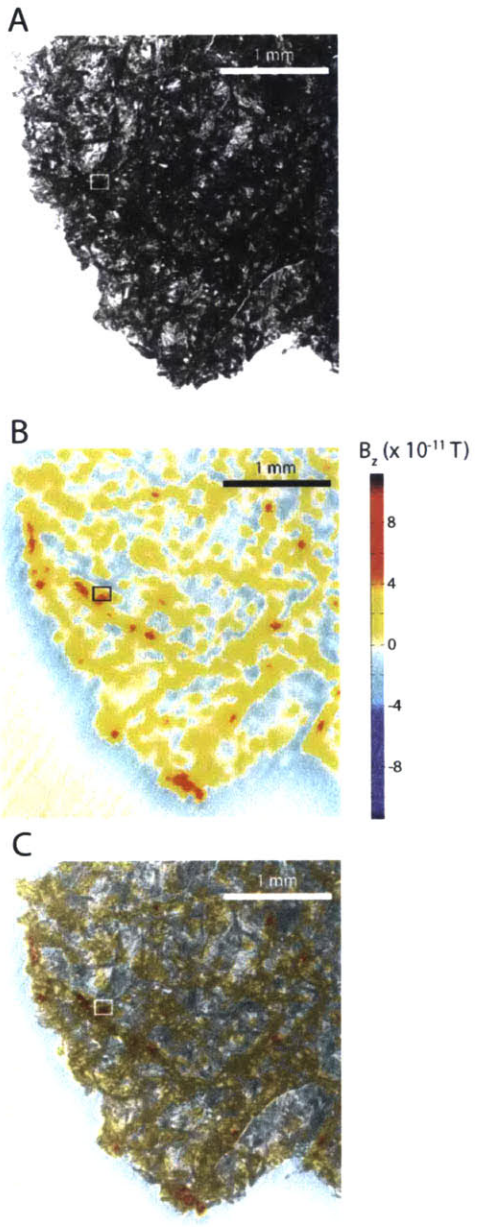

Figure 6.10. SQUID microscope study of 30 μm thin section ALHA81001,39. (**A**) Crossed polars transmitted light photograph. (**B**) SQUID microscope map of the magnitude of the vertical magnetic field (a proxy for magnetization) measured from a height of 195 μm and downward continued to 145 μm above a 30 μm thick thin section. The sample was given a strong field IRM (280 mT) in the positive direction, resulting in the predominance of positive (red) magnetic fields above regions of high local magnetization. (**C**) Overlay of crossed polars transmitted light image (A) and SQUID microscope map (B). Areas of high magnetization overlap strongly with dark, fine-grain assemblages of plagioclase and silica along with accessory ilmenite and troilite. The brighter, coarse-grain regions, which are dominated by pyroxene lathes, exhibit much weaker magnetization. Region inside small box is shown at high magnification in Fig. 6.9.

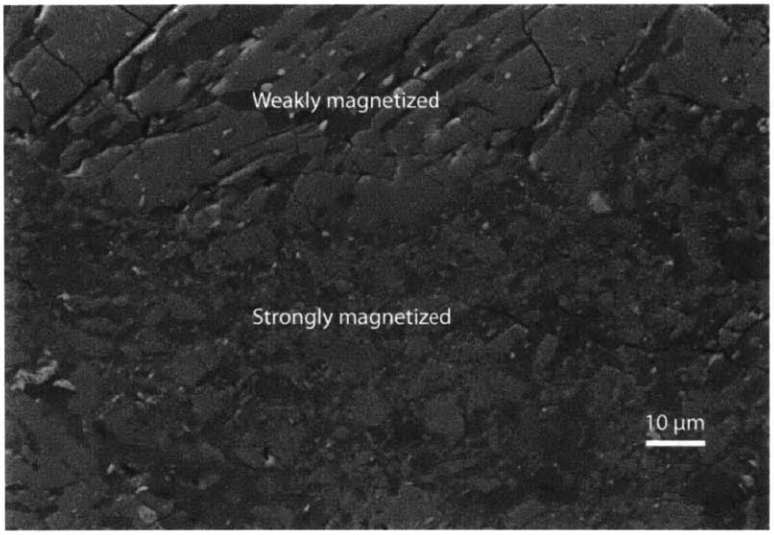

Figure S11. Electron microscopy image of regions of high magnetization as observed by the SQUID microscope as indicated by boxes in Fig. 6.8. Fine-grained regions labeled "Strongly magnetized" are only found in regions of high magnetization in the SQUID microscopy maps. Image obtained with in-lens detector on a Zeiss NVision40 SEM.

High resolution (~150 µm) SQUID microscopy maps of ALHA81001 (Fig. 6.10) show that magnetization due to a strong field IRM in ALHA81001 is associated with the fine-grained mesostasis material found in between larger lathes of mostly pyroxene (Fig. 6.11). The mesostasis consists of finely intergrown (1-10 µm width) plagioclase and silica with accessory troilite and ilmenite. Metal is thought to have been one of the last phases to have crystallized in eucrites (Stolper 1977) and therefore is also expected to be concentrated in the mesostasis of ALHA81001. Sulfide grains larger than ~1 µm in size show no statistically significant preferential distribution within areas of high magnetization, although the finer grain texture of mesostasis regions may contain higher concentrations of smaller sulfide grains. Therefore, the SQUID microscopy maps provide further evidence that one source of magnetization is the nanometer-scale grains of high atomic number material, probably kamacite, found embedded in the silica-rich portions of the mesostases (e.g., Fig. 6.8). Furthermore, because chromite is only spatially associated with the pyroxene phases in ALHA81001, this distribution of magnetization also confirms that chromite in ALHA81001 is not ferromagnetic at room temperature.

6.3. Paleomagnetic measurements

Measurement and demagnetization methodology. Most measurements of magnetization were performed on a 2G Enterprises SRM 755 in the MIT Paleomagnetism Laboratory, which has an intrinsic sensitivity of $\sim 1 \times 10^{-12}$ Am^2. In practice, because subsamples were mounted on 3 mm diameter GE 124 quartz rods or 25 mm diameter GE 124 quartz disks with cyanoacrylate or double-sided tape, the minimum distinguishable sample moment was $\leq 4 \times 10^{-12}$ Am^2. For very weak samples, extra care was taken to reduce the moments of the sample mount to $\leq 2 \times 10^{-12}$ Am^2.

Most subsamples were demagnetized using three-axis AF demagnetization, which has several key advantages over thermal demagnetization for analyzing extraterrestrial samples (Shea et al. 2012). To reduce spurious ARM noise, we made repeat three-axis AF applications (up to 4 times, depending on the field level) and calculated the vector mean for each field level. Moment measurements were made after AF application along each of the three orthogonal axes and then averaged to reduce the effects of gyroremanent magnetization (GRM) following the Zijderveld-Dunlop method (Garrick-Bethell et al. 2009). NRM component directions were estimated using principal component analysis (PCA) (Kirschvink 1980).

We extracted 13 subsamples (a set of 9 and a second set of 4) from two parent samples of ALHA81001. The subsamples within the first and second sets were mutually oriented to within 5° and 10°, respectively, while the two parent pieces were not mutually oriented. Subsamples taken from near the fusion crust produced by atmospheric passage have systematically different NRM directions compared to 7 interior subsamples, whereas two subsamples extracted from between the fusion crust and interior subsamples have intermediate NRM directions (Fig. 6.12). These data are consistent with heating and remagnetization of the meteorite's <2 mm deep exterior during atmospheric passage and suggest that the interior was not strongly contaminated by hand magnets, weathering, or viscous remagnetization since their arrival on Earth.

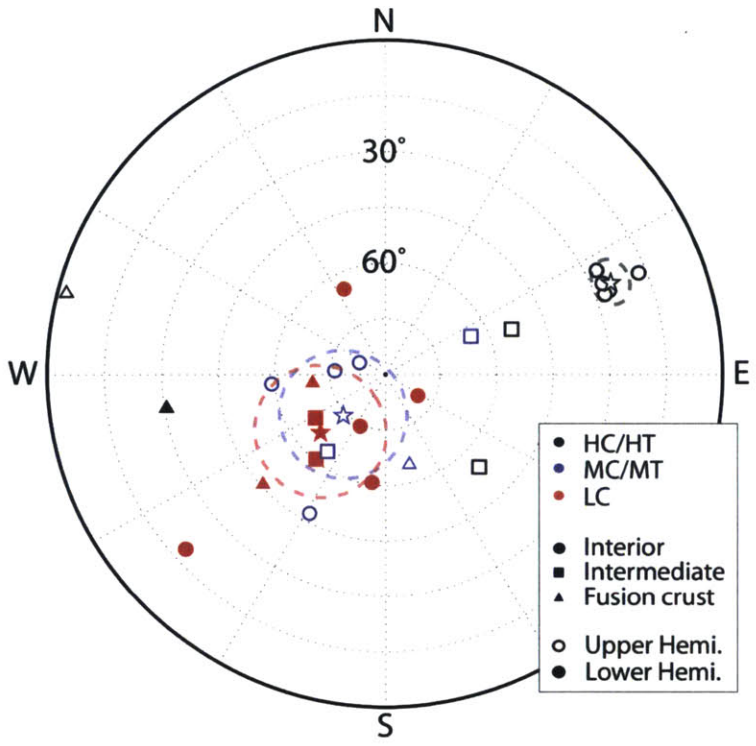

Figure 6.12. NRM directions in eucrite ALHA81001. Equal area stereographic projection showing the three components of magnetization observed in each subsample as inferred from principal component analyses. Black, blue, and red symbols represent HC/HT, MC/MT, and LC directions, respectively. Stars indicate average directions for each component and dashed circles denote the 95% confidence interval for the true direction of magnetization assuming a Fisher distribution. Exterior fusion crusted subsamples, intermediate-depth subsamples (depth from surface between 0.7 and 2.0 mm), and interior subsamples (depth >2 mm) are shown by triangles, squares, and circles, respectively. Open (closed) symbols represent upper (lower) hemisphere.

Summary of paleomagnetic results. All 13 subsamples were progressively alternating field (AF) or thermally demagnetized to characterize their NRM components. We observed three distinct components of magnetization in each subsample (Figs. 6.12, 6.13), with the exception of one fusion crusted subsample, which has only two components. A low coercivity (LC) component is blocked up to a coercivity of 3 mT. Its unidirectionality across all subsamples and low coercivity are consistent with a viscous remanent magnetization (VRM) acquired since the meteorite's recovery from Antarctica in 1981. A medium coercivity (MC) and medium blocking temperature (MT) component, blocked between 3 and 21–57 mT during AF demagnetization and up to 150°C during thermal demagnetization, is unidirectional across all subsamples (except one fusion crusted subsample that does not have an MC component). Its low blocking

temperature and unidirectionality across all subsamples strongly suggest that it is a VRM acquired during the meteorite's residence in Antarctica. The intensities of both the LC and MC/MT components are also consistent with a VRM origin according to our laboratory VRM-acquisition experiments.

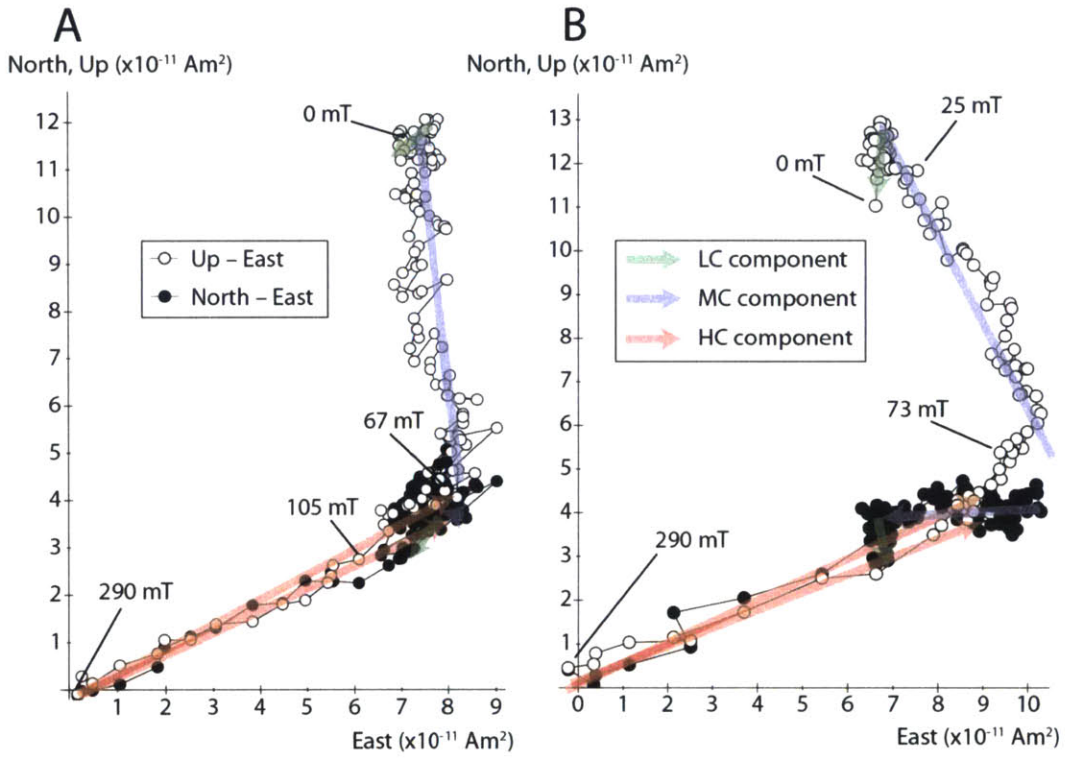

Figure 6.13. Demagnetization of eucrite ALHA81001. Orthographic projections showing the evolution of the NRM during AF demagnetization of two interior subsamples. Open and closed circles indicate the projection of the NRM vector onto the vertical (up-east) and horizontal (north-east) planes, respectively. Red, blue, and green arrows denote HC, MC, and LC components, respectively. Selected AF levels are labeled. (**A**) AF demagnetization of subsample A5. (**B**) AF demagnetization of subsample A6.

Fusion crusted and interior subsamples each carry distinct high coercivity components (which we designate HCf and HC, respectively) that are blocked between 21 to 57 mT and 62 to >290 mT. The HC component is unidirectional throughout the interior subsamples (which are separated by up to 0.9 cm) and the HCf component is unidirectional across the fusion crusted subsamples, but the HC and HCf directions are mutually divergent (Fig. 6.12). Thermal demagnetization identified a high temperature (HT) magnetization in the same direction as the HC component and blocked between

150°C and >275°C, under which most magnetic grains of ALHA81001 are blocked and above which irreversible alteration of the magnetization carriers occurs.

Upon AF demagnetization, the HC magnetization decays linearly to the origin with remarkable stability compared to the NRM observed in all previously measured HED meteorites (Collinson & Morden 1994; Cisowski 1991). Its AF demagnetization spectrum is most similar to that of an anhysteretic remanent magnetization (ARM) and differs from that of a strong field (280 mT) isothermal remanent magnetization (IRM) or pressure remanent magnetization (PRM) acquired in a laboratory field of 750 μT at a pressure of up to 1.8 GPa [an analog for shock remanent magnetization (SRM)]. All of these characteristics suggest that the HC/HT component is a thermoremanent magnetization (TRM) acquired during cooling in a magnetic field (Stephenson & Collinson 1974).

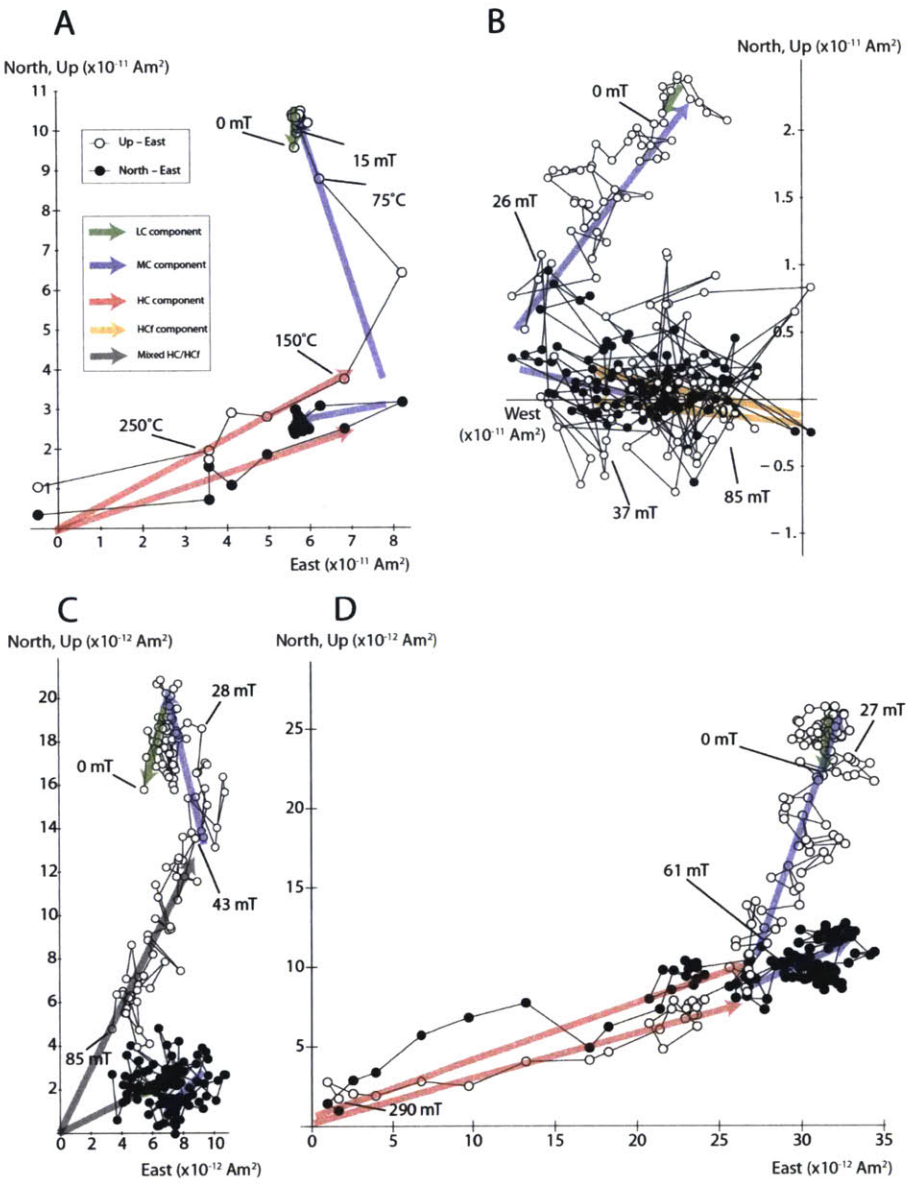

Figure 6.14. NRM demagnetization of subsamples of ALHA81001. Orthographic projections showing the evolution of the NRM during AF demagnetization of NRM for one interior and one fusion crust subsample. Open and closed circles indicate the projection of the magnetization vector onto the vertical (up-east) and horizontal (north-east) planes, respectively. (**A**) AF followed by thermal demagnetization of interior subsample B2. (**B**) AF demagnetization of fusion crusted subsample B1. Magnetic mineralogy of the fusion crust is characterized by greater noise during AF demagnetization. (**C**) AF demagntization of the intermediate subsample A3 (1.6 mm from fusion crusted surface). (**D**) AF demagnetization of the interior subsample A4. Similarly oriented LC and MC components are present in both subsamples (green and blue arrows, respectively. The two subsamples have divergent HC and HCf components (red and orange arrows, respectively). The intermediate sample (C) has a high-coercivity component that is a mixture of the HC and HCf components and is intermediate in direction.

AF and thermal demagnetization. All subsamples that contain fusion crust material (subsamples A1, B1, and C1) carry a distinct high coercivity component of magnetization (HCf) not present in samples from deeper inside the meteorite (Figs. 6.12). Subsamples deeper than 2.0 mm away from the surface of the meteorite (subsamples A4 - A6, B2 - B3, C3 - C4, which we refer to as "interior subsamples") exhibit a unidirectional HC component divergent in direction from the HCf component (Fig. 6.12). This is consistent with remagnetization of only the exterior of the meteorite during atmospheric entry. Further evidence for this is provided by the intermediate material from between 0.7 and 2.0 mm of the surface (subsamples A2 and A3), which have intermediate magnetization directions that are likely a mixture of HCf magnetization acquired during atmospheric entry and preterrestrial HC magnetization (Fig. 6.12). In summary, ALHA81001 passes a fusion crust baked contact test, indicating that the meteorite interior HC magnetization is preterrestrial.

Interior subsamples exhibit a narrow range of NRM intensities between 9.2 and 20.7×10^{-7} Am^2kg^{-1}. The ratio of these NRM intensities to saturation IRM (the REM ratio) is $\sim 4 \times 10^{-3}$, which is consistent with a TRM acquired in weak fields and inconsistent with an IRM due to strong field sources such as hand magnets (Gattacceca & Rochette 2004). This is consistent with the multicomponent IRM and ARM paleointensities (see Section 6.3)

The LC and MC components, which we interpret to be terrestrial VRM (see Section 6.4), are present in and unidirectional across all subsamples from the larger parent sample with the exception of the fusion crusted subsample A1, which lacks a clear MC component (Fig. 6.12). The LC and MC components for the twelve remaining subsamples show moderate scatter with a Fisher precision parameter (Cox 1969) κ = 9.6 and 11.3, respectively (Table 6.1).

Table 6.1: Summary of interior paleomagnetic samples and NRM components

Sample and Component	Mass (mg)	AF/Thermal Range (mT or °C)	Dec., Inc. (°)	MAD (°)	dANG (°)	N_m
A1 – Fusion	17.7					
LC		0 - 3 mT	228.8, 46.0	12.3		30
MC		30 - 49 mT	304.0, -4.0	25.2		120
HCf		49 - >85 mT	254.2, 32.2	45.8	46.8	222
B1 – Fusion	36.8					
LC		0 - 2.5 mT	265.3, 70.3	10.0		24
MC		15 - 33 mT	164.8, -65.4	18.9		116
HCf		33 - >85 mT	281.2, -7.0	74.3	41.4	318
A2 – Intermediate	29.6					
LC		0 - 3 mT	219.5, 60.5	9.6		30
MC		20 - 61 mT	245.4, -57.2	40.4		282
HC/HCf		61 - >85 mT	134.5, -54.4	58.6	45.7	150
A3 – Intermediate	31.4					
LC		0 - 3 mT	238.4, 67.8	4.6		30
MC		25 - 37 mT	217.0, -64.2	22.6		72
HC/HCf		37 - >85 mT	70.2, -53.9	22.6	16.8	294
A4 – Interior	34.9					
LC		0 - 3 mT	206.3, 74.5	7.1		30
MC		21 - 72 mT	66.1, -64.6	16.1		224
HC		72 - >290 mT	67.8, -16.2	8.6	5.6	96
A5 – Interior	90.0					
LC		0 - 5.5 mT	228.9, 18.5	11.0		60
MC		15.5 - 69 mT	294.3, -82.3	12.1		256
HC		69 - >290 mT	63.6, -27.0	6.0	3.0	136
A6 – Interior	102.6					
LC		0 - 3 mT	187.2, 60.7	15.0		92
MC		20.5 - 63 mT	265.2, -59.2	8.4		192
HC		63 - >290 mT	69.3, -26.0	8.0	2.5	136
B2 – Interior	127.1					
LC		0 - 3 mT	334.2, 64.4	8.2		20
MC		150°C	274.1, -76.3	17.2		4
HC		>275°C	71.1, -28.4	10.7	11.1	6
B3 – Interior	130.1					
LC		0 - 2.5 mT	122.8, 79.6	30.6		16
MC		17.5 - 71 mT	208.7, -47.3	29.6		248
HC		71 - 260 mT	67.1, -27.2	33.9	12.3	100

Note: All subsamples in table are mutually oriented to within ~5°. The first column gives the subsample or component name; the second column gives the subsample mass; the third column gives the range of AF fields or temperatures in which the component is blocked; the fourth column gives the orientation of the magnetization vector as determined from least squares fitting; the fifth column gives the maximum angular deviation (MAD) of the component; the sixth column gives the deviation angle (dANG); and the seventh

column gives the number of individual measurements of the magnetic moment associated with each component.

AF demagnetization removes the LC component in all subsamples by 3 mT. The MC component in interior subsamples began to demagnetize at between 16 and 21 mT and was completely removed by between 63 and 72 mT. The MC component in fusion crust and intermediate subsamples is blocked over a narrower range of coercivities between 15 mT and 61 mT (Fig. 6.14, Table 6.1). Most subsamples experienced little to no demagnetization between 3 mT and the beginning of the MC component.

The interior HC component, which likely represents extraterrestrial magnetization, is found in all interior subsamples of both parent samples. This component is found to be highly unidirectional (κ=235) across five mutually oriented subsamples in the larger parent sample separated by up to 0.9 cm.

During AF demagnetization, the HC component is isolated after AF demagnetization to between 63 and 72 mT and, in the case of three subsamples, is not fully demagnetized even by 290 mT, the maximum level achievable with our AF demagnetization system. The magnetization decays to the origin, indicating that it represents a primary remanence. We quantify the degree to which the HC component trends to the origin by comparing the deviation angle (dANG) and the maximum angular deviation (MAD) (Tauxe & Staudigel 2004). The first quantity, dANG, is the angular difference between the non-origin-constrained best-fit vector along the HC component according to PCA and the vector from the origin to the centroid of data points that make up the HC component. The second quantity, MAD, is the angular error to the PCA fit to the HC component. If dANG < MAD, then the agreement between the best-fit trend of the HC component and the closest-fit true origin-crossing trend is less than the error of the best-fit trend, qualitatively suggesting that the measured trend is truly origin-crossing. For all 5 interior subsamples from the larger parent sample, dANG < MAD (mean values are 6.9° and 13.4°, respectively). The HC component of magnetization therefore appears to be true origin trending magnetization, consistent with its being the highest coercivity (i.e., characteristic) component in ALHA81001. At the same time, the remaining intensity of the HC component after demagnetization to 290 mT is ~5%, which is similar to the ~7% moment remaining for a saturation IRM demagnetized to the same level (Fig. 6.15). This

further suggests that the HC component is a primary remanence that is blocked up to the Curie point of ALHA81001.

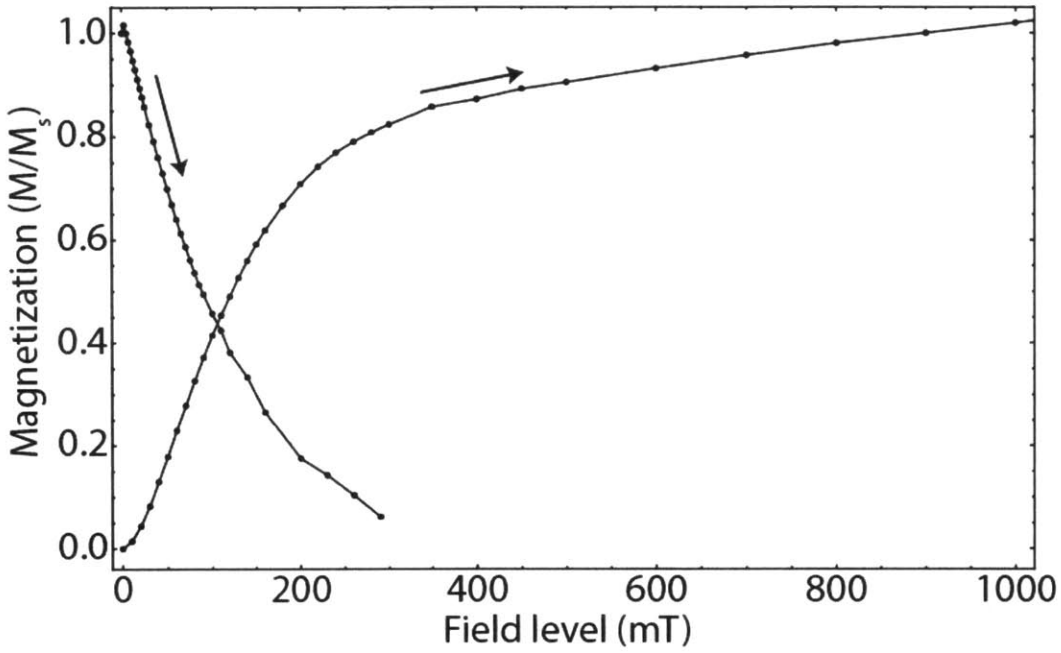

Figure 6.15. Acquisition and demagnetization of IRM on interior subsample C4. Moment is normalized to the saturation remanence (M_s). AF demagnetization was performed on 3 axes to simulate the procedure used for the AF demagnetization of NRM. The demagnetization curve terminates at 290 mT, the maximum level of our AF demagnetization system.

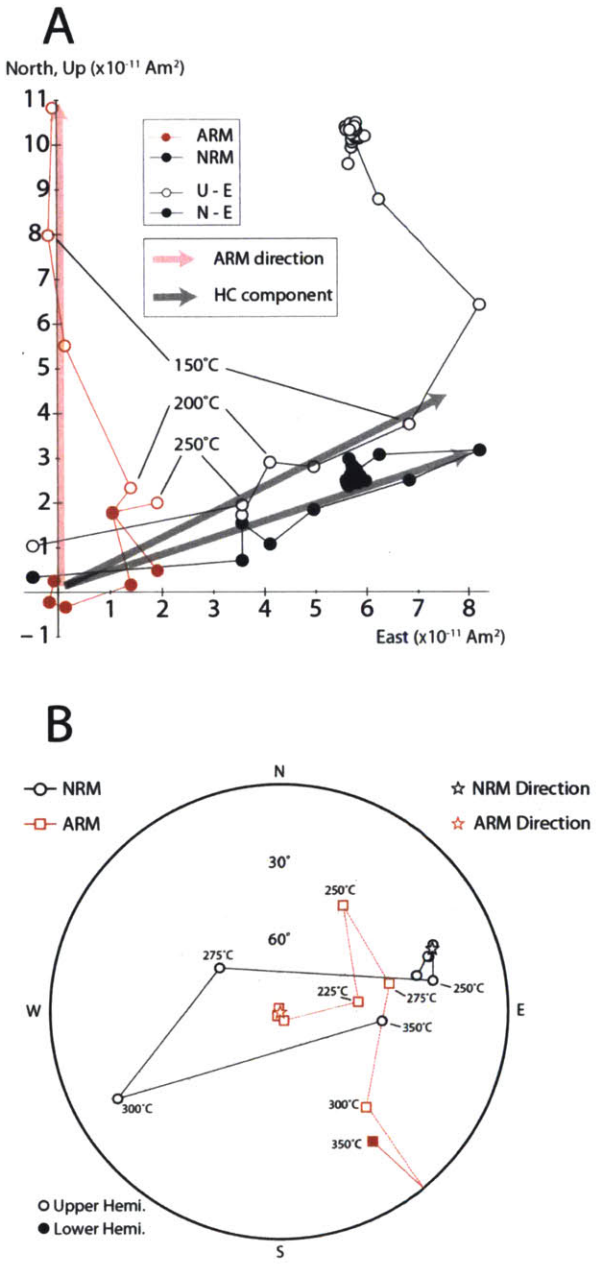

Figure 6.16. Controlled-atmosphere thermal demagnetization of interior NRM (gray) and a laboratory ARM (red) for subsamples B2 and A3, respectively. (**A**) Orthographic projections showing the evolution of the NRM during AF demagnetization of NRM for two interior subsamples. Open and closed circles indicate the projection of the magnetization vector onto the vertical (up-east) and horizontal (north-east) planes, respectively. (**B**) Equal area stereographic projection showing the three components of magnetization observed in each subsample as inferred from PCA. The similar rates of demagnetization and the loss of directional coherence for both subsamples between 225°C and 275°C suggest that alteration is occurring and that the erratic behavior of the NRM above these temperatures does not reflect true recording of a background field when the NRM was acquired.

Because only two interior subsamples were extracted from the smaller parent sample (C3 and C4), there are insufficient statistics for a quantitatively meaningful estimate of the scatter of the directions of magnetization components in these subsamples. Furthermore, the smaller sizes of these subsamples leads to greater uncertainty both in determining their mutual orientation (within ~10°) and in the precise measurement of their magnetization direction. Both interior subsamples show non-unidirectional low coercivity components and moderately unidirectional medium and high coercivity components (angular separations between magnetization in the two subsamples for the LC, MC, and HC components are 107°, 37°, and 23°, respectively). The wide scatter of the LC component (removed below 10 mT during AF demagnetization) suggests that this component in the smaller parent sample is a weak IRM overprint. Although the two parent samples of ALHA81001 are not mutually oriented, the unidirectionality of the MC and HC components within each sample and the agreement between the mean angular separation between the two components ($76° \pm 20°$ and $61° \pm 12°$ for the larger and smaller pieces, respectively, with uncertainties given as 95% confidence intervals) suggest that both the MC and HC components are unidirectional across the two parent samples.

We also performed thermal demagnetization of the NRM of an interior subsample (B2). Using a calibrated mixture of H_2 and CO_2 gas, the oxygen fugacity in the sample oven was set to 0.5 log units below the iron-wüstite buffer in an effort to reduce the alteration of kamacite in the subsample (Stolper 1977). The thermally demagnetized subsample, B2, was first AF demagnetized to 15 mT in order to remove any possible IRM overprints. This completely removed the LC component. The MC component was then observed to demagnetize between 75 and 150°C, while the HC/HT component decayed between 150 and 275°C, at which point directional coherence of the magnetization was lost. Another interior subsample imparted with a high-field laboratory ARM (AC field of 280 mT, DC bias field of 50 μT) shows a similar rate of decay upon thermal demagnetization in the same controlled atmosphere (Fig. 6.16). Directional coherence was also lost at between 225°C and 275°C. Due to the similarity between the two demagnetization patterns, the erratic behavior of the NRM above 250°C reflects sample alteration or weakening of the NRM into noise rather than a low blocking temperature for the HC/HT component. Demagnetization of saturation IRM suggests that

the block temperature spectrum of magnetic minerals in ALHA81001 is strongly biased towards low temperatures. Furthermore, the decay of NRM upon heating follows a very similar pattern as that of a saturation IRM (Fig. 6.17), suggesting that all grain populations in ALHA81001 were magnetized. The occurrence of alteration is supported by the observation that the saturation IRM intensity of the subsample heated to 350°C was factor of 6 greater than that of unheated samples (Fig. 6.18), suggesting that mineralogical changes have taken place. Such sample alteration has been previously commonly observed for kamacite and sulfide-bearing samples such as lunar rocks and most eucrites (Stephenson & Collinson 1974) and may be due to difference in the oxygen fugacity of the sample's formation environment compared to that of the laboratory oven where the sample was heated. Therefore, 275°C represents only a lower limit on the upper bound of the HC component's true blocking temperature range.

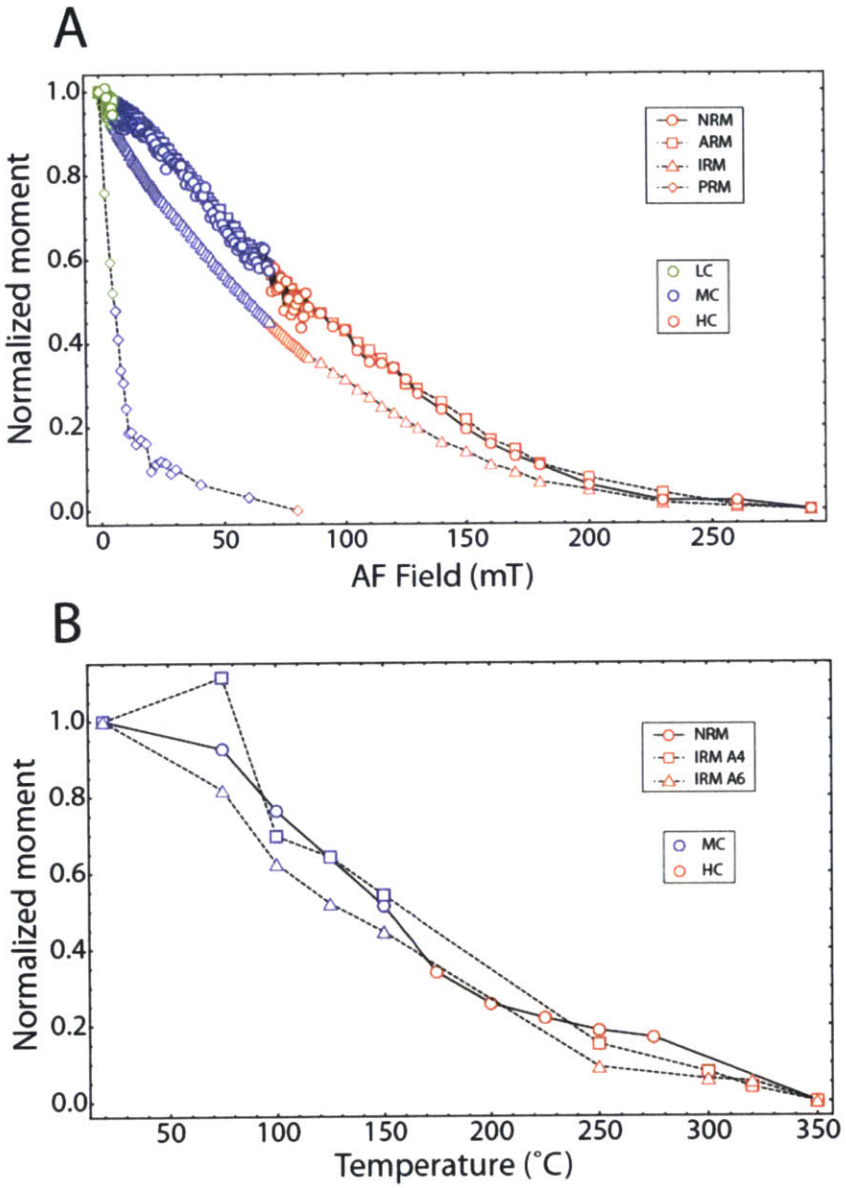

Figure 6.17. AF and thermal demagnetization spectra. (**A**) AF demagnetization of the NRM in interior subsample A5 compared to that of an ARM and IRM for the same subsample and PRM for subsample B3. For both the HC and MC components of magnetization, the NRM coercivity spectrum is similar to that of an ARM, but distinct from a strong field (280 mT) IRM or a PRM acquired at 1.8 GPa in a 750 μT background field. This suggests that the HC component is not a hand magnet overprint or a shock remanence and is consistent with a TRM origin. (**B**) Thermal demagnetization of the NRM in interior subsample B2 compared to that of a saturation IRM for the subsamples A4 and A6. Possible mineralogical alteration prevents using the same subsample for multiple thermal demagnetization runs. Plotted NRM moments have been corrected for the non-parallel directions of the HC/HT, MC/MT, and LC components.

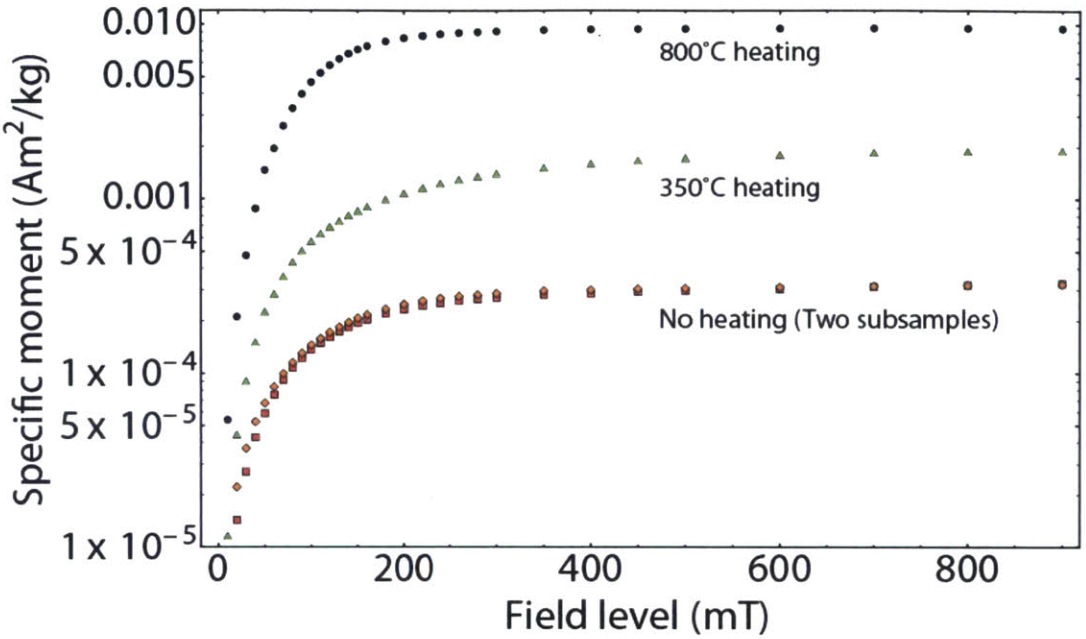

Figure 6.18. IRM acquisition experiments. Starting with an AF-demagnetized subsample, magnitude of remanent magnetization is measured after IRM acquisition at progressively higher fields up to 900 mT. Experiment performed on two unheated subsamples (A4 and C4), one subsample heated to 350°C (B2), and one subsample heated to 800°C (A3). The large increases in the intensity of saturation IRM for the heated subsamples suggest that changes to the magnetic mineralogy are occurring.

Paleointensities. Our ARM and IRM paleointensity experiments indicate that the magnetizing field that produced the HC/HT component at 3.69 Ga most likely had an intensity of ~12 μT (with a minimum value of ~2 μT). The young ^{40}Ar–^{39}Ar age of ALHA81001 precludes the direct recording of a dynamo because the longest predicted duration of a dynamo for a Vesta-sized object is on the order of several tens to ~100 My following solar system formation (Elkins-Tanton et al. 2011; Sterenborg & Crowley 2013). Likewise, solar and nebular fields could not be a source of the magnetization because they should have dissipated within the first ~6 My of solar system formation (Haisch et al. 2001). Furthermore, slow cooling of ALHA81001 over $>10^2$ years rules out the recording of any putative transient, impact-generated fields, which are expected to have persisted for less than several hundred seconds under Vestan impact conditions. This leaves remanent magnetization of the Vestan crust and underlying materials as the most likely magnetic field source. This in turn requires that the crust was magnetized by an earlier ambient magnetic field.

To constrain the strength of the magnetic field in which ALHA81001 was magnetized as summarized above, we conducted three sets of multicomponent paleointensity experiments. We performed experiments with ARM acquisition, AF demagnetization of saturation IRM, and thermal demagnetization of saturation IRM. We did not perform Thellier-Thellier dual-heating paleointensity experiments because the sample alteration that we observed during thermal demagnetization renders the necessary partial TRM acquisition steps unreliable. We also performed one ARM demagnetization experiment on the subsample A5.

For each component of the magnetization in each subsample, the ARM acquisition paleointensity is given by (Stephenson & Collinson 1974):

$$B_{ARM} = f^{-1} B_{bias} \frac{\Delta NRM}{\Delta ARM}$$

where B_{ARM} is the paleointensity, B_{bias} is the bias field of the ARM, ΔARM is the ARM moment acquired in the AF range of the component of magnetization, and f is the ratio of ARM to TRM acquired in the same background field. Because ARM paleointensity estimates are most accurate when the laboratory bias field is similar to the paleofield intensity (Kletetschka et al. 2006), we conducted these experiments using B_{bias} = 50 μT. The value of f is on the order of unity but typically varies by up to a factor of 3-5 depending on lithology (Shea et al. 2012; Garrick-Bethell et al. 2009; Levi & Merrill 1976). In the absence of heating experiments to calibrate the value of f for ALHA81001 (which are prevented by sample alteration during heating; see Section 6.3), we assume a value of f =1.34 (Shea et al. 2012).

An ARM demagnetization paleointensity determination is similar to that of ARM acquisition except a high AF level ARM (280 mT) is given first and ΔARM in the paleointensity function refers to the ARM *lost* during AF demagnetization in a given AF range. We found no systematic difference in the paleointensities inferred from ARM acquisition and ARM demagnetization experiments on subsample A5 and use only the ARM acquisition procedure on other subsamples.

Similar to ARM paleointensities experiments, the ratio between change in NRM and IRM can also be used to estimate paleofield strengths (Shea et al. 2012):

$$B_{IRM} = a\frac{\Delta NRM}{\Delta IRM}$$

where B_{IRM} is the paleointensity in μT, ΔNRM is the vector-subtracted change in NRM magnitude in the component's AF or thermal demagnetization interval and ΔIRM is the change in a saturation IRM when demagnetized through the same interval, and a is the ratio of IRM to low-field TRM in this interval. In the case of the HC/HT component, because the remanence is primary and origin-trending (see Section 6.3), ΔNRM and ΔIRM are taken to be the remaining NRM and IRM at the beginning of the component [the REMc method (Acton et al. 2007)]. The calibration factor a may typically vary by a factor of 3-5 depending on the rock type (Shea et al. 2012; Garrick-Bethell et al. 2009; Cisowski et al. 1983). Due to the absence of direct measurements of IRM/TRM for ALHA81001 (which are prevented by sample alteration during heating; see Section 6.3), for this study we adopt a value of $a = 3 \times 10^3$ (Gattacceca & Rochette 2004).

We obtained IRM paleointensities using both thermal and AF demagnetization of the NRM and a saturation IRM. We performed thermal demagnetization of NRM on one interior subsample (B2; see Section 6.3). Due to heating alteration, we could not impart and thermally demagnetize a saturation IRM on the same subsample. Therefore, thermal demagnetization curves for a saturation IRM (7 T) were obtained from two other interior subsamples (A4 and A6). Due to the similarities in the demagnetization curves (Fig. 6.17) and the similar paleointensities derived from using subsample A4 or A6 to calculate ΔIRM, we conclude that the paleointensities derived from this method are robust.

We performed AF demagnetization of both NRM and saturation IRM on two fusion crusted (A1 and B1), one intermediate (A2), and two interior subsamples (A5 and B3). However, three other interior subsamples (B2, A4, and A6) were were subjected to heating before we imparted a saturation IRM. Therefore, among interior subsamples, reliable AF demagnetization of IRM paleointensities are only available for the subsamples A5 and B3.

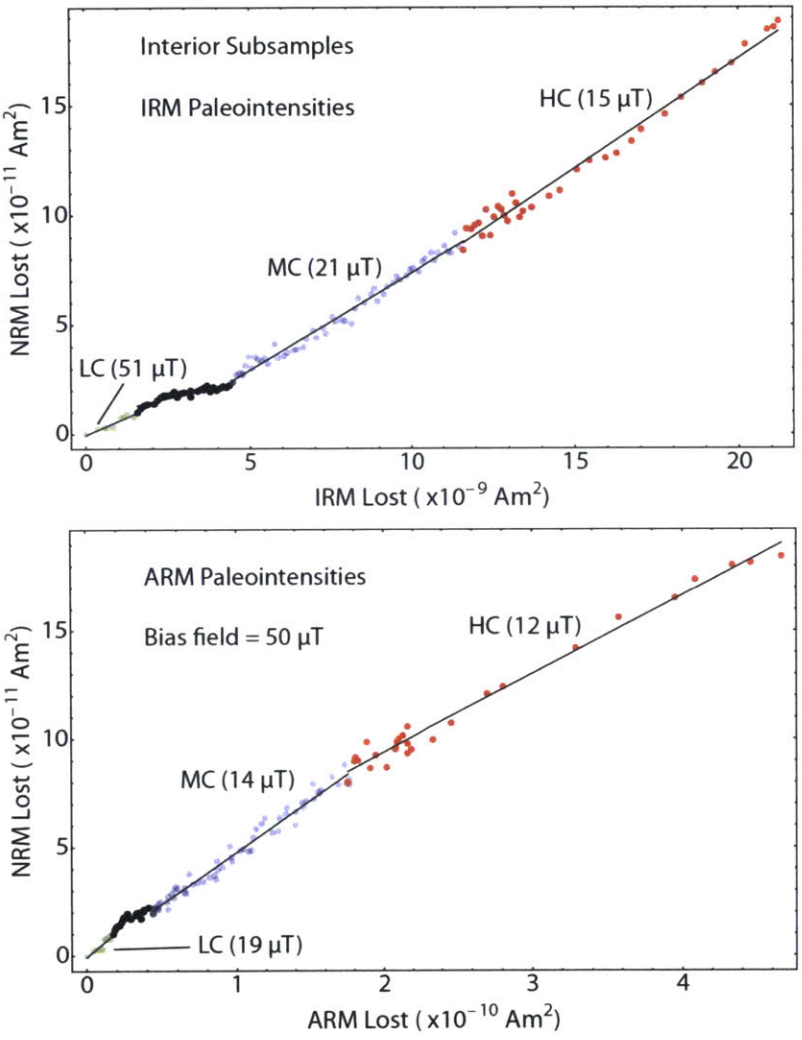

Figure 6.19. Representative IRM and ARM paleointensity experiments for the interior subsample A5. Data points within each component are color-coded for clarity (compare with Figs. 6.10, 6.13). Black data points between the LC and MC components do not constitute a component of magnetization due to lack of decay upon AF demagnetization.

Interior subsamples paleointensities obtained with the IRM and ARM methods agree to within the uncertainties of the methods for all three components of the NRM (Fig. 6.19). However, since only the HC component is a probable TRM (see Section 6.4), only the results for this component represent true paleofield intensities. We find that, for the interior subsamples, the ARM method yields an average paleointensity of 12 μT, the thermal demagnetization of IRM yields an average value of 11 μT, and the AF demagnetization of IRM yields 14 μT. The mean paleointensity derived from these three

methods is ~12 μT. Previous calibrations of a and f on samples subjected to thermal paleointensity experiments suggest that these empirical factors may vary by a factor of several among samples with different lithologies. Lunar samples have been observed with $a = 275$ (resulting in paleointensities 10 × lower than our values) and multiple lunar samples have a less than 1200 (paleointensities >3 × lower) (Cisowski et al. 1983). Values as high as 9 have been observed for f (paleointensities >6 × lower) (Levi & Merrill 1976). Following Shea et al. (2012), we adopt a factor of 5 as our uncertainty, giving ~2 μT as a lower bound on the true paleointensity of the magnetic field in which ALHA81001 was magnetized.

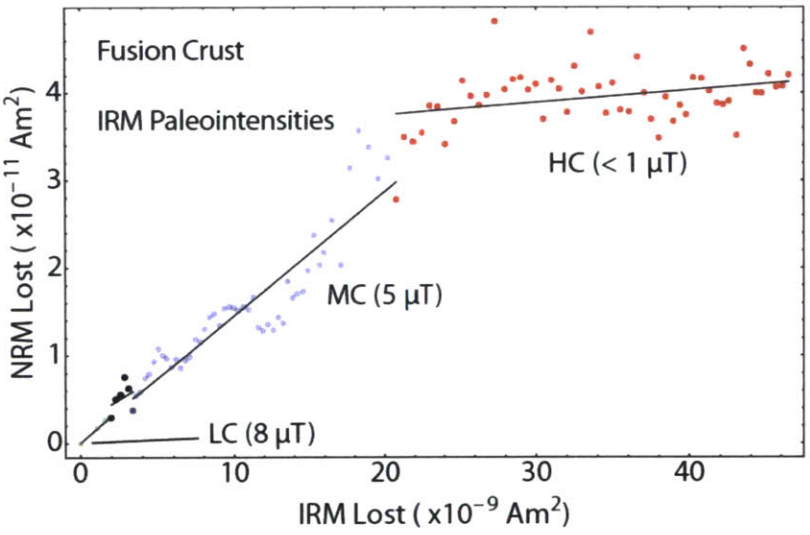

Figure 6.20. Representative IRM paleointensity experiment for the fusion crusted subsample B1. Black data points between the LC and MC components do not constitute a component of magnetization due to lack of decay upon AF demagnetization.

Fusion crusted subsamples have significantly lower paleointensities (Fig. 6.20). As in the case of interior samples, only the HCf is a probable TRM. Its weak paleointensities (< 10 μT) are anomalous compared to the majority of meteorite studies, where fusion crust magnetization is usually stronger than that of interior samples and typically have paleointensities consistent with Earth's ~50 μT field. These differences may be due to incomplete remagnetization of part of the material in fusion crusted subsamples, which would lead to mixing of the widely divergent HC and HCf magnetizations and partial

cancellation of magnetization. The intermediate NRM directions recorded in the intermediate subsamples suggest that such mixing of magnetization component has occurred and likely accounts for the weak paleointensities in those subsamples. The weak fusion crusted and intermediate subsample paleointensities may also be due to rotation or tumbling of the meteoroid during atmospheric entry.

Magnetic anisotropy in bulk samples can affect the results of IRM and ARM paleointensities (Selkin et al. 2000). To assess this possibility, we measured the IRM and ARM anisotropy of ALHA81001 by magnetizing a subsample along each of the three mutually perpendicular axes with a moderate field IRM (80 mT) and ARM (AC field of 80 mT and DC bias field of 0.2 mT). The resulting degree of anisotropy, P, is defined as the ratio between the highest and lowest eigenvalues of the anisotropy tensor and reflects the extent to which remanence acquisition is dependent on the orientation of the subsample relative to the magnetizing field. Our experiments measured $P = 1.07$ for both ARM and IRM. Following Selkin et al. (2000), this means that anisotropy corrections to paleointensity values are at most 7%. This error is much smaller than the systemic uncertainties due to the calibration constants and the variation among subsamples. We therefore have not applied anisotropy corrections to our paleointensity results.

PRM and VRM experiments. To assess the origin of each component of magnetization, we subjected several demagnetized subsamples to laboratory pressure remanent magnetization (PRM) and viscous remanent magnetization (VRM) acquisition experiments. We then compared the resulting laboratory remanences to the observed NRM.

Although ALHA81001 was never shocked to above 5 GPa following its primary crystallization as an impact melt, shock pressures below this limit can still produce shock remanent magnetization (SRM) (Gattacceca et al. 2008).

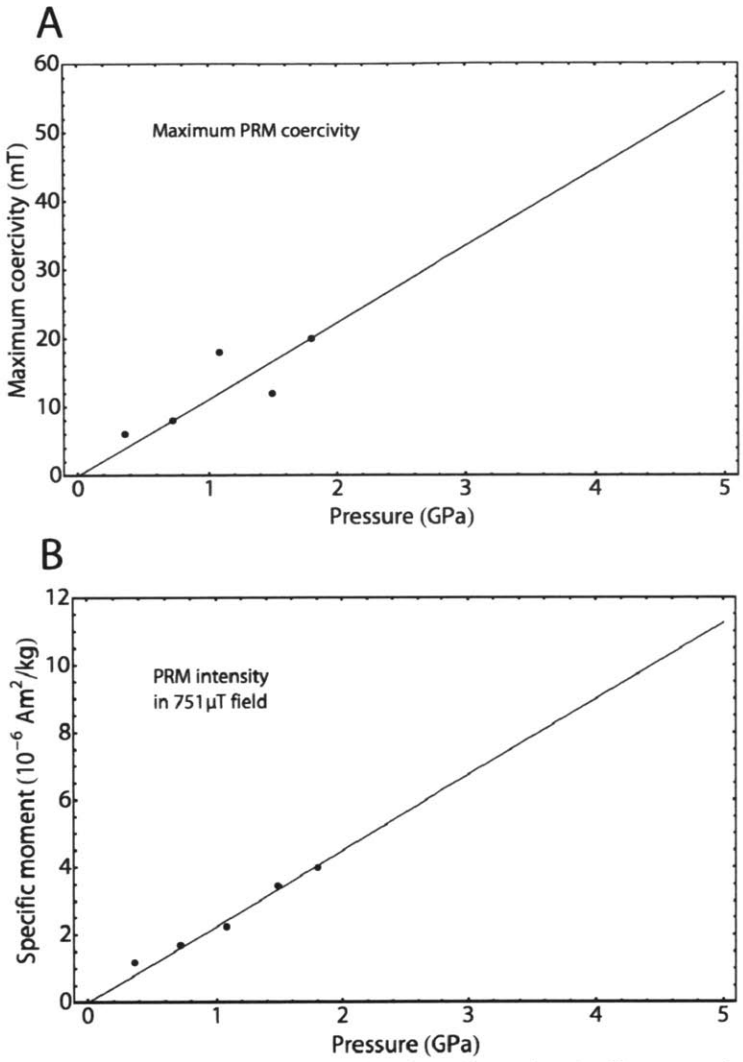

Figure 6.21. PRM experiments on interior subsample B3. Shown are the (**A**) intensity and (**B**) maximum coercivity of PRM acquired in a laboratory field of 750 μT under pressures of up to 1.8 GPa. The trends are linearly extrapolated up to a maximum possible shock pressure of 5 GPa as indicated by the petrography of ALHA81001.

To simulate such a process, we imparted a laboratory PRM to subsample B3 following AF demagnetization of its NRM in the paleomagnetism laboratory at CEREGE in Aix-en-Provence, France. The subsample was placed in a Teflon cup immersed in polyethylsiloxane fluid to insure even distribution of pressure. A press was used to bring the subsample and fluid to the designated peak pressure and a laboratory-generated field of 750 μT was turned on. The pressure was then released over the course of ~1 minute. The subsample was then subjected to AF demagnetization until the newly imparted

magnetization was removed. We repeated this process for a set of increasing pressures (0.36, 0.72, 1.08, 1.49, and 1.8 GPa). Note that although the timescale of our pressure application is longer than expected for a true impact-generated shock remanent magnetization (SRM), SRM acquisition experiments have been observed to produce similarly soft and weak (17 to 36% of a TRM in the same background field) remanence as shocks in the <5 GPa range (Gattacceca et al. 2008). We therefore regard our PRM acquisition experiments as an adequate simulation of true weak-pressure (<5 GPa) SRM. We find that both the intensity and magnetic hardness of the acquired PRM increases linearly with the peak applied pressure (Fig. 6.21).

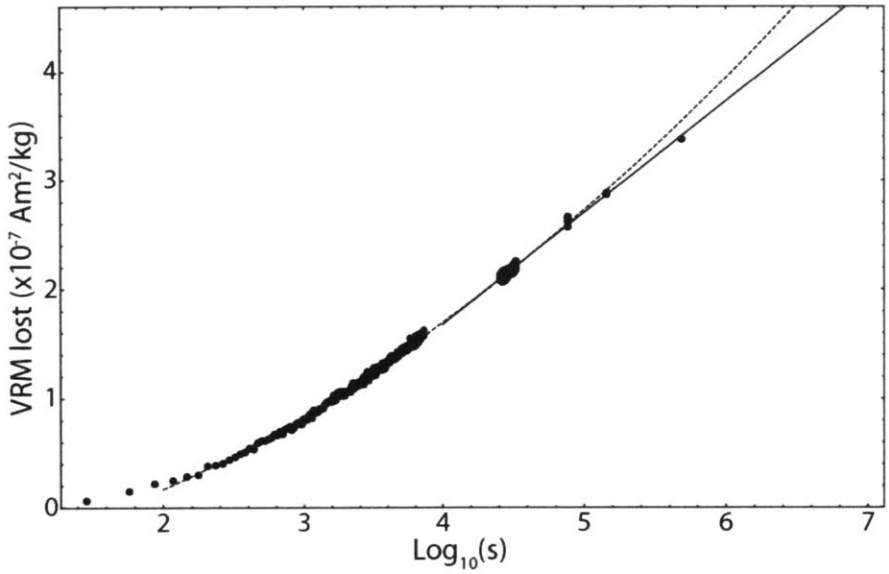

Figure 6.22. VRM decay experiments on interior subsample B2. Shown is the progressive decay of a VRM acquired at room temperature over 13 days in the Earth's field as the subsample subsequently resided for 6 days in our shielded room (DC field < 150 nT). The solid line is a linear fit to data acquired after 10^4 s. The dotted line is an alternative quadratic fit to data after 100 s.

ALHA81001 may have acquired a VRM due to exposure to the terrestrial magnetic field during its residence in Antarctica or its storage at the Johnson Space Center (JSC) since 1981. Although the terrestrial residence age of ALHA81001 has not been measured, those of other eucrites from the Allan Hills have been measured to be between 15 and 310 thousand years (ky) (Nishiizumi et al. 1989). We consider these figures to be the lower and upper bounds of the terrestrial age of ALHA81001 in the subsequent

analysis. There is also the possibility that the meteorite may have also acquired an extraterrestrial VRM on its parent body.

To constrain the efficiency of VRM acquisition, we placed one undemagnetized subsample of ALHA81001 (B2, prior to thermal demagnetization experiments) in the terrestrial field (46 μT) for a period of 13 days and 6 hours. The sample was then quickly returned to the magnetically shielded room (field <150 nT) and the decay of its VRM was monitored over the course of 6 days (Fig. 6.22). Using the fact that the rate of VRM decay is typically similar to that of VRM acquisition within a factor of 1-3 (Dunlop & Ozdemir 1997b), we used the measured VRM decay constant to estimate the expected magnitude of VRM acquired during difference periods in the history of the meteorite. We make the approximation that the acquisition of VRM varies linearly with logarithmic time. The accuracy of such an assumption varies with rock type (Yu & Tauxe 2006). We therefore also assumed a quadratic dependence of VRM on logarithmic time in order to constrain the possible error due to our assumption of linear dependence.

6.4. Origin of the natural remanent magnetization

Motivation. Our scientific interpretations rest on the inference that the HC/HT magnetization of interior samples, which remains stable to >290 mT and is blocked to >275°C, is a TRM produced by cooling in ambient magnetic fields on the surface of Vesta. In this section, we present evidence to support this view.

Origin of the LC and MC components. As described in Section 6.3, both the LC and MC magnetizations are unidirectional across all subsamples of the larger parent sample except for the fusion crusted subsample A1, which lacks a clear MC component. Furthermore, an MC-like component is quasi-unidirectional across the smaller parent sample. This unidirectionality is consistent with a VRM origin for both components. Furthermore, the observed degree of scatter in directions is expected for a VRM since the orientation of the meteorite with respect to the local field may have varied during the course of VRM acquisition.

The LC and MC components are present in fusion crust, intermediate, and interior subsamples. The presence of the LC and MC magnetization in the fusion crusted subsamples cannot be explained by the inclusion of interior material on these subsamples. This is because the presence of mixed HC/HCf magnetization in the intermediate depth subsamples (A2 and A3) implies that the HC component in these samples has been partially overprinted (Fig. 6.12). Given that the MC component is completely removed during thermal demagnetization at temperatures below that at which the HC component begins to be demagnetized (Fig. 6.14), the most heated portion of the intermediate samples must have had the entirety of any purported MC component removed during atmospheric entry. The fusion crusted subsamples themselves encountered even stronger atmospheric heating than the intermediate subsamples and therefore could not have retained any existing MC magnetization from before atmospheric entry. Therefore, the presence of the LC and MC components in the fusion crusted subsamples requires that these components were acquired after arrival on Earth. The LC and MC components are therefore extremely unlikely to be SRM, as atmospheric passage does not provide sufficient pressure to significantly alter the magnetization of small meteoroids (Kohout et al. 2004). Small meteoroids such as ALHA81001 with a mass of only 52.9 g impact the ground at velocities below ~20 m s^{-1}, which is insufficient to cause remagnetization upon landing (Baldwin & Sheaffer 1971). Finally, the AF demagnetization spectrum of the MC component is inconsistent with an IRM or a PRM (Fig. 4.22).

The blocking temperature range of the MC component also strongly suggests a VRM origin. According to the Néel theory for the relaxation of single-domain pyrrhotite and kamacite grains, a VRM acquired over 15 to 310 ky in the -30°C mean annual temperature of the Allan Hills (Atkins et al. 2002) should be removed by lab heating to between room temperature and ~145°C for a heating interval of $t_{lab} = 2400\,\mathrm{s}$, which is fully consistent with the observed removal of the MC magnetization between room temperature and 150°C (Fig. 6.14A).

The intensities of the LC and MC magnetizations are also consistent with terrestrial VRMs. Empirically, for grain size distributions that are not grossly non-uniform, the magnitude of VRM acquisition is approximately constant over each fixed interval of log time (Dunlop & Ozdemir 1997b):

$$S = \frac{\partial M_{VRM}}{\partial(\log t)} \tag{6.1}$$

where S is the viscosity coefficient, M_{VRM} is the magnitude of a VRM (in this case the mass-specific moment), and t is time. As such, values of M_{VRM} plotted against the logarithm of time (Fig. 6.21) should lie roughly along a line of slope S. Although our VRM decay experiment initially exhibits non-linear behavior, the trend becomes linear for times greater than ~1 hour after the beginning of VRM decay. Using data from this time interval, we estimate a viscosity coefficient for ALHA81001 of:

$$S = 1.0 \times 10^{-7} \frac{\mathrm{Am^2}}{\mathrm{kg\ log_{10}\ s}} \tag{6.2}$$

This constant can then be used to estimate the VRM acquired during various stages of the meteorite's history. To check the robustness of our predicted VRM intensities using the linear fit described above, we use an alternative quadratic fit to the VRM acquired as a function of logarithmic time (Shea et al. 2012), which corresponds to the following governing expression for VRM acquisition:

$$\frac{\partial M_{VRM}}{\partial(\log t)} = S_0 + S_1 \log t \tag{6.3}$$

Beginning with the most recent exposure to a background field, a VRM acquired during a maximum of 30 years of storage at JSC followed by 8 months of decay in our magnetically shielded room should have a maximum specific moment of 1.7×10^{-7} $\mathrm{Am^2kg^{-1}}$ according to the linear fit and 2.8×10^{-7} $\mathrm{Am^2kg^{-1}}$ according to the quadratic fit. These values are upper limits because they assume that the meteorite was kept in the same position relative to ambient fields during the entire period of 30 years. Furthermore, the prediction of VRM acquisition is subject to significant uncertainty due to the unknown form of the VRM acquisition function for times greater than the

laboratory VRM decay time (Yu & Tauxe 2006). The observed LC component in non-fusion crusted subsamples carries specific moments of between 0.8-1.2×10^{-7} Am^2kg^{-1}, which is 30 to 53% less than the maximum value estimated from the linear fit and 57 to 71% less than that of the quadratic fit. Therefore, the LC component is consistent with a VRM acquired after the meteorite's collection from Antarctica and suggests that the meteorite's position may have changed during its residence at JSC.

By the same analysis, a VRM acquired over 15 to 310 ky in Antarctica and left to remagnetize over 30 years at JSC is expected to have a specific intensity of between 2.2×10^{-7} and 3.3×10^{-7} Am^2kg^{-1} according to the linear fit and between 5.6×10^{-7} and 8.9×10^{-7} Am^2kg^{-1} from the quadratic fit. For this case, we have corrected for the lower VRM acquisition efficiency at Antarctic temperatures by assuming linear dependence of S on temperature (Dunlop & Ozdemir 1997b):

$$S_{ALH} = S\frac{T_{ALH}}{T_{amb}} \tag{6.4}$$

where S_{ALH} and T_{ALH} are the viscosity coefficient and average annual temperature (243 K) for the Allan Hills where the meteorite was found, and S and T_{amb} are the measured viscosity coefficient and temperature in our lab (at 293 K). The observed intensities of the MC components of non-fusion crusted samples are between 1.80-11×10^{-7} Am^2kg^{-1} with a mean value of 5.3×10^{-7} Am^2kg^{-1}, which falls between the values predicted by the linear and quadratic fits. Given the uncertainties described above as well as the significant extrapolation in timescale used in our analysis, this is consistent with an Antarctic VRM origin for the MC component (Yu & Tauxe 2006).

In summary, we find that both the LC and MC components of magnetizations represent terrestrial VRMs and as such carry no information about magnetic fields on Vesta. The HC component of interior subsamples is therefore the only magnetization with a possible extraterrestrial origin.

Origin of the HC component. Several lines of evidence suggest that the HC component of interior subsamples is extraterrestrial in origin. The systematic change from the HCf to

HC component directions from the fusion crust to interior subsamples (Fig. 6.12) suggests that the interior HC magnetization predates atmospheric entry. Furthermore, because the MC component is very likely a VRM acquired during residence in Antarctica (see Section 6.4), any component blocked to higher temperatures and coercivities must predate the arrival of the meteorite in Antarctica. The HC magnetization of the meteorite's interior, which was not affected during atmospheric entry, is therefore extraterrestrial in origin.

The reliability of our paleointensity estimates depends on the mode of acquisition of the HC component. Accurate paleointensities are only possible if the HC component is a TRM. During AF demagnetization, the decay of the HC component is distinctly more similar to that of an ARM [an analog for TRM; (Dunlop & Argyle 1997)] compared to that of an IRM (Fig. 6.22), suggesting that this component is a TRM but cannot represent an IRM (Stephenson & Collinson 1974). A non-IRM origin is also strongly supported by the HC component's low NRM/IRM values of $\sim 4 \times 10^{-3}$.

Furthermore, the blocking temperature range of the HC component is consistent with a TRM acquired at 3693 Ma. Due to viscous decay at 180 K (the blackbody temperature at 2.36 AU) over the last ~3700 Ma, such a TRM is expected to be blocked between ~90°C and 780°C for single-domain kamacite and between room temperature and 320°C for iron sulfides (Garrick-Bethell & Weiss 2010; Dunlop et al. 2000). Viscous decay also occurred during the transfer of the meteoroid to Earth, possibly at elevated temperatures. Although the CRE age of ALHA81001 is 15 My (Fig. 6.2), the orbital elements of the meteoroid during this time interval, and therefore its temperature, are unconstrained. Assuming that the meteoroid's distance from the sun was between 2.4 and 1.0 AU during its transfer, its blackbody temperature would have been between -93 and 6°C. The corresponding minimum blocking temperature of a previously existing TRM, assuming a 15 My transfer period and a blackbody temperature of -6°C, is ~70°C for remanence carried by kamacite and pyrrhotite (Dunlop et al. 2000). The lowest blocking temperature of <150°C observed for the HC component is therefore consistent with a TRM pre-dating the transfer of ALHA81001 from Vesta to the Earth.

We argue against an SRM origin for the HC component based on two lines of evidence provided by our PRM acquisition experiment (see Section 6.3). First, the

observed coercivity spectrum of the HC magnetization is much harder than is expected for a PRM (Fig. 6.22). This is because our laboratory PRM experiments show that the maximum coercivity of remanence increases linearly with applied pressure (Fig. 6.20A). Extrapolating the measured maximum coercivities to the maximum possible post-formation shock pressure of ALHA81001 (5 GPa), the PRM is projected to have a maximum coercivity of only ~56 mT, which is much weaker than the observed maximum coercivity of ≥290 mT for the HC component.

Second, the intensity of the HC magnetization is likely too strong to represent an SRM. SRM intensity increases linearly with increasing background field strength (Gattacceca et al. 2008). For low shocks below 1 GPa, SRM also increases linearly with peak pressure but likely ceases to increase above a certain pressure value (Gattacceca et al. 2008). A linear extrapolation of our PRM acquisition experiments to 5 GPa (Fig. 6.20B) therefore provides an upper bound on the possible SRM intensity in ALHA81001. We find that, in our laboratory background field of 750 μT, SRM intensity is expected to be $< 1.1 \times 10^{-5}$ $Am^2 kg^{-1}$.

Because the HC component has been overprinted by the MC component, we cannot directly compare this expected value to the observed intensity of the HC component and instead must estimate its original strength before the overprinting events. Since its demagnetization spectrum is similar to that of an ARM (Fig. 6.22), we can estimate the full, original intensity of the HC magnetization as follows:

$$M_{total} = \frac{ARM_{total}}{ARM_{HC}} M_{HC} \tag{6.5}$$

where M_{total} is the estimated original magnetization, ARM_{total} is the ARM acquired in a given bias field across the full coercivity spectrum, ARM_{HC} is the ARM acquired in the same bias field in the same coercivity range as the HC component (~70 to ~290 mT), and M_{HC} is the observed strength of the HC magnetization within the same coercivity range. The calculated M_{total} for the HC component is 2.47×10^{-6} $Am^2 kg^{-1}$. Given that SRM intensity varies linearly with local field strength, a background field of >162 μT is required to explain the high intensity of the HC component if it were an SRM. Such a

strong field, three times the value of the Earth's surface field, is unlikely to have existed on Vesta at 3.62 Ga.

Finally, the HC also is unlikely to be a terrestrial VRM, as the expected maximum blocking temperature for a 310 ky VRM is only 154°C according to single domain blocking temperature theory (Garrick-Bethell & Weiss 2010). Such a blocking temperature is too low to be consistent with the HC component. Similarly, the HC cannot be an extraterrestrial VRM, as even a 4 Gy VRM at the cryogenic temperatures of the asteroid belt (black body temperature of 180 K at 2.4 AU) should be blocked up to a similar temperature as the MC component assuming single-domain kamacite and pyrrhotite to be the magnetic carrier.

We have shown above that the HC component is unlikely to be an IRM, SRM, or VRM and that it is probably a TRM acquired upon cooling in a stable background field over a period of several thousand years. We now address the possible sources of this background field.

Origin of extraterrestrial fields. The ^{40}Ar–^{39}Ar plateau age of ALHA81001 indicates that the most recent heating event capable of full thermal remagnetization took place at 3.69 Ga (Fig. 6.2C) and that the meteorite has largely escaped subsequent thermal disturbances. In particular, the observed degassing of radiogenic ^{40}Ar can be accounted for by a mean effective temperature between -50 and 140°C during the last 15 My (i.e., during tranfer to Earth; see Fig. 6.2D). This is entirely consistent with our ^{38}Ar analysis, which reveals a cosmic ray exposure age of ~15 My, during which time the meteoroid may have been heated to a constant temperature of no greater than 140°C (Fig. 6.2A). Blocking temperature relationships for FeNi metal and iron sulfide (represented by kamacite and pyrrhotite) (Garrick-Bethell & Weiss 2010; Dunlop et al. 2000) and the degree of post-3.69 Ga heating inferred from ^{40}Ar and ^{38}Ar diffusion suggest that the HC/HT component should have survived from 3.69 Ga to the present day.

Although ALHA81001 crystallized rapidly over a ~1 hour period, the presence of pigeonite-augite exsolution shows that cooling between 1100°C and ambient blackbody temperatures likely took place over several hundred years. This cooling event likely

represents the acquisition of the HC magnetization (see Section 6.2). We now show that impact-generated fields on Vesta are not expected to be stable at such timescales.

We consider two scenarios of field generation by impacts. In the first scenario, ionized vapor from the impact undergoes charge separation, leading to an electric current and its associated magnetic field (Crawford & Schultz 1993). This phenomenon has been studied in the laboratory for impactor velocities up to ~5 km/s. According to calibrated scaling laws (Crawford & Schultz 1999), the duration (τ) in seconds of such a field is approximated by:

$$\tau = 20\frac{x}{v_{imp}} \tag{6.6}$$

where x is the distance from the impact point and v_{imp} is the impact velocity, which is approximately 5.4 km/s for large impacts on Vesta (Asphaug 1997). Taking x to be the radius of Vesta (~260 km), the maximum duration of such fields on Vesta is only ~1000 sec. In the second scenario, a plasma cloud created in an impact may expand along the surface of Vesta, concentrating ambient magnetic field near the antipode of the impact. Such a process has been proposed as an explanation for lunar surface magnetic anomalies (Hood & Artemieva 2008; Hood & Vickery 1984). However, the generation of sufficient ionized vapor to efficiently perturb ambient fields is unlikely given the low velocity of a Vesta large crater-forming impact (Hood & Vickery 1984; Pierazzo et al. 1997). Although vaporization is expected for impact velocities of the lunar basin-forming events (>10 km/s), slower impact velocities below ~7.5 km/s should produce no vapor. Therefore, neither mechanism generates magnetic fields of long duration necessary to explain the HC component, which was likely acquired over several thousand years.

Given the high inferred paleointensities for ALHA81001, this earlier magnetic field is most likely due to a core dynamo. Although nebular fields may have had intensities comparable to those of core dynamos (Turner & Sano 2008), they typically varied in direction on timescales of several tens of orbits. Petrographic studies show that Vesta's crust cooled over timescales of at least several My and therefore is unlikely to have coherently recorded such time-variable nebular fields (Miyamoto & Takeda 1994).

Another possibility is that Vesta's crust near or antipodal to large impact basins may have acquired remanent magnetization due to transient, impact-generated magnetic fields (Hood & Artemieva 2008; Crawford & Schultz 1999). However, the low velocities (~5 km/s) expected for impacts on Vesta should not have typically produced the ionized plasma clouds necessary for generating strong transient magnetic fields. On the other hand, an early dynamo field should have been capable of generating steady core magnetic fields with strengths up to 2600 μT, resulting in surface fields of up to 100 μT assuming a mainly dipolar field geometry (Christensen & Aubert 2006), providing a means of magnetizing the Vestan crust and underlying material.

Following Wieczorek et al. (2012), we calculate the expected strength of the remanent crustal field due to this earlier dynamo. Although most HED meteorites exhibit saturation remanence of 10^{-4} -10^{-2} Am^2kg^{-1} (Rochette et al. 2009), certain metal-rich HEDs such as Camel Donga display saturation remanence of up to 5×10^{-2} Am^2kg^{-1}. A 100 μT field is expected to impart a TRM (M_{TRM}) of up to 3×10^{-6}-2×10^{-3} Am^2kg^{-1} in HED material (Gattacceca & Rochette 2004). Actual magnetic field intensities due to remanent magnetization depend on the specific geometry of the magnetized material but can be estimated to be $\leq \mu_0 M_{TRM} \rho$ for a thin, circular disk magnetized perpendicular to the plane (Dunlop & Ozdemir 1997b), where μ_0 is the permeability of free space and ρ is the crustal density, assumed to be 3100 kg m^{-3}. Crustal material on Vesta magnetized in a dynamo can therefore generate magnetic field intensities between 0.01 and 7 μT.

Although the upper end of this range overlaps with our inferred paleointensities, these paleointensities are surprisingly high and may suggest, but does not require, the presence of more strongly magnetic material on or beneath the surface of Vesta that is not sampled by HED meteorites. Carbonaceous chondrite material has been observed in howardites and may be represented by scattered dark terrains observed on the surface of Vesta (Reddy et al. 2012). Mesosiderites have been hypothesized to originate on Vesta due to their isotopic composition (Greenwood et al. 2006). Carbonaceous chondrites and mesosiderites have saturation remanence in excess of 10^{-1} Am^2kg^{-1} and can readily produce >10 μT crustal magnetic fields when magnetized in a 100 μT dynamo field (Rochette et al. 2009). Therefore, such material, if present on Vesta, may result in localized, highly magnetic terrains. The uniquely high paleointensity of ALHA81001,

which is stronger than that of most previously studied HEDs [e.g., Cisowski (1991)], is consistent with the relative rarity of the purported highly magnetic terrains. Localized regions of high crustal field intensities on Mars and the moon are similarly too intense to be explained by the observed magnetism of SNC meteorites and Apollo samples, respectively, and also require the existence of unsampled, highly magnetic material on these bodies (Hood & Zakharian 2001). A magnetized crust due to a prior dynamo epoch therefore appears to be the only plausible field generation mechanism consistent with our inferred paleointensities.

A remanent crustal field is the only plausible source of magnetic fields stable over the necessary timescales at 3693 Ma on Vesta. As discussed above, for the strength of a crustal field to be consistent with our inferred paleointensities, the crust must have been magnetized in a steady, more ancient magnetic field and the crustal material must itself be sufficiently magnetic. The magnetization of a material with saturation remanent magnetization M_{rs} that cooled in a weak magnetic field of strength B_0 is approximately:

$$M_{TRM} = aB_0M_{rs} \tag{6.7}$$

where M_{TRM} is the resulting magnetization of the material and a is an empirical constant approximately equal to 3×10^{-3} μT^{-1} for B_0 in μT and M_{TRM} and M_{rs} in the same units (Gattacceca & Rochette 2004). Although previously measured HED meteorites have values of M_{rs} less than 10^{-2} Am^2kg^{-1}, a number of yet unmeasured metal-rich HED meteorites, including Petersburg, Camel Donga, and Pomozdino (Rochette et al. 2009), may have higher values of M_{rs}.

To constrain the M_{rs} of such metal-rich HED meteorites, we acquired three small (1-2.5 g) stones of Camel Donga from two different private meteorite dealers. All fusion crust material was removed with a diamond wire saw (see Section 6.2). We measured at least one large fragment from each stone consisting of pure interior material. The weighted mean value of M_{rs} is 5.07×10^{-2} Am^2kg^{-1}. Using this value as an upper bound to the M_{rs} value of an HED crust, remanent crustal fields with intensities as high as 7 μT are possible given a 0.1 mT magnetizing dynamo field. Therefore, the expected strength

of remanent crustal fields due to an earlier dynamo on Vesta is consistent with our minimum inferred paleointensity of 2 μT.

6.5. Implications

Our inferred detection of an early dynamo in Vesta provides further evidence that dynamos could have formed in small, differentiated bodies in the early solar system. The presence of a magnetized crust implies that at least parts of the Vestan surface had solidified and cooled below the Curie temperature during the presence of an active dynamo. The strong inferred intensity of remanent crustal magnetization suggests that the dynamo, when it was active, likely generated surface fields with intensities between 10 and 100 μT and that strongly magnetic material unsampled by HED meteorites may be present on or below the surface of Vesta.

Furthermore, the existence of crustal magnetization at 3.69 Ga suggests that Vesta likely has crustal magnetic fields at the present time, as impact events are unlikely to have demagnetized the entire surface. Spectral features of the Vestan surface lack characteristics of space weathering observed on the Moon (Pieters et al. 2012) and may require shielding from the solar wind ion flux at 2.36 AU by a surface field ≥0.2 μT (Vernazza et al. 2006). The existence of >2 μT magnetic fields of the intensities estimated here are therefore sufficient to stand off solar wind ions at the orbital distance of Vesta, providing a possible explanation for the apparent lack of solar wind ion generated space weathering.

6.6. The Millbillillie eucrite

Unlike nearly all other Sections of Chapters 2-7, the data and results described in this Section have not been published as of spring 2015.

Before conducting the paleomagnetic experiments on ALHA81001 described in Sections 6.1-6.5, we worked on the eucrite Millbillillie with the same motivation to understand early magnetic fields on the asteroid Vesta. Millbillillie is an observed fall from Australia. In contrast to the simple thermal and shock history of ALHA81001,

Millbillillie was assembled from more than one distinct basaltic sources (i.e., it is polymict) (Yamaguchi et al. 1994). Assembly of the meteorite likely took place shortly after 4.507 Ga (Miura et al. 1998) and was followed by up to 100 Myr of thermal metamorphism (Yamaguchi et al. 1996). The latest major thermal event, ^{40}Ar–^{39}Ar dated to 3.55 Ga, resulted in heating to ~300–700°C. Other impacts before and after this event shocked the material to above ~5–10 GPa, resulting in the production of glassy melt veins (Yamaguchi et al. 1994).

We obtained our sub-samples of Millbillillie from a single large (3 × 3 × 7 cm) slab of the meteorite provided by Dr. Alex Bevan at the Western Australian Museum. As with the ALH 81001 samples, the Millbillillie sample and its extracted sub-samples were protected from ambient field and dust contamination during the shipping and storage process before and after arrival in our lab.

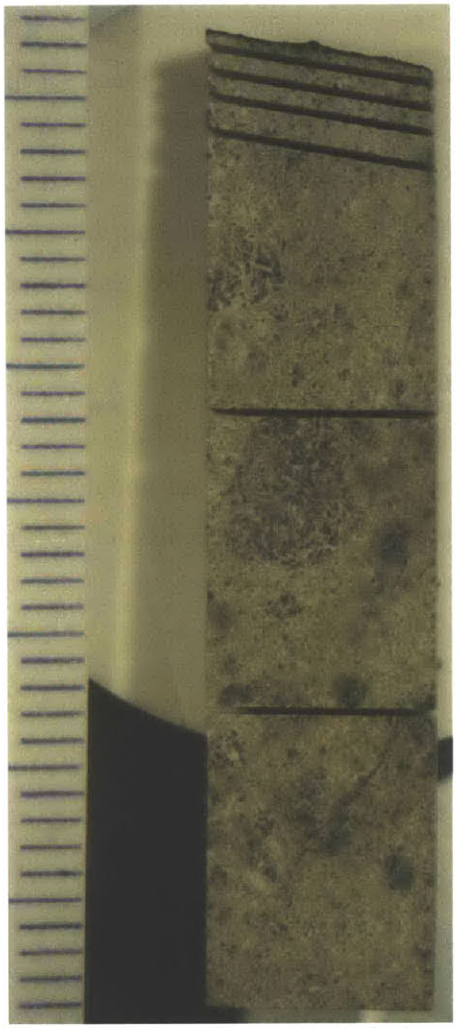

Figure 6.23. One of two sections of sub-samples extracted from the Millbillillie eucrite to conduct a fusion crust baked contact test. Each tick on the ruler at left is 1 mm. The dark edge at the top end of the section is fusion crust material.

From this parent piece we extracted 54 mutually oriented sub-samples. As in the case of other meteoritic samples analyzed in this thesis, we began our experiments with the fusion crust baked contact test (Fig. 6.23) (Nagata 1979b; Weiss et al. 2010). Atmospheric heating in Millbillillie penetrated significantly deeper into the meteorite interior as only samples more than 3.9 mm from the fusion crust were free from fusion crust components of magnetization. Interestingly, Millbillillie carries two magnetizations with distinct directions associated with heating during atmospheric entry. The first is carried by material within 0.5 mm of the surface and is, coincidentally, near the direction

of the M-M component of the interior samples (see below). The second magnetization is found in material between 0.8 and 3.6 mm of the surface and is ~90° away from the directions of the first fusion crust magnetization. Both magnetizations are uniform in direction within material of the appropriate distance from the surface throughout our sample (2-3 cm scale). We interpret the existence of two fusion crust magnetizations to be due to reorientation of the meteoroid during its flight through the atmosphere, possibly due to disintegration of a larger mass.

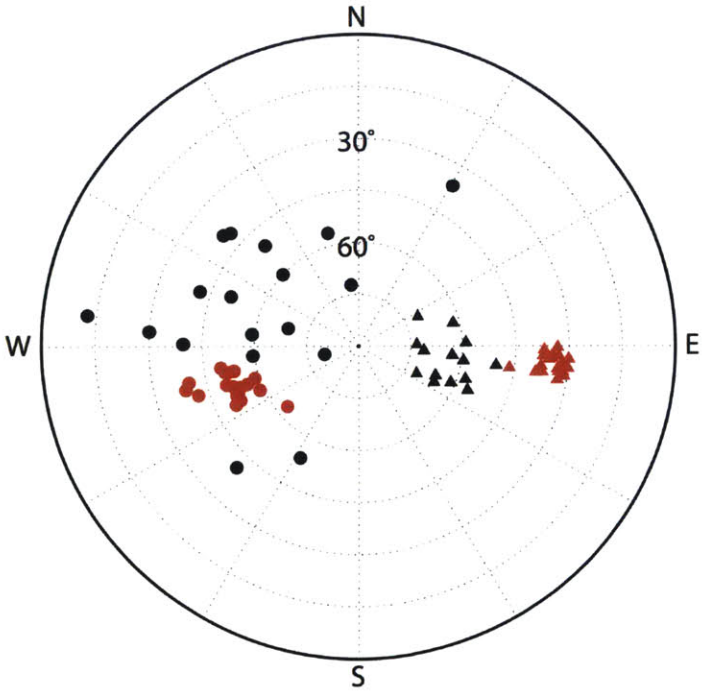

Figure 6.24. Equal area stereonet projection of interpreted VRM overprints in the Millbillillie eucrite. Circles and triangles represent the PCA-fitted directions of M-L and and M-M components, respectively. Black and red symbols represent samples subjected to AF and thermal demagnetization, respectively. All symbols lie in the lower hemisphere.

As a result of this atmospheric heating, 43 of our sub-samples extracted from Millbillillie are interior pieces that carry exclusively extraterrestrial magnetization. These interior samples reveal three components of magnetization upon both AF and thermal demagnetization. The low and medium coercivity components (M-L and M-M, respectively) are stable between 0 – 25 mT and 25 – 70 mT in AF and between 20 – 80°C and 80 – 135°C in thermal demagnetization, respectively. Both components are

unidirectional throughout the sample (>5 cm scale; Fig. 6.24), which suggests that both components are VRMs acquired during the meteorite's ~50 year residence on Earth.

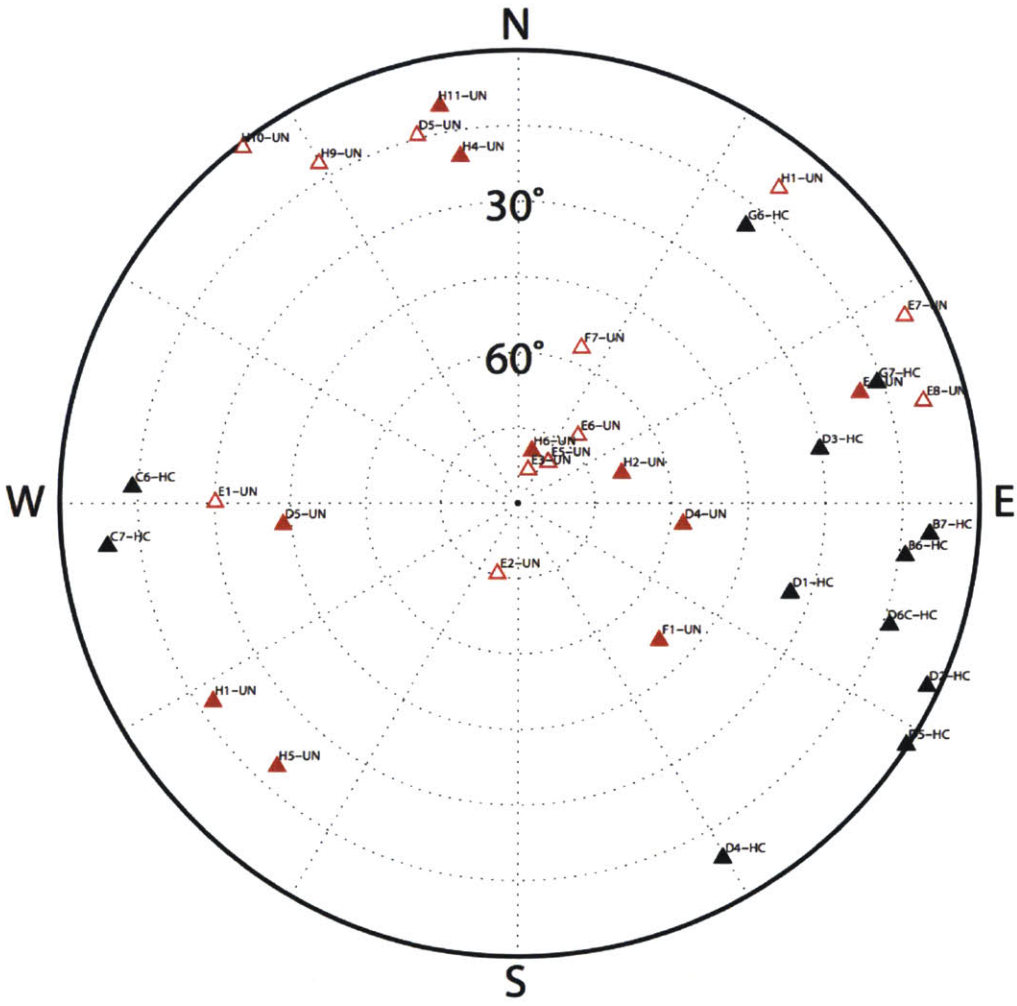

Figure 6.25. Equal area stereonet projection of high temperature and coercivity (M-H) components of magnetization in the Millbillillie eucrite. Black and red symbols represent samples interpreted to belong to unidirectional groups due to their physical proximity in the sample, respectively. Open (closed) symbols lie in the upper (lower) hemispheres.

On the other hand, in light of our VRM acquisition experiments with a duration of 15 days, the expected magnitude of a terrestrial VRM of that duration is 3-8 times weaker than the observed values. In any case, the very low blocking temperatures of the M-L and M-M components are too low for them to have survived more than ~5 years at blackbody temperature of 1 AU (Garrick-Bethell & Weiss 2010), indicating that they

post-dated delivery of the meteorite to the Earth, which took place over the course of ~20 My (Miura et al. 1998).

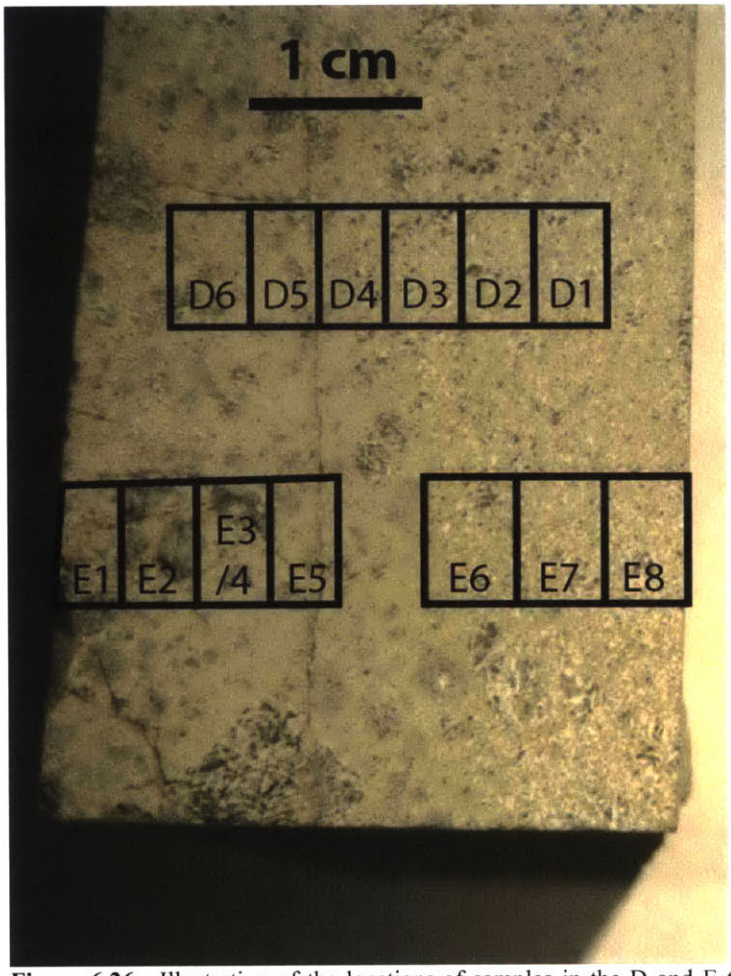

Figure 6.26. Illustration of the locations of samples in the D and E transects of the parent piece of the Millbillillie eucrite. In some cases (e.g., D1-D6, E2-3 and E5-6), physically proximal samples display unidirectional magnetization while samples separated by >1 cm distances are non-unidirectional. A tantalizing but confusing result that may reflect multiple generations of magnetization or non-unidirectional fields during the remanence acquisition process.

The high coercivity component of magnetization (M-H), on the other hand, is blocked from 135°C to >580°C upon thermal demagnetization (70 – 230 mT in AF) and is therefore stable for the age of the solar system, although it must post date the 3.55 Ga heating event. It decays to the origin upon both thermal and AF demagnetization, in the latter case at a rate most similar to an ARM (again compared with an IRM or SRM),

suggesting that it is a TRM. The M-H magnetization is unidirectional on scales up to 2-3 cm (Figs. 6.25 and 6.26). For these reasons the M-H component of magnetization may have been acquired during repeated, heterogeneous heating due to impacts after 3.55 Ga. However, the ambiguity of the origin of this magnetization prevented our publication of these results until further work can be conducted.

ARM and IRM paleointensities for the M-H component of magnetization are between 5 and 10 μT, making them consistent with the values derived from ALH 81001.

Chapter 7: Global geodynamic deformation of Vesta

7.1. Introduction

The terrestrial planets likely formed via the successive accretion of tens to hundreds of kilometer diameter objects known as planetesimals (Chambers 2004). The high abundance of short-lived radiogenic isotopes such as ^{26}Al in the early solar system led to the extensive interior melting of early-forming planetesimals. Thermal evolution models of planetesimals show that bodies as small as 20 km in diameter may have achieved >50% melting if accretion occurred sufficiently early (Hevey & Sanders 2006; Elkins-Tanton et al. 2011; Šrámek et al. 2012). Such high degrees of melting led to full or partial differentiation of these bodies (McCoy et al. 2006).

Differentiated asteroids in the present-day solar system represent a relic population of these early-formed planetesimals. Vesta (mean diameter ~525 km) is the best studied example of a differentiated asteroid. Ground-based spectroscopic studies have previously associated the surface of Vesta with meteorites of the howardite-eucrite-diogenite (HED) clan, whose geochemistries indicate igneous origins on a fully differentiated body (McCord et al. 1970; Binzel & Xu 1993; Righter & Drake 1997). More recently, the NASA Dawn mission, in orbit around Vesta between July 2011 and September 2012, deduced the presence of a metallic core with radius 110 +/- 3 km when assuming a core density similar to that of iron meteorites and measured surface spectra consistent with the HED meteorites (Russell et al. 2012; De Sanctis et al. 2012; Reddy et al. 2012).

Despite evidence for past interior and surface melting, present-day Vesta, similar to all asteroids except for Ceres, exhibits global-scale, non-hydrostatic topography. Orbital mapping of the Vestan surface has revealed the presence of two large (>400 km diameter) and relatively unrelaxed impact basins in the southern hemisphere (Marchi et al. 2012; Schenk, O'Brien, et al. 2012). Furthermore, assuming a core and mantle with uniform densities, the current rotation rate of Vesta corresponds to a hydrostatic shape with flattening factor $f_{eq} = 0.13$ (see Section 7.3). The flattening factor f is defined as $(a - c)/a$ where a and c are the equatorial and polar radii of the best-fit ellipsoid of revolution.

In contrast, the observed best-fit ellipsoid shows greater oblateness, with $f \approx 0.19$ (Ermakov et al. 2014). This equatorial bulge of Vesta represents a non-hydrostatic fossil bulge; it cannot be explained by compensated topography as thickened, isostatically relaxed crust is expected to show a negative Bouguer anomaly. However, no such feature is observed at degree-2 (Ermakov et al. 2014). The correponding global disequilibrium factor $(f - f_{eq})$ of 0.07 is more than three orders of magnitude greater than the value for the Earth (Chambat et al. 2010). The impact basins and the non-hydrostatic bulge may have formed in the same giant impact events, which may contribute to topographic disequilibrium via direct redistribution of mass and change to the rotation period or axis.

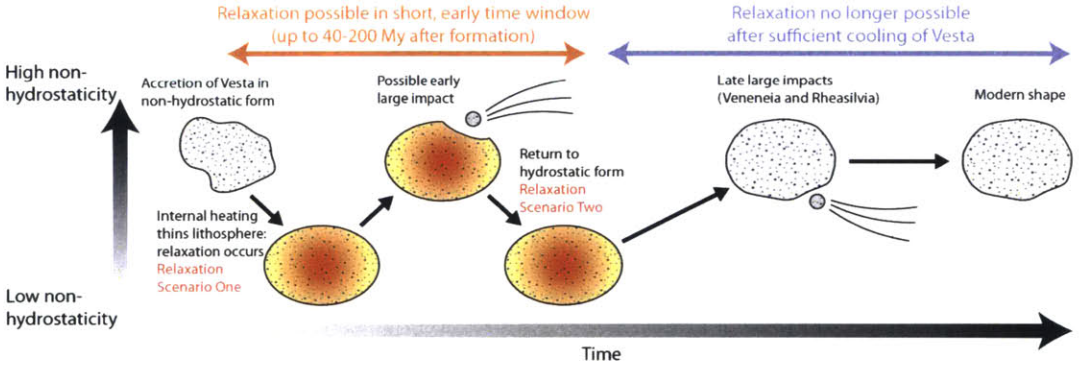

Figure 7.1: Schematic illustration of the evolution of Vesta's long wavelength topography. Upon formation, rapid internal heating (denoted by red-yellow coloration) due to short-lived radiogenic isotopes lead to a differentiated interior with a thin, cold lithosphere. Vesta therefore reached a highly hydrostatic figure with a non-hydrostatic equatorial bulge amplitude of <2 km (see Section 7.3). If early large impacts disturbed the figure of Vesta, subsequent relaxation would restore a high hydrostaticity. By 40-200 My after formation, the Vestan interior had cooled sufficiently to prevent relaxation to a figure more hydrostatic than that of the present day. The late Veneneia and Rheasilvia basin-forming impacts occurred after this transition, thereby imparting a significant non-hydrostatic component to Vesta's observed figure.

Unrelaxed global topography on Vesta and other asteroids is consistent with their low surface gravity and the high strength of cold silicates. Assuming a cool interior, large asteroids such as Vesta experience internal shear stresses on the order of ~1 MPa due to disequilibrium topography and spin axis reorientation (Johnson & McGetchin 1973; Matsuyama & Nimmo 2011), which is insufficient to cause pervasive brittle failure even in previously fractured basaltic masses [schultz1993brittle]. At the same time, viscous relaxation on asteroid-sized bodies with ambient temperatures of the present-day asteroid

belt is expected to require much longer than the age of the solar system (Johnson & McGetchin 1973).

However, given the high degree of past melting in differentiated asteroids such as Vesta, high shear stresses in a thin, chilled surface layer may have led to pervasive brittle failure and associated deformation during Vesta's early history. Likewise, the elevated temperatures may have allowed for viscous relaxation of topography on geologically short timescales.

Relaxation may have occurred on Vesta under two distinct scenarios (Fig. 7.1). In Relaxation Scenario One, Vesta may have relaxed from a non-hydrostatic shape in which it initially accreted. Although it is unclear whether Vesta and other planetesimals formed via large instabilities or incremental growth (Morbidelli et al. 2009; Weidenschilling 2011), no accretion mechanism predicts formation in an already hydrostatic figure. As such, Vesta very likely accreted in a non-hydrostatic shape. Meanwhile, energy from the accretion process was likely insufficient to melt Vesta (Poitrasson et al. 2004; Šrámek et al. 2012). Vesta was therefore at first unable to relax from the non-hydrostatic figure in which it accreted. Short-lived radioactive isotopes subsequently heated the Vestan interior, leading to differentiation and a thin lithosphere on the order of one to several million years (Ghosh & McSween 1998; Tang & Dauphas 2012). Relaxation from the originally accreted shape to a closely hydrostatic one may have occurred at this time.

After the initial relaxation, large early impacts may have led to Relaxation Scenario Two. Such large impacts may have recreated significant non-hydrostatic topography during a brief early window; there is a 12-31% probability that Vesta was struck by a Rheasilvia basin-forming impactor sized object during the first 100 My (Davison et al. 2013). Because the cooling of the Vestan interior occurred gradually (see Section 7.2), Vesta would have been able to return to a closely hydrostatic figure if a large impact occurred sufficiently early. This relaxation may obscure the long wavelength topography introduced by such early impacts, although the lack of compositionally distinct regions on the surface of Vesta excavated by such purported impacts suggests that they did not occur or that they occurred while igneous resurfacing on Vesta was still ongoing. As the interior of Vesta cooled, hydrostatic relaxation would have become impossible during its later history.

Topography on Vesta may therefore consist of a mixture of ancient terrains that achieved hydrostatic equilibrium during an early period of intense heating and late non-hydrostatic features acquired after Vesta cooled sufficiently to prevent further relaxation. Crater retention ages derived from Dawn observations show that the surface of Vesta indeed consists of both old and young terrains. The two large impact basins in Vesta's southern hemisphere are young features that have model ages of 2.1±0.2 (for the Veneneia basin) and 1.0±0.2 (Rheasilvia basin) Ga (Schenk, O'Brien, et al. 2012). Meanwhile, the northern hemisphere of Vesta may have reached crater saturation and likely has not experienced catastrophic reshaping since early in Vesta's history (Marchi et al. 2012).

In this study, we use finite element models to evaluate the potential for hydrostatic relaxation on early Vesta and thereby assess the possibility that hydrostatic terrains exist on present-day Vesta. As described in Section 7.2, we construct numerical viscoplastic deformation models using the deal.II finite element library (Bangerth et al. 2007). The flow model is coupled to a simple secular cooling model for Vesta that takes into account the effects of radiogenic heating and an insulating megaregolith layer. In Section 7.3, we report the expected extent of hydrostatic relaxation as a function of Vesta's age and assumed megaregolith thickness. We find that the global figure of early Vesta was much closer to hydrostatic equilibrium than observed today. We identify a large region in the northern hemisphere of Vesta as a likely relic of this early hydrostatic terrain and use its figure to constrain the rotation period and spin axis orientation of early Vesta. Finally, we discuss the implications of these results for the two late giant impacts and on the expected topography of other asteroids in Section 7.4.

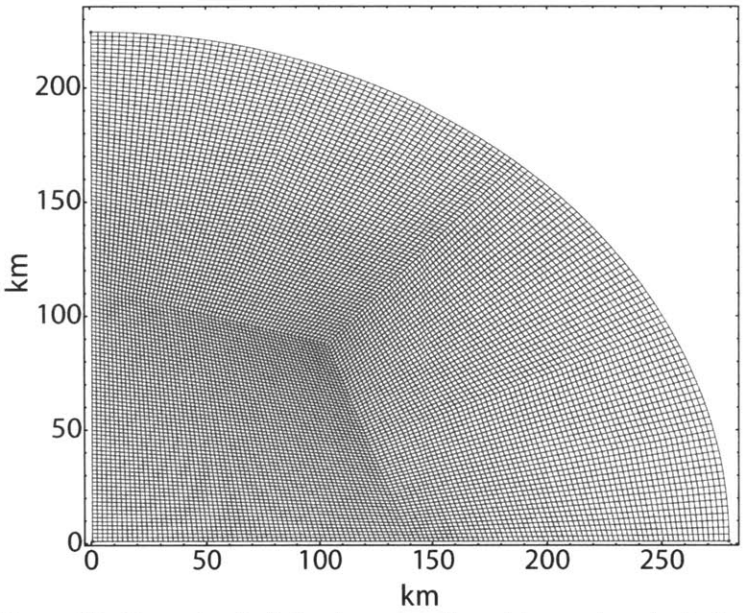

Figure 7.2. Example of a finite element mesh used in our viscoplastic flow simulations. The x- and y-axes represent the equatorial and polar axes, respectively, while the outer figure is one quarter of an ellipse. The mesh shown consists of 12288 cells and corresponds to a flattening of $f = 0.19$, which is the observed present day value for Vesta.

7.2. Finite element and cooling model description

Viscous relaxation model. To simulate the viscous relaxation of Vesta, we set up a numerical Stokes flow model in deal.II, an extensive and broadly applicable finite element library (Bangerth et al. 2007). We use an axisymmetic mesh consisting of between 5.8×10^3 and 1.2×10^4 quadrilateral cells with dimensions between 1.8 and 4.4 km and polynomial degree 1 shape functions (Fig. 7.2). The outer shape of the asteroid and the core mantle boundary are assumed to be ellipsoids of revolution. Symmetry of such bodies permits the simulation of the entire body by performing calculations on only one quadrant. Our solution mesh represents the body in the $x > 0$, $y > 0$ quadrant with the y and x axes corresponding to the polar and equatorial axes of the asteroid, respectively. On this mesh, we solve the Stokes equations, which govern incompressible flow where viscous forces dominate over inertial forces:

$$\partial_j(2\eta\dot{\epsilon}_{ij}) - \partial_i p = -g_i\rho \tag{7.1}$$

$$\partial_i u_i = 0$$

where η is dynamic viscosity, p is pressure, ρ is density, u_i is flow velocity, and ε_{ij} is the strain rate tensor defined as:

$$\dot{\epsilon}_{ij} = \frac{1}{2}\left(\partial_i u_j + \partial_j u_i\right). \tag{7.2}$$

The body acceleration g_i includes only contributions from self gravity and rotation. Self gravity is calculated analytically using the expressions for ellipsoids of revolution derived in (Pohánka 2011). We apply zero pressure and zero traction boundary conditions to the outer surface of the asteroid. By symmetry, we specify the condition of zero normal velocity on the polar and equatorial axes of our domain.

We calculate the initial viscosity of all finite elements as a function of local temperature, which is approximately a function of depth from the surface of the asteroid. The true viscosity contrast between a molten interior and surface at space temperatures is well over 30 orders of magnitude (Solomatov 2000). As in other finite element simulations of planetary interiors, such large viscosity contrasts create numerical instabilities in the solution [e.g., Moresi & Solomatov (1995)]. However, if the lowest specified interior viscosity is sufficiently small compared to the maximum near surface viscosity, the resulting global deformation field does not differ significantly from that calculated with the true, lower interior viscosity (Dombard & McKinnon 2006). In such setups, the interior material is effectively inviscid and global deformation is controlled entirely by the high viscosity near-surface material. Therefore, at all nodes where the viscosity is lower than 2×10^{-5} times the maximum viscosity (η_{max}), we set the viscosity to $2 \times 10^{-5}\ \eta_{max}$. Changing this maximum contrast factor to 10^6 results in less than 3% change in the resulting flow velocities.

Once the governing matrix equation is set up using the appropriate value for η, g_i, and ρ at each node, the stiffness matrix is first preconditioned using LU decomposition before

solution is attempted. We then solve for pressure using an iterative conjugate gradient algorithm. Flow velocities are then calculated directly from the pressure solution (Bangerth & Kronbichler 2008). Benchmark runs on rotating bodies of constant density and on non-rotating multi-layered bodies show that the analytic predictions for hydrostatic figures indeed minimize internal velocities and shear stresses as calculated from our finite element solution.

We account for brittle failure and plasticity in the early Vestan lithosphere. After each run of the finite element flow model, we calculate the local total stress tensor in each cell from the velocity and pressure solution:

$$\sigma_{ij} = 2\eta\dot{\epsilon}_{ij} - p\delta_{ij} \tag{7.3}$$

We then find the principal stresses by diagonalizing σ_{ii} using the Armadillo linear algebra library (Sanderson 2010). We note that, for incompressible, isotropic media, the equation for elastic stress is isomorphic with Eq. 7.3. We find that our calculated stress fields in the early Vestan lithosphere agree closely (<10%) with the elastic model of (Melosh 1977) at all depths, assuming a rigidity of 40 GPa in the high viscosity lid ($\eta > 10^{28}$ Pa s; see below). Because the (Melosh 1977) model applies only to figures with small deviation from equilibrium, the comparisons with this model are based on a Vesta with much smaller degree of disequilibrium ($f - feq = 0.005$) than shapes used in this study (Section 7.3). The early Vestan crust was likely heavily fractured due to impactor bombardment (Davison et al. 2013), and fracture healing processes that operate on the Earth and the Moon likely did not occur as extensively on Vesta due to the asteroid's low interior pressures and absence of igneous activity after the first several 10s of My after Vesta's formation (Wieczorek et al. 2013; Yamaguchi et al. 1996). We therefore assume that the Vestan lithosphere is strengthless under extension (i.e., cohesionless). Where all principal stresses are compressive, we identify locations of brittle failure based on Byerlee's rule (Byerlee 1978; Brace 1980). Failure occurs in cells where the most compressive principal stress σ_1 exceeds $5\sigma_3$ where σ_3 is the least compressive principal stress.

A self-consistent viscoplastic solution requires that the stress tensor does not imply further brittle failure anywhere in the solution domain (Albert et al. 2000). We implement plasticity using an iterative approach whereby the effective viscosity of each cell that experiences brittle failure is lowered after each iteration of the finite element flow model until no cells experience further failure (Kaus 2010; King & Hager 1990). Physically, the effective viscosity accounts for displacement on fractures that are below the spatial scale resolved in the model (Dombard & McKinnon 2006). We compute the new effective viscosity according to the equation:

$$\eta_{i+1}^{k} = \left(\frac{a\sigma_1^k}{b\sigma_3^k}\right)_i^{-1} \eta_i^k \tag{7.4}$$

where η_i^k represents the viscosity of cell k used during the i th iteration, b is a constant specifying the relationship between σ_1 and σ_3 upon failure (equal to 5 for Byerlee's rule), and a is a coefficient that is set to between 1 and 2 in order to control the rate of convergence. Varying a within this range does not affect the final viscosity structure upon convergence. The effective viscosity field after each run is smoothed at the 10-km scale to suppress numerical variations at the single cell level and to enhance model stability. Typically, 20 to 50 iterations were required to converge to an effective viscosity field that produces no significant further brittle failure. The viscous flow velocities of this resulting viscosity configuration represent the final viscoplastic relaxation rate of the body.

Each plasticity-corrected flow field solution represents the instantaneous viscoplastic relaxation rate for Vesta for a given shape and thermal structure. We simulate the time-dependent relaxation of Vesta by running simulations for a range of ages and degrees of disequilibrium. We interpolate these numerical results to find the instantaneous relaxation rate as a function of age and disequilibrium. The time-shape path of Vesta undergoing relaxation from an initial shape and age is then calculated with this interpolated function. Our flow model does not incorporate elasticity and therefore does not account for additional elastically-supported displacement. Large elastic displacements may lead to significant changes in the gravity field of the body; this effect is not accounted for in our

finite element model. However, the weak gravity field of Vesta implies that even thin lithospheres undergo only low-amplitude elastic deformation. Analytic estimates (Melosh 1977) of elastic displacement for Vesta with the present-day degree of non-hydrostaticity indicate that a 20-km-thick lithosphere, which is thinner than the lithosphere thicknesses characteristic of early Vesta (see Section 7.3), allows less than 3 m of elastic displacement at the equator, assuming a rigidity of 40 GPa (Matsuyama & Nimmo 2011). This displacement is small compared to the ~7 km displacement from equilibrium of modern Vesta and does not affect the gravity field.

An intact elastic layer of sufficient thickness can resist relaxation. However, for the high degrees of non-hydrostaticity modeled here, lithospheres on early Vesta undergo pervasive brittle failure and plastic deformation (see Section 7.3). Following (Dombard & McKinnon 2006), we adopt an extended Maxwell rheology for the Vesta lithosphere:

$$\epsilon_{ij} = \epsilon_{ij,elastic} + \epsilon_{ij,viscous} + \epsilon_{ij,plastic} \tag{7.5}$$

where the total strain ε_{ij} is a sum of contributions from the three mechanisms. As such, although an unfractured, cold lithosphere on Vesta would undergo only minor elastic deformation, an extensively fractured lithosphere may undergo significant total deformation dominated by the plastic component.

Thermal evolution and base viscosity model. Due to the strong dependence of viscosity on temperature, the rate of viscous relaxation depends heavily on the thermal evolution of the asteroid interior. The initial heating of early-accreting asteroids smaller than \sim 1000 km diameter is dominated by the decay of short-lived radionuclides, with impacts making a negligible contribution. Assuming cooling only by conduction, asteroids larger than 20-50 km diameter that accreted within 1.5 My of CAIs are expected to melt fully, except for a thin crust with thickness of order $(\kappa\tau)^{1/2}$, where κ is the near-surface thermal diffusivity and $\tau^{1/2}$ is the half-life of ^{26}Al, the dominant heat source for early planetesimals (Šrámek et al. 2012). Using a value of $\kappa = 5 \times 10^{-7}$ m^2 s^{-1} for a fully sintered crust Hanley et al. (1978) and $\tau_{1/2} = 7.17 \times 10^5$ years, the thickness of the unmelted crust is estimated to be ~3 km. Intrinsic microporosity of chondritic material in

the crust and additional macroporosity generated by impact brecciation may lower the value of κ by more than one order of magnitude (Warren & Rasmussen 1987). Furthermore, the onset of melting in the asteroid interior would steepen the near surface thermal gradient (Hevey & Sanders 2006). Both effects would lead to potentially much thinner crusts. The lack of primordial chondritic material on the Vestan surface also strongly suggests the past presence of extensive melting at shallow depths. On the other hand, accretion of Vesta some time [perhaps >1 M; Elkins-Tanton et al. (2011)] after the formation of CAIs would dramatically decrease its initial budget of short-lived radiogenic isotopes, leading to a thicker solid lid. We adopt an initial ~10 km conductive lid as an upper bound that is in good agreement with numerical results for heating in Vesta (Ghosh & McSween 1998).

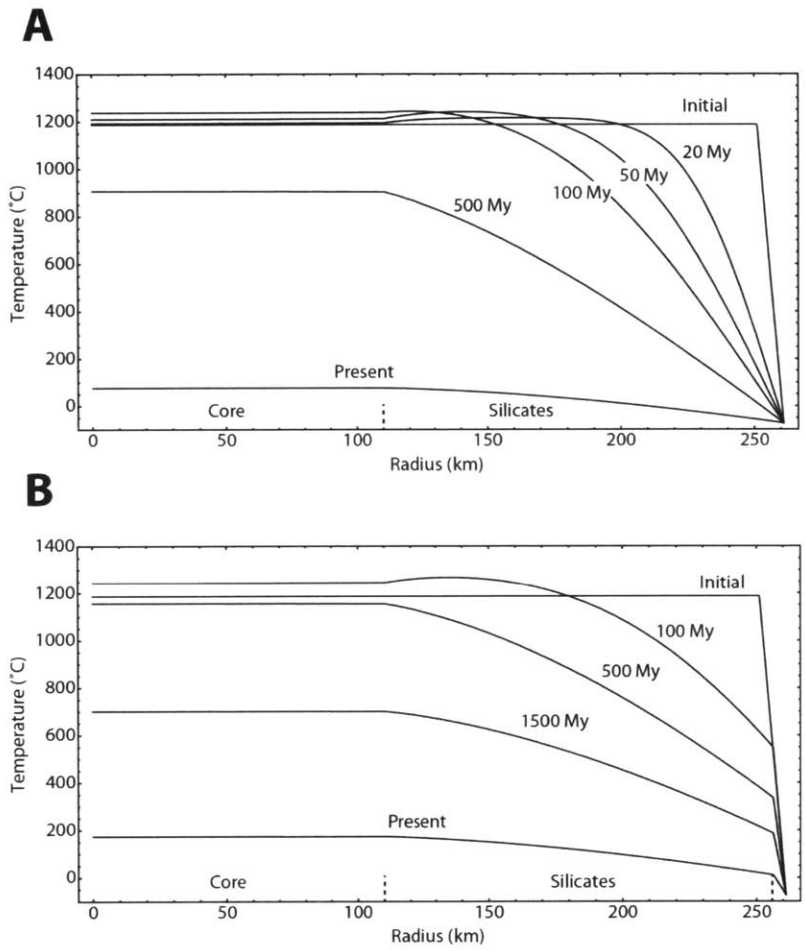

Figure 7.3. Thermal evolution of Vesta assuming (A) no megaregolith and (B) 5 km thick megaregolith. The assumed initial temperature profile consists of an isothermal interior at 1200°C underlying a 10 km conductive lid with a linear temperature profile. Decay of long-lived radioisotopes cause initial heating in the deep interior. Dashed line segments on the *x*-axis indicate the interfaces between the core, intact silicates, and megaregolith layers.

We begin our conductive cooling model at the point of convective shut down. The uniform initial interior temperature is therefore chosen to be that at which the Vestan mantle ceases to support convective flow. The 10 km thick overlying lid is assumed to have a linear, conductive thermal profile (Fig. 7.3). We adopt 1200°C for the deep interior temperature, which is close to the rheological transition for dunite, the expected primary constituent of the Vestan mantle (Righter & Drake 1997; Berckhemer et al. 1982). Below this temperature, rocks develop greater resistance to shear stress and would resist convection.

Due to this setup, all ages in our thermal evolution models refer to time after the cessation of convection. The duration of convection has been estimated to be <1 My and <<30 My (Neumann et al. 2014; Sterenborg & Crowley 2013). Because this interval is short in comparison to the ages at which we run our finite element deformation models, the ages relative to the shutdown of mantle convection closely approximate those relative to the formation of Vesta. The overlying conductive lid is 10 km thick with top and bottom temperatures of -73°C and 1200°C, respectively. The surface temperature is chosen to be close to the black body temperature (188 K) for a rapid rotator at the current orbital radius of 2.36 AU. We note, however, that the thermal state of Vesta more than several 10s of My after initial formation is relatively insensitive to the initial thermal profile assumed and, instead, is a stronger function of the thermal diffusivity structure assumed.

Using this initial temperature profile, we create 1D numerical models of subsequent conductive cooling in a spherical geometry in *Mathematica*. We take into account heat generation from radionuclides and the different thermal diffusivities of the core, unbrecciated silicate, and megaregolith layers. This cooling process is governed by the diffusion equation in spherical coordinates (Haack & Rasmussen 1990):

$$\frac{\partial T}{\partial t} = \frac{W(t)}{c_p} + \frac{1}{r^2}\frac{\partial}{\partial r}\left[\kappa(r)\, r^2 \frac{\partial T}{\partial r}\right] \tag{7.6}$$

where $W(t)$ is the per unit mass heat production due to long-lived radioisotopes, c_p is the specific heat capacity, and $\kappa(r)$ is the thermal diffusivity that varies with radius. We assume that Vesta has approximately Earth-like radioisotopic composition. The parameter $W(t)$ therefore consists mainly of contributions from the isotopes ^{232}Th, ^{238}U, ^{235}U, and ^{40}K, the last two of which have half-lives much shorter than the lifetime of the solar system. As a result, the total radiogenic heat flux from long-lived radionuclides decreased by a factor of ~3 from 4.5 Ga to the present day. In our cooling model, we use a single exponentially decaying $W(t)$ that approximates the sum of contributions from the radioisotopes listed above (Turcotte & Schubert 2002).

The insulating effect of high-porosity material at shallow depths can have a dramatic effect on the cooling rate of asteroids (Haack & Rasmussen 1990). As in the case of the Moon, the near-surface region of asteroids is expected to consist of finely-brecciated regolith overlying a deeper megaregolith consisting of fractured bedrock. The regolith layer may have thermal diffusivities up to two orders of magnitude lower than that of intact rock, while the thermal diffusivity of the megaregolith is \sim 1 order of magnitude lower than that of the underlying bedrock. In the meantime, the metallic core of differentiated asteroids is expected to have a much higher thermal diffusivity and therefore a nearly isothermal temperature profile. We adopt thermal diffusivities of 2×10^{-5} m^2 s^{-1} for the metallic core, 5×10^{-7} m^2 s^{-1} for unbrecciated silicates, and 5×10^{-8} m^2 s^{-1} for the megaregolith (Hanley et al. 1978; Haack & Rasmussen 1990).

Although Dawn observations confirm the presence of a significant megaregolith layer on present-day Vesta (Denevi et al. 2012; Hoffmann et al. 2012), the thickness of the megaregolith layer is difficult to estimate. Meanwhile, impact modeling suggests that the depth of megaregolith on the lunar surface is approximately 2 km, or 0.1% of radius of the moon (Aggarwal & Oberbeck 1979), although recent high-resolution gravity from the GRAIL mission (Zuber, Smith, Lehman, et al. 2013) indicates that the lunar crust may be substantially more fractured than previously thought (Zuber, Smith, Watkins, et al. 2013).

The depth of the megaregolith on asteroids may be significantly greater due to the lower confining pressure. An early model for ejecta build up on large asteroids predicts between ~1 and >4 km of megaregolith and regolith accumulated over the history of the solar system (Housen et al. 1979). A more recent model using a different assumed frequency of large impacts predicts that present-day megaregolith thickness can reach 1-5% of the body radius for asteroids, which corresponds to a 2.6 to 13 km thick layer on Vesta (Warren 2011). Most of this megaregolith may have formed due to a few large impacts, which occurred late in the history of Vesta. Therefore, coverage of megaregolith on early Vesta may have been much thinner and accumulated over time. In this work, we adopt megaregolith depths of 0 km and 5 km as lower and upper bounds for Vesta.

Assumption of other compositions for the Vestan mantle, such as that of lunar basalts, can result in differences up to a factor of 3 in the radiogenic output power (Haack & Rasmussen 1990). Furthermore, the thermal diffusivity of the intact mantle is uncertain to

a factor of 1.5-2 (Hanley et al. 1978; Laneuville et al. 2013), while the inclusion of a surface regolith layer with lower conductivity can lower the bulk thermal diffusivity of the brecciated surface layers by ~40% (Warren 2011). However, varying these parameters within the stated ranges lead to differences in the resulting temperature profiles smaller than the variations caused by varying the megaregolith thickness between 0 and 5 km. Therefore, our models using these two end-member megaregolith thicknesses provide the full range of likely thermal profiles at a given time. We note that major impact events can excavate deep hot material and have a significant influence on the cooling rate of planetesimals (Davison et al. 2012). This potential effect is not included in our models. Finally, the ascent of magma, which led to the formation of the eucritic surface, may have resulted in more rapid heat transfer through the crust. However, as noted above, our conductive thermal model begins at cessation of convection in Vesta. The extraction of eucritic melts likely occurred quickly after the convective lock up of the Vestan magma ocean when interior crystal fraction was 60-70% (Mandler & Elkins-Tanton 2013). Therefore, heat transport through the Vestan crust due to melt ascent likely ceased before the complete freezing of the interior and shortly after the cessation of convection.

Once the temperature profile for a given age is found, we then calculate the corresponding initial effective viscosity profile using a stress-dependent Arrhenius-type relationship. Although laboratory experiments on terrestrial mantle rocks can directly constrain viscosities at higher temperatures near the melting point [e.g., >1200°C; Hirth & Kohlstedt (1996)], such results cannot be easily extrapolated down to temperatures relevant to the near-surface of asteroids. In particular, extrapolated viscosities for the oceanic lithosphere at 300-600°C appear to be be signficantly higher than required to match the inferred elastic thickness of the oceanic lithosphere beneath seamounts (Watts & Zhong 2000; McNutt & Menard 1982). However, due to possible effects of fluids in the oceanic lithosphere, inferred viscosities from seamount-induced deformation may not be fully applicable to dry asteroids such as Vesta. Therefore, we adopt dry olivine viscosities as an upper bound estimate on the viscosity of the Vestan interior (Hirth & Kohlstedt 1996):

$$\eta(T) = \frac{1}{2} A^{-1} \sigma_{visc}^{-2.5} e^{Q/RT} \text{ Pa s} \tag{7.7}$$

where A is a constant equal to 4.85×10^4 s^{-1} $MPa^{-3.5}$, Q is the activation energy for dislocation creep, empirically found to be 535 kJ mol^{-1}, T is the temperature, and R is the ideal gas constant. We ignore the pressure dependence of Q since lithostatic pressures characteristic of the Vestan lithosphere are on the order of several 10s MPa. Such pressures increase the value of Q at the 0.1% level (Hirth & Kohlstedt 1996), which is well below experimental uncertainty and the systemic uncertainties of extrapolation to low temperatures. The viscosity also depends on the applied shear stress σ_{visc}. Because the high viscosity regions of Vesta that govern the rate of viscous relaxation are located in the lithosphere in zones of brittle failure, σ_{visc} is similar to the characteristic shear stresses at the point of brittle failure in the lithophere. We therefore adopt a value of 50 MPa as a typical value for σ_{visc} (see Section 7.3).

Viscosities calculated from Equation 7.7 increase very rapidly at low temperatures, growing by nearly 30 orders of magnitude between 600°C and 200°C. Such large viscosity contrasts cannot be reliably solved on our finite element mesh. However, materials with sufficiently high viscosity behave as elastic or elastoplastic solids on a finite timescale, and the calculated deformation field is insensitive to the viscosity chosen for such material (Zhong & Zuber 2000). The characteristic timescale of deformation is given by $\tau \approx 2\varepsilon\eta_{char}/\sigma_{char}$, where ε is the strain achieved in timescale τ, η_{char} is a characteristic viscosity, and σ_{char} is a characteristic shear stress. Even for a body significantly out of hydrostatic equilibrium such as present-day Vesta, relaxation to a hydrostatic state corresponds to a strain of ~0.03 (as discussed below in Section 7.3, the equatorial disequilibrium topography is ~7 km, which is 0.03 of the radius). Meanwhile, our adopted yield criterion implies maximum lithospheric stresses on the order of 5×10^7 Pa. Adopting 4.5 Gy as the longest relevant timescale, materials with viscosity >>2×10^{26} Pa s can be considered free of viscous deformation for the hydrostatic relaxation of Vesta. We therefore truncate all values of viscosity greater than 10^{28} Pa s and set the viscosity at all nodes with higher viscosities to 10^{28} Pa s. These purely temperature-

dependent base viscosity profiles are then subject to plasticity correction as described above.

7.3. Results

Viscous relaxation. Our conductive cooling models result in temperatures somewhat lower than those at the corresponding times from Ghosh & McSween (1998). By choosing to begin our conductive cooling model after convective shut down, we allow for the possibility that heat generated by short-lived radiogenic isotopes within the first few My after the formation of Vesta was quickly lost via convection. Therefore, the large temperature increases during the first ~100 My in the conductive models of Ghosh & McSween (1998) do not appear in our model because such high degrees of heating would have triggered efficient convection and rapid cooling within a short early timespan of <1 to several My (see Section 7.2). The global cooling history of Vesta depends strongly on the assumed thickness of the megaregolith layer (Fig. 7.3). Due to its low thermal conductivity, the megaregolith layer leads to the formation of a boundary layer that can sustain several hundred degrees of temperature contrast and substantially slow the cooling process of the asteroid. The rate of viscous relaxation and the extent of hydrostatic equilibrium are therefore closely tied to assumptions about the thickness of the megaregolith. Specifically, the timespan over which viscous relaxation is a relevant process on Vesta increases significantly with greater megaregolith depth.

In the case of no megaregolith, we simulate the viscous relaxation of Vesta for a range of ages between 15 and 60 My since its initial formation and for a range of non-hydrostaticity. Temperature profiles earlier than these ages are more strongly influenced by the assumption of initial conductive lid thickness. Furthermore, Vesta may have achieved very high degrees of equilibrium (e.g., equatorial bulge amplitude <1 km; see below); however, due to the large number of impacts that have resulted in topography of this amplitude (Marchi et al. 2012), such high degrees of relaxation cannot be maintained throughout solar system history and are not observable today. We therefore exclude very early ages from our relaxation models.

We parameterize departure from hydrostaticity using the disequilibrium factor $f - f_{eq}$. The hydrostatic flattening factor f_{eq} is a function of internal mass distibution and the rotation rate. The rotation rate of early Vesta may have changed several times due to giant impacts with similar magnitudes as the Rheasilvia event [davison2013earlyimpacts]. The true rotation rate for very early Vesta is therefore uncertain. However, the rate of viscous relaxation is a strong function of the difference $f - f_{eq}$ and only weakly dependent on the value of f_{eq} itself. We therefore avoid any a priori assumptions about the early rotation rate of Vesta and adopt the present-day rotation period of 5.34 hr to calculate f_{eq} (Russell et al. 2012).

To find the value of f_{eq}, we apply our finite element flow model to a range of trial surface and core flattening factors. For each assumed geometry, we calculate the viscous flow field given uniform viscosity and identify the surface and core flattening factor pair that minimizes internal shear stresses. Note that these uniform viscosity setups are only used to identify the equilibrium flattening; models for viscoplastic relaxation of Vesta use realistic viscosity contrasts as described in Section 7.2 Our method of calculating the equilibrium give identical results compared to first-order analytic theory for small flattening ($f \leq 0.1$), in which regime the analytic theory is most valid (Ermakov et al. 2014). Given the modern rotational period and totalTotal volume is of the best-fit ellipsoid. and core volumes of 7.46×10^{15} and 5.58×10^{15} m^3 (Russell et al. 2012), respectively, the equilibrium flattening factor of the outer surface is $f_{eq} = 0.128 \pm 0.002$ while the core is less oblate at $f_{eq,core} = 0.093 \pm 0.005$. The observed figure of Vesta therefore has a disequibrium factor of 0.065.

We perform our calculations using a range of trial disequilibrium factors potentially relevant to early Vesta. For Relaxation Scenario One (i.e., initial relaxation from non-hydrostatic accreted shape; see Section 7.1 and Fig. 7.1, the initial accreted shape of Vesta is unknown and the disequilibrium factor may have been very large, potentially greater than the present-day value. For Relaxation Scenario Two (i.e., after an early giant impact), the post-impact non-hydrostaticity was likely similar to that of modern Vesta, which is non-hydrostatic primarily due to two late giant impacts. We therefore adopt a disequilibrium factor of 0.082, which is moderately higher than the modern value, as an upper bound to our range of trial non-hydrostaticities. At the same time, we adopt 0.021

as the lowest trial disequilibrium factor. As discussed above, a large number of impacts capable of excavating >1 km exist on the surface of Vesta (Marchi et al. 2012); therefore, a very closely hydrostatic ancient figure with $f - f_{eq}$ <0.021 would not be readily preserved today.

In all simulations, we assume a core flattening of 0.093. Although this value is correct for the equilbrium figure at the present rotation rate, varying the outer figure of Vesta in principle changes the equilibrium core shape [e.g., Dermott (1979)]. For example, the equilibrium core flattening for the most non-hydrostatic assumed shape ($f - f_{eq} = 0.082$) is 0.12. However, differences in the assumed core figure within this range result in negligible variations in the surface relaxation rate.

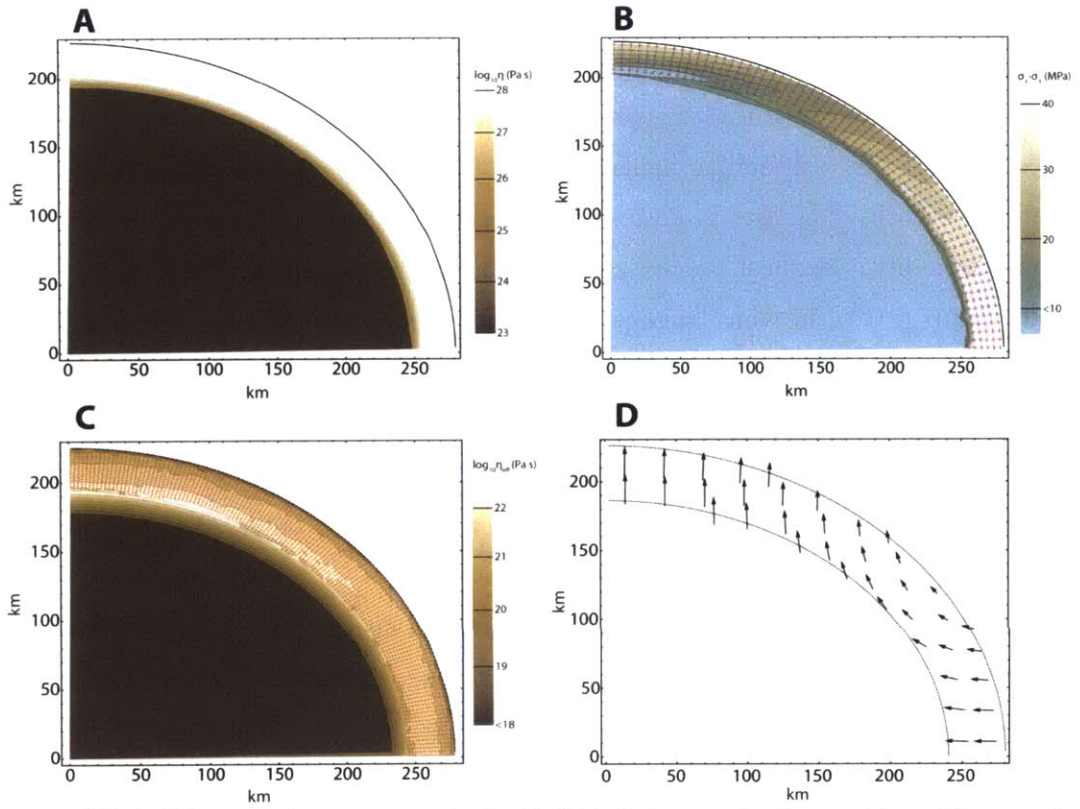

Figure 7.4. Initial setup and converged result of an individual viscous relaxation model run. The geometry and thermal structure shown correspond to Vesta with its present day shape (f = 0.19) at 30 My after convection shut down. The vertical and horizontal axes represent the polar axis and equator, respectively. (A) The initial viscosity structure based directly on the thermal profile. Viscosities above 10^{28} Pa s and below 10^{23} Pa s are set to those values, respectively (see Section [sub:Thermal-model]). (B) Shear stress ($\sigma_1 - \sigma_3$) field corresponding to the initial viscosity. Blue and red segments mark the direction of the more and less compressive stress in the r-z plane, respectively. One set of segments is plotted for every fourth finite element for clarity. Note that the direction of σ_1 and σ_3 may be in the azimuthal direction. Stress in large portions of the lithosphere imply failure according to Byerlee's rule. The effective viscosities at these

failing locations are therefore iteratively reduced to simulate plastic deformation until shear stresses do not lead to additional failure anywhere (see Section 7.2). (C) Converged effective viscosity field after iterative adjustment of local viscosity at points of brittle failure to reflect plasticity shows a limited effective viscosity range in the lithosphere and a thin transition zone to an effectively inviscid deep interior. Red points indicate cells where brittle failure occurred. Stresses at all finite element nodes imply no additional failure (according to Byerlee's rule). (D) The resulting viscous flow field in the lithosphere reflects the excess initial flattening. Vector length is directly proportional to local flow velocity. The longest vector represents a velocity of 20.0 km My^{-1}.

For $f - f_{eq}$ between 0.021 and 0.082, we find that brittle failure occurred pervasively during Vesta's early evolution. For the no megaregolith case, in the first 15-60 My after convective shut down, the lithosphere of Vesta (defined as the chilled near-surface layer that does not deform viscously over geological timescales) is between 15 and 30 km thick (Fig. 7.4A). Sufficient stresses build up in the thin lithosphere to imply extensive failure according to Byerlee's rule (Fig. 7.4B). At these ages for these large values of $f - f_{eq}$, the lithosphere is fully elastoplastic and no purely elastic layer survives (Fig. 7.4C). In contrast, the deep interior undergoes purely viscous deformation. After accounting for plasticity, effective viscosities in the lithosphere vary across two to three orders of magnitude (Fig. 7.4C), which is very narrow compared to the >10 orders of magnitude contrast in base viscosity as dictated by the temperature profile alone. Equatorial and polar regions experience higher shear stresses than intermediate latitudes, resulting in more extensive brittle failure and low effective viscosity at greater depths in these regions. Due to the steep temperature and viscosity gradient during Vesta's early history, high shear stresses and brittle failure do not occur beneath an abrupt transition depth, which represents the bottom of the lithosphere. Material beneath this depth behaves as an inviscid fluid in the deformation process while the overlying lithosphere controls the rate of relaxation. The thickness of the plastic layer is primarily a function of the degree of disequilibrium as more strongly non-hydrostatic figures cause more extensive fracturing that penetrates to greater depth.

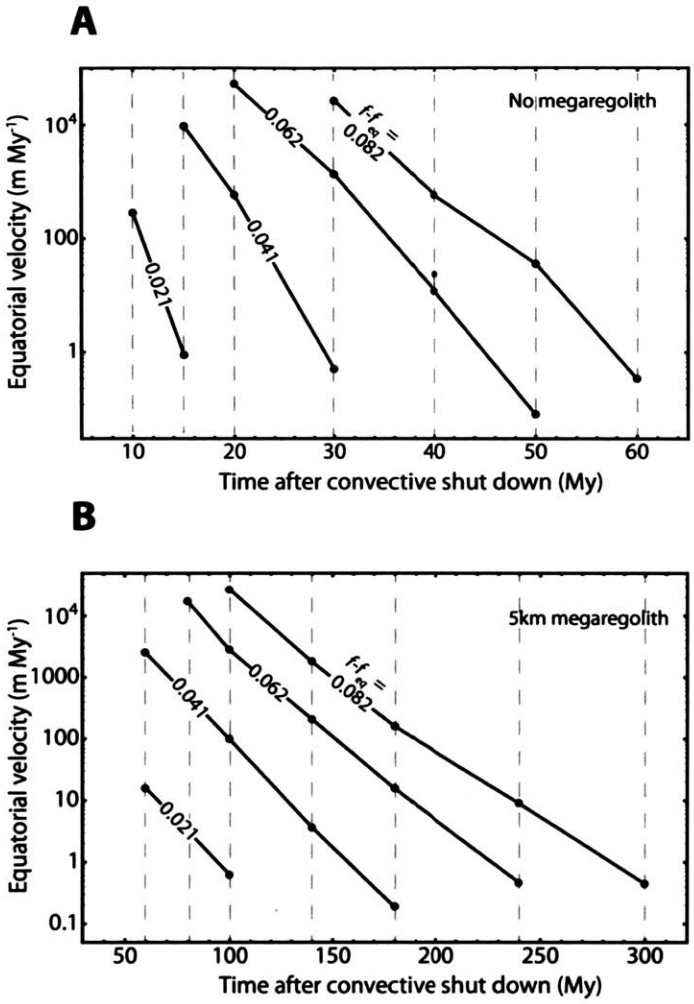

Figure 7.5. Relaxation rate of viscous flow at the equator as a function of age and non-hydrostaticity for (A) no megaregolith and (B) 5 km megaregolith. Black dots represent results of individual numerical simulations. Flow velocity varies nearly exponentially with both age and degree of disequilibrium. Note that evolution in relaxation velocity occurs over a much longer timescale in the case of a thick megaregolith. Red point in part (A) indicates velocity calculated using a 5.02 hr period to obtain f_{eq} instead of 5.34 hr.

The rate of viscous relaxation, which is calculated from the flow field after implementation of plasticity (Fig. 7.4D), for a given degree of disequilibrium decreases rapidly with increasing age (Fig. 7.5). We can explain the trends in Fig. 7.5 as follows. At timescales of several 10s to 100 My, the cooling at a given interior position is approximately linear. As such, the characteristic effective viscosity of the plastic layer increases exponentially with age while the rate of relaxation slows correspondingly. The rate of viscous relaxation is also a nearly exponential function of $f - f_{eq}$. As discussed

above, the thickness of the plastic layer increases with greater non-hydrostaticity. Given that the temperature profile in the Vestan mantle is nearly linear with respect to depth, the base of the thicker plastic layer samples a region of higher temperature and lower viscosity. Therefore, the characteristic viscosity of the plastic layer decreases rapidly with greater $f - f_{eq}$, resulting in a faster rate of relaxation.

Varying input parameters in the finite element model such as the maximum pre-plasticity viscosity, the maximum allowed viscosity contrast, the mesh refinement, and the convergence coefficient a results in variations of the final relaxation rate by less than a factor of 2 and typically within 20%. We find these model-dependent uncertainties to be negligible given the much larger variations of relaxation rate with age and $f - f_{eq}$ and systemic uncertainties such as the viscosity model and the adopted thermal diffusivities.

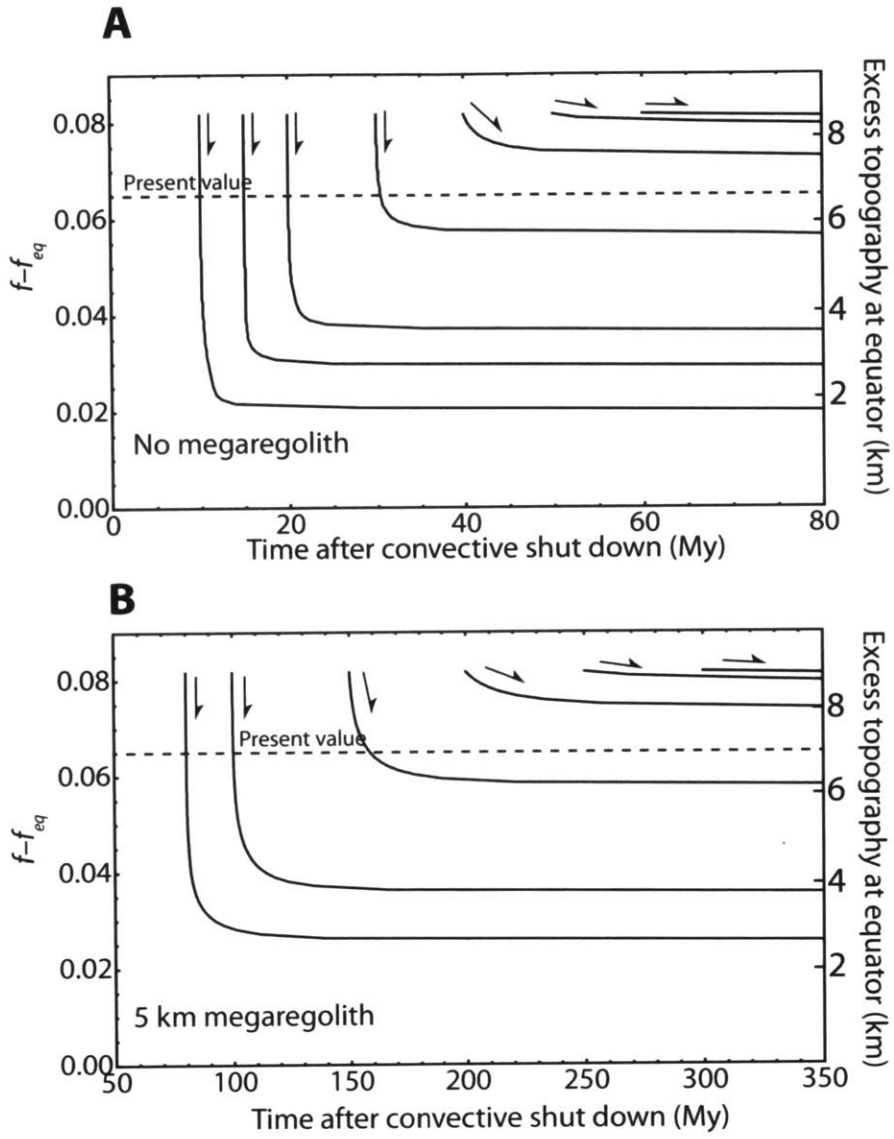

Figure 7.6. Possible relaxation paths of Vesta at a range of ages for (A) no megaregolith and (B) 5 km megaregolith. Vesta was able to relax to more hydrostatic figures during its earliest history. The observed present-day disequilibrium ($f - f_{eq} = 0.062$) was only possible after ≈4.52 Ga for the no megaregolith case and ≈4.36 Ga for 5 km megaregolith. Note that there is no constraint on whether Vesta followed any particular path. These projected relaxation paths indicate the amplitude of non-hydrostatic topography that could be supported by the Vestan lithosphere at each time: the disequilibrium factor at which each path bottoms out is the amount of non-hydrostaticity that could be sustained at the initial age for that path.

We limit our finite element models to the cases where the equatorial instantaneous relaxation rate is between ~1 and ~10^5 m My^{-1}. For relaxation rates slower than ~1 m My^{-1}, the relaxation timescale, defined as the amplitude of the non-hydrostatic anomaly

(order 10^3 m) divided by the relaxation rate, is longer than 10^3 My, which is far longer than the cooling timescale of Vesta. In such a case, little relaxation is achieved before Vesta has cooled sufficiently to prevent further relaxation. Any configuration with such low relaxation rates would therefore maintain its shape for the age of the solar system, which correspond to a flat trajectory in Fig. 7.6. Explicit modeling of further shape evolution (i.e., at even lower velocities) becomes unnecessary. On the other hand, the relaxation timescale is $<10^4$ years for instantaneous relaxation rates of $>10^5$ m My^{-1}, implying that relaxation occurs quickly with respect to the cooling timescale of Vesta. In such cases, which correspond to nearly vertical trajectories in Fig. 7.6, Vesta's figure would relax until a new figure is achieved that has relaxation timescale similar to the cooling timescale. Explicit modeling of cases with higher relaxation velocities (i.e., at higher non-hydrostaticities) is unnecessary as the ultimate figure achieved would remain the same.

Vesta at an earlier age was able to achieve a closely hydrostatic figure (Fig. 7.6). For the no megaregolith case, Vesta was initially able to relax from a non-hydrostatic accreted shape to a disequilibrium factor $f - f_{eq} \leq 0.02$. This degree of hydrostaticity was maintained for at least the first ~15 My after formation. Although such values of $f - f_{eq}$ are still large compared to that observed on the terrestrial planets, they are similar to the upper bound for unrelaxed global topography on Ceres (Thomas et al. 2005), which is widely considered to be hydrostatically relaxed and is therefore classified as a dwarf planet. If early giant impacts occurred, Vesta would have been able to relax to a more hydrostatic figure than that of the present before ~4.52 Ga, or ~40 My after formation.

A thick megaregolith layer significantly extends the time window in which Vesta was capable of maintaining hydrostatic equilibrium. In the 5-km-thick megaregolith case, $f - f_{eq}$ remained below 0.02 during the first ~80 My while the modern degree of non-hydrostaticity was possible only after ~4.36 Ga (Fig. 7.6B). The temperature gradient below the megaregolith layer is shallower in the 5 km megaregolith case. Even so, as in the no megaregolith case, this gradient is sufficiently steep to cause a narrow transition zone (thickness ~15 km) from a high-viscosity plastic surface layer to an effectively invisicid interior. The 0 km and 5 km megaregolith cases are therefore closely analogous

in their rheological structure; the primary difference is that similar temperature profiles correspond to much later ages in the 5 km megaregolith case.

In summary, our finite element flow and conductive cooling models indicate that, with probable extents of internal heating, Vesta should have initially achieved a hydrostatic figure with $f - f_{eq}$ less than 0.02. It then maintained a figure with $f - f_{eq}$ less than the present value of 0.065 during the first 40-200 My after formation, depending on the assumed thickness of megaregolith. Global non-hydrostatic topography of the amplitude observed in the present must have been acquired after this early hydrostatic epoch, implying that the Veneneia and Rheasilvia impact basins post-date 40-200 My after formation.

Relic hydrostatic terrains. Our viscous relaxation models suggest that Vesta achieved a nearly hydrostatic global figure early during its history and raise the possibility that hydrostatic terrains from early Vesta are present on the surface of the asteroid today. Although Vesta was subject to two late giant impact events, terrains far from these impact basins may have remained largely undisturbed until the present and may reflect the morphology of Vesta's early hydrostatic surface. The northern hemisphere of Vesta shows high crater densities. Some regions (the heavily cratered terrains or HCTs) are at or near crater saturation and may date to the first several 100s My after Vesta's formation (Marchi et al. 2012). Furthermore, unsaturated regions adjacent to the HCTs exhibit few craters larger than ~50 km, suggesting that they may still faithfully preserve ancient topography at the longest wavelengths.

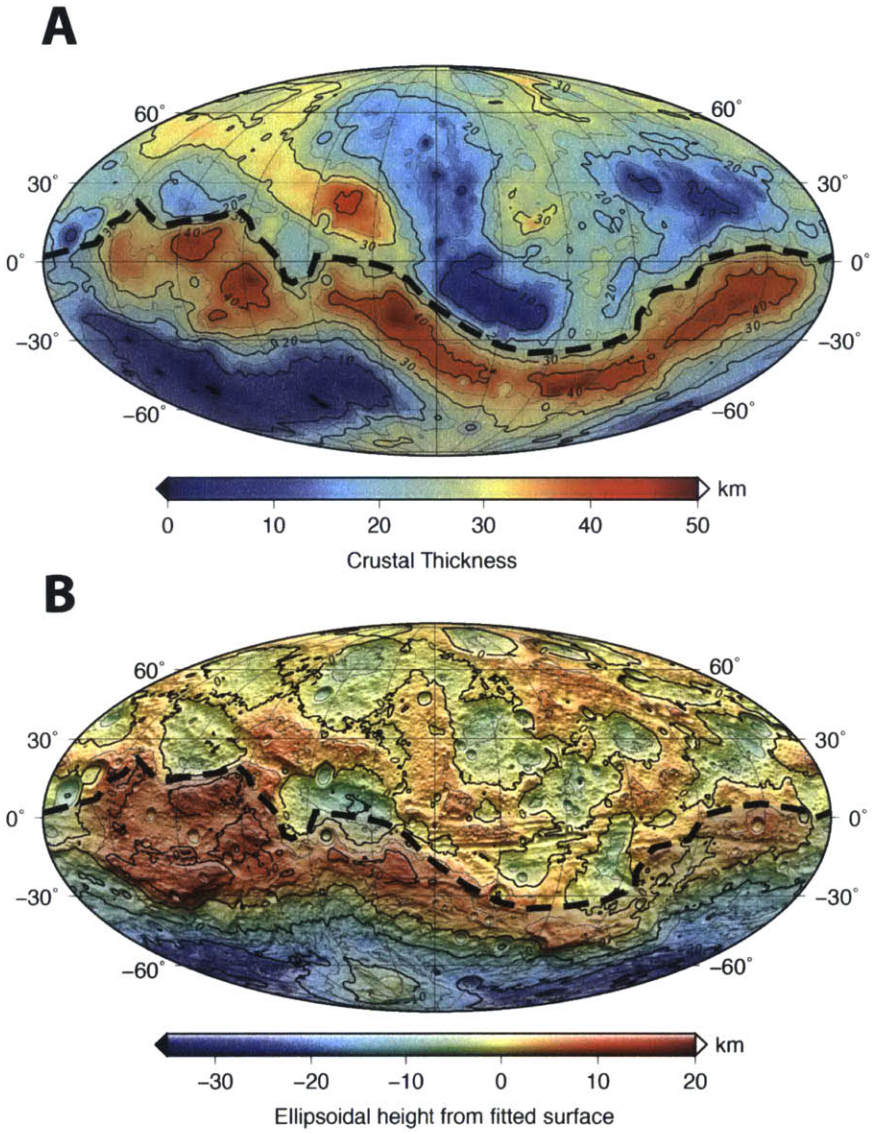

Figure 7.7. Definition of fitted region and residuals for the ellipsoid fit to the northern undisturbed terrains. (A) Crustal thickness map from Ermakov et al. (2014) showing the undisturbed terrains (north of dashed boundary) used to fit to a triaxial ellipsoid. The belt of high crustal thickness near the equator is a consequence of one or both giant impact events near the present-day south pole. Terrains north of this belt show near-saturation cratering density and likely have not suffered significant disruption since the early history of Vesta when viscious relaxation was rapid. Note that crustal thicknesses shown here are relative and that absolute crustal thickness cannot be uniquely determined for Vesta (Ermakov et al. 2014). (B) Residual topography of the ellipsoid fit as defined by the difference between the observed surface of Vesta and the fitted ellipsoid along a line normal to the fitted surface. Bold and light black contours indicate 10 and 5 km intervals, respectively. Residuals within the northern undisturbed terrains are below 10 km, in contrast to the terrains to the south. Southern terrains are lightly shaded in both panels for clarity.

At the same time, giant impact simulations suggest that ejecta from the Rheasilvia basin-forming event created a belt of increased crustal thickness near the present-day equator and that surface topography north of this equatorial ridge likely underwent minimal modification (Jutzi & Asphaug 2011; Jutzi et al. 2013; Ivanov & Melosh 2012). Crustal thickness maps derived from Bouguer gravity anomalies show a clear ring of high crustal thickness in the equatorial region (Fig. 7.7). The terrain to the north of this belt exhibits significantly more subdued topography than the surface inside the impact basins, which is consistent with a relative absence of major reshaping due to large impacts in this region (Fig. 7.7B).

Table 7.1: Output of ellipsoid fit to northern terrain

Radii (km)			Center off set (km)			Axes orientations		
a	b	c	Δx	Δy	Δz	a	b	C
280.6	274.6	236.8	-0.8	-0.2	-5.7	17.3°	107.3°	-177.3°
						2.9°	0.8°	87.0°

Note: The results of fitting the northern undisturbed terrains to a tri-axial ellipsoid with unconstrained position and orientation. The two rows for angles defining the axes orientations are planetocentric latitude and longitude, respectively, of the intersection of the principal axis of the fitted ellipsoid and the surface of Vesta. Both the center offset values and the axes orientations are given in the Claudia coordinate system (Russell et al. 2012)

We identify the region north of the equatorial belt of high crustal thickness as a likely relic hydrostatic surface from Vesta's early history. We isolate this region and fit its topography to a tri-axial ellipsoid with center position, orientation, and length of the the three principle axes as fit parameters (Bertoni 2010). We find that the best-fit tri-axial ellipsoid approximates an oblate ellipsoid of revolution with similar equatorial radii and a significantly shorter polar radius (Table 7.1). The volume of this best-fit rotational ellipsoid is 1.9% larger than that of the present shape, which is fully consistent with the expected volume of ancient Vesta before the more recent giant impacts (Schenk, O'Brien, et al. 2012). Furthermore, we find a large negative offset between the observed and fitted figures in the z direction (i.e., parallel to the rotation axis), which is consistent with the remove of material from the southern hemisphere by the giant impacts. The fitted parameters of the tri-axial ellipsoid are robust with respect to small variations in the regions chosen for the fit.

As expected, the residual topography in the northern undisturbed terrains is subdued (Fig. 7.7B). Most of the undisturbed terrains are within 5 km of the fitted surface. This residual topography is regional in scale, with wavelengths on the order of 100 - 300 km. Such topography, if it dates to the early period of rapid global scale hydrostatic relaxation, would not have relaxed fully due to its relatively small spatial scale compared to the degree-2 non-equilibrium modeled in this work. For these reasons, the fitted northern ellipsoid likely represents a faithful description of the pre-giant impacts global figure of Vesta.

The best-fit rotational ellipsoid corresponds to a flattening of $f_{ancient} = 0.147 \pm 0.001$, which is greater than that of the equilibrium figure for the present-day rotation period. Using a similar numerical grid search method as used above to find the hydrostatic flattening of Vesta, we find that this flattening factor implies a paleo-rotation period of 5.02 ± 0.01 hr, which implies 6.3% despinning due to late impacts. The flattening of the core is expected to be $f_{core} = 0.104 \pm 0.001$, with equatorial and polar radii of 114.0 and 102.2 km, respectively. The polar axis of the fitted ellipsoid is offset by 3.0° from the modern rotational axis. The stated errors are due to the discrete nature of the numerical, equilibrium figure-finding algorithm and do not include contribution from uncertainty in the interior density distribution.

This set of rotational parameters was established no later than 40-200 My after Vesta's formation, depending on the depth of megaregolith, and may represent Vesta's primordial spin state if very early giant impacts did not occur. The small amount of despinning suggests that large asteroids such as Vesta had initial rotation rates similar to those observed in the present day, which has been suggested by previous theoretical work (Schlichting & Sari 2007).

To assess the effect of varying the rotation rate on our relaxation simulations, we repeated a finite element relaxation simulation using the newly derived period of 5.02 hr (instead of 5.34 hr) to obtain f_{eq}. A model run at 40 My after convective shut down shows that, for the same disequilibrium $f - f_{eq}$, using the new f_{eq} increased the instantaneous relaxation velocity by a factor of 2.3 (Fig. 7.5A). This difference is similar to that resulting from changing model parameters (see Section 7.3) and is small compared to the two to four orders of magnitude differences resulting from changing the disequilibrium f

$-f_{eq}$. Increasing all relaxation velocities by a factor of 2.3 does not significantly alter the resulting relaxation paths or the length of the time window of efficient relaxation. Furthermore, the possibility of large early impacts (see Section 7.1) implies that the rotation period of early Vesta may have been higher or lower than 5.02 hr. As described above, we therefore avoid a priori assumptions and use 5.34 hr to calculate f_{eq}.

7.4. Discussion

The high efficiency of viscous relaxation on early Vesta implies that global scale non-hydrostatic features such as the relatively unrelaxed Venenia and Rheasilvia giant impact basins formed after the initial epoch of intense heating. Depending on the assumed thickness of megaregolith, global topography of the amplitude observed today is possible only after 4.52-4.36 Ga. The two giant impacts on Vesta therefore must have occurred after this age, which is consistent with observed crater densities in the basin floors (Schenk, O'Brien, et al. 2012). These model crater retention ages indicate that the older of the two basins, Veneneia, formed at ~2.1 Ga. By this time, core temperatures in Vesta would have fallen below 450°C even for the 5 km megaregolith layer case. The viscosity of silicates at the core-mantle boundary therefore would have been in excess of 10^{30} Pa s, which does not allow viscous relaxation on solar system timescales. Therefore, the pre-giant impact flattening of the core (f_{eq} = 0.104 ± 0.001) would be maintained into the present day, assuming that the giant impacts did not directly alter the core shape.

The longest principal axis of the best-fit ellipsoid trends towards the western edge of Vestalia Terra, which is likely an ancient mascon that predates the giant impacts and may date to the early magmatic epoch of Vesta's history within the first ~100 My of its formation (Buczkowski et al. 2013). This asymmetry in the pre-impact figure of Vesta provides additional support for a primordial origin for Vestalia Terra. Due to the regional scale of Vestalia Terra, which spans ~60° in latitude and ~100° in longitude (Jaumann et al. 2012), and the possibility of anomalously rigid local rheology as evidenced by the absence of crosscutting grooves (Buczkowski et al. 2013), Vestalia Terra was not subject to the global-scale viscoplastic relaxation modeled in this work (Anderson & O'Connell 1967). Future regional relaxation models of Vestalia Terra can potentially constrain the

rheological structure of early Vesta and place an upper bound on the degree of heating beneath this region.

The 5.02 hr period derived from the fit to the northern undisturbed terrains implies that late impacts have resulted in ~6.3% despinning. Assuming that the core was in hydrostatic equilibrium with the pre-impact rotation rate and outer figure (both approximated by ellipsoids of revolution) and that the core and silicate proportions of Vesta have densities of 7450 and 3100 kg m^{-3}, respectively, the pre-impact angular momentum of the Vesta was 2.58×10^{27} kg m^2 s^{-1}. The post-impact angular momentum of Vesta, assuming that the core maintains its fossil, pre-impact shape and orientation and that the surface is the best-fit ellipsoid of revolution (Russell et al. 2012), is 2.45×10^{27} kg m^2 s^{-1}. The bulk of this difference in angular momentum must have been delivered by the late Veneneia and Rheasilvia impactors. We estimate the upper limit of the angular momentum delivered in one such impact. Assuming a diameter of 66 km, velocity of 5400 m s^{-1} (Jutzi et al. 2013), and density of 3000 kg m^{-3} for the Rheasilvia impactor, its maximum angular momentum is 0.17×10^{27} kg m^2 s^{-1} for an impact at 75°S latitude (Schenk, O'Brien, et al. 2012). This contribution alone is sufficient to account for the change in Vesta angular momentum. Combined with a contribution of similar magnitude from the Veneneia impactor, the amount of despinning inferred from our fit to the undisturbed northern terrains is consistent with possible angular momentum transfer due to late giant impacts. Given the moderate probability of early giant impacts that can deliver a similar amount of angular momentum as the Veneneia and Rheasilvia basin-forming impactors, the rotation rate of Vesta since its formation at 2-6 My after CAIs (Tang & Dauphas 2012) has likely remained close (i.e., of order 6%) to that of the present.

In addition to despinning, both giant impacts may have led to significant true polar wander. Under the assumption of a single impact basin with axisymmetric geometry, (Matsuyama & Nimmo 2011) showed that reorientation of <20° and despinning of <20% are consistent with Hubble Space Telescope topography data available at the time. These values are fully consistent with our estimate based on undisturbed terrain morphology. However, the model does not provide accurate estimates of the non-axisymmetric coefficients of Vesta's gravity field, C_{22} and S_{22} (F. Nimmo, personal communication),

indicating that the impacts led to a more asymmetrical mass redistribution than assumed or that other effects, such as the pre-existing Vestalia Terra mascon, had introduced significant azimuthal asymmetry. Given new constraints on Vesta's gravity coefficients and the morphology of its giant impacts basins and overall shape, the range of plausible reorientation and despinning may require revision.

Our results indicate that other large asteroids that underwent extensive early heating may have also experienced significant global relaxation. Ground-based observations of Ceres provide evidence for central mass concentration although not necessarily full igneous differentiation with a metallic core (Thomas et al. 2005). The hydrostatically relaxed figure of Ceres may be due to intense early heating and viscous relaxation as described here for Vesta. Alternatively, the near-surface composition of Ceres may be sufficiently rich in low viscosity materials such as water ice or hydrated silicates to allow viscous relaxation without strong heating (Castillo-Rogez & McCord 2010; Dombard & Schenk 2013; Bland 2013). We note that the rheological profile of Ceres may be fundamentally different from that of Vesta in that the lowest viscosity material may be present at the surface due to compositional variation whereas the most inviscid material in Vesta is at depth due to the temperature gradient. Therefore, short wavelength features on Ceres may be able to relax readily while only the longest wavelength topography on Vesta, which is senstive to the rheology of the deep interior, is likely to approach hydrostatic equilibrium.

The third most massive asteroid, Pallas, is a near-twin of Vesta in terms of overall size (~532 km mean diameter). Like Vesta, the surface of Pallas is characterized by large, apparently unrelaxed impact basins (Schmidt et al. 2009). However, unlike for Vesta, no strong evidence exists for early igneous differentiation in Pallas. Its density has been estimated to be between 2400 and 3300 kg m^{-3} (Standish & Hellings 1989), which is consistent with both differentiated material and undifferentiated chondritic material. The unrelaxed impact basins on Pallas may therefore be late acquisitions after an early hydrostatic epoch or primordial features in the case of weak interior heating. More detailed mapping of Pallas in the future and the potential identification of terrains on Pallas consistent with ancient hydrostatic surfaces would imply the early heating and differentiation of the body and the late age of large impact basins. As with the northern

hemisphere of Vesta, such relic hydrostatic terrains are expected to show saturation crater densities, lack of major impact resurfacing, and freedom from topographic features due to distal giant impact basins such as a belt of thickened crust. Furthermore, an unconstrained ellipsoid fitted to purported hydrostatic terrains must produce plausible values for flattening and total volume.

The morphology of the southern hemisphere of asteroid Iris has been mapped in detail using radar observations (Ostro et al. 2010). In contrast to Vesta, Ceres, and Pallas, the surface of Iris appears to be highly irregular at all scales >30 km with topographic relief of ~20% of the body radius (the corresponding value for the Rheasilvia basin is ~6%). No region that can be closely fitted to a rotational ellipsoid similar to the undisturbed terrains on Vesta is definitively observed on Iris, although a large portion of the body still has not been mapped at high resolution. Furthermore, Iris' low density (2660 kg m^{-3}) and surface spectra consistent with that of ordinary chondrites do not suggest extensive early heating. Iris may have therefore never experienced sufficient interior heating to reach hydrostatic equilibrium similar to Vesta and Ceres. Its high non-hydrostaticity may then be due to a combination of late impacts and a primordial irregular surface acquired during accretion.

Among smaller bodies, the asteroid Lutetia (mean diameter ~100 km) is suspected to have undergone significant internal heating due to its high observed density (3400 kg m^{-3}), which requires anomalously low macroporosity or reduction of interior microporosity through sintering or melting (Pätzold et al. 2011; Weiss et al. 2012). However, sintering alone implies minimum temperatures of 760-950° C in the deep interior while the lithosphere may remain cold and resistant to deformation (Wieczorek et al. 2013; Fu & Elkins-Tanton 2014). As discussed above, such temperatures imply characteristic internal viscosities too high to allow viscous relaxation. The highly irregular shape of Lutetia is therefore consistent with early interior sintering.

7.5. Conclusion

We use finite element calculations coupled with conductive cooling models to constrain the extent of early global relaxation expected for the asteroid Vesta. Given

likely degrees of internal heating as dictated by both thermal evolution models and remote sensing data, Vesta was able to undergo relaxation towards hydrostatic equilibrium. Vesta reached a highly hydrostatic figure shortly after accretion with a maximum non-hydrostatic equatorial bulge amplitude of < 2 km during the first 15 to 80 My after formation. Vesta then maintained a figure closer to hydrostatic equilibrium than its present one during at least the first 40 My after formation. Inclusion of a thick megaregolith layer can extend this hydrostatic epoch to 200 My after formation. The Veneneia and Rheasilvia impact basins, which are essentially unrelaxed, must have occurred after this early hydrostatic epoch.

The efficient hydrostatic relaxation of early Vesta motivates the possibility of finding relic hydrostatic terrains on its present-day surface. We isolate a large region in the northern hemisphere based on its ancient crater retention ages, lack of large impact features, and location away from structures associated with the southern hemisphere giant impacts. The best-fit ellipsoid for this region indicates a pre-impact rotation period of 5.02 hr, which implies a cumulative 6.3% reduction in angular velocity due to the two late giant impacts. This rotation rate was established at some time less than 40-200 My after Vesta's formation and would represent the primordial rotation rate of Vesta if very early giant impacts did not occur. Other asteroids that experienced intense early heating and rapid cooling may also have undergone early hydrostatic relaxation. As such, the potential observation of similar hydrostatic terrains on other asteroids would provide constraints on the degree of early interior heating.

Bibliography

Acton, G. et al., 2007. Micromagnetic coercivity distributions and interactions in chondrules with implications for paleointensities of the early solar system. *J. Geophys. Res.*, 112, p.doi: 10.1029/2006JB004655.

Acuña, M.H. et al., 2002. NEAR magnetic field observations at 433 Eros: First measurements from the surface of an asteroid. *Icarus*, 155, pp.220–228. Available at: <Go to ISI>://000175164100015.

Agee, C.B. et al., 1995. Pressure-temperature phase diagram for the Allende meteorite. *J. Geophys. Res.*, 100, pp.17725–17740.

Aggarwal, H.R. & Oberbeck, V.R., 1979. Monte Carlo simulation of lunar megaregolith and implications. In *Lunar and Planetary Science Conference Proceedings*. pp. 2689–2705.

Akai, J., 1992. T-T-T diagram of serpentine and saponite, and estimation of metamorphic heating degree of Antarctic carbonaceous chondrites. *Proc. NIPR Symp. Antarct. Meteorites.*, 5, pp.120–135.

Akai, J., 1994. Void stuctures in olivine grains in thermally metamorphosed Antarctic carbonaceous chondrite B-7904. *Proc. NIPR Symp. Antarct. Meteorites*, 7, pp.94–100.

Albert, R.A. et al., 2000. A test of the validity of yield strength envelopes with an elastoviscoplastic finite element model. *Geophys. J. Int.*, 140, pp.399–409.

Alexander, C.M.O., Barber, D.J. & Hutchison, R., 1989. The microstructure of Semarkona and Bishunpur. *Geochim. Cosmochim. Acta*, 53, pp.3045–3057.

Alexander, R. et al., 2014. The dispersal of protoplanetary disks. In *Protostars and Planets VI*. Univ. Arizona Press, pp. 1–23.

Anderson, D.L. & O'Connell, R., 1967. Viscosity of the Earth. *Geophys. J. R. Astr. Soc.*, 14, pp.287–295.

Anson, G.L. & Kodama, K.P., 1987. Compaction-induced inclination shallowing of the post-depositional remanent magnetization in a synthetic sediment. *Geophys. J. Roy. Astr. Soc.*, 88, pp.673–692.

Asphaug, E., 1997. Impact Origin of the Vesta Family. *Meteorit. Planet. Sci.*, 32, pp.965–980.

Atkins, C.B., Barrett, P.J. & Hicock, S.R., 2002. Cold Glaciers Erode and Deposit: Evidence from Allan Hills, Antarctica. *Geology*, 30, pp.659–662.

Aubaud, C., Hauri, E.H. & Hirschmann, M.M., 2004. Hydrogen partition coefficients between nominally anhydrous minerals and basaltic melts. *Geophys. Res. Lett.*, 31, p.L20611.

Auster, H.U. et al., 2007. ROMAP: Rosetta Magnetometer and Plasma Monitor. *Space Sci. Rev.*, 128, pp.221–240.

Bai, Q. & Kohlstedt, D.L., 1993. Effects of chemical environment on the solubility and incorporation mechanism for hydrogen in olivine. *Phys. Chem. Minerals*, 19, pp.460–471.

Bai, X.-N., 2014. Hall-effect-controlled gas dynamics in protoplanetary disks. I. Wind solutions at the inner disk. *Astrophys. J.*, 791, p.137.

Bai, X.-N., 2011. Magnetorotational-instability-driven accretion in protoplanetary disks. *Astrophys. J.*, 739, pp.1–19.

Bai, X.-N., 2013. Wind-driven accretion in protoplanetary disks. II. Radial dependence and global picture. *Astrophys. J.*, 772, pp.1–15.

Bai, X.-N. & Goodman, J., 2009. Heat and dust in active layers of protostellar disks. *Astrophys. J.*, 701, pp.737–755.

Bai, X.-N. & Stone, J.M., 2013. Wind-driven accretion in protoplanetary disks. I. Suppression of the Magnetorotational instability and launching of the magnetocentrifugal wind. *Astrophys. J.*, 769, p.76.

Balbus, S.A., 2003. Enhanced angular momentum transport in accretion disks. *Annu. Rev. Astron. Astrophys.*, 41, pp.555–597.

Balbus, S.A. & Hawley, J.F., 1991. A powerful local shear instability in weakly magnetized disks. I. Linear analysis. *Astrophys. J.*, 376, pp.214–222.

Balbus, S.A. & Hawley, J.F., 1998. Instability, turbulence, and enhanced transport in accretion disks. *Rev. Mod. Phys.*, 70, pp.1–53.

Baldwin, B. & Sheaffer, Y., 1971. Ablation and breakup of large meteoroids during atmospheric entry. *J. Geophys. Res.*, 76, pp.4653–4668.

Bangerth, W., Hartmann, R. & Kanschat, G., 2007. deal. II- {a} general-purpose object-oriented finite element library. *ACM T. Math. Software*, 33(4), p.24.

Bangerth, W. & Kronbichler, M., 2008. The step-22 tutorial program.

Baratchart, L. et al., 2013. Characterizing kernels of operators related to thin-plate magnetizations via generalizations of Hodge decompositions. *Inverse Probl.*, 29, p.15004.

Beck, A.W. et al., 2011. MIL 03443, a dunite from asteroid 4 Vesta: Evidence of its classification and cumulate origin. *Meteorit. Planet. Sci.*, 46, pp.1133–1151.

Beitz, E. et al., 2012. Free collisions in a microgravity many-particle experiment – II: The collision dynamics of dust-coated chondrules. *Icarus*, 218, pp.701–706.

Bennett, M.E. & McSween, H.Y., 1996. Revised model calculations for the thermal histories of ordinary chondrite parent bodies. *Meteorit. Planet. Sci.*, 31, pp.783–792.

Berckhemer, H. et al., 1982. Shear modulus and \emph{Q} of forsterite and dunite near partial melting from forced-oscillation experiments. *Phys. Earth. Planet. Int.*, 29(1), pp.30–41.

Bertoni, B., 2010. *Multi-dimensional ellipsoidal fitting*,

Bibring, J.P. et al., 2007. The Rosetta Lander ("{P}hilae") investigations. *Space Sci. Rev.*, 128(1), pp.205–220.

Binzel, R.P. & Xu, S., 1993. Chips off asteroid 4 Vesta: Evidence for the parent body of basaltic achondrite meteorites. *Science*, 260, pp.186–191.

Bischoff, A. & Stoffler, D., 1992. Shock metamorphism as a fundamental process in the evolution of planetary bodies: Information from meteorites. *Eur. J. Mineral.*, 4, pp.707–755.

Bland, M.T., 2013. Predicted crater morphologies on {C}eres: {P}robing internal structure and evolution. *Icarus*, 226, pp.510–521.

Bland, P.A. et al., 2006. Weathering of chondritic meteorites. In D. S. Lauretta & H. Y. McSween, eds. *Meteorites and the Early Solar System II*. Tucson: The University of Arizona Press, pp. 853–867.

Blandford, R.D. & Payne, D.G., 1982. Hydromagnetic flows from the accretion discs and the production of radio jets. *Mon. Not. R. Astr. Soc.*, 199, pp.883–903.

Bockelée-Morvan, D. et al., 2002. Turbulent radial mixing in the solar nebula as the source of crystalline silicates in comets. *The Origin of Stars and Planets: The VLT View*, pp.445–452.

Bottke, W.F. et al., 2005. The fossilized size distribution of the main asteroid belt. *Icarus*, 175, pp.111–140.

Brace, W.F., 1980. Permeability of crystalline and argillaceous rocks. *Int. J. Rock Mech. Min. Sci. and Geomech. Abstr.*, 17, pp.241–251.

Bradley, J.P., 1994. Chemically anomalous, preaccretionally irradiated grains in interplanetary dust from comets. *Science*, 265(5174), p.925.

Brearley, A.J., 1997. Disordered biopyroboles, amphibole, and talc in the Allende meteorite: Products of nebular or parent body aqueous alteration? *Science*, 276, pp.1103–1105.

Brearley, A.J., 2003. Nebular versus parent-body processing. In K. K. Turekian & H. D. Holland, eds. *Treatise on Geochemistry*. Elsevier, pp. 247–268.

Brearley, A.J. & Krot, A.N., 2012. Metasomatism in the early solar system: The record from chondritic meteorites. In D. E. Harlov & H. Austrheim, eds. *Metasomatism and the Chemical Transformation of Rock*. Berlin: Springer-Verlag, pp. 659–789.

Brett, R. & Sato, M., 1984. Intrinsic oxygen fugacity measurements on seven chondrites, a pallasite, and a tektite and the redox state of meteorite parent bodies. *Geochim. Cosmochim. Acta*, 48, pp.111–120.

Britt, D. & Consolmagno, G.J., 2003. Stony meteorite porosities and densities: A review of the data through 2001. *Meteorit. Planet. Sci.*, 38, pp.1161–1180.

Britt, D.T. et al., 2002. Asteroid density, porosity, and structure. In W. F. Bottke et al., eds. *Asteroids III*. Tucson, AZ: Univ. Arizona Press.

Brown, R., 2007. No Title. *http://www.mathworks.com/matlabcentral/fileexchange/15125-fitellipse-m*. Available at: http://www.mathworks.com/matlabcentral/fileexchange/15125-fitellipse-m.

Buchwald, V.F. & Clarke, R.S., 1989. Corrosion of Fe-Ni alloys by Cl-containing akaganéite (β-FeOOH): The Antarctic meteorite case. *Am. Mineral.*, 74, pp.656–667.

Buczkowski, D.L. et al., 2013. Brumalia Tholus: An Indication of Magmatic Intrusion on {V}esta? In *Lunar and Planetary Science Conference Abstracts*. p. 1996.

Bunch, T.E. et al., 2008. Evidence for pervasive metamorphism on the CR chondrite parent body from highly equilibrated CR6 Northwest Africa 2994 and Northwest Africa 3100. In *Lunar Planet. Sci. Conf. XXXIX*. Houston, TX.

Burbine, T.H. et al., 2002. Meteoritic parent bodies: Their number and identification. In W. F. Bottke et al., eds. *Asteroids III*. Tucson: University of Arizona Press, pp. 653–667.

Bus, S.J. & Binzel, R.P., 2002. Phase II of the small main-belt asteroid spectroscopic survery. *Icarus*, 158, pp.146–177.

Butler, R.F., 1972. Natural remanent magnetization and thermomagnetic properties of Allende meteorite. *Earth Planet. Sci. Lett.*, 17, pp.120–128. Available at: <Go to ISI>://A1972O387100016.

Byerlee, J., 1978. Friction of rock. *Pageoph*, 116, pp.615–626.

Carporzen, L. et al., 2011. Magnetic evidence for a partially differentiated carbonaceous chondrite parent body. *Proc. Natl. Acad. Sci. USA*, 108, pp.6386–6389.

Carruba, V., Michtchenko, T.A. & Lazzaro, D., 2007. On the V-type asteroids outside the Vesta family. *Astron. Astrophys.*, 473, pp.967–978.

Cassata, W. et al., 2010. Evidence for shock heating and constraints on Martian surface temperatures revealed by 40Ar/39Ar thermochronometry of Martian meteorites . *Geochim. Cosmochim. Acta*, 74, pp.6900–6920.

Castillo-Rogez, J.C. & McCord, T.B., 2010. Ceres' evolution and present state constrained by shape data. *Icarus*, 205(2), pp.443–459.

Cazaux, S. et al., 2005. Molecular Hydrogen formation on grain surfaces. In *J. Phys. Conf. Ser.* pp. 155–160.

Chambat, F., Ricard, Y. & Valette, B., 2010. Flattening of the {E}arth: further from hydrostaticity than previously estimated. *Geophys. J. Int.*, 183(2), pp.727–732.

Chambers, J.E., 2004. Planetary accretion in the inner Solar System. *Earth Planet. Sci. Lett.*, 223, pp.241–252.

Chandrasekhar, S., 1960. The stability of non-dissipative Couette flow in hydromagnetics. *Proc. Natl. Acad. Sci. USA*, 46, pp.253–257.

Chandrasekhar, S. & Fermi, E., 1953. Magnetic fields in spiral arms. *Astrophys. J.*, 118, pp.113–115.

Chiang, E.I. & Goldreich, P., 1997. Spectral energy distributions of T Tauri stars with passive circumstellar disks. *Astrophys. J.*, 490, pp.368–376.

Cho, J. & Lazarian, A., 2007. Grain alignment and polarized emission from magnetized T Tauri disks. *Astrophys. J.*, 669, pp.1085–1097.

Choi, B.-G. et al., 1997. Origin of magnetite in oxidized CV chondrites: in situ measurement of oxygen isotope compositions of Allende magnetite and olivine. *Earth Planet. Sci. Lett.*, 146, pp.337–349.

Chopra, P.N. & Paterson, M.S., 1984. The role of water in the deformation of dunite. *J. Geophys. Res.*, 89, p.7861.

Christensen, U.R. & Aubert, J., 2006. Scaling properties of convection-driven dynamos in rotating spherical shells and application to planetary magnetic fields. *Geophys. J. Int.*, 166, pp.97–114.

Church, N.S. et al., 2012. Spatially resolved NRM of the Bishunpur LL3.1 chondrite measured by scanning SQUID microscopy: implications for chondrule formation. *AGU Fall Meeting*, GP51B-05.

Ciesla, F.J., Lauretta, D.S. & Hood, L.L., 2004. The frequency of compound chondrules and implications of chondrule formation. *Meteorit. Planet. Sci.*, 39, pp.531–544.

Cisowski, C.S., 1987. Magnetism of meteorites. In J. A. Jacobs, ed. *Geomagnetism*. London: Academic Press, pp. 525–560.

Cisowski, S.M. et al., 1983. A review of lunar paleointensity data and implications for origin of lunar magnetism. *Proc. Lunar Planet. Sci. Conf. 13th*, pp.A691–A704.

Cisowski, S.M., 1991. Remanent magnetic properties of unbrecciated eucrites. *Earth Planet. Sci. Lett.*, 107, pp.173–181.

Cody, G.D. et al., 2008. Organic thermometry for chondritic parent bodies. *Earth Planet. Sci. Lett.*, 272, pp.446–455.

Collinson, D.W., 1965. Depositional remanent magnetization in sediments. *J. Geophys. Res.*, 70, pp.4663–4668.

Collinson, D.W. & Morden, S.J., 1994. Magnetic-properties of howardite, eucrite and diogenite (HED) meteorites - Ancient mgnetizing fields and meteorite evolution. *Earth Planet. Sci. Lett.*, 126, pp.421–434. Available at: <Go to ISI>://A1994PK34500017.

Connolly, H.C. et al., 1994. Compound chondrules: an experimental investigation. *Meteoritics*, 29, p.458.

Consolmagno, G.J., Britt, D.J. & Macke, R.J., 2008. The significance of meteorite density and porosity. *Chem. Erde*, 68, pp.1–29.

Coradini, A. et al., 2011. The surface composition and temperature of asteroid 21 Lutetia as observed by Rosetta/VIRTIS. *Science*, 334, pp.492–494.

Cournède, C. et al., 2012. Magnetic study of CM chondrites. In *EGU 2012*. Vienna.

Cox, A., 1969. Confidence Limits of the Precision Parameter k. *Geophys. J. R. Astr. Soc.*, 18, pp.545–549.

Crank, J., 1975. *The Mathematics of Diffusion* 2nd ed., Oxford: Oxford University Press.

Crawford, D.A. & Schultz, P.H., 1999. Electromagnetic properties of impact-generated plasma, vapor and debris. *Int. J. Impact. Eng.*, 23, pp.169–180. Available at: <Go to ISI>://000084521500017.

Crawford, D.A. & Schultz, P.H., 1993. The production and evolution of impact-generated magnetic fields. *Int. J. Impact. Eng.*, 14, pp.205–216. Available at: <Go to ISI>://A1993LX89300020.

Crutcher, R.M. et al., 1996. CN Zeeman observations of molecular cloud cores. *Astrophys. J.*, 456, pp.217–224.

Crutcher, R.M., 2012. Magnetic fields in molecular clouds. *Annu. Rev. Astron. Astrophys.*, 50, pp.29–53.

Cuzzi, J.N. & Hogan, R.C., 2003. Blowing in the wind I. Velocities of chondrule-sized particles in a turbulent protoplanetary nebula. *Icarus*, 164, pp.127–138.

Cuzzi, J.N., Hogan, R.C. & Shariff, K., 2008. Toward planetesimals: Dense chondrule clumps in the protoplanetary nebula. *Astrophys. J.*, 687, pp.1432–1447.

Davis, L. & Greenstein, J.L., 1951. The Polarization of Starlight by Aligned Dust Grains. *Astrophys. J.*, 114, pp.206–240.

Davison, T.M. et al., 2013. The early impact histories of meteorite parent bodies. *Meteorit. Planet. Sci.*, pp.1–25.

Davison, T.M., Ciesla, F.J. & Collins, G.S., 2012. Post-impact thermal evolution of porous planetesimals. *Geochim. Cosmochim. Acta*, 95, pp.252–269.

Deamer, G.A. & Kodama, K.P., 1990. Compaction-induced inclination shallowing in synthetic and natural clay-rich sediments. *J. Geophys. Res.*, 95(B4), pp.4511–4529.

Delaney, J.S., Prinz, M. & Takeda, H., 1984. The polymict eucrites. *J. Geophys. Res.*, 89, pp.C251–C288.

Denevi, B.W. et al., 2012. Regolith Depth, Mobility, and Variability on {V}esta from {D}awn's Low Altitude Mapping Orbit. In *Lunar and Planetary Science Conference Abstracts*. p. 1943.

Dermott, S.F., 1979. Shapes and gravitational moments of satellites and asteroids. *Icarus*, 37, pp.575–586.

Desch, S.J., 2004. Linear analysis of the magnetorotational instability, including ambipolar diffusion, with applications to protoplanetary disks. *Astrophys. J.*, 608, pp.509–525.

Desch, S.J. et al., 2012. The importance of experiments: Constraints on chondrule formation models. *Meteorit. Planet. Sci.*, 47, pp.1139–1156.

Desch, S.J. & Connolly, H.C., 2002. A model of the thermal processing of particles in solar nebula shocks: Application to the cooling rates of chondrules. *Meteorit. Planet. Sci.*, 37(2), pp.183–207. Available at: <Go to ISI>://000175242700005.

Desch, S.J. & Mouschovias, T.C., 2001. The magnetic decoupling of star formation. *Astrophys. J.*, 550, pp.314–333.

Dinarès-Turell, J. & Dekkers, M.J., 1999. Diagenesis and remanence acquisition in the Lower Pliocene Trubi marls at Punta di Maiata (southern Sicily): palaeomagnetic and rock magnetic observations. In D. H. Tarling & P. Turner, eds. *Palaeomagnetism and Diagenesis in Sediments*. London: Geological Society, London, pp. 53–69.

Dombard, A.J. & McKinnon, W.B., 2006. Elastoviscoplastic relaxation of impact crater topography with application to Ganymede and Callisto. *J. Geophys. Res.*, 111, p.E01001.

Dombard, A.J. & Schenk, P.M., 2013. The Giant Cue Ball: Efficient Relaxation of {C}eres' Craters. In *Lunar and Planetary Science Conference Abstracts*. p. 1798.

Dominik, C. & Nübold, H., 2002. Magnetic aggregation: Dynamics and numerical modeling. *Icarus*, 157, pp.173–186.

Donati, J.-F. et al., 2005. Direct detection of a magnetic field in the innermost regions of an accretion disk. *Nature*, 438, pp.466–469.

Draine, B.T. & Weingartner, J.C., 1996. Radiative Torques on Interstellar Grains. {I}. {S}uperthermal Spin-up. *Astrophys. J.*, 470, pp.551–565.

Draine, B.T. & Weingartner, J.C., 1997. Radiative torques on interstellar grains. II. Grain alignment. *Astrophys. J.*, 480, pp.633–646.

Dubrulle, B., Morfill, G. & Sterzik, M., 1995. The dust subdisk in the protoplanetary nebula. *Icarus*, 114, pp.237–246.

Duffard, R., 2009. Basaltic asteroids in the solar system. *Earth Moon Planet*, 105, pp.221–226.

Duke, M.B. & Silver, L.T., 1967. Petrology of Eucrites, Howardites, and Mesosiderites. *Geochim. Cosmochim. Acta*, 31, pp.1637–1665.

Dunlop, D.J. et al., 1973. Magnetic properties and granulometry of metallic iron in lunar breccia 14313. *Proc. Lunar Planet. Sci. Conf. 4th*, pp.2977–2990.

Dunlop, D.J., 2002. Theory and application of the Day plot (Mrs/Ms versus Hcr/Hc) - 1. Theoretical curves and tests using titanomagnetite data. *J. Geophys. Res.*, 107, p.doi:10.1029/2001JB000486.

Dunlop, D.J. et al., 2000. Time-temperature relations for the remagnetization of pyrrhotite (Fe7S8) and their use in estimating paleotemperatures. *Earth Planet. Sci. Lett.*, 176, pp.107–116.

Dunlop, D.J. & Argyle, K.S., 1997. Thermoremanence, anhysteretic remanence, and susceptibility of submicron magnetites: Nonlinear field dependence and variation in grain size. *J. Geophys. Res.*, 102, pp.20199–20210.

Dunlop, D.J. & Ozdemir, O., 1997a. *Rock Magnetism: Fundamentals and Frontiers*, New York: Cambridge University Press.

Dunlop, D.J. & Ozdemir, O., 1997b. Viscous and Thermoviscous Magnetization. In *Rock Magnetism*. Cambridge, UK: Cambridge University Press, p. 573.

Elkins-Tanton, L.T., Parmentier, E.M. & Hess, P.C., 2003. Magma ocean fractional crystallization and cumulate overturn in terrestrial planets: Implications for Mars. *Meteorit. Planet. Sci.*, 38, pp.1753–1771.

Elkins-Tanton, L.T., Weiss, B.P. & Zuber, M.T., 2011. Chondrites as samples of differentiated planetesimals. *Earth Planet. Sci. Lett.*, 305, pp.1–10.

Emmerton, S. et al., 2011. Magnetic characteristics of CV chondrules with paleointensity implications. *J. Geophys. Res.*, 116, p.E12007.

Ermakov, A.I. et al., 2014. Constraints on Vesta's interior structure using gravity and shape models from the Dawn mission. *Icarus*, 240, pp.146–160.

Falgarone, E. et al., 2008. CN Zeeman measurements in star formation regions. *Astron. Astrophys.*, 487, pp.247–252.

Fechtig, H. & Kalbitzer, S.T., 1966. The diffusion of argon in potassium-bearing solids. In O. A. Schaeffer & J. Zahringer, eds. *Potassium Argon Dating*. New York: Springer-Verlag, pp. 68–107.

Feller, W., 1966. *An Introduction to Probability Theory and Its Applications*, New York: John Wiley & Sons.

Ferguson, C.C., 1979. Intersections of ellipsoids and planes of arbitrary orientation and position. *Math. Geol.*, 11, pp.329–336.

Fogel, R.A., Hess, P.C. & Rutherford, M.J., 1989. Intensive parameters of enstatite chondrite metamorphism. *Geochim. Cosmochim. Acta*, 53, pp.2735–2746.

Fong, L.E. et al., 2005. High resolution room-temperature sample scanning superconducting interference device microscope configurable for geological and biomagnetic applications. *Rev. Sci. Instrum.*, 76, p.53703.

Francombe, M.H., 1957. Lattice Changes in Spinel-Type Iron Chromites. *J. Phys. Chem. Solids*, 3, pp.37–43.

Fu, R.R. et al., 2012. An ancient core dynamo in asteroid Vesta. *Science*, 338, pp.238–241.

Fu, R.R., Hager, B.H., et al., 2014. Efficient early global relaxation of asteroid Vesta. *Icarus*, 240, pp.133–145.

Fu, R.R., Weiss, B.P., et al., 2014. Solar nebula magnetic fields recorded in the Semarkona meteorite. *Science*, 346, pp.1089–1092.

Fu, R.R. & Elkins-Tanton, L.T., 2014. The fate of magmas in planetesimals and the retention of primitive chondritic crusts. *Earth Planet. Sci. Lett.*, 390, pp.128–137.

Fu, R.R., Lima, E.A. & Weiss, B.P., 2014. No nebular magnetization in the Allende CV carbonaceous chondrite. *Earth Planet. Sci. Lett.*, 404, pp.54–66.

Fu, R.R. & Weiss, B.P., 2012. Detrital remanent magnetization in the solar nebula. *J. Geophys. Res.*, 117, p.E02003.

Fu, R.R. & Weiss, B.P., 2011. Magnetic Fields on Asteroid 4 Vesta Recorded by the Millbillillie Eucrite. *EPSC-DPS Joint Meeting Abstract #1646.*

Fuller, M., 1974. Lunar magnetism. *Rev. Geophys. Space Phys.*, 12, pp.23–69.

Funaki, M., Nagata, T. & Momose, K., 1981. Natural remanent magnetizations of chondrules, metallic grains and matrix of an Antarctice chondrite, ALH-769. *Mem. Natl. Inst. Polar Res. Spec. Issue*, 20, pp.300–315.

Funaki, M. & Wasilewski, P., 1999. A relation of magnetization and sulfidization in the parent body of the Allende (CV3) carbonaceous meteorite. *Meteorit. Planet. Sci.*, 34, p.A39.

Gaffey, M.J., Reed, K.L. & Kelley, M.S., 1992. Relationship of E-Type Apollo asteroid 3103 (1982 BB) to the enstatite Achondrite meteorites and the Hungaria asteroids. *Icarus*, 100, pp.95–109.

Galdi, G.P. & Vaidya, A., 2001. Translational steady fall of symmetric bodies in a Navier-Stokes liquid, with application to particle sedimentation. *J. Math. Fluid Mech.*, pp.183–211.

Gammie, C.F., 1996. Layered accretion in T Tauri disks. *Astrophys. J.*, 457, pp.355–362.

Garrick-Bethell, I. et al., 2009. Early lunar magnetism. *Science*, 323, pp.356–359.

Garrick-Bethell, I. & Weiss, B.P., 2010. Kamacite blocking temperatures and applications to lunar magnetism. *Earth Planet. Sci. Lett.*, 294, pp.1–7.

Gattacceca, J. et al., 2011. Low Temperature Magnetic Transition of Chromite in Ordinary Chondrites. *Geophys. Res. Lett.*, 38, p.L10203.

Gattacceca, J. et al., 2014. Metal phases in ordinary chondrites: Magnetic hysteresis properties and implications for thermal history. *Meteorit. Planet. Sci.*, 49, pp.652–676.

Gattacceca, J. et al., 2008. On the efficiency of shock magnetization processes. *Phys. Earth Planet. Inter.*, 166, pp.1–10.

Gattacceca, J. & Rochette, P., 2004. Toward a robust normalized magnetic paleointensity method applied to meteorites. *Earth Planet. Sci. Lett.*, 227, pp.377–393. Available at: <Go to ISI>://000225124900016.

Gattacceca, J., Rochette, P. & Bourot-Denise, M., 2003. Magnetic properties of a freshly fallen LL ordinary chondrite: the Bensour meteorite. *Phys. Earth Planet. Inter.*, 140, pp.343–358. Available at: <Go to ISI>://000187466300007.

Gendzwill, D.J. & Stauffer, M.R., 1981. Analysis of triaxial ellipsoids: Their shapes, plane sections, and plance projections. *Math. Geol.*, 13, pp.135–152.

Ghosh, A. & McSween, H.Y., 1998. A thermal model for the differentiation of asteroid 4 Vesta based on radiogenic heating. *Icarus*, 134, pp.187–206.

Gilmour, J.D. et al., 2009. An early I-Xe age for CB chondrite chondrule formation, and a re-evaluation of the closure age of Shallowater enstatite. *Meteorit. Planet. Sci.*, 44, pp.573–579.

Girart, J.M., Rao, R. & Marrone, D.P., 2006. Magnetic fields in the formation of sun-like stars. *Science*, 313, pp.812–814.

Glassgold, A.E., Meijerink, R. & Najita, J.R., 2009. Formation of water in the warm atmospheres of protoplanetary disks. *Astrophys. J.*, 701, pp.142–153.

Glassmeier, K.H. et al., 2007. The Rosetta mission: Flying towards the origin of the solar system. *Space Sci. Rev.*, 128(1), pp.1–21.

Gold, T., 1952. The alignment of galactic dust. *Mon. Not. R. Astr. Soc.*, 112(215-218).

Gooding, J.L., 1986. Weathering of stony meteorites in Antarctica. In *International Workshop on Antarctic Meteorites,* . Houston: LPI Technical Report 86-01, Lunar and Planetary Science Institute, pp. 48–54.

Gose, W.A. et al., 1972. On the applicability of lunar breccias for paleomagnetic interpretations. *Earth Moon Planet*, 5, pp.106–120.

Greenwood, R.C. et al., 2006. Oxygen isotope variation in stony-iron meteorites. *Science*, 313, pp.1763–1765.

Greenwood, R.C. et al., 2010. The relationship between CK and CV chondrites. *Geochim. Cosmochim. Acta*, 74, pp.1684–1705.

Greenwood, R.C. et al., 2005. Widespread magma oceans on asteroidal bodies in the early Solar System. *Nature*, (435), pp.916–918.

Grimm, R.E. & McSween, H.Y., 1989. Water and the thermal evolution of carbonaceous chondrite parent bodies. *Icarus*, 82, pp.244–280.

Grove, T.L., 1982. Use of Exsolution Lamellae in Lunar Clinopyroxenes as Cooling Rate Speedometers: an Experimental Calibration. *Am. Mineral.*, 67, pp.251–268.

Haack, H. & Rasmussen, K.L., 1990. Effects of regolith/megaregolith Insulation on the cooling histories of differentiated asteroids. *J. Geophys. Res.*, 95, pp.5111–5124.

Haggerty, S.E. & McMahon, B.M., 1979. Magnetite-sulfide-metal complexes in the Allende meteorite. *Proc. Lunar Planet. Sci. Conf. 10th*, pp.851–870.

Haigh, G., 1958. The process of magnetization by chemical change. *Phil. Mag.*, 3, pp.267–286.

Haisch, K.E., Lada, E.A. & Lada, C.J., 2001. Disk Frequencies and Lifetimes in Young Clusters. *Astrophys. J. Lett.*, 553, pp.L153 – L156.

Hamilton, D.L., Burnham, C.W. & Osborn, E.F., 1964. The solubility of water and effects of oxygen fugacity and water content on crystallization in mafic magmas. *J. Petrol.*, 5, pp.21–39.

Hanley, E.J., Dewitt, D.P. & Roy, R.F., 1978. The thermal diffusivity of eight well-characterized rocks for the temperature range 300-1000 K. *Eng. Geo.*, 12, pp.31–47.

Hartmann, L. et al., 1998. Accretion and the evolution of T Tauri stars. *Astrophys. J.*, 495, pp.385–400.

Hauri, E.H., Gaetani, G.A. & Green, T.H., 2006. Partitioning of water during melting of the Earth's upper mantle at H2O-undersaturated conditions. *Earth Planet. Sci. Lett.*, 248, pp.715–734.

Hawley, J.F. & Balbus, S.A., 1991. A powerful local shear instability in weakly magnetized disks. II. Nonlinear evolution. *Astrophys. J.*, 376, pp.223–233.

Hayashi, C., 1981. Structure of the solar nebula, growth and decay of magnetic fields and effects of magnetic and turbulent viscosities on the nebula. *Sup. Prog. Theor. Phys.*, 70, pp.35–53.

Herczeg, G.J. & Hillenbrand, L.A., 2008. UV excess measures of accretion onto young very low mass stars and brown dwarfs. *Astrophys. J.*, 681, pp.594–625.

Heslop, D., 2007. Are hydrodynamic shape effects important when modelling the formation of depositional remanent magnetization? *Geophys. J. Int.*, 171, pp.1029–1035.

Hevey, P.J. & Sanders, I.S., 2006. A model for planetesimal meltdown by 26Al and its implications for meteorite parent bodies. *Meteorit. Planet. Sci.*, 41, pp.95–106.

Hirschmann, M.M., Aubaud, C. & Withers, A.C., 2005. Storage capacity of H2O in nominally anhydrous minerals in the upper mantle. *Earth Planet. Sci. Lett.*, 236, pp.167–181.

Hirschmann, M.M. & Stolper, E.M., 1996. A possible role for garnet pyroxenite in the origin of the "'garnet signature'" in MORB. *Contrib. Mineral Petrol.*, 124, pp.185–208.

Hirth, G. & Kohlstedt, D.L., 1996. Water in the oceanic upper mantle: implications for rheology, melt extraction and the evolution of the lithosphere. *Earth Planet. Sci. Lett.*, 144, pp.93–108.

Hoffmann, M. et al., 2012. Unique crater morphologies on {V}esta, and the context of a deep regolith and intermediate gravity. In *EGU General Assembly Conference Abstracts*. p. 5530.

Hollenbach, D. & Salpeter, E.E., 1971. Surface recombination of hydrogen molecules. *Astrophys. J.*, 163, pp.155–164.

Hood, L.L. & Artemieva, N.A., 2008. Antipodal effects of lunar basin-forming impacts: Initial 3D simulations and comparisons with observations. *Icarus*, 193, pp.485–502.

Hood, L.L. & Vickery, A., 1984. Magnetic field amplification and generation in hypervelocity meteoroid impacts with application to lunar paleomagnetism. *Proc. Lunar Planet. Sci. Conf. 15th*, pp.C211–C223.

Hood, L.L. & Zakharian, A., 2001. Mapping and modeling of magnetic anomalies in the northern polar region of Mars. *J. Geophys. Res.*, 106, pp.14601–14619.

Housen, K.R. et al., 1979. Asteroidal regoliths. *Icarus*, 39(3), pp.317–351.

Hughes, A.M. et al., 2011. Empirical constraints on the turbulence in protoplanetary accretion disks. *Astrophys. J.*, 727, p.85.

Hughes, A.M. et al., 2013. Interferometric upper limits on millimeter polarization of the disks around DG Tau, GM Aur, and MWC 480. *Astrophys. J.*, 145, pp.1–7.

Ihinger, P.D. & Stolper, E., 1986. The color of meteoritic hibonite: an indicator of oxygen fugacity. *Earth Planet. Sci. Lett.*, 78, pp.67–79.

Ivanov, B.A. & Melosh, H.J., 2012. The Rheasilvia crater on Vesta: Numerical modeling. In *Lunar and Planetary Science Conference Abstracts*. p. 2148.

Ivanov, S.G. & Yanshin, A.M., 1980. Forces and moments acting on bodies rotating about a symmetry axis in a free molecular flow. *Fluid Dynamics*, 15, pp.449–453.

Jackson, M., 1991. Anisotropy of magnetic remanence: A brief review of mineralogical sources, physical origins, and geological applications, and comparison with susceptibility anisotropy. *Pageoph*, 136, pp.1–28.

Jarosewich, E., 1990. Chemical analyses of meteorites: A compilation of stony and iron meteorite analyses. *Meteoritics*, 25, pp.323–337.

Jaumann, R. et al., 2012. Vesta's shape and morphology. *Science*, 336(6082), pp.687–690.

Johansen, A. et al., 2007. Rapid planetesimal formation in turbulent circumstellar disks. *Nature*, 448, pp.1022–1025.

Johansen, A., 2009. The role of magnetic fields for planetary formation. In K. G. Strassmeier, A. G. Kosovichev, & J. E. Beckman, eds. *Cosmic Magnetic Fields: From Planets, to Stars and Galaxies*. Proc. IAU Symp. 259, pp. 119–128.

Johns-Krull, C.M. et al., 2009. First magnetic field detection on a class I protostar. *Astrophys. J.*, 700, pp.1440–1448.

Johns-Krull, C.M., 2007. The magnetic fields of classical T Tauri stars. *Astrophys. J.*, 664, pp.975–985.

Johnson, T. V & McGetchin, T.R., 1973. Topography on satellite surfaces and the shape of asteroids. *Icarus*, 18(4), pp.612–620.

Joung, M.K.R., Mac Low, M.-M. & Ebel, D.S., 2004. Chondrule formation and protoplanetary disk heating by current sheets in nonideal magnetohydrodynamic turbulence. *Astrophys. J.*, 606, pp.532–541.

Jourdan, F., Matzel, J.P. & Renne, P.R., 2007. 39Ar and 37Ar Recoil Loss During Neutron Irradiation of Anidine and Plagioclase . *Geochim. Cosmochim Acta*, 71, pp.2791–2808.

Jurewicz, A.J.G., Mittlefehldt, D.W. & Jones, J.H., 1993. Experimental partial melting of the Allende (CV) and Murchison (CM) chondrites and the origin of asteroidal basalts. *Geochim. Cosmochim. Acta*, 57, pp.2123–2139.

Jurewicz, A.J.G., MIttlefehldt, D.W. & Jones, J.H., 1995. Experimental partial melting of the St. Severin (LL) and Lost City (H) chondrites. *Geochim. Cosmochim. Acta*, 59(2), pp.391–408.

Jutzi, M. et al., 2013. The structure of the asteroid 4 {V}esta as revealed by models of planet-scale collisions. *Nature*, 494(7436), pp.207–210.

Jutzi, M. & Asphaug, E., 2011. Mega-ejecta on asteroid {V}esta. *Geophys. Res. Lett.*, 38(1), p.L01102.

Kaus, B.J.P., 2010. Factors that control the angle of shear bands in geodynamic numerical models of brittle deformation. *Tectonophysics*, 484(1), pp.36–47.

Keil, K., 2010. Enstatite achondrite meteorites (aubrites) and the histories of their asteroidal parent bodies. *Chemie der Erde*, 70, pp.295–317.

Kimura, M., Grossman, J.N. & Weisberg, M.K., 2008. Fe-Ni metal in primitive chondrites: Indicators of classification and metamorphic conditions for ordinary and CO chondrites. *Meteorit. Planet. Sci.*, 43, pp.1161–1177.

King, S.D. & Hager, B.H., 1990. The relationship between plate velocity and trench viscosity in Newtonian and power-law subduction calculations. *Geophys. Res. Lett.*, 17(13), pp.2409–2412.

Kirschbaum, C., 1988. Carrier phases for iodine in the Allende meteorite and their associated Xe-129(R)/I-127 ratios - a laser microprobe study. *Geochim. Cosmochim. Acta*, 52, pp.679–699. Available at: <Go to ISI>://WOS:A1988M671600010.

Kirschvink, J.L., 1980. The least-squares line and plane and the analysis of paleomagnetic data: examples from Siberia and Morocco. *Geophys. J. R. Astr. Soc.*, 62, pp.699–718.

Kitts, K. & Lodders, K., 1998. Survey and Evaluation of Eucrite Bulk Compositions. *Meteorit. Planet. Sci.*, 33, pp.A197–A213.

Kivelson, M.G. et al., 1993. Magnetic field signatures near Galileo's closest approach to Gaspra. *Science*, 261, pp.331–334.

Kleine, T. et al., 2009. Hf-W chronology of the accretion and early evolution of asteroids and terrestrial planets. *Geochim. Cosmochim. Acta*, 73, pp.5150–5188.

Kletetschka, G. et al., 2006. TRM in low magnetic fields: a minimum field that can be recorded by large multidomain grains. *Phys. Earth Planet. Inter.*, 154, pp.290–298.

Kohout, T. et al., 2004. The influence of terrestrial processes on meteorite magnetic records. *Phys. Chem. Earth*, 29, pp.885–897. Available at: <Go to ISI>://000224261800004.

Kojima, T. & Tomeoka, K., 1996. Indicators of aqueous alteration and thermal metamorphism on the CV parent body: Microtextures of a dark inclusion from Allende. *Geochim. Cosmochim. Acta*, 60, pp.2651–2666.

Kress, V.C. & Carmichael, I.S.E., 1991. The compressibility of silicate liquids containing Fe203 and the effect of composition, temperature, oxygen fugacity and pressure on their redox states. *Contrib. Mineral Petrol.*, 108, pp.82–92.

Krot, A.N., Petaev, M.I., Scott, E.R.D., et al., 1998. Progressive alteration in CV3 chondrites: More evidence for asteroidal alteration. *Meteorit. Planet. Sci.*, 33, pp.1065–1085.

Krot, A.N., Petaev, M.I., Zolensky, M., et al., 1998. Secondary calcium-iron-rich minerals in the Bali-like and Allende-like oxidized CV3 chondrites and Allende dark inclusions. *Meteorit. Planet. Sci.*, 33, pp.623–645.

Krot, A.N., Scott, E.R.D. & Zolensky, M.E., 1997. Origin of fayalitic olivine rims and lath-shaped matrix olivine in the CV3 chondrite Allende and its dark inclusions. *Meteorit. Planet. Sci.*, 32, pp.31–49.

Kunz, M.W., 2008. On the linear stability of weakly ionized, magnetized planar shear flows. *Mon. Not. R. Astr. Soc.*, 385, pp.1494–1510.

Lambert, I.B. & Wyllie, P.J., 1968. Stability of hornblende and a model for the low velocity zone. *Nature*, 219, pp.1240–1241.

Laneuville, M. et al., 2013. Asymmetric thermal evolution of the Moon. *J. Geophys. Res.: Planets*.

Lanoix, M., Strangway, D.W. & Pearce, G.W., 1978. The primordial magnetic field preserved in chondrules of the Allende meteorite. *Geophys. Res. Lett.*, 5, pp.73–76. Available at: <Go to ISI>://A1978EK71300020.

Lappe, S.-C.L.L. et al., 2013. Comparison and calibration of nonheating paleointensity methods: A case study using dusty olivine. *Geochem. Geophys. Geosyst.*, 14, pp.1–16.

Lappe, S.-C.L.L. et al., 2011. Mineral magnetism of dusty olivine: A credible recorder of pre-accretionary remanence. *Geochem. Geophys. Geosyst.*, 12, p.Q12Z35.

Lauretta, D.S., Buseck, P.R. & Zega, T.J., 2001. Opaque minerals in the matrix of the Bishunpur (LL3.1) chondrite: Constraints on the chondrule formation environment. *Geochim. Cosmochim. Acta*, 65, pp.1337–1353.

Lazarian, A., 2007. Tracing magnetic fields with aligned grains. *J. Quant. Spect. and Radiat. Trans.*, 106, pp.225–256.

Lazarian, A. & Hoang, T., 2008. Alignment of dust with magnetic inclusions: radiative torques and superparamagnetic barnett and nuclear relaxation. *Astrophys. J. Lett.*, 676, p.L25.

Lazarian, A. & Hoang, T., 2007. Radiative torques: analytical model and basic properties. *Mon. Not. R. Astron. Soc.*, 378, pp.910–946.

Leroux, H. et al., 2003. Experimental study and TEM characterization of dusty olivines in chondrites: Evidence for formation by in situ reduction. *Meteorit. Planet. Sci.*, 38, pp.81–94.

Lesur, G., Kunz, M.W. & Fromang, S., 2014. Thanatology in Protoplanetary Discs: The combined influence of Ohmic, Hall, and ambipolar diffusion on dead zones. *Astron. Astrophys.*, 566, p.A56.

Levi, S. & Merrill, M.T., 1976. A comparison of ARM and TRM in magnetite. *Earth Planet. Sci. Lett.*, 32, pp.171–184.

Levine, J., Renne, P.R. & Muller, R.A., 2007. Solar and cosmogenic argon in dated lunar impact spherules. *Geochim. Cosmochim. Acta*, 71, pp.1624–1635.

Levy, E.H. & Araki, S., 1989. Magnetic reconnection flares in the protoplanetary nebula and the possible origin of meteorite chondrules. *Icarus*, 81, pp.74–91.

Li, L. et al., 2011. Paleomagnetism of an Anomalous Eucrite and Implications for the Diversity of Asteroid Dynamos. *AGU Fall Meeting* , p.GP21B–1001.

Lima, E.A., Weiss, B.P., Baratchart, L., et al., 2013. Fast inversion of magnetic field maps of unidirectional planar geological magnetization. *J. Geophys. Res.*, 118, pp.2723–2752.

Lima, E.A., Weiss, B.P., Fu, R.R., et al., 2013. Paleomagnetism on sub-millimeter scales with scanning magnetic microscopy. *AGU Fall Meeting*, GP43B-07.

Lima, E.A., Irimia, A. & Wikswo, J.P., 2006. The magnetic inverse problem. In J. Clarke & A. I. Braginski, eds. *The SQUID Handbook*. Weinheim: Wiley-VCH, pp. 139–267.

Lima, E.A. & Weiss, B.P., 2009. Obtaining vector magnetic field maps from single-component measurements of geological samples. *J. Geophys. Res.*, 114, pp.B06102, doi:10.1029/2008JB006006,.

Lima, E.A. & Weiss, B.P., 2012. Ultra-high sensitivity moment magnetometry of geological samples. *AGU Fall Meeting* , p.GP21A–1151.

Lorand, J.-P., Chevrier, V. & Sautter, V., 2005. Sulfide mineralogy and redox conditions in some shergottites. *Meteorit. Planet. Sci.*, 40, pp.1257–1272.

Lord, R.G., 1964. The aerodynamic resistance to a rotating sphere in the transition regime between free molecule and continuum creep flow. *P. R. Soc. Lond.*, 279, pp.39–49.

Lowrie, W., 1990. Identification of ferromagnetc minerals in a rock by coercivity and unblocking temperature properties. *Geophys. Res. Lett.*, 17, pp.159–162.

Lundstrom, C.C. et al., 1995. Mantle melting and basalt extraction by equilibrium porous flow. *Science*, 270(1958-1961).

Lynden-Bell, D. & Pringle, J.E., 1974. The evolution of viscous discs and the origin of the nebular variables. *Mon. Not. R. Astr. Soc.*, 168, pp.603–337.

MacPherson, G.J., 2007. Calcium-aluminum-rich inclusions in chondritic meteorites. In *Treatise on Geochemistry*. Elsevier, pp. 1–47.

Mandler, B.E. & Elkins-Tanton, L.T., 2013. The origin of eucrites, diogenites, and olivine diogenites: Magma ocean crystallization and shallow magma chamber processes on Vesta. *Meteorit. Planet. Sci.*, pp.1–17.

Marchi, S. et al., 2012. The violent collisional history of asteroid 4 Vesta. *Science*, 336, pp.690–694.

Martín-Hernández, F. et al., 2008. Magnetic anisotropy behaviour of pyrrhotite as determined by low- and high-field experiments. *Geophys. J. Int.*, 174, pp.42–54.

Matas, J. et al., 2000. An improved thermodynamic model of metal-olivine-pyroxene stability domains. *Contrib. Mineral Petrol.*, 2000, pp.73–83.

Matsuyama, I. & Nimmo, F., 2011. Reorientation of {V}esta: Gravity and tectonic predictions. *Geophys. Res. Lett.*, 38(14), p.L14205.

Mayne, R.G. et al., 2009. Petrology of unbrecciated eucrites. *Geochim. Cosmochim. Acta*, 73, pp.794–819.

McCarthy, T.S., Erlank, A.J. & Willis, J.P., 1973. On the origin of eucrites and diogenites. *Earth Planet. Sci. Lett.*, 18, pp.433–442.

McCord, T.B., Adams, J.B. & Johnson, T. V, 1970. Asteroid Vesta: Spectral reflectivity and compositional implications. *Science*, 168, pp.1445–1447.

McCoy, T., Mittlefehldt, D.W. & Wilson, L., 2003. Asteroid differentiation. In D. Lauretta & H. Y. McSween, eds. *Meteorites and the Early Solar System II*. Tucson: Univ. of Arizona Press, pp. 733–745.

McCoy, T.J. et al., 1997. Partial melting and melt migration in the acapulcoite-lodranite parent body. *Geochim. Cosmochim. Acta*, 61(3), pp.639–650.

McCoy, T.J., Dickinson, T.L. & Lofgren, G.E., 1999. Partial melting of the Indarch (EH4) meteorite: A textural, chemical, and phase relations view of melting and melt migration. *Meteorit. Planet. Sci.*, 34, pp.735–746.

McCoy, T.J., Mittlefehldt, D.W. & Wilson, L., 2006. Asteroid differentiation. In D. S. Lauretta & H. Y. McSween, eds. *Meteorites and the Early Solar System II*. Tucson: University of Arizona Press.

McNally, C.P. et al., 2013. Mineral processing by short circuits in protoplanetary disks. *Astrophys. J.*, 767, p.L2.

McNown, J.S. & Malaika, J., 1950. Effects of particle shape on settling velocity at low Reynolds numbers. *Eos Trans. AGU*, 31, pp.74–82.

McNutt, M.K. & Menard, H.W., 1982. Constraints on yield strength in the oceanic lithosphere derived from observations of flexure. *Geophys. J. R. Astr. Soc.*, 71, pp.363–394.

McSween, H.Y., 1977. Petrographic variations among carbonaceous chondrites of the Vigarano type. *Geochim. Cosmochim. Acta*, 41, pp.1777–1790.

Melosh, H.J., 1977. Global tectonics of a despun planet. *Icarus*, 31, pp.221–243.

Metzler, K., Bischoff, A. & Stöffler, D., 1992. Accretionary dust mantles in {CM} chondrites: Evidence for solar nebula processes. *Geochim. Cosmochim. Acta*, 56, pp.2873–2897.

Meyer, C., 2011. Lunar Sample Compendium. , http://www.

Mittlefehldt, D.W. & Lindstrom, M.M., 1991. Generation of abnormal trace element abundances in Antarctic eucrites by weathering processes. *Geochim. Cosmochim. Acta*, 55, p.77.

Miura, H., Nakamoto, T. & Doi, M., 2008. Origin of three-dimensional shapes of chondrules: I. Hydrodynamics simulations of rotating droplet exposed to high-velocity rarefied gas flow. *Icarus*, 197, pp.269–281.

Miura, Y.N. et al., 1998. Noble gases, 81Kr-Kr exposure ages and 244Pu-Xe ages of six eucrites, Bereba, Binda, Camel Donga, Juvinas, Millbillillie, and Stannern. *Geochim. Cosmochim. Acta*, 62, pp.2369–2387.

Miyamoto, H. & Takeda, H., 1994. Cooling Rates of Several Cumulate Eucrites. *Meteoritics*, 29(4), pp.505–506.

Moore, J.G., 2001. Density of basalt core from Hilo drill hole, Hawaii. *J. Volcanol. Geoth. Res.*, 112, pp.221–230.

Morbidelli, A. et al., 2009. Asteroids were born big. *Icarus*, 204, pp.558–573.

Morden, S.J., 1992. A magnetic study of the Millbillillie (eucrite) achondrite: Evidence for dynamo-type magnetising field. *Meteoritics*, 27, pp.560–567.

Morden, S.J. & Collinson, D.W., 1992. The implications of the magnetism of ordinary chondrite meteorites. *Earth Planet. Sci. Lett.*, 109, pp.185–204. Available at: <Go to ISI>://A1992HN98900015.

Moresi, L.N. & Solomatov, V.S., 1995. Numerical investigation of 2{D} convection with extremely large viscosity variations. *Phys. Fluids*, 7, p.2154.

Morin, D., 2008. *Introduction to Classical Mechanics: With Problems and Solutions*, Cambridge University Press.

Mostefaoui, S. et al., 2004. Evidence for live 60Fe in meteorites. *New Astron. Rev.*, 48, pp.155–159.

Mostefaoui, S. et al., 2002. The relative formation ages of ferrmagnesian chondrules inferred from there initial aluminum-26/aluminum-27 ratios. *Meteorit. Planet. Sci.*, 37, pp.421–438.

Muenow, D.W., Keil, K. & McCoy, T.J., 1995. Volatiles in unequilibrated ordinary chondrites: Abundances, sources and implications for explosive volcanism on differentiated asteroids. *Meteorit. Planet. Sci.*, 30, pp.639–645.

Muenow, D.W., Keil, K. & Wilson, L., 1992. High-temperature mass spectrometric degassing of enstatite chondrites: Implications for pyroclastic volcanism on the aubrite parent body. *Geochim. Cosmochim. Acta*, 56, pp.4267–4280.

Muxworthy, A.R. et al., 2011. Heterogeneous shock In porous chondrites: implications for Allende magnetization. *AGU*, p.GP11B–07.

Nagata, T., 1983. High magnetic coercivity of meteorites containing the ordered FeNi (tetrataenite) as the major ferromagnetic constituent. *Proc. Lunar Planet. Sci. Conf. 13th*, pp.A779–A784.

Nagata, T., 1980. Magnetic Classification of Antarctic Meteorites. *Proc. Lunar Planet Sci. Conf. 11th*, pp.1789–1799.

Nagata, T., 1979a. Meteorite magnetism and the early solar system magnetic field. *Phys. Earth Planet. Inter.*, 20, pp.324–341.

Nagata, T., 1979b. Natural remanent magnetization of the fusion crust of meteorites. *Mem. Natl. Inst. Polar Res.*, 15, pp.253–272.

Nagata, T., 1979c. Paleomagnetism of stony meteorites. *Mem. Natl. Inst. Polar Res. Spec. Issue*, 15, pp.280–293.

Nagata, T. & Funaki, M., 1983. Paleointensity of the Allende carbonaceous chondrite. *Mem. Natl. Inst. Polar Res. Spec. Issue*, 30, pp.403–434.

Nakagawa, Y., Sekiya, M. & Hayashi, C., 1986. Settling and growth of dust particles in a laminar phase of a low-mass solar nebula. *Icarus*, 67, pp.375–390.

Nakamura, T. et al., 2008. Chondrulelike objects in short-period comet 81P/Wild 2. *Science*, 321(5896), p.1664.

Nakamura, T. et al., 2011. Itokawa dust particles: A direct link between S-type asteroids and ordinary chondrites. *Science*, 333, pp.1113–1116.

Nakamura, T., 2005. Post-hydration thermal metamorphism of carbonaceous chondrites. *J. Miner. Petrol. Sci.*, 100, pp.260–272.

Nakato, A. et al., 2013. PCA 02012: A unique thermally metamorphosed carbonaceous chondrite. In *Lunar Planet. Sci. Conf. XLIV*. Houston, TX, p. 1696.

Neumann, W., Breuer, D. & Spohn, T., 2014. Differentiation of Vesta: Implications for a shallow magma ocean. *Earth Planet. Sci. Lett.*, 395, pp.267–280.

Neumann, W., Breuer, D. & Spohn, T., 2013. The thermo-chemical evolution of Asteroid 21 Lutetia. *Icarus*, 224, pp.126–143.

Niida, K. & Green, D.H., 1999. Stability and chemical composition of pargasitic amphibole in MORB pyrolite under upper mantle conditions. *Contrib. Mineral Petrol.*, 135, pp.18–40.

Nishiizumi, K., Elmore, D. & Kubik, P.W., 1989. Update on Terrestrial Ages of Antarctic Meteorites. *Earth Planet. Sci. Lett.*, 93, pp.299–313.

Niu, Y. & Batiza, R., 1991. In situ densities of MORB melts and residual mantle: Implications of buoyancy forces beneath mid-ocean ridges. *J. Geol.*, 99, pp.767–775.

Nübold, H. et al., 2003. Magnetic aggregation: II. Laboratory and microgravity experiments . *Icarus*, 165, pp.195–214.

Nübold, H. & Glassmeier, K.-H., 2000. Accretional remanence of magnetized dust in the solar nebula. *Icarus*, 144, pp.149–159.

Ochs, F.A. & Lange, R.A., 1999. The density of hydrous magmatic liquids. *Science*, 283, pp.1314–1317.

Ohtani, E. et al., 2004. Water transport into the deep mantle and formation of a hydrous transition zone. *Phys. Earth Planet. Inter.*, 143, pp.255–269.

Ormel, C.W., Cuzzi, J.N. & Tielens, A., 2008. Co-accretion of chondrules and dust in the solar nebula. *Astrophys. J.*, 679, p.1588.

Ostro, S.J. et al., 2010. Radar imaging of Asteroid 7 {I}ris. *Icarus*, 207(1), pp.285–294.

Papale, P., 1997. Modeling of the solubility of a one-component H2O or CO2 fluid in silicate liquids. *Contrib. Mineral Petrol.*, 126, pp.237–251.

Papoulis, A., 2002. *Probability, Random Bariables and Stochastic Processes* 3rd ed., New York: Mcgraw-Hill College.

Paraskov, G.B., Wurm, G. & Krauss, O., 2007. Impacts into weak dust targets under microgravity and the formation of planetesimals. *Icarus*, 191, pp.779–789.

Pätzold, M. et al., 2011. Asteroid 21 Lutetia: Low mass, high density. *Science*, 334, pp.491–492.

Peale, S.J., 1977. Rotation histories of the natural satellites. In J. A. Burns, ed. *Planetary Satellites*. Tucson, AZ: University of Arizona.

Pearce, C.I., Pattrick, R.A.D. & Vaughan, D.J., 2006. Electrical and magnetic properties of sulfides. *Rev. Mineral. Geochem.*, 61, pp.127–180.

Pham, L.M. et al., 2011. Magnetic field imaging with nitrogen-vacancy ensembles. *New J. Phys.*, 13, p.45021.

Phatak, C. et al., 2009. Determination of magnetic vortex polarity from a single Lorentz Fresnel image. *Ultramicroscopy*, 109, pp.264–267.

Phillips, J.C. & Woods, A.W., 2002. Suppression of large-scale magma mixing by melt-volatile separation. *Earth Planet. Sci. Lett.*, 204, pp.47–60.

Pierazzo, E., Vickery, A.M. & Melosh, H.J., 1997. A Reevaluation of Impact Melt Production. *Icarus*, 127, pp.408–423.

Pieters, C. et al., 2012. Space Weathering on 4 Vesta: Processes and Products. *43rd Lunar Planet. Sci. Conf. Abstract #1254.*

Pohánka, V., 2011. Gravitational field of the homogeneous rotational ellipsoidal body: a simple derivation and applications. *Contrib. Geophys. Geodes.*, 41(2), pp.117–157.

Poitrasson, F. et al., 2004. Iron isotope differences between {E}arth, {M}oon, {M}ars and {V}esta as possible records of contrasted accretion mechanisms. *Earth Planet. Sci. Lett.*, 223(3), pp.253–266.

Pravdivtseva, O. V et al., 2003. The I-Xe record of alteration in the Allende CV chondrite. *Geochim. Cosmochim. Acta*, 67, pp.5011–5026.

Prettyman, T.H. et al., 2012. Elemental mapping by Dawn reveals exogenic H in Vesta's regolith. *Science*, 338, pp.242–246.

Pullaiah, G. et al., 1975. Magnetization changes caused by burial and uplift. *Earth Planet. Sci. Lett.*, 28, pp.133–143.

Purcell, E.M., 1979. Suprathermal rotation of interstellar grains. *Astrophys. J.*, 231, pp.404–416.

Rambaldi, E.R. & Wasson, J.T., 1982. Fine, nickel-poor Fe-Ni grains in the olivine of unequilibrated ordinary chondrites. *Geochim. Cosmochim. Acta*, 46, pp.929–939.

Reddy, V. et al., 2012. Color and Albedo Heterogeneity of Vesta from Dawn. *Science*, 336, pp.700–704.

Reif, F., 1985. *Fundamentals of statistical and thermal physics* E. U. Condon, ed., Singapore: McGraw-Hill.

Reisener, R.J. & Goldstein, J.I., 2000. Experimental studies of taenite decomposition in ordinary chondrites during continuous cooling. *Meteorit. Planet. Sci.*, 35, p.A135.

Reisener, R.J. & Goldstein, J.I., 1999. Microstructural and chemical study of Fe-Ni metal inside Semarkona chondrules. *Lunar Planet. Sci. Conf. XXX* , p.1868.

Reisener, R.J. & Goldstein, J.I., 2003. Ordinary chondrite metallography: Part 1. Fe-Ni taenite cooling experiments. *Meteorit. Planet. Sci.*, 38, pp.1669–1678.

Renne, P.R. et al., 2010. Joint determination of 40K decay constants and 40Ar*/40K for the Fish Canyon sanidine standard, and improved accuracy for 40Ar/39Ar geochronology. *Geochimica et Cosmochimica Acta*, 74(18), pp.5349–5367.

Renne, P.R. et al., 2011. Response to the Comment by W. H. Schwarz et al. on "Joint determination of 40K decay constants and 40Ar*/40K for the Fish Canyon sanidine standard, and improved accuracy for 40Ar/39Ar geochronology" by P.R. Renne et al. (2010). *Geochim. Cosmochim. Acta*, 75, pp.5097–5100.

Richter, I. et al., 2001. First direct magnetic field measurements of an asteroidal magnetic field: DS1 at Braille. *Geophys. Res. Lett.*, 28, pp.1913–1916.

Righter, K. & Drake, M.J., 1997. A magma ocean on Vesta: Core formation and petrogenesis of eucrites and diogenites. *Meteorit. Planet. Sci.*, 32, pp.929–944.

Righter, K. & Neff, K.E., 2007. Temperature and oxygen fugacity constraints on CK and R chondrites and implications for water and oxidation in the early solar system. *Polar Sci.*, 1, pp.25–44.

Rochette, P. et al., 2009. Magnetic classification of stony meteorites: 3. Achondrites. *Meteorit. Planet. Sci.*, 44, pp.405–427.

Roig, F. & Gil-Hutton, R., 2006. Selecting candidate V-type asteroids from the analysis of the Sloan Digital Sky Survey colors. *Icarus*, 183, pp.411–419.

Rozyczka, M., Bodenheimer, P. & Lin, D.N.C., 1996. A numerical study of magnetic buoyancy in an accretion disk. *Astrophys. J.*, 459, pp.371–383.

Rubie, D.C., Nimmo, F. & Melosh, H.J., 2007. Formation of Earth's Core. In P. Olson, ed. *Treatise on Geophysics*. Elsevier, pp. 51–90.

Russell, C.T. et al., 2012. Dawn at Vesta: Testing the Protoplanetary Paradigm. *Science*, 336, pp.684–686.

Le Sage, D. et al., 2013. Optical magnetic imaging of living cells. *Nature*, 496(486-489).

Sahijpal, S. & Gupta, G., 2011. Did the carbonaceous chondrites evolve in the crustal regions of partially differentiated asteroids? *J. Geophys. Res.*, 116, p.doi:10.1029/2010JE003757.

Salmeron, R. & Wardle, M., 2003. Magnetorotational instability in stratified, weakly ionized accretion discs. *Mon. Not. R. Astr. Soc.*, 345, pp.992–1008.

De Sanctis, M.C. et al., 2012. Spectroscopic characterization of mineralogy and its diversity across Vesta. *Science*, 336, pp.697–700.

Sanderson, C., 2010. *Armadillo: An open source {C}++ linear algebra library for fast prototyping and computationally intensive experiments*,

Sano, T. et al., 2000. Magnetorotational instability in protoplanetary disks. II. Ionization state and unstable regions. *Astrophys. J.*, 543, pp.486–501.

Schenk, P., Marchi, S., et al., 2012. Mega-Impacts into Planetary Bodies: Global Effects of the Giant Rheasilvia Impact Basin on Vesta. *43rd Lunar Planet. Sci. Conf. Abstract # 2757.*

Schenk, P., O'Brien, D.P., et al., 2012. The geologically recent giant impact basins at Vesta's south pole. *Science*, 336, pp.694–697.

Schlichting, H.E. & Sari, R., 2007. The effect of semicollisional accretion on planetary spins. *Astrophys. J.*, 658(1), p.593.

Schmidt, B.E. et al., 2009. The shape and surface variation of 2 {P}allas from the {H}ubble {S}pace {T}elescope. *Science*, 326(5950), pp.275–278.

Schmidt, M.W. & Poli, S., 1998. Experimentally based water budgets for dehydrating slabs and consequences for arc magma generation. *Earth Planet. Sci. Lett.*, 163, pp.361–379.

Scott, E.R.D., 2007. Chondrites and the protoplanetary disk. *Annu. Rev. Earth Planet. Sci.*, 35, pp.577–620.

Scott, E.R.D. et al., 2009. Oxygen isotopic constraints on the origin and parent bodies of eucrites, diogenites, and howardites. *Geochim. Cosmochim. Acta*, 73, pp.5835–5853.

Sears, D.W., 1975. Temperature gradients in meteorites produced by heating during atmospheric passage. *Modern Geology*, 5, pp.155–164.

Selkin, P.A. et al., 2000. The effect of remanence anisotropy on paleointensity estimates: a case study from the Archean Stillwater Complex. *Earth Planet. Sci. Lett.*, 183, pp.403–416. Available at: <Go to ISI>://000166030100008.

Sengers, J. V & Kamgar-Parsi, B., 1984. Representative equations for the viscosity of water substance. *J. Phys. Chem. Ref. Data*, 13, pp.185–205.

Shea, E.K. et al., 2012. A Long-Lived Lunar Core Dynamo. *Science*, 335, pp.453–456.

Shimizu, H., Masuda, A. & Tanaka, T., 1983. Cerium anomaly in REE pattern of Antarctic Eucrite. *Mem. Natl. Inst. Polar Res.*, 30, p.341.

Shu, F.H., Shang, H. & Lee, T., 1996. Toward an astrophysical theory of chondrites. *Science*, 271(5255), pp.1545–1552. Available at: <Go to ISI>://A1996TZ98300031.

Sierks, H. et al., 2011. Images of asteroid 21 Lutetia: A remnant planetesimal from the early solar system. *Science*, 334, pp.487–490.

Smits, P.J. et al., 1994. Equation of state description of thermodynamics properties of near-critical and supercritcal water. *J. Phys. Chem.*, 98, pp.12080–12085.

Solomatov, V.A., 2000. Fluid dynamics of a terrestrial magma ocean. In R. Canup & K. Righter, eds. *Origing of the Earth and Moon*. Tucson: University of Arizona Press, pp. 323–338.

Spiegelman, M. & Elliott, T., 1993. Consequences of melt transport for uranium series disequilibrium in young lavas. *Earth Planet. Sci. Lett.*, 118, pp.1–20.

Spitzer, L. & Tukey, J.W., 1951. A theory of interstellar polarization. *Astrophys. J.*, 114, pp.187–205.

Spruit, H.C., 1996. Magnetohydrodynamic jets and winds from accretion disks. In R. A. M. J. Wijers, M. B. Davies, & C. A. Tout, eds. *NATO ASIC Proc. 477: Evolutionary Processes in Binary Stars*. pp. 249–286.

Šrámek, O. et al., 2012. Thermal evolution and differentiation of planetesimals and planetary embryos. *Icarus*, 217, pp.339–354.

Stacey, F.D., 1972. On the role of Brownian motion in the control of detrital remanent magnetization of sediments. *Pure and Applied Geophysics*, 98(1), pp.139–145.

Standish, E.M. & Hellings, R.W., 1989. A determination of the masses of {C}eres, {P}allas, and {V}esta from their perturbations upon the orbit of {M}ars. *Icarus*, 80(2), pp.326–333.

Steiger, R.H. & Jager, E., 1977. Subcommission on Geochronology - Convention on use of decay constants in geochronology and cosmochronology. *Earth Planet. Sci. Lett.*, 36, pp.359–362. Available at: <Go to ISI>://WOS:A1977DX88000001.

Stephens, I.W. et al., 2014. Spatially resolved magnetic field structure in the disk of a T Tauri star. *Nature*, 514, pp.597–599.

Stephenson, A., 1993. Three-axis alternating field demagnetization of rocks and the identification of natural remanent magnetization, gyromagnetic magnetization, and anisotropy. *J. Geophys. Res.*, 98, pp.373–381.

Stephenson, A. & Collinson, D.W., 1974. Lunar magnetic field palaeointensities determined by an anhysteretic remanent magnetization method. *Earth Planet. Sci. Lett.*, 23, pp.220–228.

Stepinski, T.F., 1992. Generation of dynamo magnetic fields in the primordial solar nebula. *Icarus*, 97, pp.130–141.

Sterenborg, M.G. & Crowley, J.W., 2013. Thermal evolution of early solar system planetesimals and the possibility of sustained dynamos. *Phys. Earth Planet. Inter.*, 214, pp.53–73.

Stevenson, D.J., 2010. Planetary magnetic fields: Achievements and prospects. *Space Sci. Rev.*, 152, pp.651–664.

Stöffler, D., Keil, K. & Scott, E.R.D., 1991. Shock metamorphism of ordinary chondrites. *Geochim. Cosmochim. Acta*, 55, pp.3845–3867.

Stolper, E. et al., 2008. The final phase of drilling of the Hawaii Scientific Drilling Project. *AGU*, p.V13D–2141.

Stolper, E.M., 1977. Experimental petrology of eucritic meteorites. *Geochim. Cosmochim. Acta*, 41, pp.587–611.

Strangway, D.W., McMahon, B.E. & Honea, R.M., 1967. Stable Magnetic Remanence in Antiferromagnetic Goethite. *Science*, 158, pp.785–787.

Suavet, C. et al., 2011. Constraining the terrestrial age of micrometeorites using their record of the Earth's magnetic field polarity. *Geology*, 39, pp.123–126.

Suavet, C., Weiss, B.P. & Grove, T.L., 2014. Controlled-atmosphere thermal demagnetization and paleointensity analyses of extraterrestrial rocks. *Geochem. Geophys. Geosyst.*, 15.

Sugiura, N., Lanoix, M. & Strangway, D.W., 1979. Magnetic fields of the solar nebula as recorded in chondrules from the Allende meteorite. *Phys. Earth Planet. Inter.*, 20, pp.342–349. Available at: <Go to ISI>://A1979HY29700029.

Sugiura, N. & Strangway, D.W., 1983. A paleomagnetic conglomerate test using the Abee E4 meteorite. *Earth Planet. Sci. Lett.*, 62, pp.169–179.

Sugiura, N. & Strangway, D.W., 1985. NRM directions around a centimeter-sized dark inclusion in Allende. *Proc. Lunar Planet. Sci. Conf. 15th*, pp.C729–C738.

Swartzendruber, L.J., Itkin, V.P. & Alcock, C.B., 1991. The Fe-Ni (iron-nickel) system. *J. Phase Equilibria*, 12, pp.288–312.

Swindle, T.D. et al., 1983. I-Xe studies of individual Allende chondrules. *Geochim. Cosmochim. Acta*, 47, pp.2157–2177. Available at: <Go to ISI>://WOS:A1983RV31700008.

Swindle, T.D., Caffee, M.W. & Hohenberg, C.M., 1988. Iodine-xenon studies of Allende inclusions: Eggs and the Pink Angel. *Geochim. Cosmochim. Acta*, 52, pp.2215–2227.

Tang, H. & Dauphas, N., 2012. Abundance, distribution, and origin of 60Fe in the solar protoplanetary disk. *Earth Planet. Sci. Lett.*, 359-360, pp.248–263.

Tauxe, L. & Staudigel, H., 2004. Strength of the geomagnetic field in the Cretaceous Normal Superchron: New data from submarinc basaltic glass of the Troodos Ophiolite. *Geochem. Geophys. Geosyst.*, 5, p.doi:10.1029/2003GC000635.

Tauxe, L., Steindorf, J.L. & Harris, A., 2006. Depositional remanent magnetization: Toward an improved theoretical and experimental foundation. *Earth Planet. Sci. Lett.*, 244, pp.515–529.

Taylor, J.R., 2005. *Classical Mechanics*, Univ Science Books.

Teiser, J. & Wurm, G., 2009. High-velocity dust collisions: forming planetesimals in a fragmentation cascade with final accretion. *Mon. Not. R. Astron. Soc.*, 393, pp.1584–1594.

Teplyakova, S.N. et al., 2012. A common parent for the IIE iron meteorites and H chondrites. *Proc. Lunar Planet. Sci. Conf. 43rd*, p.abstract #1130.

Thomas, P.C. et al., 2005. Differentiation of the asteroid {C}eres as revealed by its shape. *Nature*, 437(7056), pp.224–226.

Tikoo, S.M. et al., 2012. Magnetic fidelity of lunar samples and implications for an ancient core dynamo. *Earth Planet. Sci. Lett.*, 337-338, pp.93–103.

Till, C.B., Grove, T.L. & Withers, A.C., 2012. The beginnings of hydrous mantle wedge melting. *Contrib. Mineral Petrol.*, 163, pp.669–688.

Toplis, M.J. et al., 2012. Chondritic models of 4 Vesta: Comparison of predicated internal structure and surface composition/mineralogy with data from the Dawn mission. *Lunar Planet. Sci. Conf. XLIII*, 2152.

Tsuchiyama, A. et al., 2003. Three-dimensional structures of chondrules and their high-speed rotation. *Lunar Planet. Sci. Conf. XXXIV*, p.1271.

Turcotte, D.L. & Schubert, G., 2002. *Geodynamics*, New York : University of Cambridge Press.

Turner, N.J. et al., 2014. Transport and accretion in planet-forming disks. In *Protostars and Planets VI.* Tucson, AZ: University of Arizona Press.

Turner, N.J. & Sano, T., 2008. Dead Zone Accretion Flows in Protostellar Disks. *Astrophys. J. Lett.*, 679, pp.L131 – L134.

Turner, N.J., Sano, T. & Dziourkevitch, N., 2007. Turbulent mixing and the dead zone in protostellar disks. *Astrophys. J.*, 659, pp.729–737.

Uehara, M. et al., 2011. Magnetic microstructures of metal grains in equilibrated ordinary chondrites and implications of paleomagnetism of meteorites. *Earth Planet. Sci. Lett.*, 306, pp.241–252.

Uehara, M. et al., 2012. Magnetic study of meteorites recovered in the Atacama desert (Chile): Implications for meteorite paleomagnetism and the stability of hot desert surfaces. *Phys. Earth Planet. Inter.*, 200-201, pp.113–123.

Uehara, M. & Nakamura, N., 2006. Experimental constraints on magnetic stability of chondrules and the paleomagnetic significance of dusty olivines. *Earth and Planetary Science Letters*, 250, pp.292–305.

Usui, Y. et al., 2009. Evidence for a 3.45-billion-year-old magnetic remanence: Hints of an ancient geodynamo from conglomerates of South Africa. *Geochem. Geophys. Geosyst.*, 10, pp.Q09Z07, doi:10.1029/2009GC002496.

Vaughan, D.J. & Craig, J.R., 1978. *Mineral Chemistry of Metal Sulfides*, Cambridge, UK: Cambridge University Press.

Velbel, M.A., 1988. The Distribution and Significance of Evaporitic Weathering Products on Antarctic Meteorites. *Meteoritics*, 23, pp.151–159.

Vernazza, P. et al., 2006. Asteroid colors: A novel tool for magnetic field detection: The case of Vesta. *Astron. Astrophys.*, 451, pp.L43–L46.

Walker, D. et al., 1978. Dynamic Crystallization of a Eucrite Basalt. *Proc. Lunar Planet Sci. Conf. 9th*, pp.1369–1391.

Walker, D. & Grove, T.L., 1993. Ureilite smelting. *Meteoritics*, 28, pp.629–636.

Wang, M., Chen, Q. & Ding, Q., 2010. Synthesis of SiO2 spheres with magnetic cores: Implications for the primary accretion in the solar nebula. *J. Geophys. Res.*, 115, p.E05005.

Wardle, M., 2007. Magnetic fields in protoplanetary disks. *Astrophys. Space Sci.*, 311, pp.35–45.

Warren, P.H., 2011. Ejecta--megaregolith accumulation on planetesimals and large asteroids. *Meteor. Planet. Sci.*, 46(1), pp.53–78.

Warren, P.H. & Jerde, E.A., 1987. Composition and origin of Nuevo Laredo Trend eucrites. *Geochim. Cosmochim. Acta*, 51, pp.713–725.

Warren, P.H. & Rasmussen, K.L., 1987. Megaregolith insulation, internal temperatures, and bulk uranium content of the {M}oon. *J. Geophys. Res.*, 92(B5), pp.3453–3465.

Wasilewski, P., 1988. Magnetic characterization of the new magnetic mineral tetrataenite and its contrast with isochemical taenite. *Phys. Earth Planet. Inter.*, 52, pp.150–158.

Wasilewski, P., 1981. New magnetic results from Allende C3(V). *Phys. Earth Planet. Inter.*, 26(1-2), pp.134–148. Available at: <Go to ISI>://A1981MA37300013.

Wasilewski, P.J. & Saralker, C., 1981. Stable NRM and mineralogy in Allende: Chondrules. *Proc. Lunar Planet. Sci. Conf. 12th*, pp.1217–1227.

Wasson, J.T., 1990. Ungrouped iron meteorites in Antarctica: Origin of anomalously high abundance. *Science*, 249, pp.900–902.

Watson, G.S., 1956. A test for randomness. *Mon. Not. R. Astr. Soc.*, 7, pp.160–161.

Watts, A.B. & Zhong, S., 2000. Observations of flexure and the rheology of oceanic lithosphere. *Geophys. J. Int.*, 142, pp.855–875.

Weaver, R., Roberts, A.P. & Barker, A.J., 2002. A late diagenetic (syn-folding) magnetization carried by pyrrhotite: implications for paleomagnetic studies from magnetic iron sulphide-bearing sediments. *Earth Planet. Sci. Lett.*, 200, pp.371–386.

Webster, J.D., 1997. Chloride solubility in felsic melts and the role of chloride in magmatic degassing. *J. Petrol.*, 38, pp.1793–1807.

Weidenschilling, S.J., 1977. Aerodynamics of solids bodies in the solar nebula. *Mon. Not. R. Astr. Soc.*, 180, pp.57–70.

Weidenschilling, S.J., 1984. Evolution of grains in a turbulent solar nebula. *Icarus*, 60, pp.553–567.

Weidenschilling, S.J., 2011. Initial sizes of planetesimals and accretion of the asteroids. *Icarus*, 214(2), pp.671–684.

Weidenschilling, S.J. & Cuzzi, J.N., 2006. Accretion dynamics and timescales: Relation to chondrites. In D. S. Lauretta & H. Y. McSween, eds. *Meteorites and the Early Solar System II*. Tucson: University of Arizona Press, pp. 473–485.

Weisberg, M.K., McCoy, T.J. & Krot, A.N., 2006. Systematics and evaluation of meteorite classification. In D. S. Lauretta & H. Y. McSween, eds. *Meteorites and the Early Solar System II*. Tucson: Univesity of Arizona, pp. 19–52.

Weiss, B.P. et al., 2008. Magnetism on the angrite parent body and the early differentiation of planetesimals. *Science*, 322, pp.713–716.

Weiss, B.P. et al., 2007. Paleomagnetic analysis using SQUID microscopy. *J. Geophys. Res.*, 112, pp.B09105, doi:10.1029/2007JB004940.

Weiss, B.P. et al., 2010. Paleomagnetic records of meteorites and early planetesimal differentiation. *Space Sci. Rev.*, 152, pp.341–390.

Weiss, B.P. et al., 2012. Possible evidence for partial differentiation of asteroid Lutetia from Rosetta. *Planet. Space Sci.*, 66, pp.137–146.

Weiss, B.P. & Elkins-Tanton, L.T., 2013. Differentiated planetesimals and the parent bodies of chondrites. *Annu. Rev. Earth Planet. Sci.*, 41, p.21.

Weisstein, E.W., Circle point picking. *Mathworld- A Wolfram Web Resource*. Available at: http://mathworld.wolfram.com/CirclePointPicking.html.

Weisstein, E.W., Sphere point picking. *MathWorld- A Wolfram Web Resource*. Available at: http://mathworld.wolfram.com/SpherePointPicking.html.

Wieczorek, M.A. et al., 2013. The crust of the moon as seen by GRAIL. *Science*, 339, pp.671–675.

Wieczorek, M.A., Weiss, B.P. & Stewart, S.T., 2012. An Impactor Origin for Lunar Magnetic Anomalies. *Science*, 335, pp.1212–1215.

Willacy, K. et al., 1998. Gas and grain chemistry in a protoplanetary disk. *Astron. Astrophys.*, 338, pp.995–1005.

Williams, J.P. & Cieza, L.A., 2011. Protoplanetary disks and their evolution. *Annu. Rev. Astron. Astrophys.*, 49, pp.67–117.

Wilson, L. & Keil, K., 2012. Volcanic activity on differentiated asteroids: A review and analysis. *Chem. Erde*, 72, pp.289–321.

Winklhofer, M., Fabian, K. & Heider, F., 1997. Magnetic blocking temperatures of magnetite calculated with a three-dimensional micromagnetic model. *J. Geophys. Res.*, 102, pp.22695–22709.

Wood, J.A., 1959. *Silicate Meteorite Structures and the Origin of Meteorites*. Cambridge, MA: Massachusetts Institute of Technology.

Wurm, G., Paraskov, G. & Krauss, O., 2005. Growth of planetesimals by impacts at 25 m/s. *Icarus*, 178, pp.253–263.

Yamaguchi, A. et al., 2002. A New Source of Basaltic Meteorites Inferred from Northwest Africa 011. *Science*, 296, pp.334–336.

Yamaguchi, A. et al., 1994. Textural variations and impact history of the Millbillillie eucrite. *Meteoritics*, 29, pp.237–245.

Yamaguchi, A., Taylor, G.J. & Keil, K., 1996. Global crustal metamorphism of the eucrite parent body. *Icarus*, 124, pp.97–112.

Yang, C.-W. & Williams, D.B., 1996. A revision of the Fe Ni phase diagram low temperatures. *J. Phase Equilibria*, 17, pp.522–531.

Young, E., Zhang, K. & Schubert, G., 2003. Conditions for pore water convection within carbonaceous chondrite parent bodies: Implications for planetesimal size and heat production. *Earth Planet. Sci. Lett.*, 213, pp.249–259.

Young, E.D., 2001. The hydrology of carbonaceous chondrite parent bodies and the evolution of planet progenitors. *Phil. Trans. R. Soc. London A*, 359, pp.2095–2110.

Yu, Y. & Tauxe, L., 2006. Acquisition of viscous remanent magnetization. *Phys. Earth Planet. Inter.*, 159, pp.32–42.

Zhong, S. & Zuber, M.T., 2000. Long-wavelength topographic relaxation for self-gravitating planets and implications for the time- dependent compensation of surface topography. *J. Geophys. Res.*, 105, pp.4135–4164.

Zolensky, M.E. et al., 2006. Mineralogy and petrology of comet 81P/{W}ild 2 nucleus samples. *Science*, 314, pp.1735–1739.

Zsom, A. et al., 2010. The outcome of protoplanetary dust growth: pebbles, boulders, or planetesimals? *Astron. Astrophys.*, 513, p.A57.

Zuber, M.T., Smith, D.E., Lehman, D.H., et al., 2013. {G}ravity {R}ecovery and {I}nterior {L}aboratory ({GRAIL}): Mapping the lunar interior from crust to core. *Space Sci. Rev.*, pp.1–22.

Zuber, M.T., Smith, D.E., Watkins, M.M., et al., 2013. Gravity field of the {M}oon from the {G}ravity {R}ecovery and {I}nterior {L}aboratory ({GRAIL}) mission. *Science*, 339(6120), pp.668–671.